UNIVERSITY OF BELGRADE
SCHOOL OF ELECTRICAL ENGINEERING

Marko M. Krstić

STATICAL AND DYNAMICAL CHARACTERISTICS OF INJECTION-LOCKED FABRY-PÉROT LASER DIODES

Doctoral Dissertation

Belgrade, 2015.

UNIVERZITET U BEOGRADU
ELEKTROTEHNIČKI FAKULTET

Marko M. Krstić

STATIČKE I DINAMIČKE KARAKTERISTIKE INJEKCIONO SINHRONIZOVANIH FABRI-PERO LASERSKIH DIODA

doktorska disertacija

Beograd 2015.

Mentor:

dr Dejan Gvozdić, redovni profesor
Univerzitet u Beogradu – Elektrotehnički fakultet

Članovi komisije:

dr Jasna Crnjanski, docent
Univerzitet u Beogradu – Elektrotehnički fakultet

dr Jovan Radunović, redovni profesor u penziji
Univerzitet u Beogradu – Elektrotehnički fakultet

dr Ljupčo Hadžievski, naučni savetnik
Univerzitet u Beogradu – Institut za nuklearne nauke "Vinča"

dr Željko Đurović, redovni profesor
Univerzitet u Beogradu – Elektrotehnički fakultet

Datum odbrane: _____

Dissertation title: Statical and dynamical characteristics of injection-locked Fabry-Pérot laser diodes

Abstract: Injection locking is a nonlinear phenomenon in which two (or more) self-sustained oscillators can synchronize their oscillations, i.e., their operating frequencies and phases, provided that there exists some kind of coupling between them. This phenomenon can be observed in diverse disciplines such as mechanics, physics, engineering, even biology, psychology, etc. With development of electronics, injection locking has been used in a number of engineering applications comprising oscillators such as electrical or microwave, while recent breakthroughs in photonics paved the way for injection locking to be employed in optical systems such as lasers. Semiconductor lasers represent a kind of electrically driven self-sustained oscillators, which support electromagnetic oscillations inside the resonator cavity. By using various feedback mechanisms, the number of supported oscillations or modes can be controlled, providing single- or multi-mode operation of the laser. One of the sophisticated methods to control oscillations in one laser indeed relies on synchronization with another laser, i.e., on the technique of injection locking. In the case of injection-locked lasers, light from one, which is referred as "master" laser, is injected into the cavity of another ("slave") laser, to provide for the coupling of the two oscillators. Under certain conditions, the slave laser can become stably locked to the frequency of the master one. In this technique, successful synchronization, i.e., stable locking of the two lasers, depends on injection parameters, which are the number of injected photons, (injection power), and the frequency detuning between the free-running frequencies of the master and slave lasers.

The technique of injection locking has been proven to benefit laser dynamics, by increasing side-mode-suppression-ratio, thus providing single-mode operation, damping the relaxation oscillations, increasing the modulation bandwidth, reducing the linewidth and frequency chirping, etc. For that matter, injection-locked semiconductor lasers are proposed as cost-effective transmitter solutions in modern architectures of optical networks, such as wavelength division multiplexing passive optical networks, where injection-locked lasers can substitute for much more expensive tunable lasers, since their frequency, i.e., wavelength can be controlled via injection locking. On the other hand, injection locking in semiconductor lasers can lead to optical bistability, which can be employed in modern photonics integrated circuits, aiming for all-optical signal processing, tending to surpass the bottleneck imposed by the electronic layer in existing hybrid optical networks. Injection-locked optically bistable components can be used for realization of all-optical flip-flops, memories, switches, logic gates, for all-optical wavelength conversion and other fundamental building blocks of every all-optical signal processing system.

This thesis deals with semiconductor laser diodes with Fabry-Pérot cavities, i.e., multi-mode lasers, which are subjected to side-mode (intermodal) injection locking, meaning that external light is injected into one of the slave laser's longitudinal side-modes. The investigation is based on a multi-mode rate equations system which comprises extra terms describing the locking phenomenon. On the basis of this model, with exactly calculated gain for InGaAsP/InGaAlAs multiple quantum well active region, static and dynamic characteristics are studied theoretically, while some results are experimentally confirmed.

At first, a detailed asymmetrical locking range is defined and discussed with respect to the injection power, frequency detuning and linewidth enhancement factor. Special attention is paid to the locking range in the domain of negative frequency detuning, where folding of the locking range along the four-wave mixing boundary is found. In the boundaries of the locking range, stationary analysis shows that for a fixed slave laser bias current, there is a range of injection parameters (injection power and frequency detuning), in which the slave laser can exhibit up to three steady-states. The nature of the steady-states is discussed from the perspective of carrier rate versus carrier concentration phase plot which reveals that one of these states is not a consequence of injection locking, but emerges due to the interplay of the unlocked modes, and can be obtained only by a detailed model, which includes at least one longitudinal mode besides the injection-locked one. Further on, these phase plots reveal that one stationary solution represents a repelling stationary point, and thus remaining two attractors can provide bistable output of the slave laser. As a consequence of this bistability, the slave laser exhibits a hysteresis cycle in the output, in terms of output power (and consequently side-mode-suppression-ratio) and phase. The hystereses can be circulated by varying the injection power or frequency detuning, and their formation and circulation is explained by the means of carrier rate versus carrier concentration phase plots. In addition to this, our model predicts that the hysteresis cycle can also be obtained with fixed values of injection power and frequency detuning, and by varying the slave laser bias current. However, our further analysis, regarding the slave laser dynamical stability, switching time and switching energy between the two stable hysteresis branches, preliminarily shows that higher values of the bias current deteriorate the slave laser stability, and lead to high switching times and high required switching energies, making these kinds of loops unattractive from the perspective of applications in all-optical systems. For these reasons, in this thesis we focus on the injection power and frequency detuning variations as the two mechanisms for outlining the hysteresis loops and switching between the branches, and leave the bias current dependent hysteresis for some future work. As a matter of fact, the presence of the hysteresis in the power output of the laser, and its counterclockwise circulation by variation of the injection power is experimentally confirmed. In addition to this, widths and heights of output power,

side-mode-suppression-ratio and phase hystereses are theoretically studied with respect to injection power, frequency detuning, as well as injection-locked side-mode order.

On the basis of derived small-signal model, obtained hystereses are subjected to Lyapunov stability analysis, and detailed, multivalued stability map, with respect to injection power and frequency detuning, is presented. This map thoroughly studies characteristics of the available stationary states in the domain of the locking range, and shows that in a certain range of injection parameters, two attractive stationary points can be simultaneously stable, and provide for bistability. In addition to this, the map emphasises the importance of the unlocked modes, since it proves that the slave laser stability is greatly affected by the number of the longitudinal modes included in the model. In the case of a simple model, comprising only the injection-locked mode, the map resembles the common stability map found in the literature. However, a detailed model leads to a significantly different stability map, comprising a complex stability distribution.

Motivated by possible applications of the injection-locked induced optical bistability in realization of all-optical signal processing components, such as all-optical flip-flops, the thesis deals with possible switching between stable states of the slave laser. For that matter, a simple analytical method for characterization of the switching processes is derived. The analytical method is derived under certain approximations, which reduce the accuracy of the calculation, but the method proves to be very useful for both phenomenological, i.e., qualitative, as well as quantitative description of the switching process. The exact numerical method gains its significance once highly precise calculation, and deeper insight in the slave laser dynamics during the switching process, are required. On the premises of the analytical method, two switching mechanisms are analyzed: switching by master laser's injection power variation, which provides an amplitude controlled slave laser, and switching by frequency detuning variation, which provides a phase controlled slave laser. Again, by the means of the carrier rate versus carrier concentration phase plots, under the assumptions of the analytical method, the trajectories of both switching methods are predicted and analyzed. This method predicts that switching times and energies can be very low, in order of 10 ps, and 1 fJ, respectively, although it shows that, in terms of switching time and energy, there is a discrepancy between the two switching directions. However, in the case of frequency detuning variation, it can predict the switching time for just one switching direction. Nevertheless, the method provides a possibility to more directly investigate the influence of parameters such as linewidth enhancement factor and active region volume of the slave laser on the switching characteristics. The presented results show that, in the case of amplitude controlled switching, higher values of linewidth enhancement factor and active region volume can lead to shorter switching time, and lower switching energies.

Finally, a detailed numerical model, which relies on the full scale multi-mode rate equations system, is employed in investigation of the switching characteristics in the case of frequency detuning variation. New, exact transient switching trajectories are presented in the carrier rate versus carrier concentration phase plot, and studied to find that they differ from the trajectories predicted by the stationary analysis. The switching time is here classified as the switching time of the master laser, i.e., the duration of the frequency detuning variation, which gives results comparable with the results obtained from our analytical model. However, the exact numerical model provides a possibility to study the switching time of the slave laser, defined as the slave laser locking time, after the variation of the frequency detuning. This classification, as well as quantitative description of both master and slave lasers' switching times can be very attractive from the viewpoint of advanced modulation formats, which can employ amplitude of phase modulation, since injection power or frequency detuning variation switching can provide such modulations. Our results show that there is a high discrepancy between the switching directions in terms of overall switching time, hence three methods for switching time optimization are proposed. Methods comprise the change of the initial conditions of the slave laser, variation of the master laser's switching time, which proves to affect the slave laser's switching time, and finally introduction of the external cavity, in order to modify the cavity losses for the injection-locked side-mode. It has been found that the shortest switching time of the master laser, which allows for the slave laser to be successfully switched by frequency detuning variation, reaches the values of several picoseconds, and goes up to 200 ps. A disproportion of the slave laser's switching times with respect to the switching direction is found (3 ns versus 0.3 ns). Upon applying the proposed optimization methods, it has been found that a modest increase of the master laser's switching time establishes a balance between the two directions of the slave laser's switching, providing almost one order of magnitude improvement in comparison to the results achieved for the shortest possible master laser's switching times.

Keywords: injection locking, optical bistability, amplitude controlled switching, phase controlled switching, switching time

Research area: Photonics and Quantum Electronics

Research sub-area: Optoelectronics and Photonics Communication

UDC number: 621.3

Naslov teze: Statičke i dinamičke karakteristike injekciono sihronizovanih Fabri-Pero laserskih dioda

Rezime: Injekciona sinhronizacija je nelinearni fizički fenomen u kome dva (ili više) oscilatora mogu da sinhroniziju svoje frekvencije i faze, ukoliko postoji određena sprega između njih. Ovaj fizički fenomen prisutan je u raznim sferama nauke, od mehanike, fizike i inženjerstva, preko biologije, čak i do psihologije, itd. Sa razvojem elektronike, injekciona sinhronizacija počinje da nalazi svoje mesto u oscilatornim električnim i mikrotalasnim sistemima, dok poslednja otkrića na polju fotonike pružaju priliku da ova tehnika bude primenjena i u optičkim oscilatornim sistemima, poput lasera. Poluprovodnički laseri su vrsta električno pobuđenih oscilatora koji podržavaju elektromagnetne oscilacije u laserskom rezonatoru. Postoje razni tipovi mehanizama na bazi povratne sprege koji se koriste za kontrolu podržanih modova oscilacija, čime je moguće postići monomodni ili multimodni rad lasera. Jedna od naprednijih tehnika se upravo bazira na efektu injekcione sinhronizacije sa drugim laserom, tj. svetlost iz jednog (vodećeg) lasera se injektuje u rezonator drugog (pratećeg) lasera, koji u slučaju da su ispunjeni određeni uslovi, postaje stabilno sinhronizovan prema frekvenciji i fazi pratećeg lasera. Uspešnost injekcione sinhronizacije zavisi od parametra injekcije, na prvom mestu od koncentracije injektovanih fotona, tj. injektovane snage kao i od frekvencijske razdešenosti dva lasera.

Pokazano je da ova tehnika može da doprinese poboljšanju dinamike lasera, tako što povećava potiskivanje neželjenih modova i obezbeđuje monomodni režim rada, prigušuje relaksacione oscilacije u prelaznim režimima pratećeg lasera, povećava propusni opseg, smanjuje širinu linije i frekvencijski čirp, itd. Zbog pomenutih prednosti, injekciono sinhronizovani laseri predloženi su za primenu u modernim arhitekturama optičkih mreža, poput pasivnih optičkih mreža sa multipleksiranjem po talasnim dužinama, u kojima bi mogli da zamene daleko skuplje i složenije podesive lasere, s obzirom na to da se njihova talasna dužina može kontrolisati pomoću jednog vodećeg lasera. Drugi važan domen primene oslanja se na optičku bistabilnost koja se javlja u ovakvim laserskim sistemima, a koja može biti upotrebljena u modernim fotonskim integrisanim kolima, sa ciljem realizacije sve-optičke obrade signala, koja ima potencijal da prevaziđe ograničenja elektronskog procesiranja u hibridnim optičkim sistemima. Optička bistabilnosti injekciono sihronizovanih lasera može se koristiti za realizaciju fotonskih bistabilnih komponenti poput sve-optičkih flip-flopova, memorija, prekidača, logičkih kola, sve-optičkih konvertora talasnih dužina i ostalih fundamentalnih, gradivnih komponenata svakog sistema za sve-optičku obradu signala.

Ova disertacija bavi se poluprovodničkim multimodnim laserima sa Fabri-Pero rezonatorom, na koje se primenjuje injekciona sihronizacija pomoću vodećeg lasera, pri

čemu se svetlost injektuje u neki od sporednih, longitudinalnih modova pratećeg lasera. Teorijska analiza statičkih i dimaničkih karakteristika pratećeg lasera sprovedena je na bazi izvedenog modela brzinskih jednačina koje opisuju dinamiku pratećeg lasera u režimu injekcione sinhronizacije i egzaktno proračunatog pojačanja InGaAsP/InGaAlAs aktivne oblasti na bazi višestrukih kvantnih jama, dok su određeni rezultati potvrđeni i eksperimentalno.

Izvedena je detaljna analiza asimetrične oblasti sprezanja u funkciji od injekcione snage, frekvencijske razdešenosti i Henrijevog faktora. Posebna pažnja je posvećena oblasti sprezanja u domenu negativnih frekvencijskih razdešenosti, gde je pokazano savijanje ove oblasti po granici četvorotalasnog mešanja. Unutar granica sprezanja sprovedena je stacionarna analiza, koja pokazuje da postoji opseg injekcionih snaga i frekvencijskih razdešenosti u kome prateći laser može da ima do tri stacionarna stanja. Iz perspektive faznih dijagrama vremenske promene koncentracije nosilaca u funkciji koncentracije nosilaca, diskutovana je priroda ovih stacionarnih stanja i pokazano je da jedno od tri stanja nije posledica injekcione sinhronizacije, već uticaja nespregnutih modova pratećeg lasera. Pokazano je da je ovo stanje moguće identifikovati i karakterisati samo primenom detaljnog modela koji uzima u obzir uticaj nespregnutih modova. Analizom faznih dijagrama potvrđeno je da jedna od tri tačke predstavlja repulzivnu (odbojnu) stacionarnu tačku, dok druge dve imaju atraktivan (privlačan) karakter i mogu da dovedu do bistabilnosti pratećeg lasera. Kao posledica ove bistabilnosti, u izlazu pratećeg lasera formiraju se histerezisne petlje, od kojih su prikazane tri vrste: petlje po izlaznoj snazi, po faktoru potiskivanja sporednih modova i po fazi pratećeg lasera. Kretanje po histerezisima je moguće izvršiti varijacijom snage injekcije ili frekvencijske razdešenosti. Pored toga, naš model predviđa i formiranje histerezisa varijacijom struje polarizacije pratećeg lasera. Ipak, naša dalja, preliminarna analiza ovakvih histerezisa, pokazuje da ovakvi histerezisi nisu previše atraktivni sa aspekta praktične primene u sve-optičkim sistemima, s obzirom na to da se pokazuje da prateći laser, u slučaju visokih struja polarizacije ispoljava izražene nestabilnosti, kao i loše karakteristike sa aspekta komutacije između stabilnih stanja. Iz pomenutih razloga, u ovoj tezi fokus je prebačen na histerezise koji su dobijeni varijacijom snage injekcije i frekvencijske razdešenosti, dok se analiza histerezisa po struji ostavlja za neki budući rad. Proces formiranja i kretanja po histerezisnim petljama teorijski je analiziran i objašnjen iz perspektive faznih dijagrama vremenske promene koncentracije nosilaca u zavisnosti od koncentracije nosilaca. Postojanje histerezisa u izlaznoj snazi pratećeg lasera, kao i kretanje kroz histerezis varijacijom injekcione snage iz vodećeg lasera, potvrđeno je i eksperimentalno. Konačno, teorijski je ispitivana zavisnost širina i visina histerezisa u funkciji od injekcione snage, frekvencijske razdešenosti i izbora injektovanog moda.

Za potrebe analize stabilnosti, razvijen je model “malih signala” na osnovu kog je primenjena analiza stabilnosti po teoriji Ljapunova. Predstavljena je nova, detaljna mapa stabilnosti pratećeg lasera u funkciji od injekcione snage i frekvencijske razdešenosti. Pomoću ove mape, indirektnom metodom Ljapunova, detaljno je analizirana priroda stacionarnih stanja pratećeg lasera i pokazano je da u određenom opsegu injekcionih parametara, oba atraktora pokazuju stabilan karakter i time obezbeđuju bistabilnost pratećeg lasera. Pored toga, prezentovana mapa naglašava značaj nespregnutih modova na stabilnost pratećeg lasera. U slučaju prostog modela koji uračunava samo uticaj injektovanog moda, dobijena mapa podseća na rezultat prisutan u relevantnoj literaturi. Ipak, detaljan model vodi ka bitno drugačijoj i složenoj raspodeli stabilnosti u domenu sprezanja, čime se naglašava pomenuti uticaj nespregnutih modova.

U skladu sa predloženom primenom injekciono sinhronizovanih bistabilnih lasera u realizaciji sve-optičkih komponenti poput sve-optičkih flip-flopova, teza se bavi analizom komutacije između stabilnih stanja pratećeg lasera. Za potrebe ove analize izveden je i predstavljen analitički metod za karakterizaciju komutacionih procesa u pratećem laseru. Ovaj model razvijen je na premisama određenih aproksimacija koje redukuju preciznost dobijenih rezultata, ali se pokazuje da ovaj model može relativno dobro da opiše procese komutacije, kako fenomenološki, tj. kvalitativno, tako i kvantitativno. Egzaktan numerički model dobija na značaju onda kada se ukazuje potreba za preciznim izračunavanjem karakteristika komutacije, kao i za dublje razumevanje dinamike pratećeg lasera, tokom procesa komutacije. Na bazi analitičkog modela, predstavljene su i analizirane dve metode komutacije: varijacija injekcione snage, koja obezbeđuje amplitudski kontrolisanu komutaciju i varijacija frekvencijske razdešenosti, koja obezbeđuje fazno kontrolisanu komutaciju. Na primeru faznih dijagrama vremenske promene koncentracije nosilaca u funkciji koncentracije nosilaca, pokazane su i analizirane trajektorije komutacije za obe predložene metode. Analitički metod predviđa jako mala vremena i male energije komutacije, koja su reda veličine 10 ps i 1 fJ, respektivno, ali i veliku razdešenost komutacionih vremena i energija po smerovima komutacije. S druge strane, analitički metod, u slučaju frekvencijski, odnosno fazno kontrolisane komutacije, ne može u potpunosti da karakteriše komutaciju, tj. ne može da proračuna vreme komutacije za jedan komutacioni smer. I pored toga, metod je koristan jer pruža priliku da se direktno ispituje uticaj pojedinih parametara na vreme i energiju komutacije, kao što je Henrijev faktor i zapremina aktivne oblasti pratećeg lasera. Rezultati ove analize pokazuju da veće vrednosti Henrijevog faktora i veće vrednosti zapremine aktivne oblasti pratećeg lasera dovode do brže i energetski efikasnije komutacije.

Konačno, na bazi multimodnih brzinskih jednačina pratećeg lasera, razvijen je detaljan numerički model, koji je upotrebljen za karakterizaciju fazno kontrolisane ko-

mutacije. Kroz fazne dijagrame vremenske promene koncentracije nosilaca u funkciji koncentracije nosilaca, predstavljene su i diskutovane egzaktne tranzijentne trajektorije komutacije, koje se razlikuju od stacionarnih trajktorija dobijenih na osnovu analitičkog modela. Ukupno vreme komutacije rasčlanjeno je na vreme komutacije vodećeg lasera, koje je definisano kao vreme trajanja varijacije frekvencijske razdešenosti i dobijeni rezultati pokazuju kvalitativno slaganje sa rezultatima analitičkog modela. Ipak, egzaktan numerički model pruža šansu da se ispituje i vreme komutacije pratećeg lasera, definisano kao vreme uspostavljanja stacionarnog stanja nakon završene varijacije vodećeg lasera. Rezultati dobijeni na osnovu ovog modela pokazuju izraženu razdešenost vremena po smerovima komutacije. Ovakva klasifikacija vremena komutacije, kao i njihov egzaktan proračun, značajni su sa aspekta naprednih modulacionih formata, koji koriste amplitudsku ili faznu modulaciju, a koju je moguće ostvariti komutacijom pomoću injekcione snage ili frekvencijske razdešenosti. Predložene su tri metode optimizacije: varijacija početnog stanja pratećeg lasera, varijacija vremena komutacije vodećeg lasera i upotreba eksterne laserske rezonatorske šupljine u postojećem rezonatoru pratećeg lasera u cilju varijacije rezonatorskih gubitaka injekcionog moda. Pokazano je da za minimalno vreme komutacije vodećeg lasera, za koje je moguće izvršiti komutaciju pratećeg lasera, vreme komutacije ima vrednosti u opsegu od nekoliko ps do 200 ps. Pokazuje se da disproporcija vremena komutacije po smerovima komutacije dominantno potiče od različitih vremena komutacije pratećeg lasera, koje za jedan smer iznosi oko 0.3 ns, dok za drugi smer ima vrednosti za red veličine veće, oko 3 ns. Predložene metode optimizacije dovode do ujednačavanja vremena komutacije po smerovima, a da pri tome malo povećanje vremena komutacije vodećeg lasera dovodi do značajnog (za red veličine) smanjenja vremena komutacije pratećeg lasera.

Ključne reči: injekciona sinhronizacija, optička bistabilnost, amplitudski kontrolisana komutacija, fazno kontrolisana komutacija, vreme komutacije

Naučna oblast: Fotonika i kvantna elektronika

Uža naučna oblast: Optoelektronika i fotonske komunikacije

UDK broj: 621.3

Contents

Chapter 1

Introduction

Oscillations locking is as well known physical phenomenon in which, under the assumption that certain criteria is met, two coupled oscillators can adjust their frequencies and phases and thus operate in unison. Semiconductor lasers represent a kind of electrically driven oscillators which support oscillations of electromagnetic field and as such, two (or more) lasers can be subjected to oscillations locking, provided that there is some kind of coupling between them. This coupling can be provided by injecting the light from one (master) into the resonator cavity of the other (slave) laser. As this presented technique of injection locking can lead to optical bistability of slave laser, injection-locked lasers receive more and more attention in the field of photonics, where bistable components play an highly important role. This thesis deals with side-mode, i.e., inter-modal injection locking in Fabry-Pérot semiconductor laser diodes, and investigates both static and dynamics characteristic of such systems. The thesis is organized as follows:

- In the Introduction Chapter of the thesis, we explain the basic principles of this phenomenon in general, give historical perspective of oscillations locking discoveries and applications and classify different regimes of oscillations coupling (Section 1.1). In Section 1.2 we present some important bistable components used in modern photonics systems, in particular all-optical switches and all-optical flip-flops which represent elementary building blocks of the all-optical networks architectures. In Section 1.3 we focus on the nature of optical bistabilities found in injection-locked lasers. Finally, in the last section of the introduction chapter (1.4), we give a short conspectus of the current trends in the investigation and employment of injection-locked lasers in the domain of photonics.

- In Chapter 2 we present theoretical model used to describe dynamics of the Fabry-Pérot multi-mode lasers. We present derivation of the rate equations for the slave laser in the regime of injection locking (Section 2.1) and extend the model to ac-

count for all supported longitudinal modes of Fabry-Pérot slave laser cavity (Section 2.2). Finally, we set theoretical model for investigation of the locking range and small-signal stability of injection-locked Fabry-Pérot laser diodes, which is based on the multi-mode rate equations system (Section 2.3).

- In Chapter 3 we present static characteristics of injection-locked Fabry-Pérot laser diodes. We present calculated optical gain and spontaneous emission of our InGaAsP/InGaAlAs multiple quantum well laser, and calculate all other parameters of the structure appearing in the multi-mode rate equation system (Section 3.1). Next, we calculate the locking range in both cases of intra- (dominant mode) and inter-modal (side-mode) injection locking (Section 3.2). On the basis of our mathematical model for stationary analysis (Section 3.3) we derive carrier rate versus carrier concentration phase plots (Section 3.4), through which we explain the formation of the hysteresis loops in the slave laser output (Section 3.5). Finally, we theoretically investigate hysteresis widths and heights with respect to the injection power and frequency detuning (Section 3.6).

- In Chapter 4 we present dynamic characteristics of injection-locked Fabry-Pérot laser diodes. Firstly, we present map of stationary points distribution in the frequency detuning–relative injection power space, as well as detailed stability map with respect to relative injection power and frequency detuning (Section 4.1). On the basis of this map we recognize regions in which slave laser exhibits instabilities, and in which the slave laser acquires two simultaneously stable states, providing bistability. In Section 4.2 we provide an analytical method for characterization of the switching in the region of the slave laser bistability, while in Section 4.3 we extend this analysis on the exact, full scale numerical model and present exact switching trajectories, as well as methods for slave laser's switching time optimization.

- In Chapter 5 we give final conclusion to the thesis.

1.1 The phenomenon of synchronization

1.1.1 A historical perspective

Should one perform a search of any scientific database in order to find publication tittles that contain words with the root "synchro", the results of such search would yield thousands of entries. Moreover, in the case of similar Google search, unconstrained to

scientific databases, the entries would be in order of millions. Indeed, the word "synchronous" is encountered both in everyday and scientific language. The word itself has an etymology in Greek words $\sigma\upsilon\nu$ ("syn"), meaning the same, common, and $\chi\rho\upsilon\nu\sigma\varsigma$ ("chronos"), meaning time. Literally, "synchronous" means "acting/occurring/operating at the same/common time". Generally, the synchronization phenomena are abundant in large number of diverse systems, for instance mechanical clocks, various kinds of electronic circuits, singing crickets, fireflies, cardiac pacemakers, firing neurons, musical instruments or even applauding audiences, violinists in an orchestra, etc., which all tend to achieve synchronization, i.e., to operate in unison under certain conditions. Obviously, the synchronization phenomena are omnipresent in the world around us, noticeable in various branches of science, from physics and engineering through medicine and biology, up to music and social life. Although these phenomena occur in various forms which appear to be different, they usually obey some universal laws.

The world around us is filled with oscillatory motion: light is a form of an electromagnetic oscillation, radio communications are based on electromagnetic oscillations outside of the visible spectrum, vast number of electronic devices operate on the basis of electrical current oscillations, numerous mechanical systems deploy all kinds of oscillatory, rotatory and vibrational motions, some chemical systems exhibit oscillatory variations of reagents concentration, the alternations of ebb and flow follow an oscillatory pattern, human heart produces oscillatory contractions which is connected with the respiratory cycles of the human lungs, patients with Parkinson's disease exhibit involuntary oscillatory shaking of their limbs,...just to name a few. All these systems produce some internal rhythms while being open systems, i.e., they are not isolated from the environment but rather interact with the surroundings, albeit this interaction is often extremely weak and unnoticeable. Nevertheless, this interaction is the key factor in adjusting the mutual rhythms, which represents the essence of the synchronization phenomenon.

Historically, the first noticed example of the oscillations synchronization was related to mechanical systems, in particular to pendulum clocks. First one to observe and fully describe the phenomenon was Dutch scientist Christiaan Huygens (1629–1695), who was the inventor of the pendulum clock [1]. After he had invented the pendulum clock, Huygens paid a special attention to improving its stability and precision, especially in order to make pendulum clocks suitable for use on the ships in the open sea, so that the sailors could keep track of the longitude, and thus determine a position on the Earth's surface. For that purpose Huygens attempted to make one of the first marine chronometers, a primitive global positioning system (GPS) by using the pendulum clock. In order to determine the exact position, sailors needed to calculate their altitude, latitude and longitude. Calculation of the altitude did not play an important role and could be neglected, since ships

were sailing at the sea level. The latitude could be determined by measuring the Sun's angle at the noon, or, in Northern Hemisphere, by measuring the angle that the North Star (Polaris) makes with the horizon. However, in order to determine the longitude, sailors needed to use a clock that is precise and accurate enough to be used as a portable time reference. The purpose of such a device is to accurately measure time of some known and fixed location, e.g. Greenwich Mean Time (GMT). Before the invention of the pendulum clocks, the accuracy of the mechanical clocks was 15 minutes a day, while Huygen's pendulum clocks increased this accuracy to around 15 seconds a day [2]. Having such accurate time reference, sailors could calculate the time difference between GMT and the local noon, when the Sun reaches the highest point in the sky. Since the Earth rotates with the constant angular velocity, by using this time difference and some basic geometry, they could determine the longitude relative to the Greenwich Meridian. However, due to rough sea and pronounced vibrations of the ship, as well as due to small variations in the Earth's gravitation, basic gravity-based constructions of pendulum clocks showed unsatisfactory precision and stability. Inspired with this problem, Huygens made efforts to make alternative constructions of such clocks so to improve their stability, when he observed a phenomenon, which he defined as "odd kind of sympathy" between two pendulum clocks suspended on the same wooden beam. He reported his observations to his father in the series of letters, which he sent to him. In the letter sent on February 26th in 1665, he wrote [1]:

"*While I was forced to stay in the bed for a few days and made my observations on my two clocks of the new workshop, I noticed a wonderful effect that nobody could have thought of before. The two clocks, while hanging side by side with a distance of one or two feet between, kept in pace relative to each other with a precision so high that the two pendulums always swung together and never varied. While I admired this for some time, I finally found that this happened due to a sort of sympathy: when I made the pendulums swing at different paces, I found that half an hour later, they always returned to synchronism and kept it constantly afterwards, as long as I let them go...*"

In 1673 Huygens published his memoirs *Horologium Oscillatorium sive de motu pendulorum*, in which he wrote [1]:

"*It is quite worth noting that when we suspended two clocks so constructed from two hooks imbedded in the same wooden beam, the motions of each pendulum in opposite swings were so much in agreement that they never receded the least bit from each other and the sound of each was always heard simultaneously. Further, if this agreement was disturbed by some interference, it reestablished itself in a short time. For a long time I was amazed at this unexpected result, but after a careful examination finally found that the cause of this is due to the motion of the beam, even though this is hardly perceptible...*"

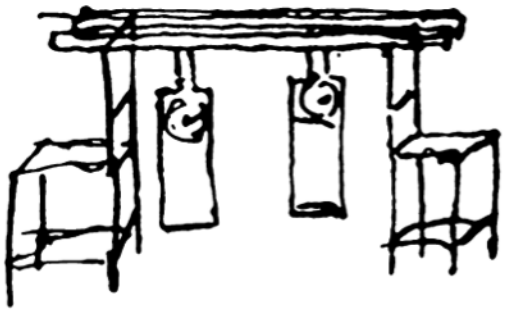

Figure 1.1: *Original drawing of Christiaan Huygens illustrating the two suspended pendulum clocks [1].*

In modern language, one could say that the two observed oscillators, in this case pendulum clocks, synchronized their frequencies, i.e., they become mutually frequency coupled in anti-phase, since Huygens reported that pendulums swung in the opposite directions. Apart from being present in the mechanical systems, or more generally, related to engineering, the synchronization or locking phenomena are manifested in living systems as well. In 1729 Jean-Jacques d'Ortous de Mairan (1678–1771), the French astronomer and mathematician, observed that the movement of the haricot bean leaves was locked to the movement of the Sun, i.e., in the accordance with day- and night-time. The haricot bean retained this "internal clock" even when de Mairan placed it in a dark room for some period of time [3]. Nowadays, it is well known that even considerably complicated and more organized biological systems posses this internal clock, known as circadian (a complex word formed in 1950s from Latin *circa* meaning about and *dies* meaning day) rhythm. Circadian rhythm is also found in humans, and while it slightly differs from 24 hours, it becomes entrained by the environment. It is very common that some people classify themselves as "night owls", which is a consequence of their internal cycle being somewhat longer than 24 hours, while others consider themselves as "early birds", i.e., their cycle is slightly shorter than 24 hours. However, experiences with prisoners in the dark cells, isolated from the environmental influences such as natural illuminance, temperature, pressure etc., showed that in this cases the circadian rhythm collapses, and can significantly differ from the standard 24 hour.

More interestingly, the effects of synchronization also occur in some large population systems. The first reported observation of such synchronization was made by Dutch physician Engelbert Kaempfer (1651–1716), who, after his voyage to Siam in 1680, wrote [3]:

"*The glow worms...represent another shew, which settle on some trees, like a fiery cloud, with this surprising circumstance, that a whole swarm of these insects, having*

taken possession of a one tree, and spread themselves over its branches, sometimes hide their light all at once, and moment after make it appear again with the utmost regularity and exactness..."

The interesting fact is that this phenomenon is geographically localized only to fireflies (glow worms) in southeastern Asia and related only to male units, which use their light to attract females [3]. Moreover, fishermen in this part of the world use this effect in the purposes of navigation. However, fireflies do not start synchronized. They settle on the trees at dusk and the mutual synchronization gradually builds up as the night goes on. In the 1980s Frank Hanson [4] conducted an experiment in which he managed to entrain the lightening of the fireflies by exposing them to a flashing light close to their natural period, which is about 0.9 seconds. However, for periods that were considerably different from this, fireflies could not keep up and the synchrony collapsed, even, kind of a beating phenomenon occurred. Thus, the phenomenon of the synchronization is a natural phenomenon, which occurs when conditions for its appearance are met (as in the case of circadian rhythm, or fireflies self-synchronization), or it can be deliberately triggered, as in the case of coupled pendulum clocks, or fireflies in the Hanson's experiment. However, one more biology related synchronization shows that it can also be an unwanted effect, like in an epileptic seizure, which is actually excessive, synchronized activity of neurons in a particular part of a human brain.

Further on, the effect of the mutual synchronization was noticed in acoustics, by Sir John William Strutt, Lord Rayleigh (1842–1919) in the 19^{th} century [1]. He noticed that two organ pipes, standing side by side, which are considered to have the same pitch, could play in perfect unison, i.e., achieve perfect mutual synchronization, albeit their very small, but inevitable initial dissonance. Moreover, Rayleigh not only noticed this mutual coupling, but also the effect of quenching (oscillation death) when the coupling results in suppression of the oscillations of the interacting systems, which lead to organ pipes reducing one another to almost complete silence.

First modern example of oscillations coupling was related to the development of engineering and radio communication during the 1920s. W. H. Eccles (1875–1966) and J. H. Vincent were first to report successful synchronization in triode generators, which had slightly different frequencies [1, 5]. Following their work, E. Appleton (1892–1965) and B. van der Pol (1889–1959) extended the experiment and made a first step in the theoretical study of the effect [1]. Appleton systematically investigated both mutual synchronization of the two coupled oscillators, as well as synchronization by an external force. The set-up of his experiment in which he achieved mutual coupling is depicted in the Fig. 1.2 [6]. Each generator consists of an amplifier in a form of a triode vacuum tube, an oscillatory LC circuit, and an additional inductance, which provides the feed-

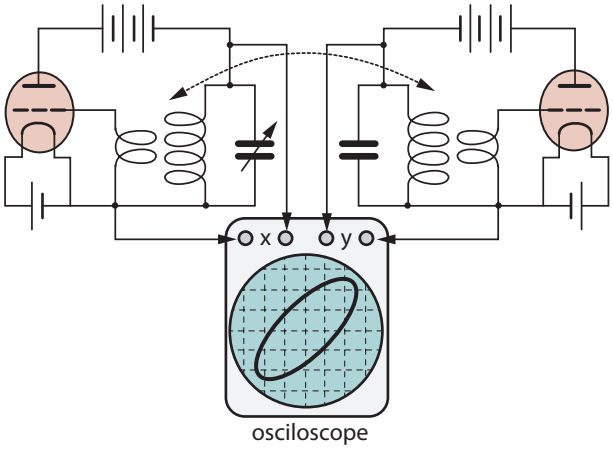

Figure 1.2: *Generators are coupled through two coils, which are placed close enough and enable the overlapping of their magnetic fields and thus mutual coupling. The synchronization can be identified from Lissajous figures on the oscilloscope. In synchronous regime, the curves are closed due to equality of the periods of the two oscillators. [6]*

back. In his experiment, Appleton realized the synchronization by placing the coils of the two generators close to each other, so their magnetic fields overlapped, hence the currents in the LC circuits influenced each other [6]. The tunable capacitor in the left generator Fig. 1.2 was used to introduce and vary the detuning between the two generators. In the second experiment Appleton and van der Pol showed that the frequency of the generator could also be synchronized by some weak external signal, slightly detuned in frequency, which was a crucial discovery in the field of radio communication, because it enabled the stabilization of a powerful generator with a help of a weak, yet highly precise one [7, 8]. Further van der Pol's investigations in the field of triode generator oscillators led to derivation of the van der Pol differential equation, a milestone in the field of nonlinear dynamics [8].

Couple of decades later, Robert Adler (1913–2007) has derived a differential equation which described a variety of synchronization phenomena, or as he defined "locking phenomena in oscillators" [9], which further served as a paradigm for modeling these kind of phenomena in lasers. In 1965, Pantell [10] extended Adler's theory to include synchronization phenomena in laser systems, while a year later, in 1966, Stover and Steiner [11] realized first injection locking with two red He-Ne lasers. Later on, the injection locking was successfully demonstrated in CO_2 lasers by Buczek and Freiberg in 1972 [12]. Finally, injection locking came into the spotlight again during 1980s, when the development of semiconductor lasers paved the way for employing the technique of injection locking.

This thesis focuses on the theoretical investigation of synchronization and induced bistability in modern photonics devices such as semiconductor lasers, which represent a

kind of electrically driven oscillators, supporting oscillations of electromagnetic field. In his paper in 1982 [13], Roy Lang published first detailed theoretical work regarding injection locking technique in semiconductor lasers, where one (slave) laser can be frequency and phase locked with another (master) one, providing that the injection locking parameters (injection strength and frequency detuning) are within the certain boundaries. Before this thesis starts to deal with injection locking in semiconductor lasers and its applications in modern photonics systems and components, a short unified theory (Subsection 1.1.2) and some basic classification of the synchronization phenomena will be presented (Subsection 1.1.3).

1.1.2 Synchronization parameters

One of the universal features of previously mentioned oscillatory systems is that they are all active systems, which means that they contain some kind of internal energy, responsible for maintaining the oscillatory movement. Being isolated, this kind of movement continues as long as energy supply exists. In addition to this, if such system is slightly perturbed, upon the end of the perturbation, it will restore its initial rhythm. This type of oscillator is defined as self-sustained oscillator, or mathematically, an autonomous (without explicit time dependence) dynamical system. Such systems have the possibility to be synchronized. Every such oscillatory system is characterized with oscillations period, i.e., frequency, and phase. For instance, a pendulum clock is a self-sustained oscillator, which transfers the potential energy of the lifted dumbbell (or some kind of suppressed spring, or, in more modern realizations, electrical battery) into the movement of the clock pendulum, which in turn moves cogwheels in the clock mechanism. Even if two such clocks are formally identical, some fine mechanical, and thus oscillatory differences are inevitable, leading to a small frequency difference, i.e., there exists some frequency detuning between the two clocks. The phase of the oscillations is defined as the position of the pendulum in the initial moment, when oscillations start. If two clocks are suspended on the same wooden beam, than this beam can transmit the motion of the pendulums, so those very small and hardly perceptible, yet crucial vibrations, lead to the mutual synchronization of the clocks in which the clocks operate at the same, common frequency, and with some constant phase difference. Moreover, the two clocks do not even need to be formally identical, i.e., the frequency detuning between them can be considered “not small”, while the synchronization can still occur. However, experimental investigations show that in this case the successfulness of the coupling depends on the structural parameters (in this case dimensions/weight/elasticity/rigidness...) of the connecting medium (in this case wooden beam). As a general conclusion, the synchronization depends on two important parameters:

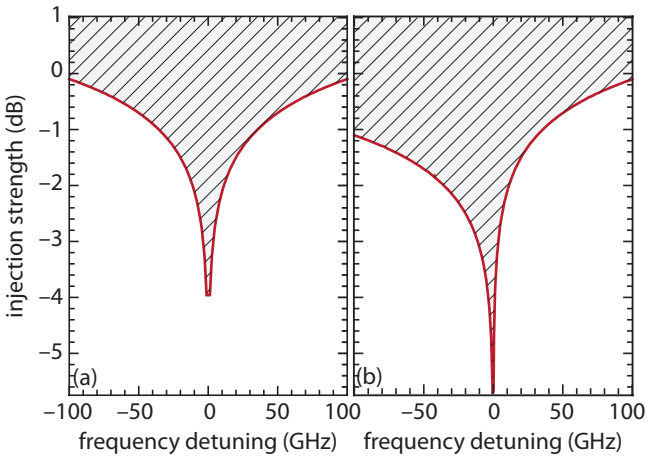

Figure 1.3: *Illustration of the (a) symmetrical and (b) asymmetrical Arnold tongue in frequency detuning–injection strength space (the hatched area corresponds to the area of the synchronization).*

- coupling strength, which qualitatively describes the interaction between two systems and since synchronization can occur in diverse systems, this parameter is defined with respect to the physics of the particular system;
- frequency detuning, which quantifies how different the two isolated oscillators are in terms of their frequencies.

Generally, it is expected that an increase in the coupling strength leads to larger allowed frequency detuning in which synchronization occurs. Very common plot, which represents the region of successful synchronization in the frequency detuning–injection (coupling) strength space is referred to as Arnold plot (Arnold tongue) [1], illustrated in the Fig. 1.3. Depending on the physics of the system, the synchronization, i.e., the locking region defined by the Arnold tongue can be symmetrical [cf. Fig. 1.3(a)] or in favour of the one side, e.g. negative frequency detuning [cf. Fig. 1.3(b)]. The important feature of the locked system, which can be observed from this plot is that, theoretically, for infinitesimally small frequency detuning (i.e., close to 0), system could be synchronized with infinitesimally weak coupling. Exactly this feature is, as mentioned before, used in radio-communications, where a powerful generator is synchronized and in that manner stabilized, by means of a weak, yet highly precise small generator, that serves as a high-quality reference.

In terms of the phase of the oscillations, the two oscillators can have different initial phases, e.g. in the Huygens clocks analogy, the starting positions of the two pendulums can be different. However, synchronization, besides frequency equalization, also assumes the phase locking, meaning that in the synchronous regime the two clocks will have, not

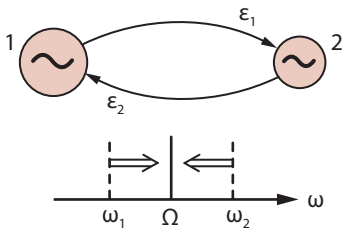

Figure 1.4: *An illustration of the bidirectional synchronization in which both oscillators interact and influence one on each other [1]. Coupling strengths ϵ_1 and ϵ_2 are considered to be comparable. The natural frequencies of two oscillators are ω_1 and ω_2, while synchronous state is described with mutual frequency Ω.*

necessarily the same phase, but rather constant phase difference. On contrary, the asynchronous regime corresponds to unbounded growth of the phase difference. In the original Huygens experiment, the pendulums of the coupled clocks moved in exactly opposite directions [1, 3], i.e., while one reached the rightmost position, the other reached the leftmost position, hence the synchronization is denoted as anti-phase. The other extreme case would be the in-phase synchronization, in which the pendulums simultaneously reach the boundary positions.

1.1.3 Different forms of synchronization

Bidirectional (mutual) synchronization

The presented example of two pendulum clocks represents the case of mutual synchronization in which both oscillatory systems mutually interact, more or less equally influence on each other and adjust their rhythms according to each other, i.e., synchronization can be considered to be bidirectional, as illustrated in Fig. 1.4 [1]. Frequency synchronization is accompanied by the phase locking.

An interesting example of mutual synchronization is the relation between respiratory frequency and wing beat frequency of free-flying barnacle geese *Branta leucopsis* [1]. Experiments conducted by Butler and Woakes [1] showed 3:1 correspondence between the wing beat frequency and the respiratory frequency, as well as tight phase locking between the two. This means that there were 3 wing beats during 1 respiratory cycle, with the wing fully elevated at the transition between expiration and inspiration, very tightly locked to the moments determined to be around 6, 40.5 and 74% of the respiratory cycle. Moreover, there has been reported synchronization between the breathing patterns and locomotory movements during the running in mammals. It has been observed that quadrupedal species like rabbits, dogs, horses, normally synchronize their locomotory and respiratory cycles at a constant ratio 1 stride per breath (1:1), both in cases of trot or

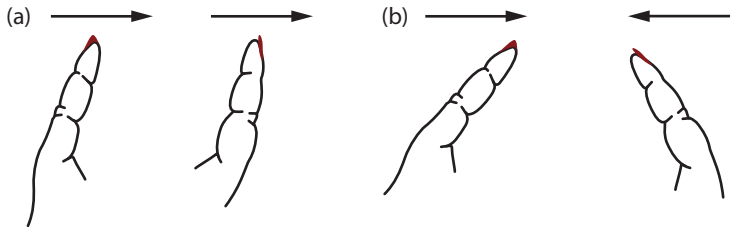

Figure 1.5: *(a) Anti-phase movement (left finger activates flexor, while the right finger activates extensor muscle). (b) In-phase movement (both fingers activate flexor muscles). [1]*

gallop. On the other hand, human runners establish several patterns 4:1, 3:1, 2:1, 1:1, 5:2 and 3:2, although the most common and favoured one is 2:1. So far there has not been derived a connection between established locking pattern and athletic performance while running [1].

Another interesting example, showing different possible phase-locked states is an easy experiment in which a human subject is instructed to perform an anti-phase motion of index fingers and while doing that, the subject is supposed to gradually increase the frequency [1]. At some point, for some frequency high enough, this kind of movement becomes unstable and synchronization collapses to in-phase locking. Motion is considered anti-phase when one finger activates flexor, while the other activates extensor muscle, as illustrated in Fig. 1.5(a). On the other hand, motion is considered in-phase when both flexor or extensor muscles are activated simultaneously, Fig. 1.5(b). The reason for this lies in kind of "over-clocking" of the particular brain centre responsible for the control of the finger motion, called a central pattern generator (CPG). The synchronization of the two index fingers is accompanied by the synchronization of the two corresponding CPGs. However, CPGs acquire information about the finger movement through special sensors (proprioceptors) located in muscles, but with a certain time delay. Every signal from a particular proprioceptor influences both corresponding, as well as the other CPG, thus enabling the interaction between two CPGs. For established anti-phase synchronization, in the case of low frequency, this time delay in information delivery is negligible in comparison to the period of the oscillations. However, once this time delay becomes comparable to half the period, it corresponds to proprioceptor signal having the phase shift equal to π, which is responsible for the transition in the movement of the fingers.

Unidirectional (external force) syhncronization

Unlike pendulum clocks, previously mentioned example of human (or other living system) circadian rhythm synchronization cannot be considered to be bidirectional. Namely,

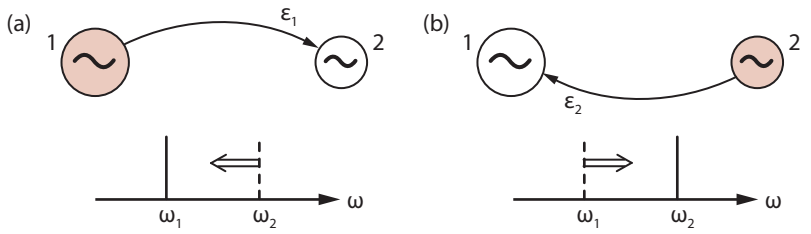

Figure 1.6: *Unidirectional synchronization — master-slave configuration [1]. (a) Oscillator "1" is the master oscillator, while "2" acts as a slave one, locking its frequency (ω_2) to the frequency of the master oscillator (ω_1). (b) Slave oscillator "1" locks its frequency to the master oscillator "2" frequency.*

the possible changes in the circadian rhythm of human are not capable of making influence, and thus changing the rate of the Earth's rotation around the Sun. For example, flying across the Pacific ocean will result in a very known and common feeling of a "jet lag", which is a perturbation of a circadian rhythm, but the "jet lag" itself is not going to make a repercussion on the Earth's rotation rate. Another similar example is the tidal locking, or the fact that the Moon adjusted the rate at which it orbits around its own spin axis to be the same as the rate at which it orbits around the Earth, which is why we see only one side of the Moon. The rotation of the Earth is, however, in no way influenced by the Moon's rotation. As mentioned before, one of the very common engineering applications is synchronization of a system by weak, yet highly precise signal, e.g. radio-controlled clocks, where a weak radio signal broadcasted from a highly precise "central" clock, makes once-a-minute fine rhythm adjustments to other clocks, thus improving their precision.

In all these examples synchronization is performed by some external force in one direction, hence the name "unidirectional" (illustrated in Fig. 1.6) [1]. In technical terms such a system can be defined as a master-slave configuration, where the master oscillator is, so to speak the stronger one, which influences and entrains, i.e., locks the slave one. Another real-life example of external force synchronization is the entrainment of respiration by a mechanical ventilator, which is a common clinical procedure, although still not perfected, due to shortcomings in the process of patient cardiac and consequently respiratory patterns monitoring. Some novel optoelectronic, non-invasive approaches may provide better continious monitoring of respiratory volume, and thus provide more precise mechanical synchronization of the respiratory function in patients [14].

Ensembles of oscillators

In natural systems there are usually more than two oscillators involved in the interaction. One of the mentioned examples is the population of the fireflies in which global, i.e., all-to-all synchronization takes place [3]. Another interesting example is the synchronization of applause in large audiences, which is usually, provided that the audience is large enough, experienced as several transitions from noise to a rhythmic, almost periodical applause [3]. Apart from being present in nature, this kind of synchronization is also present in man-made systems, such as laser arrays or series of Josephson junctions [3].

Synchronization of chaotic oscillators

Most of the natural oscillatory systems are nonlinear, highly complex, and exhibit complex and chaotic behavior [Fig. 1.7(a) and (b)] [1]. Even though they generate chaotic signals, when subjected to coupling, they are capable to undergo the synchronization. Since such systems are chaotic, instead of defining the frequency of the signal, it is more convenient to define the mean frequency. Due to their complex nature, weak coupling cannot provide complete synchronization, i.e., coupled systems synchronize their mean frequencies, but their amplitudes remain irregular and chaotic in behaviour, though constant phase difference may be established. Figs. 1.7 (c) and (d) illustrate a case in which, two initially chaotic signals synchronize their mean frequencies, which can be concluded from the fact that the number of maxima for both signals is the same, unlike the case depicted in the Fig. 1.7(a). However, the amplitudes of the signals remain different. On the other hand, strong coupling can lead to the complete synchronization of two chaotic signals in which, not only the mean frequencies, but also the amplitudes completely coincide, as illustrated in the Fig. 1.7(e) and corresponding phase diagram Fig. 1.7(f).

Finally, the effect of the synchronization can be sometimes easily confused and mistaken for resonance. However, resonance is a response of a non-active system, in which oscillations are dependent on an external force, while it has been defined that synchronization occurs in conceptually different self-sustained oscillators, which do not depend on the external force, but as defined, have their internal energy. An illustrative example would be the difference between radio-controlled and railway station clocks [1]. Radio-controlled clocks are self-oscillating, independent on the periodical radio signal, which is sent to them. The purpose of this signal is only to synchronize them with some highly accurate time reference, and thus slightly correct their natural frequency. However, the railway clocks receive their signal from some central clock, thus, if this signal is switched off it instantaneously stops all connected clocks.

According to the presented classification, injection locking in semiconductor lasers is

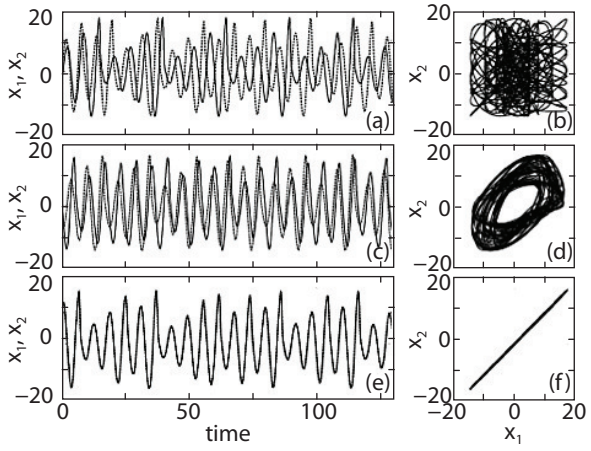

Figure 1.7: *(a) Two chaotic signals, with different mean frequencies, i.e., different number of maxima in depicted time span and (b) corresponding chaotic phase plot, showing no structure. (c) Case of weak coupling. Mean frequencies are equal, though amplitudes are still different. (d) Phase plot shows a circular structure, which is typical for two signals with same periods and constant phase shift. (e), (f) Strong coupling leads to the complete synchronization, i.e., complete coinciding of the two initially chaotic signals. [1]*

an unidirectional synchronization, i.e., a master-slave configuration, in which an external optical signal coming from the master laser serves as a reference. In such configuration, injection strength, i.e., injection power is defined as the power of the injected optical signal, while the frequency detuning would be the frequency difference between the master and the slave lasers. In this thesis, the special attention is paid to the optical bistability (and multistability) reported in the injection-locked semiconductor lasers. Generally, bistable components play a very important role in the field of modern photonics, providing possibility to upgrade electronic layer in the modern hybrid optical communications networks and provide all-optical solutions. In the next Section (1.2) we give an overview of the bistable components used in photonics, after which we focus on the injection locking induced bistability in semiconductor lasers (Section 1.3) and its possible applications (Section 1.4).

1.2 Bistable components in photonics

A dynamical system is considered to be bistable if it has two stable equilibrium states, i.e., two fixed points [3]. The system can end up in either of the two stable steady-states, depending on its prehistory. Once the system settles down in one of the stable states, transition to the other can be performed by some kind of perturbation, which is

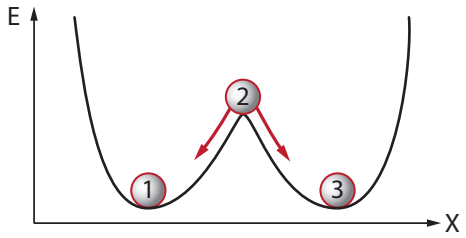

Figure 1.8: *In the positions 1 and 3 ball is in the stable state which corresponds to the potential energy minimum. At the position 2, ball is in the unstable state since a small perturbation would shift the ball in the position 1 or 3. The ball can commute (make the transition) between positions 1 and 3 only if provided sufficient energy to surpass the energy barrier ΔE.*

strong enough to push the system into the desired state, instead of returning back to the originating point. In terms of the potential energy, a bistable system has two local minima of potential energy, between which lies a local maximum, forming an energy barrier. Equilibrium states correspond to the points of minimal energy and the transition between them is possible if the system acquires energy sufficient to surpass the barrier 1.8.

Optical systems can exhibit bistability, i.e., optically bistable system has two possible stable outputs for the same value of some input parameter. Since the first experimental observation of the optical bistability in a passive, unexcited medium of sodium (Na) vapor in 1976 [15], optical bistability has been investigated in wide spectrum of materials and constructed devices. In past decades it has become a hot-research topic, greatly in virtue of highly attractive application to all-optical logic and because of the interesting phenomena it encompasses. From the perspective of modern information era, the field of telecommunications emerges as one of the most tempting and rapidly growing research areas. Constant demands for new, highly complex and bandwidth wise consumptive services, like diverse video-based multimedia, different cloud services, or fast peer-to-peer data transfers, reveal the limitations of electronic signal processing. Indeed, photonics components, rather then electronic ones, tend to surpass the bottleneck imposed by electronic data processing; hence more and more attention is aimed to all-optical signal processing. For instance, instead of electronic routing, all-optical packet-switched networks offer all-optical routing through the network on the basis of the information imprinted in the optical packet header [16]. All-optical flip-flops, memory elements, and optical switches represent some of the crucial building blocks of such architectures. There are many proposed, both theoretically and experimentally investigated, realizations of these devices, employing different approaches in harnessing the benefits of the optical bistability.

Optical switches

A switch is a device that establishes and releases connections among transmission paths in a communication or signal-processing system [17]. There are several different engineering approaches for realization of optical switches. Mechanically controlled optical switches consist of one movable optical fiber attached to a mechanical wheel with a number of fixed optical fibers and switching is performed by mechanical rotation of the wheel and coupling with desired fixed fiber [17]. The major limitations of these devices are slow operation, as well as inability to be integrated, as well as mechanical sensitivity due to the movable components. Another approach relies on electro-optically controlled switches, which employ electro-optic effect on a pair of optical waveguides [17]. The main limitations of this architecture are polarization sensitivity, large physical size and cross-talks. Other different classes of optical switches comprise acousto-optically controlled switches [17], which make use of sound waves to alter the refractive index of an optical medium, magneto-optically controlled switches [17], employing the Faraday effect in which the polarization of the electrical field can be rotated in the presence of a magnetic field, thermo-optic switches [17] in which refractive index change is due to thermo-optic effect, liquid-crystal switches [17], etc...Another important class of electrically controlled switches represent switches on the basis of semiconductor optical amplifiers (SOAs) [17]. In the "ON" state, i.e., in the presence of the optical gain, SOA acts as amplifier, while in the "OFF" state, it operates as a strong absorber. SOAs may be rapidly turned "ON" and "OFF" by applying or removing the injection current. Specially important class of switches represent all-optical ones, in which light controls light with the help of a nonlinear material. Usual nonlinear interactions used in these kinds of switches include light induced Kerr effect, light sensitive retardation or absorption coefficient, or optical soliton collision [17].

A more recent proposition is to employ optical bistability for the purpose of all-optical switching. Generally, optically bistable systems manifest an output hysteresis loop with respect to the system input (Fig. 1.9). For small values of the system input I_{i} (usually optical power), the output I_{o} can be in the state of low output power, which can be denoted as the "OFF" state. As input power increases, at some critical value which can be denoted as the threshold ν_2, system exhibits a sudden jump to the state of high output power, which can be denoted as the "ON" state, and remains in this state with further increase in the input power. As a matter of fact, the system remains in that state until input power is decreased to some other critical value, threshold ν_1 ($\nu_2 > \nu_1$, cf. Fig. 1.9), when system makes a sudden drop to the "OFF" state, and remains there with further decrease of the input power. The illustrated excursion of the input power writes up a counterclockwise hysteresis cycle. This hysteresis loop can act as a switch which turns the output on and

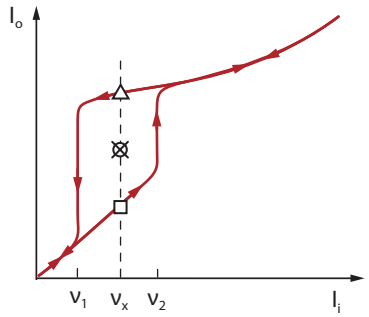

Figure 1.9: *Counterclockwise hysteresis cycle. In the region $\nu_1 < I_i < \nu_2$ each input value (e.g. ν_x) corresponds to three possible output values (denoted with rectangle, crossed circle, and triangle), out of which two are stable and correspond to the lower (state denoted with rectangle) and upper hysteresis branch (denoted with triangle). The third stationary state (denoted with crossed circle) stands on the line connecting two stable states and represents an unstable state, since a small perturbation will promote it to either upper or lower hysteresis branch. For input intensity smaller than the threshold ν_1, or higher than the threshold ν_2, the system has only one possible state, the lower or higher hysteresis tail part, respectively, i.e., in this case the lower and upper hysteresis branch merge.*

off by controlling the input. Moreover, if a light source is used to control the input light, then it is an optically controlled optical switch. If needed, the thresholds ν_1 and ν_2 can be adjusted to coalesce to a single value, resulting in a single threshold "S-shaped" hysteresis [17].

Obviously, an optical bistablity is a nonlinear phenomenon, although the nonlinearity itself is not sufficient; yet the necessary catalyst for operation of the bistable device is some kind of a feedback. It is the feedback that permits the transmission of light through nonlinear optical material to become multivalued. Figure 1.10 depicts a generic optical system with a feedback, which makes the transmittance T of the system dependent of the output intensity I_o in some nonlinear fashion $T = T(I_o)$. From the output-input dependence $I_o = TI_i$, yields that $I_i = I_o/T(I_o)$. For illustration purposes, let $T(I_o)$ be non-monotonic function, like a bell-shaped function as in Fig. 1.10(a). According to the relation between them, I_i must also be a non-monotonic function of I_o, as illustrated in Fig. 1.10(b). Consequently, I_o must be a multivalued function of I_i [Fig. 1.10(c)]. The system exhibits multistability, i.e., bistabilty, since there exists a region of input parameter $\nu_1 < I_i < \nu_2$ in which each input value corresponds to three possible output values [e.g. for ν_x system exhibits three output states denoted with rectangle, crossed circle and triangle, cf. Fig. 1.10(c)]. However, only the two states are stable, the upper (denoted with triangle) and the lower one (denoted with rectangle), while the third, intermediate state, standing on the line joining points 1 and 2 (denoted with crossed circle) is unstable, since a small perturbation would promote this state either to the upper or the lower one,

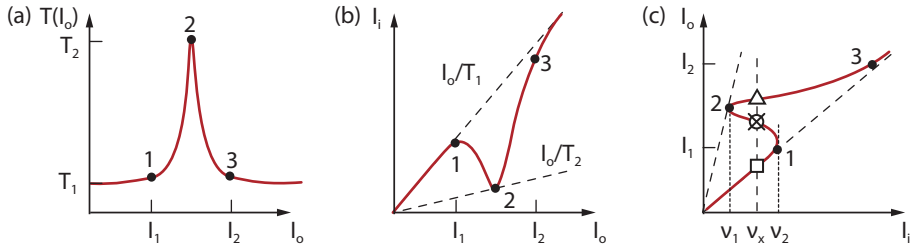

Figure 1.10: *Optical bistability illustration for a generic system with a feedback. (a) Nonlinear dependence of the system transmittance T on the output intensity I_o. (b) Input versus output intensity dependence. (c) Output versus input intensity dependence, showing multivalued character. [17]*

similar to the case of a ball in Fig. 1.8. Starting from some small value of I_i, up to the threshold ν_1, the system has only one possible output, i.e., the lower I_o hysteresis tail part (Fig. 1.9). In the range from ν_1 to ν_2, the system has two possible outputs, though, due to its prehistory, the system retains in the lower hysteresis branch. Surpassing the threshold ν_2 leads to a sudden jump on the upper hysteresis tail part. When the input is decreased, the system remains in the upper branch until threshold value ν_1 after which it makes a sudden drop back to the lower tail part, i.e., the system outlines a hysteresis cycle as in Fig. 1.9.

One simple bistable optical device that can be used as an optical switch consists of a concave, semitransparent mirror Fabry-Pérot resonator with some nonlinear optical material between them as depicted in the Fig. 1.11. Such system exhibits the bistability due to the presence of the nonlinear material, and generally, upon the choice of the used nonlinear material, there are two classifications of such bistable systems: absorptive, if nonlinearity is related to the intensity dependent absorption and dispersive, if nonlinearity is related to the intensity dependent refractive index. The two effects can also be simultaneous. Another, more sharp distinction is classification on intrinsic (all-optical) and hybrid (mixed electronics and optics). In an intrinsic system, the light directly interacts with the optical material, while in the hybrid systems intensity dependence arises from an electrical signal from a detector monitoring the transmitted intensity.

Modern proposed realizations of all-optical switches employ injection locking as a mechanism which provides the switching possibilities and comprise optical switches on the basis of single-mode injection-locked Fabry-Pérot lasers [18], multi-wavelength injection-locked Fabry-Pérot lasers [19], injection-locked distributed feedback lasers (DFB) [20], or injection-locked micro-ring semiconductor lasers [21]. Proposed architectures achieve rise and fall times in order of 50–100 ps, and can support 10 or even 40 Gbit/s data rates.

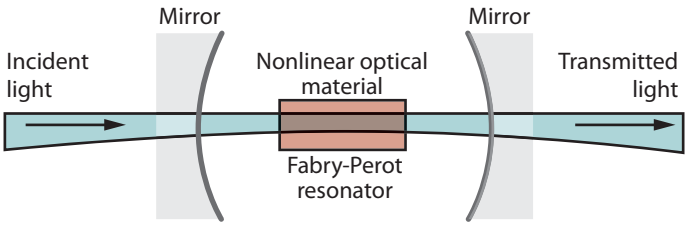

Figure 1.11: *Fabry-Pérot resonator with nonlinear optical material exhibits bistable operation and as such can be used in optical switching.*

All-optical flip-flops

All-optical flip-flops are for sure building blocks of modern photonics systems, and in general their application is settled in two fields of optical communications: all-optical routing and all-optical signal processing. Indeed, all-optical devices may provide lower power consumption and higher processing speeds in comparison to their electronics counterparts [22]. Different construction schemes of all-optical flip-flops have been proposed for all-optical packet switching, where optical packets are forwarded to the appropriate destination based on the address information, located in the imprinted optical header or label. The packet is sent through if the flip-flop is in the "ON" state and blocked otherwise. 40 Gbit/s optical packet switching performance has been reported in [23, 24]. In addition to this, all-optical flip-flops are proposed for all-optical contention resolution, when multiple optical packets, for the same output port, arrive at the same time, and when contention occurs [25]. In terms of all-optical signal processing, all-optical flip-flops can be used to perform a variety of functions, to serve as all-optical binary counters [26], all-optical shift registers [27], all-optical random access memories [28], all-optical memories based on dispersive bistability in injection-locked Fabry-Pérot laser diodes (FP LDs) [29], or on polarization bistability in injection-locked VCSEL [23], regenerators based on dispersive bistability in injection-locked DFB lasers [30], or on polarization bistability in injection-locked VCSEL [31] all-optical logic gates, such as all-optical inverting, NOR and NAND gates [32, 33], optical switching [33, 34], and all-optical address decoder [35], all-optical demultiplexing [31], or all-optical square-wave generators [36]. The common feature of proposed systems is that they employ variation of injection power in order to perform switching in the bistability region of injection-locked laser diode. Obviously, in the recent years, all-optical flip-flops have been attracting high research attention among the scientific community. Figure 1.12 illustrates this fact, with data regarding "IEEE Xplore" annual citations with index terms referring to optical flip-flops [37].

All-optical flip-flops can be realized by combination of nonlinear material and feedback mechanism, providing bistability operation in the "S-shaped" hysteresis region [31].

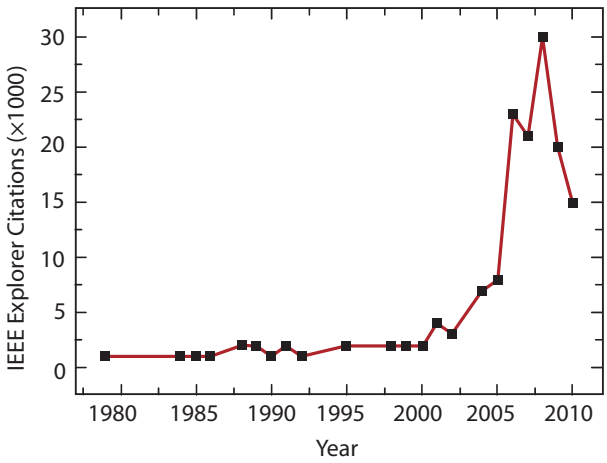

Figure 1.12: *"IEEE Xplore" annual citations with index terms referring to optical flip-flops [37].*

The output state is distinguished by means of optical power, while in the case of optical memories the states can be distinguished by different operating wavelengths [38]. Some other schemes include all-optical flip-flops using two coupled ring lasers, where each laser has its own gain element, usually semiconductor optical amplifier (SOA) and an arrayed waveguide grating (AWG) [39], or instead of ring lasers, two coupled Mach-Zehnder interferometers could be coupled with SOA [40], or with two SOA fiber lasers [41]. The effect responsible for operation of such architectures is gain-quenching effect, where signal from one laser suppresses the lasing of the other one, through SOA gain saturation. On the similar basis, using the same effect, even multi-valued, in particular three-state optical flip-flop has been proposed [42]. In [43] and [44], all-optical flip-flops are demonstrated on the basis of micro-ring lasers, which usually support two lasing modes, clockwise and counterclockwise. In [43], all-optical flip-flop is realized with single micro-ring laser, while in [44] waveguide coupled micro-ring lasers are used. Vertical-cavity surface-emitting lasers' polarization bistability is used for all-optical flip-flop realization in [31]. Spatial hole burning effect in distributed feedback (DFB) laser with continuous wave (CW) injection signal has been employed in [20] for realization of all-optical Set-Reset (SR) flip-flop. The proposed scheme consists of a single DFB laser, with CW injection signal and two additional "Set" and "Reset" optical pulses. In one state, when DFB laser is lasing, i.e., turned on, the injected signal will experience small gain, due to the gain clamping caused by spatial hole burning effect. Thus, in this state the injected signal is negligible and has almost no influence on the laser output. In the other state, when DFB laser is turned off, the external signal will acquire considerable amplification and cause non-uniform carrier distribution in the active region of the DFB laser. "Reset" signal is injected on the same side as CW injection signal and the "Reset"

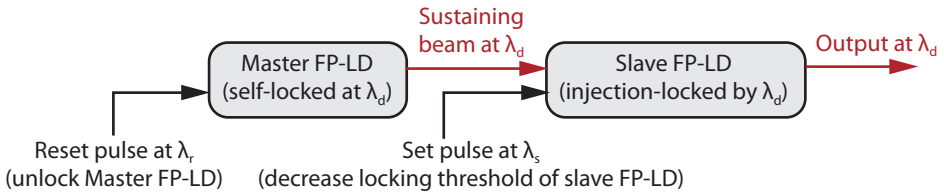

Figure 1.13: *Schematic view of injection-locked Fabry-Pérot all-optical set-reset flip-flop architecture [45, 46].*

signal turns DFB laser off, causing the non-uniformity of the carrier distribution. The "Set" signal is injected from the other side of the DFB laser and it turns it on, restoring the carrier distribution.

Of particular interest for this thesis is the realization by means of injection-locked Fabry-Pérot laser diodes (IL FP-LD), where for the slave laser is used standard commercial multi-mode FP-LD, while for the master laser a built-in external-cavity FP-LD is used in order to ensure single-mode operation and stability [38, 45–47]. In this proposed scheme, the master laser is self-locked at the wavelength λ_d and produces CW optical signal, which locks the slave FP-LD at the same wavelength (Fig. 1.13). The purpose of the "Set" impulse, which is also injected into the slave laser, is only to lower the locking threshold and to perform higher side-mode suppression-ratio (SMSR) in the slave laser. Either with or without the "Set" impulse, the slave laser is locked at λ_d and in this state the device output is high in optical power, which is why this state is denoted as "ON" state. In order to switch the state, master laser should be unlocked by the means of the "Reset" impulse, which now decreases the power of its CW signal, consequently leading to the unlocking of the slave laser, when it enters the "OFF" state in which λ_d output is low in optical power.

Key performance indicators of all-optical flip-flops are extinction ratio, which should have high values, switching times and energies, which should, ideally, have low values. Extinction ratio is defined as a ratio between two output power levels corresponding to the logical "ON" and "OFF" states. The presented all-optical technologies offer extinction ratios in order of tens of dB, which is suitable for applications in optical signal processing. In the schemes comprising coupled SOA ring lasers, switching times (usually defined as rise and fall times) and switching energies vary from few μs and tens on nJ, respectively, while they take values from 50 to 100 ps and around 100 fJ, respectively, in the schemes employing injection-locking. Coupled micro-cavity lasers report promising less than 20 ps switching times and around 5.5 fJ switching energies [44].

1.3 Bistabilities in injection-locked lasers

Depending on an origin of the bistabilty, i.e., type of nonlinearity in the active medium, lasers can exhibit bistabilites of absorptive or dispersive kind, two-mode bistability via gain saturation, or polarization bistability [31].

Absorptive kind of bistability can be found in laser diodes with saturable absorber in their cavity, i.e., with a material that decreases its absorption with an increase in the light intensity. This kind of bistability is reflected in optical output versus current input dependence, as well as in optical output versus optical input dependence. Examples of absorptive bistable laser diodes are given in [31], with either Fabry-Pérot or DFB cavities split into gain and saturable absorption regions.

Dispersive kind of bistability originates from the fact that refractive index depends on the light intensity, as well as on carrier concentration. This kind of bistability is present in injection-locked laser diodes and it leads to the asymmetric locking range as depicted in Fig. 1.3(b) [13, 31, 48–50]. Numerical description of injection-locked laser dynamics is usually performed through rate equations system describing carrier, photon and phase dynamics of a slave laser with external light coupling. The linewidth enhancement factor α [51], involved in the phase rate equation, takes into account the dispersive nature of the laser diode and defines the asymmetrical shape of the locking region. Non-dispersive media, which are described with $\alpha = 0$ exhibit symmetrical locking region, as illustrated in Fig. 1.3(a).

Fabry-Pérot lasers are generally multi-mode lasers, supporting a number of different cavity modes. In systems where oscillations take place in two modes, the cross-effect between the two modes can arise from gain saturation and intensity in one mode depends on the intensity of the other. In the case of strong coupling between modes, bistability may occur [31]. Mathematical analysis of the bistability in two-mode lasers has been performed in [52, 53]. In [52] the theory was extended to bistability controlled by an injected optical signal.

The polarization type of bistability arises from the competition of two polarization modes, transverse electric field (TE) mode and transverse magnetic field (TM) mode. The first report of this kind of bistability is given in [54]. The mathematical description of this kind of bistability, via rate equations, has been given in [55]. This kind of bistability is also confirmed in injection-locked lasers. Indeed, [56–58] show that if Fabry-Pérot cavity type laser, oscillating with TE polarization, undergoes optical injection with TM polarization with zero detuning, the lasing will be stopped due to the gain quenching effect (similar to organ pipes silencing each other, described in Section 1.1.1). However, with introduction of slight detuning, i.e., if injected light has slightly longer wavelength in comparison to the cavity resonance wavelength for TM polarization, dispersive bistability

both in TE and TM polarization occurs [31]. Polarization bistabilites have been mostly researched in VCSEL structures [31].

1.4 History and applications of bistable injection-locked laser diodes

The history of injection locking in lasers sets in owing to pioneer works of Van der Pol [7, 8] and Adler [9] in the field of electrical oscillators locking, and invention of a laser in 1960s. The first reported experimental realizations of injection locking in lasers were published in 1965 by Pantell [10] in He-Ne laser and in 1966 by Stover [11] in CO_2 laser. Invention of a semiconductor laser in 1980s introduced a possibility to apply the same technique in the new circumstances and Kobayashi and Kimura demonstrated optical injection locking in AlGaAs gain medium heterostructure semiconductor laser [59]. Shortly after that, Iwashita and Nakagawa showed side-mode suppression in Fabry-Pérot semiconductor laser as a result of injection locking, thus making a single-mode output from an originally multi-mode laser [60]. Indeed, injection locking was showed to suppress supported side-modes and promote the central, i.e., dominant mode, and thus to ensure single-mode operation, which was first reported in [61]. Roy Lang was first to give theoretical description and analysis of the phenomenon in his paper from 1982 [13], which serves as a paradigm for injection locking in semiconductor laser diodes.

Figure 1.14(a) depicts one possible realization of injection locking technique in which light signal from the master laser (usually a tunable laser) is injected into the slave laser and the light from the slave laser serves as the useful system output. The depicted setup is often called transmission-style injection locking [62]. In this kind of setup light from the master laser enters at one slave laser facet, while the system output is taken from the other slave laser facet. An isolator is placed between the two lasers in order to eliminate the back reflection and coupling of the light back to the master laser. The other often used setup is called reflection-style [62] and the illustration is given in Fig. 1.14(b). Here, the system output is taken from the same facet where master laser light is injected. An optical circulator is used to ensure that only the output beam goes to the photodetector. In addition to this, in fiber systems, polarization controller is often necessary in order to ensure that the polarizations of the master and the slave laser are matched.

One of the first applications of injection locking was to improve characteristics of directly modulated lasers [62]. Indeed, directly modulated lasers are more compact and more cost-effective solutions for transmitters in both analog and digital photonics communications systems. However, directly modulated lasers comprise some performance issues like mode partition noise (in Fabry-Pérot lasers), pronounced relaxation oscillations, large

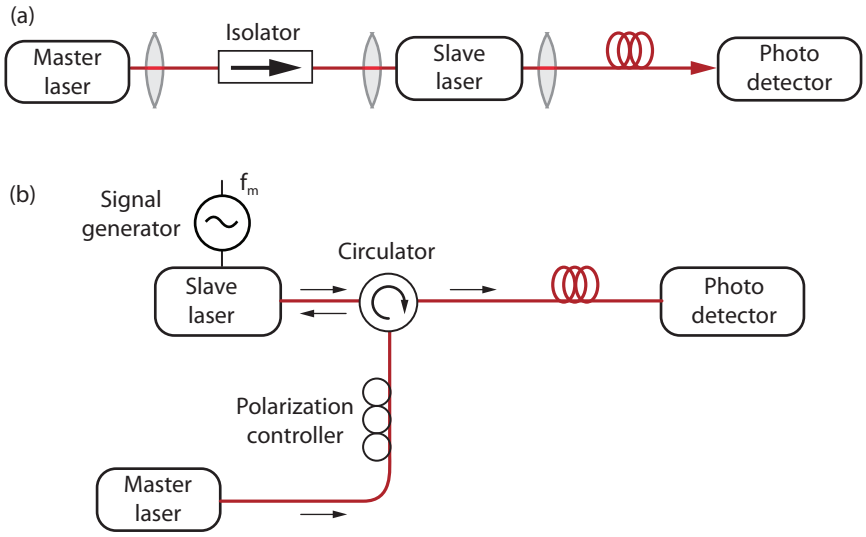

Figure 1.14: *Schematic of optical injection-locked laser system: (a) transmission-style (the output signal is taken from the facet opposite to the facet receiving the injection signal) (b) reflection-style (the output signal is taken from the same facet at which injection signal is applied).*

amplified spontaneous emission noise and wavelength chirp due to the non-zero linewidth enhancement factor [62]. The technique of injection locking was found to reduce frequency chirping and linewidth in directly modulated lasers [63–65] and chirp-free transmission at 2 Gbit/s was realized using injection-locked DFB lasers [66]. In 1990s, further improvements were demonstrated, raising the modulation speeds up to 10 Gbit/s [67, 68]. The technique of injection locking was demonstrated to significantly improve modulation bandwidth compared to the free-running electrical modulation, both in DFB or VCSEL structures [69–73] and in Fabry-Pérot cavity lasers [74, 75]. Numerical analysis of the rate equations system for injection-locked laser showed that strong injection power can improve modulation bandwidth by a factor of 4 in comparison to the free-running regime, even for low bias currents [70]. It has been shown that the cutoff frequency is linearly proportional to the injection power, though zero detuning was assumed [70]. However, modulation properties of injection-locked lasers are detuning dependent and the modulation bandwidth could be maximized for some intermediate injection power and frequency detuning [75].

Reduction of relative intensity noise (RIN) was also observed under injection locking [76, 77]. Here, the concept of inter-modal injection locking was presented, meaning that the external light was injected with a frequency close to one of the slave laser's side-modes, as opposed to the intra-modal injection locking when the external light is injected in the vicinity of the slave laser's central mode. Inter-modal injection locking was also investigated in [74], where enhancement of the resonance frequency was found to be

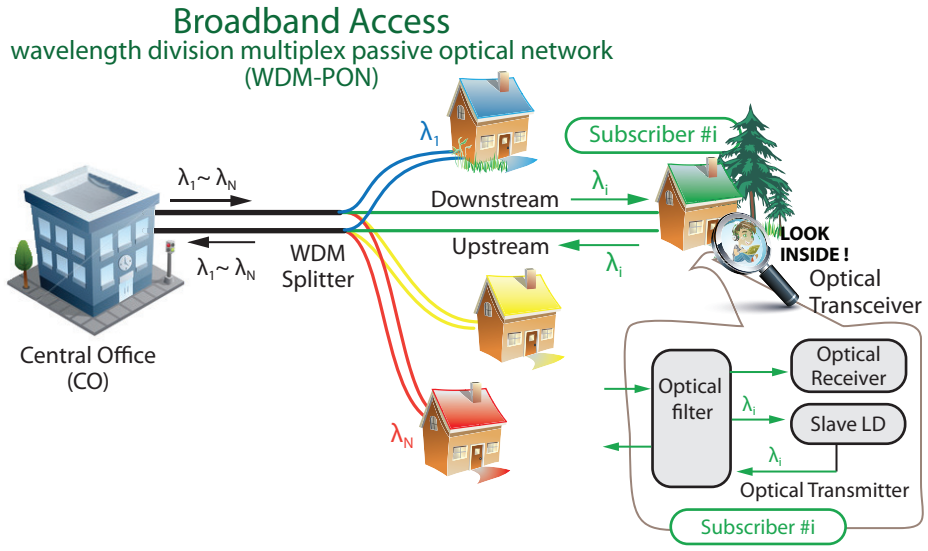

Figure 1.15: *WDM PON architecture with injection-locked FP-LDs in optical networks units (ONUs). Every ONU communicates with the central office (CO) in up- and downstream direction via some dedicated wavelength λ_i, i.e., tunable laser located in the CO remotely locks FP-LDs in ONUs in order to establish desired communication wavelength, i.e., channel.*

higher for longer wavelength side-modes. Inter-modal injection locking become attractive due to the fact that in this scenario the slave laser switches its wavelength from original (corresponding to the central mode) to new, locked one, corresponding to the injection-locked side-mode. The described phenomenon promoted this technique for wavelength conversion [32, 78]. A very recent publication demonstrated a 2.5 Gbit/s non-return-to-zero (NRZ) conversion with extinction ratio over 4 dB and side-mode suppression-ratio of 36 dB [79]. Furthermore, phase locking achieved by variation of injection power may provide an efficient way for conversion of on-off keying (OOK) into advanced modulation formats, as binary phase-shift keying [80]. Similarly, variation of detuning corresponding to frequency shift keying can be converted into OOK or phase-shift keying (PSK) [81, 82].

By the end of the 20th century, optical transmission technologies have made rapid upturn, increasing the demand for improvements in transmission technologies, and network architectures. One of the proposed concepts is wavelength-division-multiplexed (WDM) passive optical network (PON) [83, 84]. The architecture of WDM PON network splits subscribers, i.e., optical network units (ONUs) in terms of dedicated wavelengths, meaning that every ONU communicates with the central office (CO) via dedicated wavelength both in downstream and upstream direction (Fig. 1.15). In this way WDM PON provides independent wavelength channel to each user, while sharing the common fiber architecture. One of the proposed solutions using this wavelength routing technologies was investigated in [83, 84]. More cost- and complexity-effective solution removes necessity

for tunable lasers in each ONU, by implementing simple Fabry-Pérot laser diodes, which are remotely locked by the signal from the CO, thus enabling upstream communication via locked wavelength [85–89]. The proposed setup was investigated both with CW and pulse master laser signals [86]. In the pulse regime, wavelength switching was performed and it has been demonstrated both theoretically and experimentally, that switching times are around 0.2 ns. The switching times were defined as the sum of the rise and fall time, i.e., the time needed to achieve 30 dB of side-mode suppression-ratio (SMSR) when master laser is in "ON" state, and time needed to degrade SMSR to around 20 dB, when master laser is in "OFF" state [86]. It has been observed that the fall time significantly rises with an increase in photon lifetime of a slave Fabry-Pérot laser diode. Generally, it has been pointed out that the fall time is longer than the rise time [87]. In addition to this, Kashima investigated direct, small-signal modulation properties of slave FP-LD, such as chirp, which is highly important in high-bit-rate transmission systems, the influence of the optical injection power, longitudinal mode, and frequency detuning [87]. In [89], wide tunability of Fabry-Pérot laser diodes has been reported, demonstrating up to 16 cavity modes which can be injection-locked to achieve 30 dB of SMSR, leading to the frequency tunability range of around 3.6 GHz. Using CW master laser light, upstream and downstream links at 10 Gbit/s were demonstrated [89].

In terms of other telecommunication-based applications, injection-locked lasers were proposed in Radio-over-Fiber (RoF) systems [90], where injection-locked DFB laser was modulated with 125 Mbit/s digital signal multiplexed to a RF carrier of 18 GHz. In addition to this, injection locking was used to realize improved CATV transmission [91, 92].

On the other hand, since injection-locked lasers are essentially chaotic systems, the matter of stability has been very attractive field of research. In early works, stability was examined under the weak injection locking regime [93–97]. It has been reported that stable injection locking was found only for negative frequency detuning (meaning that the master laser has smaller frequency in comparison to the slave laser), while the positive frequency detuning led to unstable operation and chaotic behaviour. The asymmetric stability boundaries were attributed to the dispersive nature of the active medium, i.e., the non-zero definite value of the linewidth enhancement factor α, which, as previously said, plays and important role in optical injection locking and refers to the refractive index dependence on the carrier concentration fluctuations [50, 51, 94]. In [98, 99] a special attention was paid to influence of α in injection-locked Fabry-Pérot lasers. In [48–50] a stability map was presented, as in Fig. 1.16. Fig. 1.16 depicts stability regions in function of frequency detuning and injection ratio, which is defined as ratio of injection power and power of the injection mode in the free-running regime. Solid curves in Fig. 1.16 dispart

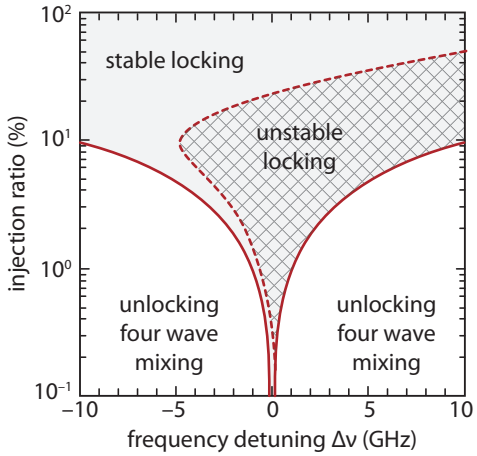

Figure 1.16: *Stability map in frequency detuning-injection power space. Instabilities are found for positive and small magnitude negative frequency detuning (hatched part). Higher injection power enable wider region of stable locking, which starts to spread over the region of positive frequency detuning.[48]*

regions of locking and non-locking, in which a variety of peculiar dynamics occur, such as four-wave mixing and chaotic oscillations. On the other hand, in the region of locking, slave laser can exhibit either stable or unstable operation, with boundary outlined with dotted line in Fig. 1.16. As in previous works [93–96], for weak injection power, stable locking can be observed only for negative frequency detuning, while for strong injection it starts to spread over positive values of detuning. More detailed stability map, with special attention paid to the classification of types of instabilities in the region of positive detuning, is given in [100]. Analytical study of the stability region in the domain of the negative frequency detuning revealed a bistability region [101], which originates from the competing attractors representing locking and unlocking regimes. In terms of steady-state carrier concentration it has been shown that smaller carrier density corresponds to the locked solution. Similar to [101], in [102] a region of bistability in the domain of negative detuning, in which pulsating intensity regime may coexist with a stable steady-state, was observed and experimentally confirmed. Moreover, in [103] experimental observation of optical bistability in a semiconductor laser under inter-modal injection locking has been reported. It has been concluded that very small changes of just several micro watts in the injection power, can result in about 300 GHz change in the lasing frequency of the slave laser, with strong change in the slave laser's power output. The variation of the injection power revealed a counterclockwise hysteresis cycle (as illustrated in Fig. 1.9) in the slave laser's power output, proving the presence of the bistabilty.

Finally, in most recent years, injection-locked lasers find numerous applications in the field of all-optical signal processing, as discussed in Section 1.2.

Chapter 2

Theoretical model

The dynamics of a solitary, free-running slave laser can be modeled with rate equations system, which describes the dynamics of the carriers and electric field, i.e., photons inside the cavity of the slave laser [104]. However, the presence of the external light in the cavity of the slave laser requires some extra terms in the rate equations system, in order to model the coupling of the external electromagnetic field with the field inside the resonator of the slave laser. At first, in the Section 2.1 we derive a model with one longitudinal mode subjected to an optical injection, typical for single-mode laser systems such as DFB lasers. Later, in the Section 2.2 we expand the model to comprise other longitudinal modes supported by the cavity, in order to set a detailed equation system describing multi-mode Fabry-Pérot cavities. As it will be discussed later (Chapters 3 and 4), these unlocked longitudinal modes play highly important role in the slave laser dynamics, especially in the field of the slave laser stability. Thus, in the Section 2.3 we set the theoretical model for investigation of the locking range and Lyapunov asymptotical stability of the slave laser in the regime of injection locking.

2.1 Rate equations in case of injection locking

To obtain model of an injection-locked laser, we start from the wave equation for the electric field [51]:

$$\frac{\partial^2 E(z,t)}{\partial z^2} = \frac{1}{c^2}\frac{\partial^2(\epsilon E(z,t))}{\partial t^2}, \tag{2.1}$$

where $E(z,t)$ stands for the electric field, c stands for the speed of light in the vacuum, and ϵ stands for the complex dielectric constant. The electric field can be written in the form of propagating wave, as [51]:

$$E(z,t) = E(t)\exp[i(\omega t - kz)] + E^*(t)\exp[-i(\omega t - kz)], \tag{2.2}$$

where $E(t)$ represents slowly varying envelope function of the electric field, while $E^*(t)$ stands for its conjugate complex. In the case of the free-running laser, in [51, 105] it has been shown that this envelope function satisfies:

$$\frac{\mathrm{d}E}{\mathrm{d}t} = \frac{A}{2}(1 + i\alpha)E, \tag{2.3a}$$

$$\frac{\mathrm{d}E^*}{\mathrm{d}t} = \frac{A}{2}(1 - i\alpha)E^*. \tag{2.3b}$$

In (2.3a) and (2.3b) $A = G - \gamma$ stands for the effective stimulated emission rate, i.e., the difference between the stimulated emission G and the rate of loss γ. Furthermore, α represents the linewidth enhancement factor, which accounts for the dispersivity of the semiconductor laser diode originating from the fact that the refractive index of the active region is carrier concentration dependent. The linewidth enhancement factor α is defined as the ratio of the change in the real part of the refractive index to the change in the imaginary part as $\alpha = \Delta n'/\Delta n''$ [51, 104].

In the regime of injection locking, the electric field of the slave laser E_{SL} couples with externally injected electric field from the master laser E_{ML}, leading to small modifications of the system (2.3a) – (2.3b) [73, 106]:

$$\frac{\mathrm{d}E_{\mathrm{SL}}}{\mathrm{d}t} = \frac{A}{2}(1 + i\alpha)E_{\mathrm{SL}} + k_{\mathrm{c}}E_{\mathrm{ML}} - i\Delta\omega E_{\mathrm{SL}}, \tag{2.4a}$$

$$\frac{\mathrm{d}E^*_{\mathrm{SL}}}{\mathrm{d}t} = \frac{A}{2}(1 - i\alpha)E^*_{\mathrm{SL}} + k_{\mathrm{c}}E^*_{\mathrm{ML}} + i\Delta\omega E^*_{\mathrm{SL}}. \tag{2.4b}$$

In the equations above parameter k_{c} stands for the coupling coefficient and will be discussed in more detail later, while $\Delta\omega = \omega_{\mathrm{ML}} - \omega_{\mathrm{SL}}$ stands for the frequency detuning between the master and the slave laser. The electric fields can be further decomposed into slowly varying amplitude and the term comprising the phase of the electromagnetic field:

$$E_{\mathrm{SL}}(t) = \widetilde{E}_{\mathrm{SL}}\mathrm{e}^{i\phi_{\mathrm{SL}}} = \sqrt{S(t)}\mathrm{e}^{i\phi_{\mathrm{SL}}}, \tag{2.5a}$$

$$E_{\mathrm{ML}}(t) = \widetilde{E}_{\mathrm{ML}}\mathrm{e}^{i\phi_{\mathrm{ML}}} = \sqrt{S_{\mathrm{inj}}(t)}\mathrm{e}^{i\phi_{\mathrm{ML}}}. \tag{2.5b}$$

Here, both slave and master laser electric fields are assumed to be normalized so that $|E_{\mathrm{SL}}(t)|^2 = S(t)$ and $|E_{\mathrm{ML}}(t)|^2 = S_{\mathrm{inj}}(t)$ where S and S_{inj} are the slave laser output photon number and the injected photon number, respectively. Starting from the $S = E_{\mathrm{SL}}E^*_{\mathrm{SL}}$ we get:

$$\frac{\mathrm{d}S}{\mathrm{d}t} = \dot{E}_{\mathrm{SL}}E^*_{\mathrm{SL}} + E_{\mathrm{SL}}\dot{E}^*_{\mathrm{SL}}. \tag{2.6}$$

Inserting $\dot{E}_{\mathrm{SL}}$ and $\dot{E}^*_{\mathrm{SL}}$ from (2.4a) and (2.4b) yields:

$$\begin{aligned}\frac{\mathrm{d}S}{\mathrm{d}t} =& \frac{A}{2}(1+i\alpha)E_{\mathrm{SL}}E^*_{\mathrm{SL}} + k_{\mathrm{c}}E_{\mathrm{ML}}E^*_{\mathrm{SL}} - i\Delta\omega E_{\mathrm{SL}}E^*_{\mathrm{SL}} \\ &+\frac{A}{2}(1-i\alpha)E^*_{\mathrm{SL}}E_{\mathrm{SL}} + k_{\mathrm{c}}E^*_{\mathrm{ML}}E_{\mathrm{SL}} + i\Delta\omega E^*_{\mathrm{SL}}E_{\mathrm{SL}}.\end{aligned} \tag{2.7}$$

Substituting decomposed forms of electric fields from (2.5a) and (2.5b) we get:

$$\begin{aligned}\frac{\mathrm{d}S}{\mathrm{d}t} &= AS + k_{\mathrm{c}}\sqrt{S\,S_{\mathrm{inj}}}\left[\mathrm{e}^{-i(\phi_{\mathrm{SL}}-\phi_{\mathrm{ML}})} + \mathrm{e}^{i(\phi_{\mathrm{SL}}-\phi_{\mathrm{ML}})}\right] \\ &= AS + 2k_{\mathrm{c}}\sqrt{S\,S_{\mathrm{inj}}}\cos\theta(t),\end{aligned} \tag{2.8}$$

where $\theta(t) = \phi_{\mathrm{SL}}(t) - \phi_{\mathrm{ML}}(t)$ stands for the phase difference between the slave and the master laser.

In order to derive the phase equation, we apply the following procedure. From (2.5a) we extract the phase of the slave laser:

$$\phi_{\mathrm{SL}} = \frac{1}{i}\ln\frac{E_{\mathrm{SL}}}{\sqrt{S}} = \frac{1}{2i}\ln\frac{E_{\mathrm{SL}}}{E^*_{\mathrm{SL}}} \tag{2.9}$$

Taking the time derivate of the equation above leads to:

$$\frac{\mathrm{d}\phi_{\mathrm{SL}}}{\mathrm{d}t} = \frac{1}{2iS}(\dot{E}_{\mathrm{SL}}E^*_{\mathrm{SL}} - E_{\mathrm{SL}}\dot{E}^*_{\mathrm{SL}}) \tag{2.10}$$

Substituting $\dot{E}_{\mathrm{SL}}$ and $\dot{E}^*_{\mathrm{SL}}$ from (2.4a) and (2.4b) yields:

$$\begin{aligned}\frac{\mathrm{d}\phi_{\mathrm{SL}}}{\mathrm{d}t} &= \frac{1}{2iS}(i\alpha AS + k_{\mathrm{c}}E_{\mathrm{ML}}E^*_{\mathrm{SL}} - k_{\mathrm{c}}E^*_{\mathrm{ML}}E_{\mathrm{SL}} - 2i\Delta\omega S) \\ &= \frac{\alpha}{2}A - \Delta\omega + \frac{1}{2iS}k_{\mathrm{c}}\sqrt{S\,S_{\mathrm{inj}}}\left[\mathrm{e}^{-i(\phi_{\mathrm{SL}}-\phi_{\mathrm{ML}})} - \mathrm{e}^{i(\phi_{\mathrm{SL}}-\phi_{\mathrm{ML}})}\right] \\ &= \frac{\alpha}{2}A - \Delta\omega - k_{\mathrm{c}}\sqrt{\frac{S}{S_{\mathrm{inj}}}}\sin\theta(t).\end{aligned} \tag{2.11}$$

Assuming that the phase of the master laser is constant in time, i.e., the time derivate $\dot{\phi}_{\mathrm{ML}} = 0$, equation (2.11) can also be written as:

$$\frac{\mathrm{d}\theta}{\mathrm{d}t} = \frac{\alpha}{2}A - \Delta\omega - k_{\mathrm{c}}\sqrt{\frac{S}{S_{\mathrm{inj}}}}\sin\theta(t). \tag{2.12}$$

In order to set highly detailed model of the rate equations, we account for the coupling of the spontaneous emission to the lasing mode and add an extra term in the differential

equation regarding the dynamics of the photon density S (2.8) [104]:

$$\frac{\mathrm{d}S}{\mathrm{d}t} = AS + \Gamma\beta_{\mathrm{sp}}R_{\mathrm{sp}} + 2k_{\mathrm{c}}\sqrt{S\,S_{\mathrm{inj}}}\cos\theta(t), \tag{2.13}$$

where Γ stands for the confinement factor, which defines the fraction of the photons located within the boundaries of the active region, β_{sp} stands for the spontaneous emission coupling factor, defined as the ratio of the spontaneous emission rate into the lasing mode and the total spontaneous emission rate [104], and finally R_{sp} stands for the total spontaneous optical emission rate.

Finally, the third equation of the system describes the dynamics of the carrier concentration inside the active region and can be written as [104]:

$$\frac{\mathrm{d}n}{\mathrm{d}t} = G_{\mathrm{gen}} - R_{\mathrm{rec}}, \tag{2.14}$$

according to the well known analogy with the process of simultaneously filling and draining the tank with water, where the tank represents the active region with volume V, as depicted in Fig. 2.1 [104]. Here $G_{\mathrm{gen}} = \eta_{\mathrm{i}}I/qV$ is the rate of injected electrons by the electrical current I, i.e., the rate of the water supply in the water tank analogy. The current leakage can be created by possible shunt paths around the active region and is modeled by introducing the internal efficiency η_{i}, which gives the percentage of the carriers actually reaching the active region. On the other hand, the process of recombination comprises several different mechanisms: spontaneous recombination rate R_{sp}, of which a certain fraction couples into the mode of interest, as modeled in (2.13), the carrier leakage R_{l}, due to carriers "splashing" out of the active region by thermionic emission, or by lateral diffusion [104]. Furthermore, R_{nr} stands for the non-radiative recombination rate which comprises several recombination mechanisms and can be modeled by $R_{\mathrm{nr}} = A_{\mathrm{SRH}}n + C_{\mathrm{A}}n^3$. Here $A_{\mathrm{SRH}}n$ represents the Shockley-Reed-Hall recombination rate, while $C_{\mathrm{A}}n^3$ stands for the Auger recombination rate, which is several orders of magnitude higher that the Shockley-Reed-Hall recombination [104]. Finally, R_{st} stands for the radiative recombination, i.e., stimulated emission of the photons. The steady-state is reached once the generation rate becomes equal to the recombination rate, when carriers reach their threshold value n_{th} and stimulated emission starts, i.e., the lasing starts (in the water tank analogy, the water starts to spill over the right tank edge, illustrating the beginning of the stimulated emission, while maintaining the steady liquid level in the tank, illustrating the carrier threshold level). Further increase in the carrier injection through the electrical current will not change the threshold value n_{th}, nor R_{sp} and R_{nr}, it will only increase the number of the emitted photons, i.e., R_{st}. It can be assumed that the stimulated emission is negligible below the laser threshold. Thus, the carrier rate equation (2.14) can be written

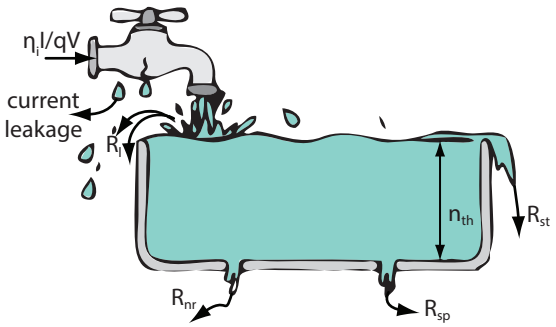

Figure 2.1: *Schematic illustration of the active region - water tank analogy. $\eta_i I/qV$ is the rate of injected carriers, while R_l, R_{nr}, and R_{sp} stand for the leakage, non-radiative recombination rate, and spontaneous emission rate, respectively. Stimulated emission, R_{st}, starts once the threshold is reached; in the water tank analogy, water starts to spill over the edge. Further increase in the rate of injected electrons will only increase the stimulated emission.*

as:

$$\frac{\mathrm{d}n}{\mathrm{d}t} = \frac{\eta_\mathrm{i} I}{qV} - (A_\mathrm{SRH} n + R_\mathrm{sp} + C_\mathrm{A} n^3) - v_g g S(t), \tag{2.15}$$

where $v_\mathrm{g} g S(t)$ stands for R_st [104], with $v_\mathrm{g} = c/n_\mathrm{g}$ representing the group velocity, calculated via the speed of light in the the vacuum c and the group index of refraction n_g. Finally, g stands for the optical gain provided in the active region of the laser.

Optical gain in the active region of the laser is carrier concentration dependent and monotonically increases with an increase in n. However, once the steady-state is reached, i.e., once the carriers reach the threshold value n_th which provides $\mathrm{d}n/\mathrm{d}t = 0$, the gain clamps at the threshold value $g_\mathrm{th} = g(n_\mathrm{th})$. If the gain were higher than g_th, than the field amplitude inside the cavity of the laser would continue to increase without bound, which cannot exist in the steady-state. Indeed, once the gain reaches its threshold value, all the propagation and mirror losses are compensated, so the electromagnetic field in the laser resonator exactly replicates itself after one round-trip around the cavity, thus satisfying the condition for lasing to begin. Mathematically, compensation of the losses in the cavity can be written as:

$$\Gamma g_\mathrm{th} = \langle \alpha_\mathrm{i} \rangle + \alpha_\mathrm{m}, \tag{2.16}$$

where loss factors $\langle \alpha_\mathrm{i} \rangle$ and α_m stand for average internal cavity losses and mirror losses, respectively. Internal cavity losses can be further decomposed as:

$$\langle \alpha_\mathrm{i} \rangle = \Gamma \alpha_\mathrm{a} + (1 - \Gamma)\alpha_\mathrm{c}, \tag{2.17}$$

with α_a representing losses in the active section, while α_c stands for the losses in the cladding.

The total cavity losses can be written with respect to the photon decay rate, i.e., photon lifetime τ_p as [104]:

$$\langle \alpha_i \rangle + \alpha_m = \frac{1}{v_g \tau_p}. \tag{2.18}$$

Now, the previously introduced effective stimulated emission rate term A in (2.3a) – (2.3b) can be written as:

$$A(n) = \Gamma v_g g(n) - \frac{1}{\tau_p}. \tag{2.19}$$

While the carrier concentration is below its threshold value ($n < n_{th}$) the effective stimulated emission rate is negative, $A(n) < 0$, since the rate of the photon generation $\Gamma v_g g(n)$ is still smaller than the rate of losses $1/\tau_p$. Once the threshold is reached, the rate of photon generation becomes equal to the rate of loss, yielding $A(n_{th}) = 0$.

Finally, the rate equation system for the injection-locked mode of the slave laser has the form:

$$\frac{dn}{dt} = \frac{\eta_i I}{qV} - [A_{SRH} n + R_{sp}(n) + C_A n^3] - v_g g(n) S, \tag{2.20a}$$

$$\frac{dS}{dt} = [\Gamma v_g g(n) - 1/\tau_p] S + \Gamma \beta_{sp} R_{sp}(n) + 2k_c \sqrt{S S_{inj}} \cos(\theta), \tag{2.20b}$$

$$\frac{d\theta}{dt} = \frac{\alpha}{2} [\Gamma v_g g(n) - 1/\tau_p] - \Delta\omega - k_c \sqrt{\frac{S}{S_{inj}}} \sin(\theta). \tag{2.20c}$$

2.2 Multi-mode rate equations

Cavities of in-plane lasers, such as DFB and Fabry-Pérot lasers, support more than one longitudinal mode. However, in DFB lasers, mirror loss profile is designed in such manner to suppress all longitudinal modes expect one, making DFB lasers practically single-mode. On the other hand, FP laser diodes have constant mirror loss profile, thus several longitudinal modes compete in the laser output. Different cavity designs, like cavities in vertical cavity surface emitting lasers (VCSELs), usually can support just one, or two longitudinal modes. Regardless of the type of the cavity, both for the intra- and inter-modal injection locking, the most common approach in investigating the injection-locking involves inclusion of only one, injection-locked mode [48–50, 73, 85–87, 102, 106–110]. In the case of intra-modal injection locking, meaning that light is injected into the central, dominant mode, inclusion of the side-modes is advised only in the cases in which injection locking is able to excite more than one longitudinal mode [50]. On the other hand, in the case of inter-modal injection locking, when light is injected into one of the side-modes, there are several studies in which at least central, i.e., free-running dominant mode is taken into account, besides the injection-locked mode [99, 101, 111–113]. How-

ever, in [112] multi-mode rate equations (MREs) have not been used in their full scale, since the the linewidth enhancement factor was neglected and consequently, the phases of all modes were neglected as well. In order to set a detailed model of FP-LD under the inter-modal, i.e., side-mode injection-locking, we extend the single-mode rate equations system (2.20a) – (2.20c) to a multi-mode rate equation system which comprises all modes supported by the FP cavity and by the optical gain [75, 114–119]:

$$\frac{\mathrm{d}n}{\mathrm{d}t} = \frac{\eta_\mathrm{i} I}{qV} - [A_\mathrm{SRH} n + R_\mathrm{sp}(n) + C_\mathrm{A} n^3] - \sum_j v_\mathrm{g} g(n) S_\mathrm{j}, \tag{2.21a}$$

$$\frac{\mathrm{d}S_j}{\mathrm{d}t} = [\Gamma v_\mathrm{g} g(n, \omega_j) - 1/\tau_\mathrm{p}] S_j + \Gamma \beta_\mathrm{sp} R_\mathrm{sp}, \qquad \text{for all } j \neq m, \tag{2.21b}$$

$$\frac{\mathrm{d}S_m}{\mathrm{d}t} = [\Gamma v_\mathrm{g} g(n, \omega_m + \Delta\omega) - 1/\tau_\mathrm{p}] S_m + \Gamma \beta_\mathrm{sp} R_\mathrm{sp} + 2k_\mathrm{c} \sqrt{S_m S_\mathrm{inj}} \cos(\theta_m), \tag{2.21c}$$

$$\frac{\mathrm{d}\theta_m}{\mathrm{d}t} = \frac{\alpha}{2} [\Gamma v_\mathrm{g} g(n, \omega_m + \Delta\omega) - 1/\tau_\mathrm{p}] - \Delta\omega - k_\mathrm{c} \sqrt{\frac{S_m}{S_\mathrm{inj}}} \sin(\theta_m). \tag{2.21d}$$

Presented model comprises not only the injection-locked side-mode, denoted with index m, but also all other unlocked modes, denoted with index j. Since the phases of the unlocked modes are not coupled with their photon densities, system comprises only the phase equation regarding the phase of the injection-locked mode m. If the laser cavity and optical gain support N longitudinal modes, the dimension of the system is N equations regarding the photon dynamics, 1 equation regarding the phase of the injection-locked mode, and 1 equation regarding the carrier dynamics, thus $N + 2$ coupled nonlinear differential equations.

Another extension to the system can be added, by inclusion of the nonlinear gain suppression effect. Apart from the gain saturation at high carrier concentration (which is more pronounced in lower-dimensional systems [120]), the optical gain also tends to saturate at high levels of the photon density inside the cavity. The dominant triggers of the nonlinear gain suppression are considered to be spectral, spatial hole burning, and transient carrier heating [104, 120, 121]. In the spectral hole burning model, large densities of photons cause large carriers depletion in the spectral vicinity of the lasing mode, i.e., in the vicinity of the gain peak, which consequently causes the gain reduction [120]. Spatial hole burning emerges as a result of the interference pattern in optical modes standing waves. Finally, since the lasing energy is smaller than the separation of the quasi-Fermi levels, in the recombination process the cold carriers are removed from the conduction and the valence band, which leads to the effective rise in the carriers temperature and hence the gain reduction, which represents the essence of the transient carrier heating model of nonlinear gain suppression [120]. In the case of multi-mode lasers, the nonlinear gain suppression can be modeled by the gain correction [104]:

$$g(n, \omega_j, S) = \frac{g(n, \omega_j)}{1 + \sum_k \varepsilon_{kj} S_k}, \tag{2.22}$$

where ε_{kj} is called nonlinear gain suppression coefficient. There are two extreme cases. In the first one, the gain of one side-mode is influenced only by it's photon density, meaning that neighboring modes have no impact on the considered side-mode with angular frequency ω_j. In this case $\varepsilon_{kk} = \varepsilon$, for $k = j$, while $\varepsilon_{jk} = 0$ for $k \neq j$, so the upper equation can be written as:

$$g(n, \omega_j, S_j) = \frac{g(n, \omega_j)}{1 + \varepsilon S_j}. \tag{2.23}$$

In the other extreme case, the gain in one mode is equally influenced by the photon density in every other supported longitudinal mode, i.e., $\varepsilon_{jk} = \varepsilon$. In this case:

$$g(n, \omega_j, S) = \frac{g(n, \omega_j)}{1 + \varepsilon \sum_j S_j}. \tag{2.24}$$

In reality, the gain suppression is somewhere between these extreme cases [104]. However for moderate photon densities, when $\varepsilon S_j \ll 1$, or $\varepsilon \sum_j S_j \ll 1$, the effect of the gain compression can be neglected. Usually, ε takes values in order of 10^{-17} cm^{-3} [104].

2.3 Stability of injection-locked laser diodes

2.3.1 The locking range

Essentially, there are two mechanisms responsible for forcing the slave laser field, with nominal angular frequency ω_{SL}, to oscillate at the angular frequency of the master laser field (ω_{ML}), which is injected into the cavity of the slave laser. The first mechanism is defined and discussed in the pioneer paper written on the subject of the injection locking [9], where Adler investigated the locking of the radio frequency oscillators. Adler explained that the injected field adds new out-of-phase component of the electric field to the existing field in the slave oscillator, which introduces a phase shift in the resultant field over the time of the injection. This phase shift results in the frequency shift of the slave oscillator. The whole process can be depicted as in Fig. 2.2, via phasor diagram, which can be found in the [9], referring to the injection locking in radio frequency oscillators, or in [122], referring to the injection locking in the semiconductor lasers. The Fig. 2.2 [122] shows an Adler type phasor diagram of injection locking, depicting the Adler's locking mechanism in semiconductor lasers. The figure depicts the complex slave laser field E_{SL} and the change $k_{\mathrm{c}} E_{\mathrm{ML}} \Delta\tau$, occurring in the time interval $\Delta\tau$, in which injection field from master laser (E_{ML}) couples with the existing field in the laser cavity. The injected field

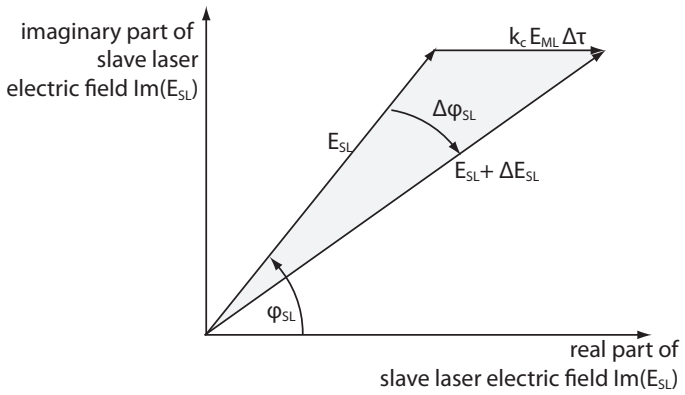

Figure 2.2: *Phasor diagram of injection locking [122]. The presence of the external electric field E_{ML} leads to the change in both phase and intensity of the slave laser field, during the time of the injection $\Delta\tau$, due to the field coupling defined with coupling coefficient k_c which is in the unit of inverse time.*

adds an out-of-phase component $E_{\mathrm{SL}} + \Delta E_{\mathrm{SL}}$, which in turns, alters the phase of the of the slave laser field. As mentioned in the Section 2.1, the fields are normalized to the corresponding photon numbers ($|E_{\mathrm{SL}}(t)|^2 = S(t)$ and $|E_{\mathrm{ML}}(t)|^2 = S_{\mathrm{inj}}(t)$). It can be showed [122] that the phase change, according to the Fig. 2.2, is given as:

$$\Delta\phi_{\mathrm{SL}} = -k_{\mathrm{c}} \sqrt{\frac{S_{\mathrm{inj}}}{S}} \sin\phi_{\mathrm{SL}} \Delta\tau, \tag{2.25}$$

as it was already implemented in the rate equation regrading the phase difference between the master and the slave laser (2.21d).

However, in the semiconductor lasers, one more mechanism is responsible for locking the slave laser to the frequency of the master one. This mechanism originates from the dispersive nature of the semiconductor laser diodes, reflected in the fact that the refractive index is carrier concentration dependent. In the semiconductor lasers, this is modeled through the linewidth enhancement factor α, with typical values in the range 2 – 6 [104]. The presence of the external field, i.e., the presence of the external photons inside the cavity of the slave laser will deplete the carriers, change (increase) the refractive index, which consequently leads to the reduction of the available gain in the active region. This change of the gain results in the shift in the cavity resonance frequency [122]. The change in the gain also leads to the change in the number of the photons in the slave laser output, which can be calculated from the phasor diagram in Fig. 2.2 as:

$$\Delta S = 2k_{\mathrm{c}} \sqrt{S\, S_{\mathrm{inj}}} \cos\phi_{\mathrm{SL}} \Delta\tau, \tag{2.26}$$

as it was implemented in the rate equation regarding the photon dynamics of the injection-

locked mode (2.21c). This output intensity change is accompanied by the change in the net gain (ΔA), i.e., in the effective stimulated emission $\Delta A S \Delta\tau$, so that the steady-state, meaning $\Delta S = 0$ is maintained. From this fact and equation (2.26), effective stimulated emission rate change is obtained:

$$\Delta A = -2k_c \sqrt{\frac{S_{inj}}{S}} \cos\phi_{SL}. \tag{2.27}$$

The accompanying change in the cavity resonance frequency is given as in [51]:

$$\Delta\omega = \frac{\alpha}{2}\Delta A = -k_c\alpha \sqrt{\frac{S_{inj}}{S}} \cos\phi_{SL}. \tag{2.28}$$

On the other hand, from (2.25), the change in the cavity resonance frequency $\Delta\phi_{SL}/\Delta\tau$, yields:

$$\Delta\omega = -k_c \sqrt{\frac{S_{inj}}{S}} \sin\phi_{SL}. \tag{2.29}$$

Finally, combination of the two mechanisms, yields the total angular frequency change:

$$\Delta\omega = -k_c \sqrt{\frac{S_{inj}}{S}}(\alpha\cos\phi_{SL} + \sin\phi_{SL}) = -k_c \sqrt{\frac{S_{inj}}{S}} \sqrt{1+\alpha^2} \sin(\phi_{SL} + \arctan\alpha). \tag{2.30}$$

Keeping in mind that depletion of the carriers leads to the lowering of the gain, the net gain change ΔA has to be negative, thus, from (2.27), since $k_c, S_{inj}, S > 0$ it can be concluded that the cosine term has to be positive, i.e., $\cos\phi_{SL} > 0$ and $-\pi/2 < \phi_{SL} < \pi/2$. On the other hand, the sine term in the equation (2.30) has boundaries $-1 \leq \sin(\phi_{SL} + \arctan\alpha) \leq 1$, giving $-\pi/2 - \arctan\alpha \leq \phi_{SL} \leq \pi/2 - \arctan\alpha$. The intersection of two ranges for ϕ_{SL} give $-\pi/2 < \phi_{SL} \leq \pi/2 - \arctan\alpha$. Insertion of this range in (2.30) defines the locking range, i.e., shows that the available range for $\Delta\omega$ is given by:

$$-k_c \sqrt{\frac{S_{inj}}{S}} \sqrt{1+\alpha^2} \leq \Delta\omega \leq k_c \sqrt{\frac{S_{inj}}{S}}. \tag{2.31}$$

This equation defines an asymmetrical Arnold's plot, as illustrated in Fig. 1.3, which defines the locking range of the injection-locked semiconductor laser. The locking range would become symmetrical in the theoretical case of $\alpha = 0$, i.e., for non-dispersive active material. The asymmetrical locking range can also be theoretically predicted by inspection of the physics of the semiconductor lasers. More precisely, the depletion of the carriers in the case of injection locking will, due to dispersivity of the laser diode and through Kramers-Kroning relations, result in the increase of the active region refractive index. This increase is directly proportional to the magnitude of α and results in lowering

of the cavity resonance, i.e., the slave laser exhibits a red frequency shift. If the injected light is also detuned towards the "red side" with respect to the slave laser, meaning the the frequency detuning $\Delta\omega$ is negative, it can be expected that the locking is easier to be achieved, compared to the case of positive $\Delta\omega$, i.e., the locking range is expected to be asymmetrical with respect to the frequency detuning. However, even if injection parameters are inside this asymmetrical locking range, the dispersive nature of the semiconductor laser diode can bring about dynamic instabilities in certain regions of the locking range.

2.3.2 Lyapunov linearization method

The system of MRE (2.21a) – (2.21d) in its full form is a system of $N+2$ coupled nonlinear differential equations. Since we investigate a multi-mode laser, we may assume that in addition to the central, i.e., dominant mode, which we denote with $j = 0$, the laser cavity supports a number of side-modes on both frequency spectrum sides with respect to the frequency of the central mode ω_0. We introduce l_1 as the number of supported longitudinal side-modes with angular frequencies lower than the frequency of the central mode, $\omega_j < \omega_0$ (long-wavelength side), for which $j < 0$ and l_2 as the number of supported longitudinal side-modes with $\omega_j > \omega_0$ (short-wavelength side), for which $j > 0$. Thus, the index j in (2.21a) – (2.21d) falls in the range $-l_1 \leq j \leq l_2$, i.e., the total number of modes $N = l_1 + l_2 + 1$. Since slave laser operates at the system steady-state, i.e., at its equilibrium point, our goal is to investigate the stability of the slave laser at the steady-state, i.e., to analyze system behavior for some small variation around the steady-state.

The original Lyapunov stability method is applicable to unforced autonomous systems, which can be described with autonomous ordinary differential equations, i.e.:

$$\frac{\mathrm{d}x}{\mathrm{d}t} = f(x). \tag{2.32}$$

The point x_e represents an stable equilibrium point of the system ($f(x_\mathrm{e}) = 0$) if for every given ε, there exists $\delta(\varepsilon) > 0$ so that $\forall t$ [123]:

$$\|x(0) - x_\mathrm{e}\| < \delta \Rightarrow \|x(t) - x_\mathrm{e}\| < \varepsilon, \tag{2.33}$$

where $\|$ stands for the vector norm.

Moreover, the equilibrium point is asymptotically stable if it is stable and if:

$$\lim_{t\to\infty} x(t) = x_\mathrm{e}. \tag{2.34}$$

In other words, if the system, which is put near the equilibrium point, stays forever in the vicinity of this equilibrium point, the system is considered to be Lyapunov stable.

Moreover, if the system converges to the equilibrium point, for every point in its vicinity, the system is considered to be asymptotically stable.

If the system can be represented in the form $\dot{x} = f(x) = \widetilde{\mathcal{X}}x$, then the stability of the system can be discussed from the perspective of the eigenvalues of the matrix $\widetilde{\mathcal{X}}$. The equilibrium state at $x_e = 0$ is globally asymptotically stable if and only if all eigenvalues of $\widetilde{\mathcal{X}}$ lie in the left-half of the complex plane, i.e., that the real parts of all eigenvalues have negative values [123].

In order to investigate the stability of this nonlinear system we linearize the system in the vicinity of the system equilibrium, find the complex eigenvalues of such linearized system and discuss the system stability with respect to the positions of the eigenvalues in the complex plane. In other words, we perform small-signal analysis, which means that we discuss the system response to the small perturbation around the steady-state. For that manner, we assume that the slave laser is modulated with $I = \overline{I} + \delta I \exp \xi t$, where $\overline{I}$ is the steady-state value of the bias current, while $\delta I \ll \overline{I}$ is an amplitude of the small variation around this steady-state value. Finally, $\xi = \lambda + i2\pi f$ is a complex modulation phase, where f stands for the frequency of the modulation, while λ represents the damping factor. The current modulation leads to modulation of carrier concentration n, photon densities S_j for all modes, including the injection-locked side-mode $j = m$, i.e., $-l_1 \leq j \leq l_2$, and finally injection-locked mode phase difference θ_m, which follow the same form:

$$n = \overline{n} + \delta n \mathrm{e}^{\xi t}, \tag{2.35a}$$

$$S_j = \overline{S}_j + \delta S_j \mathrm{e}^{\xi t}, \tag{2.35b}$$

$$\theta_m = \overline{\theta}_m + \delta \theta_m \mathrm{e}^{\xi t}, \tag{2.35c}$$

where $\overline{n}$, $\overline{S}_j$, and $\overline{\theta}_m$ stand for the stationary values, while $\delta n \ll \overline{n}$, $\delta S_j \ll \overline{S}_j$, and $\delta\theta_m \ll \overline{\theta}_m$ stand for the amplitudes of their small perturbations around the corresponding stationary values. Substituting (2.35a) in (2.21a) we get:

$$\begin{aligned} &\frac{\mathrm{d}}{\mathrm{d}t}\left(\overline{n} + \delta n \mathrm{e}^{\xi t}\right) = \\ &\frac{\overline{I} + \delta I \mathrm{e}^{\xi t}}{qV} - \left[A_{\mathrm{SRH}} \cdot \left(\overline{n} + \delta n \mathrm{e}^{\xi t}\right) + R_{\mathrm{sp}}\left(\overline{n} + \delta n \mathrm{e}^{\xi t}\right) + C_{\mathrm{A}} \cdot \left(\overline{n} + \delta n \mathrm{e}^{\xi t}\right)^3\right] - \\ &\sum_{j=-l_1}^{l_2} v_{\mathrm{g}} g\left(\overline{n} + \delta n \mathrm{e}^{\xi t}, \omega_j + \delta_{jm}\Delta\omega\right) \cdot \left(\overline{S}_j + \delta S_j \mathrm{e}^{\xi t}\right). \end{aligned} \tag{2.36}$$

Here δ_{jm} stands for Kronecker delta, which includes the frequency detuning for the injection-locked mode $j = m$. Noting that time derivates of the steady-state values are equal to zero, expanding $R_{\mathrm{sp}}\left(\overline{n} + \delta n \mathrm{e}^{\xi t}\right)$ and $g\left(\overline{n} + \delta n \mathrm{e}^{\xi t}\right)$, keeping in mind that the am-

plitudes of the small variations are much smaller in comparison to the "dc" values, and finally neglecting the small variations of the higher orders (i.e., δn^2, δn^3, and $\delta n \delta S_j$) we get:

$$\begin{aligned}\delta n \xi e^{\xi t} = \frac{\overline{I}}{qV} - \left[A_{\mathrm{SRH}}\overline{n} + R_{\mathrm{sp}}(\overline{n}) + C_{\mathrm{A}}\overline{n}^3\right] - \sum_{j=-l_1}^{l_2} v_{\mathrm{g}} g(\overline{n}, \omega_j + \delta_{jm}\Delta\omega)\overline{S}_j + \\ \frac{\delta I}{qV} e^{\xi t} - \left[A_{\mathrm{SRH}} + \left.\frac{\mathrm{d}R_{\mathrm{sp}}}{\mathrm{d}n}\right|_{n=\overline{n}} + 3C_{\mathrm{A}}\overline{n}^2\right]\delta n e^{\xi t} - \\ \sum_{j=-l_1}^{l_2} v_{\mathrm{g}} g(\overline{n}, \omega_j + \delta_{jm}\Delta\omega)\delta S_j e^{\xi t} - \sum_{j=-l_1}^{l_2} v_{\mathrm{g}} \left.\frac{\partial g(n, \omega_j + \delta_{jm}\Delta\omega)}{\partial n}\right|_{n=\overline{n}} \overline{S}_j \delta n e^{\xi t}.\end{aligned} \tag{2.37}$$

The contribution of the first three terms in the equation above is equal to zero, since it corresponds to the laser steady-state. After losing the first three terms and dividing the whole equation with $\exp(\xi t)$, we rewrite the equation with terms regrouped with respect to δn and δS_j:

$$\xi \delta n = \frac{\delta I}{qV} - \left[\left.\frac{\mathrm{d}Q}{\mathrm{d}n}\right|_{n=\overline{n}} + \sum_{j=-l_1}^{l_2} v_{\mathrm{g}} \frac{1}{\Gamma} \left.\frac{\partial A_j}{\partial n}\right|_{n=\overline{n}} \overline{S}_j\right]\delta n - \sum_{j=-l_1}^{l_2} v_{\mathrm{g}} g(\overline{n}, \omega_j + \delta_{jm}\Delta\omega)\delta S_j, \tag{2.38}$$

where total recombination rate $Q(n)$ was introduced as $Q(n) = A_{\mathrm{SRH}} n + R_{\mathrm{sp}}(n) + C_{\mathrm{A}} n^3$, while $v_{\mathrm{g}}(\mathrm{d}g/\mathrm{d}n)$ was substituted with $(1/\Gamma)(\partial A_j/\partial n)$.

In (2.21b) and (2.21c) we introduce the effective spontaneous emission rate $B(n)$ as $B(n) = \Gamma \beta_{\mathrm{sp}} R_{\mathrm{sp}}(n)$ and derive small-signal equations regarding photon densities S_j and S_m and phase difference θ_m:

$$\xi \delta S_j = \left(\left.\frac{\partial A_j}{\partial n}\right|_{n=\overline{n}} \overline{S}_j + \left.\frac{\mathrm{d}B}{\mathrm{d}n}\right|_{n=\overline{n}}\right)\delta n + A_j(\overline{n}, \omega_j)\delta S_j, \tag{2.39}$$

$$\begin{aligned}\xi \delta S_m = \left(\left.\frac{\partial A_m}{\partial n}\right|_{n=\overline{n}} \overline{S}_m + \left.\frac{\mathrm{d}B}{\mathrm{d}n}\right|_{n=\overline{n}}\right)\delta n + \\ \left[A_m(\overline{n}, \omega_m) + k_{\mathrm{c}}\sqrt{\frac{S_{\mathrm{inj}}}{\overline{S}_m}}\cos(\overline{\theta}_m)\right]\delta S_m - 2k_{\mathrm{c}}\sqrt{S_{\mathrm{inj}}\overline{S}_m}\sin(\overline{\theta}_m)\delta\theta_m,\end{aligned} \tag{2.40}$$

$$\xi \delta\theta_m = \frac{\alpha}{2}\left.\frac{\partial A_m}{\partial n}\right|_{n=\overline{n}} + \frac{k_{\mathrm{c}}}{2}\left(\overline{S}_m\right)^{-3/2} S_{\mathrm{inj}}^{1/2}\sin(\overline{\theta}_m)\delta S_m - k_{\mathrm{c}}\sqrt{\frac{S_{\mathrm{inj}}}{\overline{S}_m}}\cos(\overline{\theta}_m)\delta\theta_m. \tag{2.41}$$

The system can be written in matrix form as:

$$\left[\widetilde{\mathcal{X}} - \xi\widetilde{I}\right]\begin{bmatrix}\delta S_{-l_1}\\ \vdots\\ \delta S_0\\ \vdots\\ \delta S_{l_2}\\ \delta\theta_m\\ \delta n\end{bmatrix} = -\frac{\delta I}{qV}\begin{bmatrix}0\\ \vdots\\ 0\\ \vdots\\ 0\\ 0\\ 1\end{bmatrix}, \tag{2.42}$$

where $\widetilde{I}$ is identity matrix, while $\widetilde{\mathcal{X}}$ is the $N+2\times N+2$ matrix of a system given by:

$$\widetilde{\mathcal{X}} = \begin{bmatrix}
\chi_{-l_1,-l_1} & \cdots & \chi_{-l_1,m} & \cdots & \chi_{-l_1,l_2} & \chi_{-l_1,\theta} & \chi_{-l_1,n}\\
\vdots & \ddots & & & & & \vdots\\
\chi_{m,-l_1} & & \chi_{m,m} & & \chi_{m,l_2} & \chi_{m,\theta} & \chi_{m,n}\\
\vdots & & & \ddots & & & \vdots\\
\chi_{l_2,-l_1} & & \chi_{l_2,m} & & \chi_{l_2,l_2} & \chi_{l_2,\theta} & \chi_{l_2,n}\\
\chi_{\theta,-l_1} & & \chi_{\theta,m} & & \chi_{\theta,l_2} & \chi_{\theta,\theta} & \chi_{\theta,n}\\
\chi_{n,-l_1} & \cdots & \chi_{n,m} & \cdots & \chi_{n,l_2} & \chi_{n,\theta} & \chi_{n,n}
\end{bmatrix}. \tag{2.43}$$

The non-zero matrix elements are:

$$\begin{aligned}
\chi_{j,j} &= A_j(\overline{n},\omega_j) \qquad -l_1 \le j \le l_2 \qquad j \ne m,\\
\chi_{j,n} &= \left(\left.\frac{\partial A_j}{\partial n}\right|_{n=\overline{n}}\overline{S}_j + \left.\frac{\mathrm{d}B}{\mathrm{d}n}\right|_{n=\overline{n}}\right) \qquad -l_1 \le j \le l_2,\\
\chi_{m,m} &= A_m(\overline{n},\omega_m) + k_\mathrm{c}\sqrt{\frac{S_\mathrm{inj}}{\overline{S}_m}}\cos(\overline{\theta}_m),\\
\chi_{m,\theta} &= -2k_\mathrm{c}\sqrt{S_\mathrm{inj}\overline{S}_m}\sin(\overline{\theta}_m),\\
\chi_{\theta,m} &= \frac{k_\mathrm{c}}{2}\left(\overline{S}_m\right)^{-3/2}S_\mathrm{inj}^{1/2}\sin(\overline{\theta}_m),\\
\chi_{\theta,\theta} &= -k_\mathrm{c}\sqrt{\frac{S_\mathrm{inj}}{\overline{S}_m}}\cos(\overline{\theta}_m),\\
\chi_{\theta,n} &= \frac{\alpha}{2}\left.\frac{\partial A_m}{\partial n}\right|_{n=\overline{n}},\\
\chi_{n,j} &= -v_\mathrm{g}g(\overline{n},\omega_j+\delta_{jm}\Delta\omega) \qquad -l_1 \le j \le l_2,\\
\chi_{n,n} &= -\left[\left.\frac{\mathrm{d}Q}{\mathrm{d}n}\right|_{n=\overline{n}} + \sum_{j=-l_1}^{l_2} v_\mathrm{g}\frac{1}{\Gamma}\left.\frac{\partial A_j}{\partial n}\right|_{n=\overline{n}}\overline{S}_j\right].
\end{aligned} \tag{2.44}$$

The matrix $\widetilde{\mathcal{X}}$ represents the system response to the small perturbation around the steady-state, defined with stationary values of carrier concentration, photon densities for all modes, including the injection-locked side-mode $j = m$, and phase difference of the injection-locked mode m, $\overline{n}$, $\overline{S}_j$, and $\overline{\theta}_m$, respectively. According to (2.42), $\xi = \lambda + i2\pi f$ are the eigenvalues of the system, thus, the system is asymptotically stable if all λ, i.e., damping factors have negative values, providing for the asymptotic behaviour. In other words, the equilibrium point $\left(\overline{n}, \overline{S}_j, \overline{\theta}_m\right)$ is asymptotically stable if all the eigenvalues lie in the left-half of the complex plane. In case that one, or more, eigenvalues lie in the right-half of the complex plane, system is considered to be unstable [123].

Chapter 3

Static characteristics of injection locking induced bistability

In this chapter we present theoretical investigation of the steady-state characteristics of injection-locked Fabry-Pérot laser diodes. At first (Section 3.1), we present the calculation of the material gain and spontaneous emission rate, for the material used in the active region of our laser (Section 3.1.1). Further on, we calculate all relevant parameters from our rate equation model (Section 3.1.2). On the basis of the locking range theory from the Section 2.3.1, we calculate and discuss the locking range in the cases of intra- and intermodal injection locking (Section 3.2). In order to further investigate static characteristics of the injection-locked lasers, we set a mathematical model by deriving a transcendental equation with respect to the carrier concentration n, from which we calculate carrier concentration steady-states (Section 3.3). We introduce the $\mathrm{d}n/\mathrm{d}t$ versus n phase plot from which we discuss and analyze the conditions for the simultaneous coexistence of several steady-states, giving rise to optical multistability of the slave laser (Section 3.4). As a consequence of this multistability, we theoretically calculate and present hysteresis loops in the optical output of the slave laser, analyze their formations with correlations to the $\mathrm{d}n/\mathrm{d}t$–n phase plots (Section 3.5), and investigate their characteristics with respect to the injection locking parameters: injection power, frequency detuning and order of the injection-locked mode (Section 3.6). In this thesis, we focus on the hysteresis loops formed by variation of the injection power or frequency detuning. However, our model predicts that the hysteresis loops can also be obtained by variation of the slave laser bias current. Nevertheless, we do not present nor discuss this type of the hysteresis loops, since our analysis shows that the dynamic response of the slave laser to the bias current variation is much worse in comparison to injection power or frequency detuning variation.

Table 3.1: *Material parameters used for band calculation.*

Quantity	$In_{0.75}Ga_{0.25}As_{0.87}P_{0.13}$	$In_{0.46}Ga_{0.39}Al_{0.15}As$
Split-off energy	Δ_{SO} = 321.4 meV	Δ_{SO} = 326.7 meV
Interband matrix element	E_p = 23.48 eV	E_p = 24.97 eV
Electron effective mass	$m_e^* = 0.0389m_0$	$m_e^* = 0.0517m_0$
Luttinger parameters	γ_1 = 10.71 γ_2 = 4.01 γ_3 = 4.88	γ_1 = 8.5 γ_2 = 2.93 γ_3 = 3.65
Average VB position	$E_{v,av}$ = −6.75 eV	$E_{v,av}$ = −6.79 eV
Elastic stiffness constant	c_{11} = 953.27 GPa c_{12} = 493.28 GPa	c_{11} = 1046.00 GPa c_{12} = 509.95 GPa
CB deformation potential	a_c = −5.99 eV	a_c = −6.02 eV
VB deformation potential	a_v = −1.02 eV	a_v = −1.24 eV
Shear deformation	b = −1.86 eV	b = −1.94 eV

3.1 Parameters of IL Fabry-Pérot laser diode

3.1.1 Material gain and spontaneous emission

As an active region of the Fabry-Pérot laser diode, an $In_{0.75}Ga_{0.25}As_{0.87}P_{0.13}$ (well)/$In_{0.46}Ga_{0.39}Al_{0.15}As$ (barrier) 1.55-μm strain-compensated multiquantum well (MQW) material is used. This material system is recognized as the one that provides high modulation bandwidth of lasers [124], due to the balanced and, therefore, improved carrier transport through the MQW structure. In order to calculate the conduction band (CB) and the valence band (VB) edges for a given alloys compositions, the "model-solid-theory" [125], combined with the interpolation schemes and material parameters as given in [126], is applied. The simulations assume a constant device temperature of 300 K. The material parameters used for electronic band calculation are given in Table 3.1. By utilizing 1.05% compressive strained well and 0.5% tensile strained barrier, a precise band structure adjustment is performed, resulting in λ = 1698 nm optimized well (E_g = 0.73 eV) with conduction band discontinuity ratio $\Delta E_c/(\Delta E_c + \Delta E_{v,HH-LH})$ = 81.1%. The band-edge diagrams for InGaAsP/InGaAlAs hetero-junction with and without strain taken into account are shown in Fig. 3.1. In our model, the MQW active region consists of 3 equally spaced quantum wells with well thickness d = 8.7 nm, although the number of wells can be increased and still maintain good carrier transport and population inversion in all the wells simultaneously [124].

In order to set a detailed and precise model of the rate equations, material gain $g(n, \hbar\omega)$ versus carrier concentration n and photon energy $\hbar\omega$ (Fig. 3.2), and spontaneous emis-

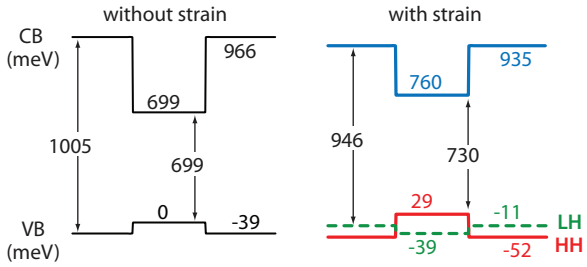

Figure 3.1: *Band-edge levels.*

sion $R_{sp}(n, \hbar\omega)$ [Fig. 3.3(a)] are calculated. Although $R_{sp}(n, \hbar\omega)$ can be exploited directly, we do not find its contribution to the calculated mode intensity significant and, therefore, use more convenient dependence for total spontaneous recombination rate: $R_{sp}(n) = \int R_{sp}(n, \hbar\omega)\mathrm{d}(\hbar\omega)$ [Fig. 3.3(c)]. The gain calculation is based on the single-QW band structure obtained by the 8×8 k.p method [127] that takes into account Burt-Foreman Hermitianization [128] and biaxial strain generated by lattice mismatched growth of the well-barrier layers. An appropriate basis set is used, which enables decoupling of 8×8 Hamiltonian into two 4×4 Hamiltonians as in [129]. In calculating the band structure, the finite-difference method is used.

3.1.2 Laser parameters

For the active region consisting of $N_w = 3$ quantum wells of thickness $d = 8.7$ nm, assuming $L = 250\,\mu$m long Fabry-Pérot resonator, and $w = 4\,\mu$m laser width, we calculate the volume of the active region as $V = N_w L w d = 2.61 \times 10^{-11}$ cm^3. We calculate the confinement factor per well to be $\Gamma_1 = 0.0187$ resulting in total confinement factor of the active region of $\Gamma = N_w \Gamma_1 = 0.056$ [114].

Next, taking the refractive index of the active material to be $n_r = 3.6$, we calculate resonator mirror reflectivities $R_1 = R_2 = R = [(n_r - 1)/(n_r + 1)]^2 = 0.32$. The mirror losses are then calculated to be $\alpha_m = (1/L)\ln(1/R) = 45.58$ cm^{-1} [104, 114]. Internal losses of active region and cladding are taken to be $\alpha_a = 40$ cm^{-1} and $\alpha_c = 22$ cm^{-1}, respectively. By the means of (2.16) and (2.17) we get $g_{th} = 1222.5$ cm^{-1}. For the calculated gain threshold value, knowing that the gain spectrum is centered around $\hbar\omega_0 = 0.8$ eV, we calculate the carrier threshold concentration $n_{th} = 2.85 \times 10^{18}$ cm^{-3}. Assuming that stimulated emission starts for $I > I_{th}$ and taking $\eta_i = 1$, under the assumption that stimulated emission can be negligible under the laser threshold, from (2.21a) we calculate the threshold current I_{th} as:

$$I_{th} = qV(A_{SRH} n_{th} + R_{sp}(n_{th}) + C_A n_{th}^3) = 8.16\ \text{mA}, \tag{3.1}$$

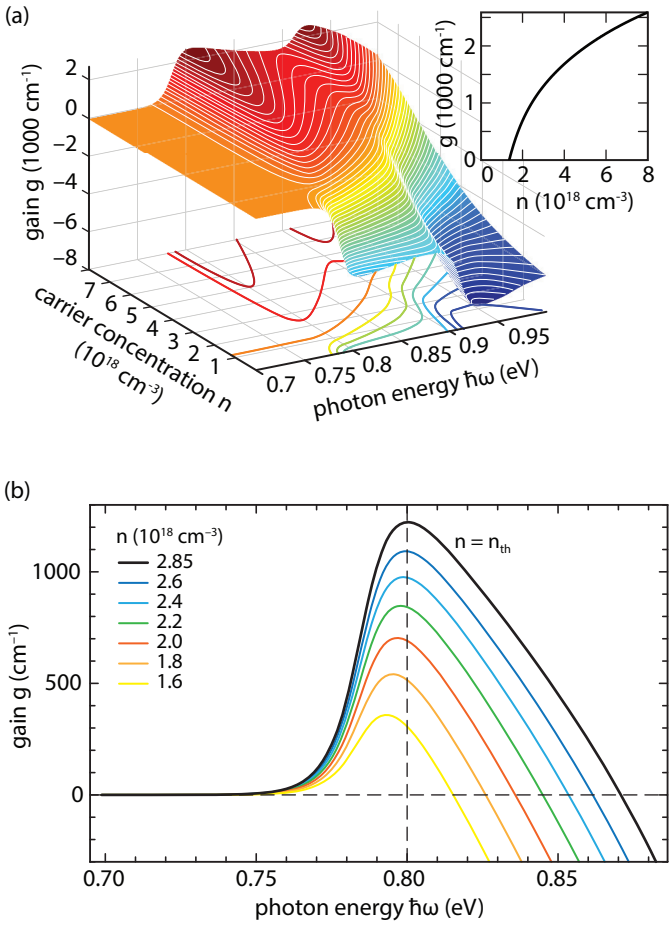

Figure 3.2: *(a) Material gain spectrum for $In_{0.75}Ga_{0.25}As_{0.87}P_{0.13}$ 1.05% compressive well with $In_{0.46}Ga_{0.39}Al_{0.15}As$ 0.5% tensile barrier versus photon energy ($\hbar\omega$) and carrier concentration (n). Inset: Gain versus carrier concentration at $\hbar\omega_0$ = 0.8 eV. (b) Gain profile versus photon energy for different levels of carrier concentration [114].*

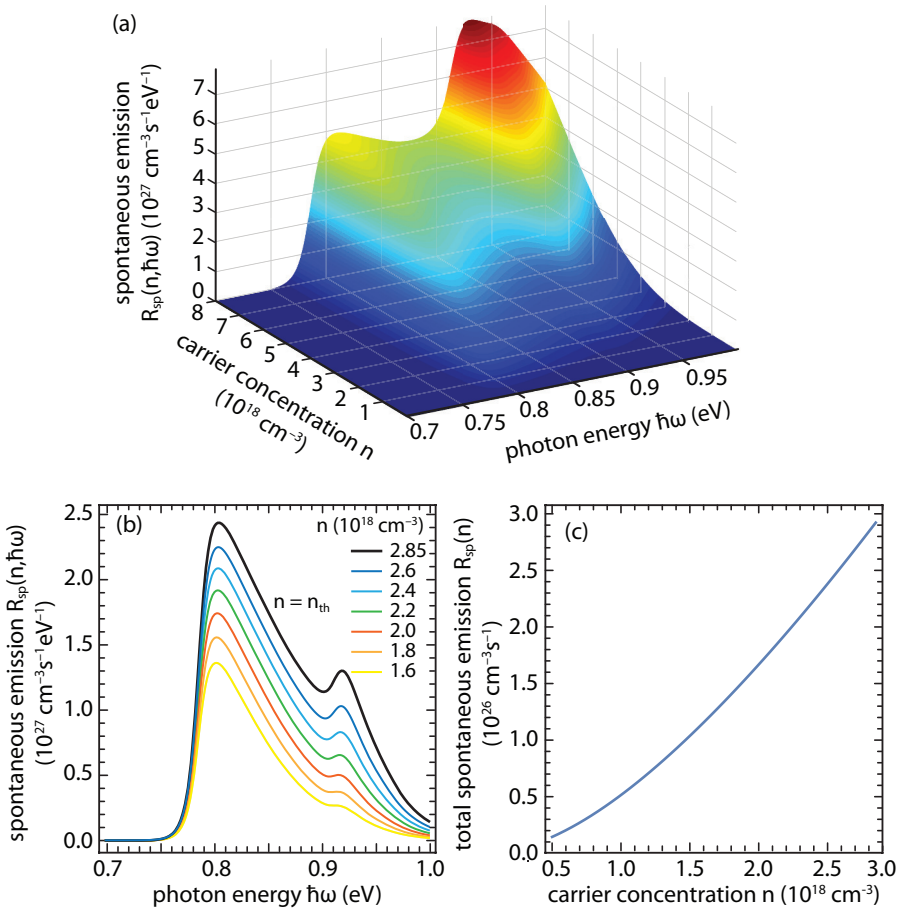

Figure 3.3: *(a) Spontaneous emission $R_{sp}(n,\hbar\omega)$ versus carrier concentration (n) and photon energy ($\hbar\omega$). (b) Spontaneous emission profile $R_{sp}(\hbar\omega)$ for different levels of carrier concentration n. (c) Total spontaneous recombination rate $R_{sp}(n)$ used in (2.21b) and (2.21c).*

where $A_{\mathrm{SRH}} = 1.1 \times 10^{8}$ s^{-1} [130] and $C_{\mathrm{A}} = 5.82 \times 10^{-29}$ cm^{6}s^{-1} [130].

The group index of refraction for the selected active material in the laser has the value $n_{\mathrm{g}} = 4.2$, which through (2.18) gives the value for the photon lifetime $\tau_{\mathrm{p}} = 2.04$ ps. In order to calculate β_{sp} we apply definition [104]:

$$\beta_{\mathrm{sp}} = \frac{R_{\mathrm{sp}}^{'}}{R_{\mathrm{sp}}(n)}, \tag{3.2}$$

where $R_{\mathrm{sp}}(n)$ is calculated total spontaneous recombination rate, while $R_{\mathrm{sp}}^{'}$ is the spontaneous emission rate per unit volume into one optical mode, defined as [104]:

$$R_{\mathrm{sp}}^{'} = \frac{\Gamma v_{\mathrm{g}} g(n) n_{\mathrm{inv}}}{V}. \tag{3.3}$$

In equation above, n_{inv} stands for dimensionless population inversion factor [104]:

$$n_{\mathrm{inv}} = \frac{1}{1 - \exp[(E_{\mathrm{g}} - \Delta E_{\mathrm{f}})/(k_{\mathrm{B}} T)}, \tag{3.4}$$

with $E_{\mathrm{g}} = 0.7298$ eV standing for the energy of the bandgap of our active material, while ΔE_{f} is the quasi-Fermi level separation, k_{B} is the Boltzmann constant, and T stands for the active region temperature. Positive optical gain is achieved when $n_{\mathrm{inv}} > 0$, meaning that the carrier population is inverted, i.e., that the carrier concentration at higher energy level is greater than the concentration at the lower energy level, which is one of the prerequisites for the lasing to start. In semiconductor lasers this parameter usually takes values around 1.25 [104], while in our simulation it has somewhat smaller value around 1.01. At the threshold carrier concentration $n = n_{\mathrm{th}}$, we calculate $\Delta E_{\mathrm{f}} = 0.8716$ eV and combining (3.2), (3.3) and (3.4), we get $\beta_{\mathrm{sp}} = 6.46 \times 10^{-5}$, which is in order of usual values encountered in the semiconductor lasers [104].

At the threshold, the gain profile is centred at the photon energy of $\hbar\omega_0 = 0.8$ eV, which corresponds to the lasing wavelength of 1.55 μm, though the gain profile is asymmetrical with respect to this central photon energy, as it is depicted in the Fig. 3.2(b). The given resonator length implies intermodal spacing $\Delta\omega_{\mathrm{IM}}$ of:

$$\Delta\omega_{\mathrm{IM}} = \frac{\pi c}{n_{\mathrm{g}} L} = 89.7 \times 10^{10} \text{ rad/s} = 89.7\Omega, \tag{3.5}$$

where we introduce Ω as $\Omega = 10^{10}$ rad/s. At the threshold level $n = n_{\mathrm{th}}$, the laser cavity supports only those longitudinal modes for which $g(n_{\mathrm{th}}, \hbar\omega) > 0$. Using the formula for the intermodal spacing, we calculate that, apart from the central mode corresponding to $\hbar\omega = 0.8$ eV, the number of the supported modes is $l_1 = 170$ on the long-wavelength side

(modes with $\hbar\omega < 0.8$ eV) and $l_2 = 120$ on the short-wavelength side ($\hbar\omega > 0.8$ eV). Accounting for the central mode, this gives the total number of the supported modes by the Fabry-Pérot cavity to be $N = l_1 + l_2 + 1 = 291$.

The coupling coefficient is calculated using the common formula for Fabry-Pérot cavity types, found in the literature [133]:

$$k_c = \frac{c}{2n_g L} \ln\left(1 + \frac{1-R}{\sqrt{R}}\right) = 1.13 \times 10^{11}\ \mathrm{s}^{-1}. \tag{3.6}$$

However, for other laser cavity types, calculation of the coupling coefficient can be more demanding. In [131] we conducted a rigorous analytical analysis of the photon lifetime in index-coupled phase-shifted DFB lasers and showed that the photon lifetime exhibits a strong spectral dependence. The external coupling coefficient k_c depends on the photon lifetime, i.e., due to the presence of the external optical field, the photon lifetime is altered [132, 133]. As a consequence, the external coupling coefficient should also depend on the photon frequency, i.e., on the frequency detuning $\Delta\omega$.

Finally, instead of injected photon density S_{inj} as a merit of injection strength, we shall rather use injection power P_{inj}, which is related to S_{inj} via:

$$P_{\mathrm{inj}} = S_{\mathrm{inj}} \frac{\eta_0 \hbar\omega V}{\tau_p \Gamma}, \tag{3.7}$$

where $\eta_0 = 0.33$ is optical efficiency, defined as in [104]. The equation (3.7) gives injection power in units of watts, though in further text we choose to refer to it in units of Decibel-milliwatts (dBm), which are related to watts through $10 \log_{10} \frac{P_{\mathrm{inj}}}{1\ \mathrm{mW}}$.

3.2 The locking range

In order to more thoroughly mathematically define the boundaries of the locking range and later on perform stability analysis inside of the locking range, we rewrite the MRE system, Eqs. (2.21a) – (2.21d) in more compact form [115], in which we introduce r defined as the relative injection power, i.e., the ratio of the density of the injected photons to the density of the photons in the injection side-mode m ($r = S_{\mathrm{inj}}/S_m$):

$$\frac{\mathrm{d}n}{\mathrm{d}t} = \frac{I}{qV} - Q(n) - \sum_{j=-l_1}^{l_2} v_g g(n, \omega_j + \delta_{jm}\Delta\omega) S_j, \tag{3.8a}$$

$$\frac{\mathrm{d}S_j}{\mathrm{d}t} = A_j S_j + B(n) + 2k_c \delta_{jm} \sqrt{r} S_j \cos(\theta_j), \tag{3.8b}$$

$$\frac{\mathrm{d}\theta_m}{\mathrm{d}t} = \frac{\alpha}{2} A_m - \Delta\omega - k_c \sqrt{r} \sin(\theta_m). \tag{3.8c}$$

Here we use the total recombination rate $Q(n)$ and effective spontaneous emission $B(n)$, defined as in (2.38), while $A_j = \Gamma v_g g(n, \omega_j + \delta_{jm}\Delta\omega) - \tau_p^{-1}$ is the already defined effective rate of stimulated photon generation for mode j. Finally, equation (3.8b) applies on all modes including the injection-locked mode m, which is regulated by Kronecker delta δ_{jm}, which includes the part regarding the injection locking only for $j = m$. In all our calculations the total number of the photons present in the resonator of the slave laser is at least two orders of magnitude smaller than the one needed to trigger the mechanism of the nonlinear gain suppression, which is why we do not take it into account in our model.

We start the injection locking range analysis by neglecting the $B(n)$ term in the injection-locked photon density equation (3.8b), in the case of injection-locked mode, i.e., for $j = m$, since it turns out to be few orders of magnitude smaller in comparison with the other terms. From the steady-state form of this equation, $\mathrm{d}S_m/\mathrm{d}t = 0$, we get:

$$A_m = -2k_c \sqrt{r} \cos(\theta_m). \tag{3.9}$$

Inserting (3.9) in the steady-state form of (3.8c) ($\mathrm{d}\theta_m/\mathrm{d}t = 0$), we obtain:

$$\Delta\omega = -k_c \sqrt{r}[\sin(\theta_m) + \alpha \cos(\theta_m)] = -k_c \sqrt{r}\sqrt{1+\alpha^2} \sin[\theta_m + \arctan(\alpha)]. \tag{3.10}$$

From the equation above we derive:

$$\theta_m = \mathrm{Arcsin}\left[\frac{-\Delta\omega}{k_c \sqrt{r}\sqrt{1+\alpha^2}}\right] - \arctan(\alpha). \tag{3.11}$$

Here, the first term is generalized inverse sine, which is given by $\varphi(-1)^z + z\pi$, with $\varphi = \arcsin[-\Delta\omega/(k_c \sqrt{r}\sqrt{1+\alpha^2})]$ being its principal value, while z is an integer, which in this case has a physical meaning only for $z \in \{0, 1\}$. Introducing $\psi = \arctan(\alpha)$, from the steady-state form of (3.11) we obtain:

$$r = \frac{-\Delta\omega}{k_c \sqrt{1+\alpha^2} \sin(\theta_m + \psi)}. \tag{3.12}$$

For extreme values of the sine function $\sin(\theta_m + \psi) = \pm 1$, the equation (3.12) defines the four-wave-mixing (FWM) boundaries [48–50]. The phenomenon of FWM is a frequency conversion process, which involves the interaction of the slave laser beam (the pump) at the frequency f_{SL} and the injected beam (the probe) with the frequency f_{inj}. Due to the nonlinear interaction between them, a set of two new frequencies emerge, resulting in laser spectra consisting of four equidistant frequencies separated by the frequency detuning $f_{SL} - f_{ML}$. The newly generated waves are the phase conjugates of the injected signal [134].

However, in terms of the locking range, besides FWM boundary, an additional constraint comes from the fact that $\cos(\theta_m)$ should be positive, which makes the locking range asymmetrical, as discussed in the Section 2.3.1. The locking boundary can be derived from $\cos(\theta_m) = 0$, which can be converted to $\sin(\theta_m) = \pm 1$. Looking at the the steady-state form of (3.8c) and keeping in mind that A_m is negative, we can conclude that for $\Delta\omega > 0$, the sine term has to be $\sin(\theta_m) = -1$ in order to compensate for the negative first two terms in (3.8c). Similarly, for $\Delta\omega < 0$, $\sin(\theta_m) = 1$. Returning back to the stationary form of (3.8c) we can write:

$$\frac{\alpha}{2} A_m = \Delta\omega - \mathrm{sgn}(\Delta\omega) k_c \sqrt{r}. \tag{3.13}$$

At this moment it becomes important to discuss and clearly distinguish the locking range map for two possible cases: when the injection locking is intra-modal, i.e., applied in the central mode $j = m = 0$, and when injection locking is inter-modal, i.e., applied in one of the side-modes $j = m \neq 0$.

Intra-modal injection locking

In the case in which injection locking is applied in the central mode $j = m = 0$, for the extreme case of $\cos(\theta_m) = 0$, in the steady-state, the carrier threshold is reached which sets $A_m = 0$, thus from (3.13), we get the locking range boundary:

$$r = \left(\frac{\Delta\omega}{k_c} \right)^2. \tag{3.14}$$

In the Fig. 3.4, according to (3.12), we plot the FWM boundary for $\alpha = 3$ (black dotted line), as well as the FWM boundaries for somewhat smaller value, $\alpha = 2$ (higher red dotted line), and for somewhat higher value, $\alpha = 6$ (lower green dotted line). The non-FWM region is depicted as yellow shaded area in Fig. 3.4. It can be seen that larger values of α give wider locking range in terms of FWM boundaries. Indeed, higher values of α give higher fluctuations of the refractive index and optical gain with respect to the carrier concentration variations. This means that for the same r, laser with higher α will exhibit higher red frequency shift, allowing for higher values of frequency detuning, thus making the locking range wider. Additional constraint, introduced with $\cos(\theta_m) > 0$, i.e., with (3.14) is depicted with dot-dashed lines in Fig. 3.4. However, as we will discuss later, within the inter-modal locking, only the right boundary actually shrinks the region outlined by the FWM boundaries, i.e., the asymmetrical locking range is given by the hatched over yellow region, from the left FWM boundary, to the right $\cos(\theta_m)$ boundary [115].

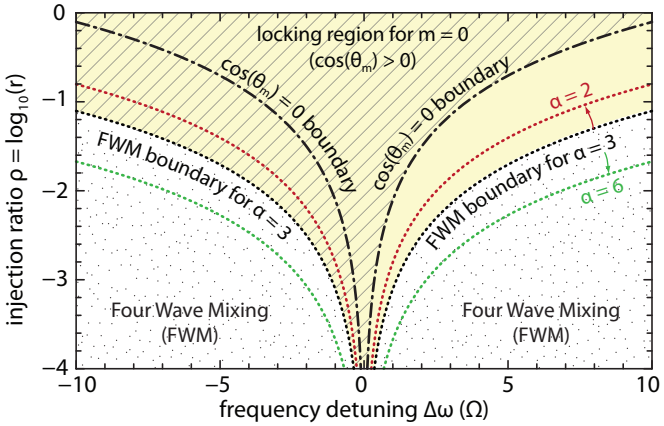

Figure 3.4: *The locking range for intra-modal injection locking ($m = 0$) (hatched over yellow region). The FWM boundaries for $\alpha = 2$ and $\alpha = 6$ are depicted with red and green dotted lines, respectively. The yellow shaded area, outlined with black dotted line is non-FWM region for $\alpha = 3$. Dot-dashed lines represent $\cos(\theta_m) = 0$ locking boundaries. [115].*

Inter-modal injection locking

If m is a side-mode ($m \neq 0$), at extreme case when $\cos(\theta_m) = 0$, A_m in (3.13) cannot be equal to zero, as in the case of intra-modal injection locking. In this case the carrier threshold is not reached, i.e., $A_m(n_c) < 0$, where $n_c < n_{th}$ is the steady-state carrier concentration in the case of inter-modal injection locking for the limit case of $\cos(\theta_m) = 0$. In order to define the locking boundary, we have to obtain the value of n_c which corresponds to the locking boundary and thus represents the highest possible value of the carrier concentration steady-state in the case of inter-modal injection locking. According to (3.8b), the stationary photon densities are given by $S_j = -B(n)/A_j(n)$, for all modes $j \in [-l_1, l_2]$, since $\cos(\theta_m) = 0$ excludes the extra terms in the injection-locked mode photon density equation. Substituting this into the stationary form of carrier concentration equation (3.8a), we get:

$$0 = \frac{I}{qV} - Q(n) + \sum_{j=-l_1}^{l_2} v_g g(n, \omega_j + \delta_{jm}\Delta\omega)\frac{B(n)}{A_j(n)}. \tag{3.15}$$

which we solve for the stationary carrier concentration $n_c < n_{th}$. This relation ($n_c < n_{th}$) stays valid regardless of the number of modes we take into account in (3.15). The minimum requirement, in order to obtain a valid solution to (3.15), is to take into account the central mode, $j = 0$ and the injection-locked one, $j = m$, while the exactness of the model increases with an increase in number of modes taken into account. However, the common models in the literature take into account only injection-locked mode [48–50, 73, 85–87, 102, 106–110]. If only side-mode m is taken into account, the solution to

the (3.15) will be $n_c > n_{th}$, which corresponds to the gain threshold of the mode m, as if it were the central mode in the free-running regime. In other words, taking into account only the injection-locked mode in the case of inter-modal injection locking mistakenly produces previously discussed case of intra-modal injection locking, though with side-mode m acting as the dominant mode. In reality, in the free-running regime of a multi-mode laser diode, a side-mode m cannot reach its threshold and emerge as a dominant mode, since mode $j = 0$ reaches the threshold first, due to the smaller gain defect. For that reason, in the case of inter-modal injection locking, it is crucial to take into account at least two modes, injection-locked and the central one. Inclusion of other unlocked longitudinal modes in addition to the injection-locked one will also prove to be crucial when it comes to stability analysis [114, 115], which will be discussed later. Locking boundaries in the case of side-mode injection locking can be still derived from (3.13), though this time $A_m(n_c < 0)$. This results in locking boundaries:

$$r_{\pm} = \left[\frac{1}{k_c}\left(\pm|\Delta\omega| - \mathrm{sgn}\,(\Delta\omega)\frac{\alpha}{2}A_m(n_c)\right)\right]^2, \tag{3.16}$$

where sign "+" corresponds to positive and small magnitude negative $\Delta\omega$, while sign "−" corresponds to sufficiently negative $\Delta\omega$.

In Fig. 3.5 we depict FWM (dotted lines) and $r_{\pm}$ boundaries (dot-dashed lines), i.e., the locking range in the case of inter-modal injection locking into the side-mode $m = -5$. The FWM boundary is again defined as in the previous case of intra-modal locking, with $\sin(\theta_m + \arctan\psi) = b = \pm 1$, where sign "−" corresponds to $\Delta\omega > 0$, while sign "+" corresponds to $\Delta\omega < 0$. Thus, according to the previously introduced definition for generalized inverse sine:

$$\theta_m + \psi = \varphi(-1)^z + z\pi, \tag{3.17}$$

where $\varphi = \arcsin(b)$, while integer z takes values 0 or 1, making two possible outcomes $\theta_m + \psi = \varphi$, or $\theta_m + \psi = \pi - \varphi$. For the right FWM boundary ($\Delta\omega > 0$), $b = -1$, thus, according to (3.17), the boundary defines $\theta_m = -\pi/2 - \psi$ or, taking the $\pi - \varphi$ branch, $\theta_m = 3\pi/2 - \psi$, where $\psi = \arctan(\alpha) \approx 2\pi/5$, though we shall keep it in general form ψ for the sake of the generality of the analysis. Condition $\Delta\omega = 0$ corresponds to $\sin(\theta_m + \psi) = 0$, i.e., $\theta_m = -\psi$, or taking the $\pi - \varphi$ branch, $\theta_m = \pi - \psi$. Thus, for $\Delta\omega \geq 0$, the range of θ_m inside the FWM boundaries is defined with $-\psi \leq \theta_m \leq -\pi/2 - \psi$ or $\pi - \psi \leq \theta_m \leq 3\pi/2 - \psi$ [yellow shaded regions in Fig. 3.6(a)]. However, an additional constraint $\cos\theta_m > 0$ defined with Eq. (3.16) (hatched regions in Fig. 3.6) excludes the $\pi - \varphi$ branch from consideration, since it leads to negative values of $\cos\theta_m$. This additional constraint also shrinks the available range of θ_m in the φ branch [cf. Fig. 3.6(a)] and gives $-\pi/2 < \theta_m \leq -\psi$. This means that r_+ boundary shrinks the locking range, rising the boundary of the

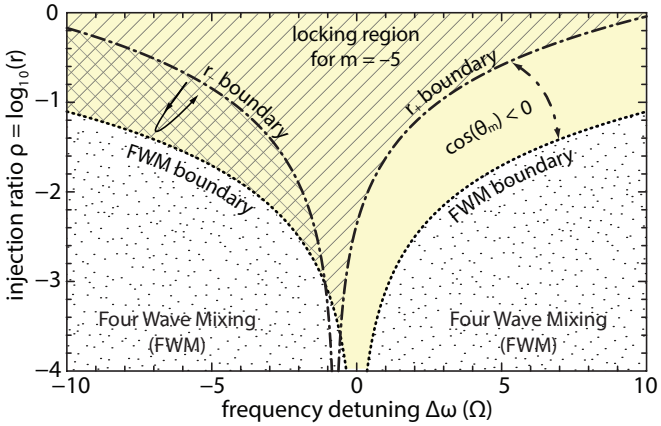

Figure 3.5: *The locking range for inter-modal injection locking ($m = -5$) for $I = 1.2I_{th}$ (hatched and double hatched over yellow region). The yellow shaded area, outlined with black dotted line is non-FWM region. Dot-dashed lines represent* $\cos(\theta_m) = 0$ *locking boundaries for the model comprising all supported modes, which practically overlaps with the model taking into account only $j = 0$ and $m = -5$ [115]. Double hatched region represents the locking region which is folded along the FWM boundary and overlaps with the hatched region [115].*

locking above the FWM line, as depicted in Fig. 3.5.

For the left FWM boundary ($\Delta\omega < 0$), $b = +1$, thus, according to (3.17) both branches of the generalized inverse sine define $\theta_m = \pi/2 - \psi$. Combining with the condition for θ_m at $\Delta\omega = 0$, shows that both branches can be taken into the consideration, since both branches comprise regions in which $\cos\theta_m > 0$ [cf. Fig. 3.6(b)]. More precisely, the φ branch gives $-\psi \leq \theta_m \leq \pi/2 - \psi$, while the other branch gives $\pi/2 - \psi \leq \theta_m \leq \pi - \psi$. Finally the union of this ranges, intersecting with $\cos\theta_m > 0$ gives $-\psi \leq \theta_m < \pi/2$. In this case, the θ_m range comprises $\theta_m = \pi/2 - \psi$ corresponding to the left FWM boundary. This means that for $\Delta\omega < 0$, the left FWM boundary divides the θ_m range into two segments, $-\psi \leq \theta_m \leq \pi/2 - \psi$ and $\pi/2 - \psi \leq \theta_m < \pi/2$. Since FWM boundary corresponds to the smallest r for a given $\Delta\omega$, it can be concluded that the locking range in the $\Delta\omega$–r space is folded down along the FWM boundary, leading to the overlap of the two locking regions in the $r-$range between the FWM and r_- boundaries (double hatched region in Fig. 3.5). For small negative detuning, $\Delta\omega \approx -1.13\Omega$, the left FWM boundary crosses the locking range $\cos(\theta_m) \geq 0$. The intersection of the FWM boundary and the $\cos(\theta_m) = 0$ boundary is possible, since at this point and its vicinity, there is more than one stationary solution, which can satisfy either one or the other condition imposed by these two boundaries. Within the locking range, the FWM boundary sets θ_m to $\pi/2 - \psi$, but it becomes irrelevant, since on its both sides, injection locking is possible. The folding down along the FWM boundary and overlap of the locking regions between FWM and

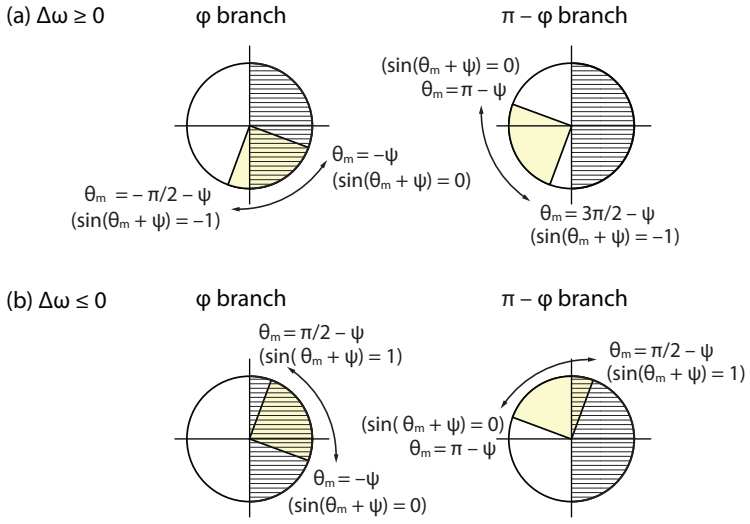

Figure 3.6: *(a) The range of θ_m corresponding to non-FWM region for $\Delta\omega \geq 0$ (yellow region). Hatched region corresponds to additional constraint $\cos(\theta_m) > 0$. Union of the hatched over yellow areas (locking area) correspond to hatched over yellow locking region for $\Delta\omega \geq 0$ from Fig. 3.5. (b) Same for $\Delta\omega \leq 0$. Here the locking region comprises the FWM boundary, as in Fig. 3.5.*

corresponding r boundaries is also valid for $m = 0$, though we do not present this case, since we are focused on the inter-modal injection locking.

From Fig. 3.5 it can be seen that the locking range in the case of inter-modal injection locking exhibits a nonzero detuning offset for small injection ratios r. The essential reason for this is in our definition of ω_m and the uneven change of the frequencies for the dominant mode and side longitudinal modes when the carrier density varies. The dominant frequency ω_0 is the lasing frequency defined to correspond to the threshold carrier concentration $n = n_{\text{th}}$, while ω_m is the frequency for the injection-locked side-mode, defined in the free-running regime by $\omega_m = \omega_0 + m(\pi c/n_{\text{g}}L)$. However, the carrier concentration in the regime of the injection locking is bellow n_{th}, i.e., the carrier concentration and consequently gain, exhibit decrease. The central mode exhibits higher gain reduction in comparison to any side-mode (cf. Fig. 3.2(b)). As the linewidth enhancement factor α correlates the change in the real part of the refractive index to the change in the imaginary part (i.e., gain) [51, 104], assuming a constant α for both modes, a smaller decrease of the gain for the side-mode m leads to its smaller frequency decrease, in comparison to the decrease of the frequency of the central mode. This means that the definition of ω_m overestimates its value for regime of injection-locking in which $n \leq n_{\text{th}}$. The correction term for the injection-locked mode frequency ω_m, i.e., the frequency shift of the side-mode frequency ω_m, is proportional to its gain defect. For example, the gain defect is zero ($A_m = 0$) for the dominant mode $m = 0$ (ω_0) and it is negative ($A_m < 0$) for any side-mode $m \neq 0$

(ω_m). Therefore, side-modes should exhibit a negative frequency shift (red shift) with respect to the frequencies given by $\omega_m = \omega_0 + m(\pi c/n_g L)$. This shift is taken into account by the first term in (3.8c) and for small or negligible injection ratio r ($r \approx 0$), in the stationary state ($\mathrm{d}\theta_m/\mathrm{d}t = 0$), it can be compensated only by the negative detuning offset $\Delta\omega_{\mathrm{offset}}$. This small red shift detuning offset can be calculated from (3.16) from the condition that $(\alpha/2)A_m(n_c) = |\Delta\omega|$, which gives $\Delta\omega_{\mathrm{offset}} = -0.741\Omega$ for the case when we include modes $m = -5$ and $j = 0$ and $\Delta\omega_{\mathrm{offset}} = -0.729\Omega$ with all supported modes included in (3.15). In these calculations we take $I = 1.2I_{\mathrm{th}}$. The locking range boundary, thus, stays practically the same, wether we, besides injection-locked mode m, take into account only the central mode $j = 0$, or all supported longitudinal modes (dot-dashed line).

3.3 Mathematical model for static characteristic investigation

For the sake of investigating the static characteristics of injection locking, we start from the stationary form of the MRE system (2.21a) – (2.21d):

$$\frac{\mathrm{d}n}{\mathrm{d}t} = 0 = \frac{I}{qV} - Q(n) - \sum_{j=-l_1}^{l_2} v_g g(n, \omega_j + \delta_{jm}\Delta\omega) S_j, \tag{3.18a}$$

$$\frac{\mathrm{d}S_j}{\mathrm{d}t} = 0 = A_j(n, \omega_j) S_j + B(n), \qquad \text{for all } j \neq m, \tag{3.18b}$$

$$\frac{\mathrm{d}S_m}{\mathrm{d}t} = 0 = A_m(n, \omega_m + \Delta\omega) S_m + B(n) + 2k_c\sqrt{S_m S_{\mathrm{inj}}}\cos(\theta_m), \tag{3.18c}$$

$$\frac{\mathrm{d}\theta_m}{\mathrm{d}t} = 0 = \frac{\alpha}{2}A_m(n, \omega_m + \Delta\omega) - \Delta\omega - k_c\sqrt{\frac{S_m}{S_{\mathrm{inj}}}}\sin(\theta_m), \tag{3.18d}$$

with $Q(n)$, A_j, A_m, and $B(n)$ defined as in (3.8a) – (3.8c).

From (3.18b) we can calculate every photon density S_j, except the injection-locked one ($j = m$), as:

$$S_j(n) = -\frac{B(n)}{A_j(n, \omega_j)}. \tag{3.19}$$

In order to calculate $S_m(n)$ we eliminate θ_m from (3.18c) and (3.18d). We start from dividing (3.18c) with S_m and multiplying (3.18d) with 2, which yields:

$$0 = A_m(n, \omega_m + \Delta\omega) + \frac{B(n)}{S_m} + 2k_c\sqrt{\frac{S_{\mathrm{inj}}}{S_m}}\cos(\theta_m), \tag{3.20a}$$

$$0 = \alpha A_m(n, \omega_m + \Delta\omega) - 2\Delta\omega - 2k_c\sqrt{\frac{S_{\mathrm{inj}}}{S_m}}\sin(\theta_m). \tag{3.20b}$$

The equations above can be rewritten in the form:

$$-2k_{\mathrm{c}}\sqrt{\frac{S_{\mathrm{inj}}}{S_m}}\cos(\theta_m) = A_m(n,\omega_m+\Delta\omega)+\frac{B(n)}{S_m}, \tag{3.21a}$$

$$2k_{\mathrm{c}}\sqrt{\frac{S_{\mathrm{inj}}}{S_m}}\sin(\theta_m) = \alpha A_m(n,\omega_m+\Delta\omega)-2\Delta\omega, \tag{3.21b}$$

and after we raise each equation to the power of 2, we add them to get:

$$4k_{\mathrm{c}}^2\frac{S_{\mathrm{inj}}}{S_m} = (\alpha A_m-2\Delta\omega)^2+\left(A_m+\frac{B}{S_m}\right)^2. \tag{3.22}$$

By rearranging the terms in the equation above we get a quadratic equation with respect to the photon density in the injection-locked mode S_m [114]:

$$\left[A_m^2+(\alpha A_m-2\Delta\omega)^2\right]S_m^2+\left(2A_mB-4k_{\mathrm{c}}^2S_{\mathrm{inj}}\right)S_m+B^2=0. \tag{3.23}$$

The solution to the (3.23) is given by [114]:

$$S_m^{\pm}=\frac{-\left(2A_mB-4k_{\mathrm{c}}^2S_{\mathrm{inj}}\right)\pm\sqrt{\left(2A_mB-4k_{\mathrm{c}}^2S_{\mathrm{inj}}\right)^2-4B^2\left[A_m^2+(\alpha A_m-2\Delta\omega)^2\right]}}{2\left[A_m^2+(\alpha A_m-2\Delta\omega)^2\right]}. \tag{3.24}$$

The denominator in (3.24) is always positive. In addition to this, the term $-(2A_mB-4k_{\mathrm{c}}^2S_{\mathrm{inj}})$ is also always positive, since $A_m<0$, while $B,k_{\mathrm{c}},S_{\mathrm{inj}}>0$. Moreover, the square root term is smaller than the $-(2A_mB-4k_{\mathrm{c}}^2S_{\mathrm{inj}})$ term, yielding that both "+" and "–" signs can be taken into consideration, since they both can lead to positive values of S_m. However, in our simulations, corresponding photon rate loss for S_m^-, i.e., S_m^-/τ_{p} turns out to be few orders of magnitude smaller than the effective spontaneous emission rate B, so therefore S_m^- cannot be considered as stimulated emission, which is why we only take "+" into consideration and assume that $S_m=S_m^+$.

Additionally, the term under the square root must be positive, leading to the quadratic equation with respect to injected photon density:

$$S_{\mathrm{inj}}^2+\frac{|A_m|B}{k_{\mathrm{c}}^2}S_{\mathrm{inj}}-\frac{B^2}{4k_{\mathrm{c}}^4}(-\alpha|A_m|-2\Delta\omega)^2\geq 0, \tag{3.25}$$

where we made use of the fact that $A_m<0$ so that $A_m=-|A_m|$. The zeros of the quadratic

equation above are:

$$S_{\text{inj}}^{\pm} = \frac{1}{2}\left[-\frac{|A_m|B}{2k_c^2} \pm \sqrt{\left(\frac{A_m B}{k_c^2}\right)^2 + \frac{B^2}{k_c^4}(-\alpha|A_m| - 2\Delta\omega)^2}\right]. \tag{3.26}$$

Here, the term under the square root is for sure positive and obviously larger than $-|A_m|B/k_c^2$ term, thus "−" sign leads to a negative value of $S_{\text{inj}} = S_{\text{inj}}^-$, while "+" sign leads to a positive value $S_{\text{inj}} = S_{\text{inj}}^+$. Mathematically, the inequality (3.25) is satisfied for both $S_{\text{inj}} \leq S_{\text{inj}}^-$ and $S_{\text{inj}} \geq S_{\text{inj}}^+$, where only the latter one is physically justified, thus injected photon density has to satisfy:

$$S_{\text{inj}} \geq \frac{|A_m|B}{2k_c^2}\left[-1 + \sqrt{1 + \frac{(-\alpha|A_m| - 2\Delta\omega)^2}{A_m^2}}\right]. \tag{3.27}$$

If effective spontaneous emission rate B is neglected, which is a common approach in the literature, the quadratic equation with respect to S_m (3.23) yields two solutions, $S_m^- = 0$ and the other, physically justified, solution as in [13]:

$$S_m = \frac{4k_c^2 S_{\text{inj}}}{A_m^2 + (-\alpha|A_m| - 2\Delta\omega)^2}. \tag{3.28}$$

Finally, we can substitute Eqs. (3.24) and (3.19) in (3.18a) and obtain a transcendental equation with respect to the carrier concentration n [114]:

$$0 = \frac{I}{qV} - Q(n) + \sum_{-l_1 \leq j \leq l_2}^{j \neq m} v_g g(n, \omega_j)\frac{B(n)}{A_j(n, \omega_j)} - v_g g(n, \omega_m + \Delta\omega) S_m(n, S_{\text{inj}}, \Delta\omega). \tag{3.29}$$

For defined values of the bias current I, injected photon density S_{inj} and the frequency detuning $\Delta\omega$ we can calculate S_j and S_m dependences on n using Eqs. (3.19) and (3.24), respectively, and then solve (3.29) for stationary points n_{sp}. In case of no injection ($S_{\text{inj}} = 0$), Eq. (3.29) describes the free-running laser, which has one stationary state, corresponding to the carrier threshold n_{th}, already calculated in Section 3.1.2. Since injection of the photons increase the total number of the photons inside the cavity of the slave laser, it can be expected that the new steady-state will be smaller than n_{th}. In order to find all steady-states of (3.29) we investigate the sign changes for the wide range of carrier concentrations below n_{th}. In the domains in which we find sign changes, we apply bisection method to calculate stationary points. Once a stationary point n_{sp} is found, we can return to (3.19) and (3.24) to calculate corresponding stationary values of S_j and S_m, respectively. Finally, from (3.18d), we can calculate the stationary value of the phase

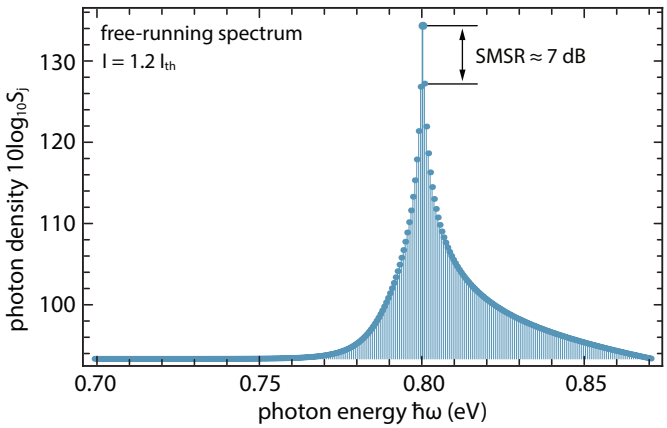

Figure 3.7: *The free-running spectrum of FP LD for $I = 1.2I_{th}$. Side-modes with higher photon energies (short-wavelength side) are slightly more pronounced in comparison to the same order side-modes on the long-wavelength side, due to the gain asymmetry. The photon densities are given in logarithmic ratio.*

difference θ_m:

$$\theta_m(n_{\mathrm{sp}}) = \arcsin\left[\frac{\alpha A_m(n_{\mathrm{sp}}, \omega_m + \Delta\omega) - 2\Delta\omega}{2k_{\mathrm{c}}\sqrt{S_{\mathrm{inj}}/S_m(n_{\mathrm{sp}})}}\right]. \tag{3.30}$$

3.4 Analysis of injection locking phase plot

Before we start to deal with injection locking, in Fig. 3.7 we present the free-running spectrum of our Fabry-Pérot laser diode, under the bias current of $1.2I_{\mathrm{th}}$. The spectrum of modes is obtained by solving the steady-state system (3.18a) – (3.18c) in which $S_{\mathrm{inj}} = 0$, with already calculated threshold carrier concentration n_{th}. The obtained spectrum is centered at 0.8 eV, with around 7 dB of side-mode-suppression-ratio (SMSR) which is defined as:

$$\mathrm{SMSR} = 10\log_{10}\frac{S_{\mathrm{high}}}{S_{\mathrm{low}}}. \tag{3.31}$$

Here S_{high} stands for the mode with the highest power output in the spectrum, in this case the central mode $j = 0$ (S_0), while S_{low} stands for the strongest side-mode, in this case mode $j = +1$ (S_1). Usual requirement for the laser to be considered to have single-mode output is to have SMSR over 30 dB [85–87]. The side-modes with higher photon energies have somewhat smaller gain defect in comparison to the same order side-modes on the other, low energy side of the spectrum 3.2(b). This produces that the "positive" side-modes ($j > 0$) are slightly more pronounced than same order "negative" side-modes ($j < 0$) (c.f. Fig. 3.7). The photon density of the central mode is in the order of 10^{13} cm^{-3}, while nearest side-modes have one order smaller densities.

In Fig. 3.8 we depict photon density dependences on the carrier concentration n for

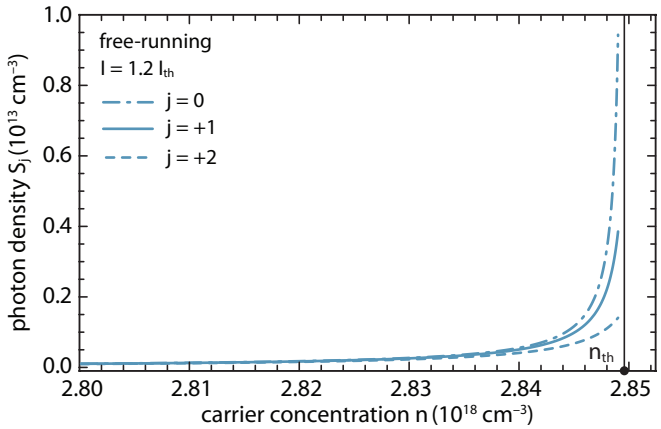

Figure 3.8: *Dependences $S_j(n)$ for central mode $j = 0$ (dash-dotted line), mode $j = +1$ (solid line), and mode $j = +2$ (dashed line). The thin vertical line represents the free-running carrier threshold concentration n_{th} asymptote.*

the central mode $j = 0$ and modes $j = +1, +2$, calculated according to (3.19). As carrier concentration reaches its threshold value n_{th}, the photon densities rapidly grow, since the effective rate of the stimulated emission $A_j(n, \omega_j)$, which stands in the denominator of (3.19), becomes closer to zero. The central mode experiences the steepest growth, being the closest mode to the gain maximum. However, for the injection-locked mode, in a certain range of injection parameters S_{inj} and $\Delta\omega$, this dependence can look quite different. Example of this dependence, calculated from the Eq. (3.24), is given in Fig. 3.9, which is obtained for injection into the side-mode $m = -5$, with $S_{\text{inj}} = 6.53 \times 10^{12}$ cm^{-3}, which corresponds to $P_{\text{inj}} = -12$ dBm, according to Eq. (3.7). The frequency detuning is set to $\Delta\omega = -7\Omega$. Figure 3.9 shows that, except for carrier concentration n, corresponding to the maximum photon density value, there are two carrier concentrations leading to the same photon density, i.e., the function $n(S_m)$ is a multivalued function. From Fig. 3.9 it can be seen that for carrier concentrations lower than the threshold concentration, the injection-locked side-mode m has few orders of magnitude higher photon density than the central mode. However, as the carrier concentration reaches its free-running threshold level n_{th}, the photon density of the injection-locked side-mode decreases, while the photon density of the central mode rapidly increases, since the denominator in Eq. (3.19) approaches zero. In other words, as the carrier concentration approaches n_{th}, slave laser approaches the free-running dynamics in which the central mode is the dominant one.

The presented $S_m(n)$ profile is injection power and frequency detuning dependent, as depicted in Fig. 3.10(a) and (b), respectively. In Fig. 3.10(a) we depict the $S_m(n)$ profile for a fixed negative frequency detuning $\Delta\omega = -7\Omega$ and various values of the injection power P_{inj}. It can be seen that an increase in the injection power leads to higher maximum for the injection-locked mode m, due to larger number of externally injected photons. The

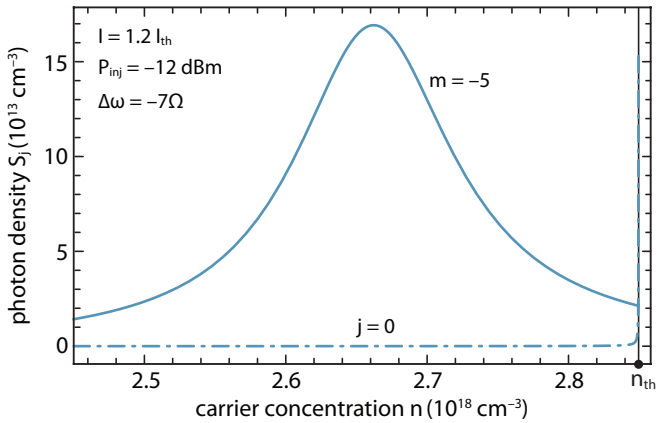

Figure 3.9: *Photon densities $S_m = S_m^+$ for $m = -5$, according to (3.24) (solid line) and S_j for $j = 0$ (dash-dotted line), versus carrier concentration n. The thin vertical line represents the free-running carrier threshold concentration n_{th} asymptote.*

maximum is always reached for the same value of the carrier concentration n regardless of the injection level. On the other hand, Fig. 3.10(b) illustrates the influence of the frequency detuning $\Delta\omega$ on the $S_m(n)$ profile. For a small magnitude negative detuning [e.g., $\Delta\omega = -2\Omega$ in Fig. 3.10(b)], the maximum photon density is reached close to the free-running carrier threshold concentration n_{th}. As detuning becomes more negative, the maximum is shifted towards smaller carrier concentrations. However, for a fixed injection power, these maxima become smaller, since smaller n provides smaller gain and thus higher injected photon density is required to maintain the same level of the photon density in the injection-locked mode m. On the other hand, positive frequency detuning $\Delta\omega$ will cause the maximum to shift towards higher values of carrier concentration n and even a small positive detuning, e.g. $\Delta\omega = 0.1\Omega$ [dashed line in Fig. 3.10(b)] is already sufficient enough to shift it beyond the free-running threshold concentration n_{th}. However, since we are interested in multivalued character of the $n(S_m)$ function below the slave laser free-running threshold, we do not present $S_m(n)$ profiles for positive values of the frequency detuning. In addition to this, the $S_m(n)$ profile is dependent on the order of the injection-locked mode m, as presented in Fig. 3.11. As the order of the injection-locked mode m becomes higher, both on the long- or short-wavelength side, i.e., as $|m|$ increases, the maximum of the $S_m(n)$ profile is shifted towards the higher carrier concentrations. For a given injection power ($P_{\text{inj}} = -12$ dBm) and frequency detuning ($\Delta\omega = -7\Omega$), at some critical injection-mode order ($m = -22$ for long-wavelength and $m = 15$ for short-wavelength side), maximum of the $S_m(n)$ profile is shifted beyond the free-running threshold concentration n_{th}. For fixed P_{inj} and $\Delta\omega$, as the injection moves further away from the central mode, either on the long- or short-wavelength side, the available gain at some fixed carrier concentration n, for the particular side-mode, becomes smaller, or, in

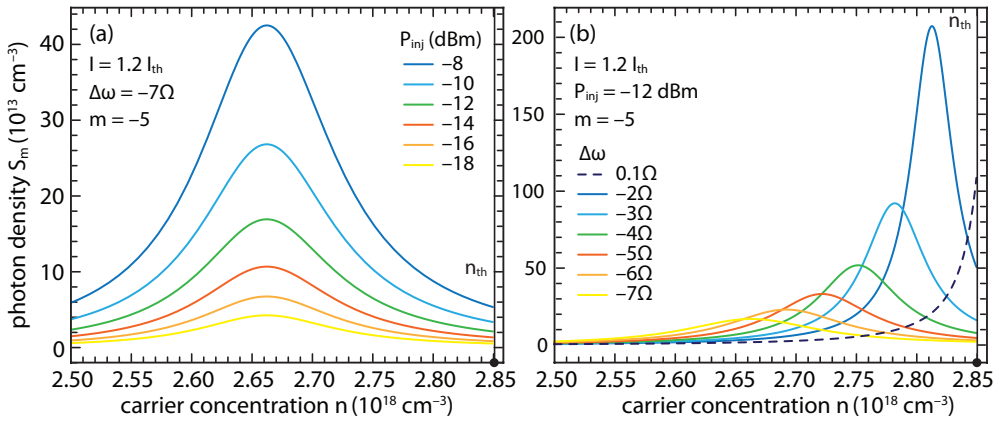

Figure 3.10: *(a) $S_m(n)$ profile versus injection power P_{inj}, for a fixed negative $\Delta\omega = -7\Omega$. (b) $S_m(n)$ profile versus frequency detuning $\Delta\omega$, for a fixed injection power $P_{inj} = -12$ dBm. The thin vertical line in both (a) and (b) stands for the free-running carrier threshold concentration n_{th} asymptote.*

other words, the gain defect becomes larger. For this reason, the maximum of the $S_m(n)$ profile of the higher order side-modes is reached at higher carrier concentrations, which provide higher gain and thus compensate for the increasing gain defect.

Once we calculate $S_j(n)$ and $S_m(n)$ profiles we can substitute them in the carrier rate equation (3.18a). At first we examine the model which comprises only injection-locked mode (case 1), so we let all $S_j = 0$ except $j = m = -5$ and set $I = 1.2I_{th}$, $P_{\text{inj}} = -12$ dBm, and $\Delta\omega = -7\Omega$. We base our investigation of the static characteristics of injection-locking on the careful analysis of (3.18a), i.e., we substitute calculated $S_m(n)$ in the Eq. (3.18a) and study its stationary solutions. For that purposes, in Fig. 3.12, we introduce the carrier concentration rate $\mathrm{d}n/\mathrm{d}t$ versus carrier concentration n phase plot, which we use to find carrier concentration steady-states. In the case 1, we find two stationary points denoted as $n_{\text{sp}}^{(1)}$ and $n_{\text{sp}}^{(2)}$, which are both smaller than the free-running threshold concentration n_{th}. These two solutions emerge as a direct consequence of the parabolic shape of the $S_m(n)$ profile. The bias current pumps the carriers inside the active region through the I/qV term, while recombination mechanisms, both non-radiative and radiative ones deplete the carriers. The parabolic profile of the photon density inside the injection-locked mode m leads to the depletion which produces a "dip" in the $\mathrm{d}n/\mathrm{d}t$–n phase plot, resulting in the formation of two stationary points (Fig. 3.12). Nevertheless, these two solutions, also predicted in [101], are insufficient for the optical bistability as predicted in [101], since it turns out that the stationary point $n_{\text{sp}}^{(2)}$ is unstable. The unstable character of this stationary point can be, at some extent, discussed and inferred from the phase plot introspection. If the system were settled in the $n_{\text{sp}}^{(2)}$ point and were to exhibit some small perturbation that would decrease the carrier concentration, then the negative slope of $\mathrm{d}n/\mathrm{d}t$ versus n phase

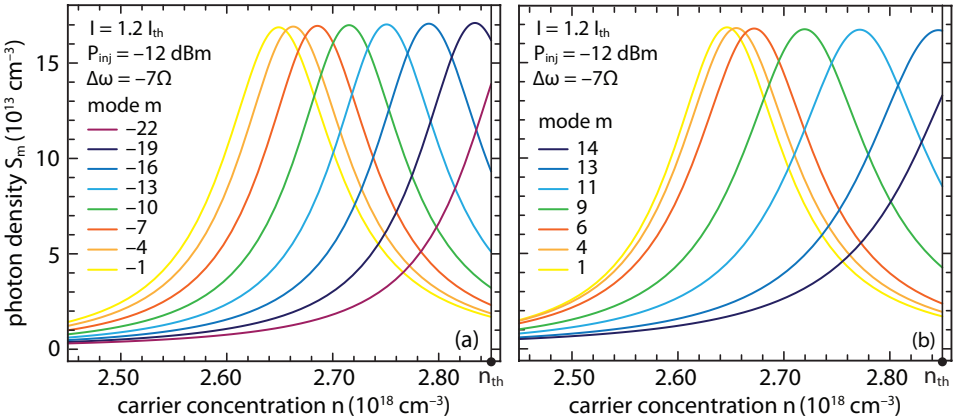

Figure 3.11: *$S_m(n)$ profile with respect to injection into various side-modes on the (a) long-wavelength side ($m < 0$) and on the (b) short-wavelength side ($m > 0$). Injection power P_{inj} and frequency detuning $\Delta\omega$ are set to -12 dBm and -7Ω, respectively. The thin vertical line in both (a) and (b) stands for the free-running carrier threshold concentration n_{th} asymptote.*

plot for $n < n_{\mathrm{sp}}^{(2)}$ would lead to a further decrease of n, thus pushing the system away from $n_{\mathrm{sp}}^{(2)}$. Similarly, a small variation which would cause the carrier concentration to increase, would also push the system away from the $n_{\mathrm{sp}}^{(2)}$ point, since, in this region, positive slope of dn/dt–n would support the further increase of n. This defines the $n_{\mathrm{sp}}^{(2)}$ point as a repulsive stationary point. On the other hand, the $n_{\mathrm{sp}}^{(1)}$ point represents an attractive stationary point, due to the fact that the slopes of dn/dt–n phase plot on both sides of the stationary point compensate carrier variation induced by a system perturbation and thus push the system back to the $n_{\mathrm{sp}}^{(1)}$ point. The dynamic stability has to be, however, investigated by the Lyapunov stability analysis, as described in 2.3.2. As it will be showed later, this point proves to have instabilities only for positive values of $\Delta\omega$ [115], thus the model which comprises only one, injection-locked side-mode, although giving two slave laser steady-states, predicts only one stable state, eliminating the possibility of the bistable slave laser output. The bistability can be observed only once we include at least the central mode $j = 0$ into account, as in the case 2 (c.f. Fig. 3.12) [114]. The rapid growth of photon density in the central mode in the vicinity of the carrier threshold concentration leads to a sudden decrease of dn/dt–n phase plot and formation of the third stationary point $n_{\mathrm{sp}}^{(3)}$ in the vicinity of n_{th}. According to this, the $n_{\mathrm{sp}}^{(3)}$ point is not a consequence of injection locking, rather the consequence of the unlocked modes interplay. As $n_{\mathrm{sp}}^{(1)}$, the stationary point $n_{\mathrm{sp}}^{(3)}$ is also an attractive stationary point, and, as it will be showed later, stability analysis shows that there is a range of injection power and frequency detuning in which both $n_{\mathrm{sp}}^{(1)}$ and $n_{\mathrm{sp}}^{(3)}$ are dynamically stable, thus providing optical bistability [114, 115]. The number of longitudinal modes included in Eq. (3.18a) affects the accuracy of the calculated stationary

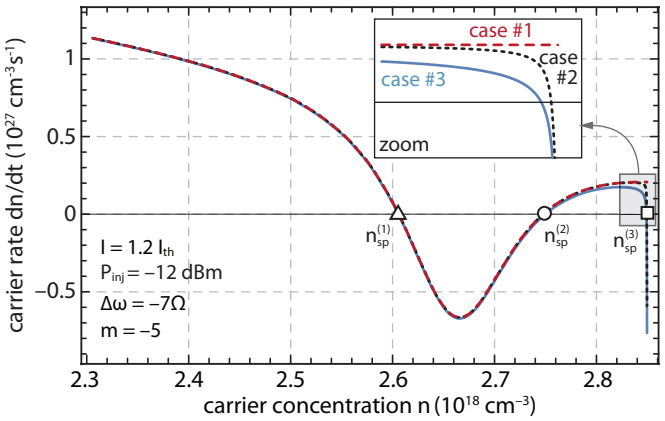

Figure 3.12: *Carrier concentration rate dn/dt versus carrier concentration n phase plot for: (case 1) only injection-locked mode m included, (case 2) injection-locked m and central mode $j = 0$ included, and (case 3) all modes included. The inset shows the detailed view of the concentration rate dependence in the vicinity of the free-running threshold.*

points, especially $n_{\mathrm{sp}}^{(3)}$, which moves further away from the n_{th}, as depicted in the case 3 in Fig. 3.12. Although the difference between calculated stationary values obtained by including only the central mode on one side (case 2) and the central and many side-modes, on the other (case 3), is not too large, its value considerably affects the calculated gain and photon density for various modes. Therefore, in our further consideration based on case 3, we use all 291 supported longitudinal modes.

As the shape of the dn/dt–n phase plot is dominantly influenced by injection-locked mode m and the central mode $j = 0$, we analyze the phase plot dependence on the injection parameters, since $S_m(n)$ strongly depends on the injection parameters. Figure 3.13 shows the evolution of dn/dt–n phase plot with change in the injection power P_{inj} for a fixed value of $\Delta\omega$, and consequently shows the range of injection power in which phase plot has more than one stationary point (shaded area in Fig. 3.13). Starting from the low injection power ($P_{\mathrm{inj}} = -20$ dBm, upper dot-dashed line in Fig. 3.13), for a fixed value of $\Delta\omega = -7\Omega$, the phase plot has only one stationary point, which is close to the free-running threshold carrier concentration n_{th}. This state is mainly a consequence of the interplay of the unlocked modes, dominantly the central one, as it does not emerge as a result of injection locking into the side-mode m. The reason for that comes from the fact that for such low injection power, the maximum of the $S_m(n)$ profile is not high enough [cf. Fig. 3.10(a)] to lower the phase plot so that it intersects with the dn/d$t = 0$ axis. In this state, the slave laser is close to the free-running regime, which means that it exhibits the similar dynamics, with central mode emerging as the dominant mode, as depicted in the Fig. 3.14(a). For a certain injection level ($P_{\mathrm{inj}} = -15$ dBm), the contribution of the

injection-locked mode m in Eq. (3.18a) becomes sufficient enough to form a new stationary point, which, for a little bit higher injection power, splits into two stationary points $n_{\mathrm{sp}}^{(1)}$ and $n_{\mathrm{sp}}^{(2)}$ (cf. Fig. 3.13). Further increase in the injection power makes the two points to move further away from each other, i.e., the $n_{\mathrm{sp}}^{(1)}$ point shifts towards lower carrier concentrations, while $n_{\mathrm{sp}}^{(2)}$ point shifts towards higher carrier concentrations, approaching the $n_{\mathrm{sp}}^{(3)}$ point. At $P_{\mathrm{inj}} = -9.5$ dBm, $n_{\mathrm{sp}}^{(2)}$ and $n_{\mathrm{sp}}^{(3)}$ coincide, while for slightly higher injection power ($P_{\mathrm{inj}} > -9.5$ dBm), dn/dt–n phase plot again has only one stationary point, $n_{\mathrm{sp}}^{(1)}$ (lower dot-dashed line in Fig. 3.13). Shaded region, corresponding to -15 dBm $< P_{\mathrm{inj}} < -9.5$ dBm, represents the region of multiple stationary points (RMSP), in which two, out of three stationary points can be stable, thus providing bistability. Points $n_{\mathrm{sp}}^{(1)}$ and $n_{\mathrm{sp}}^{(2)}$ are results of the injection locking, since they emerge as a direct consequence of the parabolic $S_m(n)$ profile, while $n_{\mathrm{sp}}^{(3)}$ point still remains the consequence of the unlocked modes interplay. Figures 3.14(b) and (c) depict the slave laser mode spectra for a case of moderate injection power ($P_{\mathrm{inj}} = -12$ dBm) in the case of slave laser settled in steady-states $n_{\mathrm{sp}}^{(3)}$ and $n_{\mathrm{sp}}^{(1)}$, respectively. The stationary point $n_{\mathrm{sp}}^{(3)}$ is close to the free-running threshold carrier concentration n_{th} and, as in the case of low injection power, mode spectrum resembles the free-running, except injection-locked mode is now somewhat pronounced, due to the injected photons and can be comparable to the central mode [c.f. Fig. 3.14(b)]. On the other hand, stationary point $n_{\mathrm{sp}}^{(1)}$ has lower carrier concentration, which reduces the available gain and suppresses all longitudinal modes except the injection-locked one, which is highly pronounced due to the coupling of the injected photons. In this state the injection-locked mode $m = -5$ is pronounced with over 30 dB of SMSR with respect to the central mode $j = 0$ [c.f. Fig. 3.14(c)]. Finally, Fig. 3.14(d) shows slave laser's mode spectrum for high injection power, when only one, $n_{\mathrm{sp}}^{(1)}$ steady-state exists, in which injection-locked mode is even more pronounced in comparison to the unlocked modes, and as P_{inj} increases, the injection-locked mode increases its power and SMSR.

Similarly to the Fig. 3.13, Fig. 3.15 shows the evolution of the dn/dt–n phase plot, but for a fixed P_{inj} and varying frequency detuning $\Delta\omega$, and again the shaded area represent the range of $\Delta\omega$ in which the phase plot comprise more than one stationary solution. For a fixed value of injection power $P_{\mathrm{inj}} = -16.5$ dBm and for large magnitude negative detuning ($\Delta\omega = -9\Omega$), as already discussed and presented in the Fig. 3.10(b), $S_m(n)$ exhibits a small maximum, insufficient to create additional stationary points in the dn/dt–n phase plot. For this reason, in this case the slave laser has only one steady-state, close to the n_{th}, which makes the dynamics of the slave laser similar to the free-running case (upper dot-dashed line in Fig. 3.15). As detuning becomes less negative, the maximum of the $S_m(n)$ profile increases and shifts towards higher carrier concentration n, and at some critical value around $\Delta\omega = -6.1\Omega$, the phase plot acquires two additional stationary

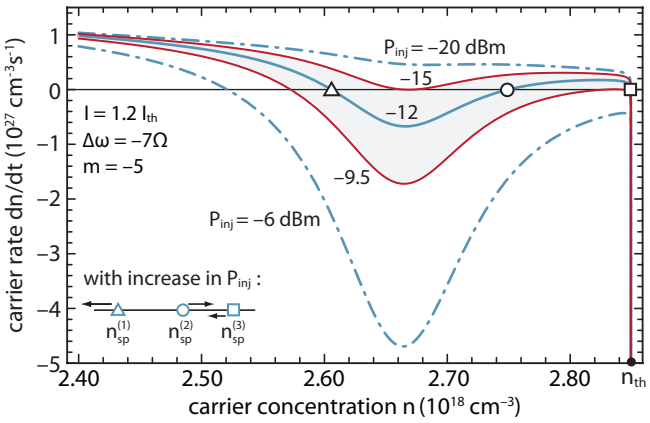

Figure 3.13: *Carrier concentration rate versus carrier concentration for different values of injection power P_{inj}. Inset shows trends of stationary points' positions with respect to the horizontal $dn/dt = 0$ axis with increase in P_{inj}.*

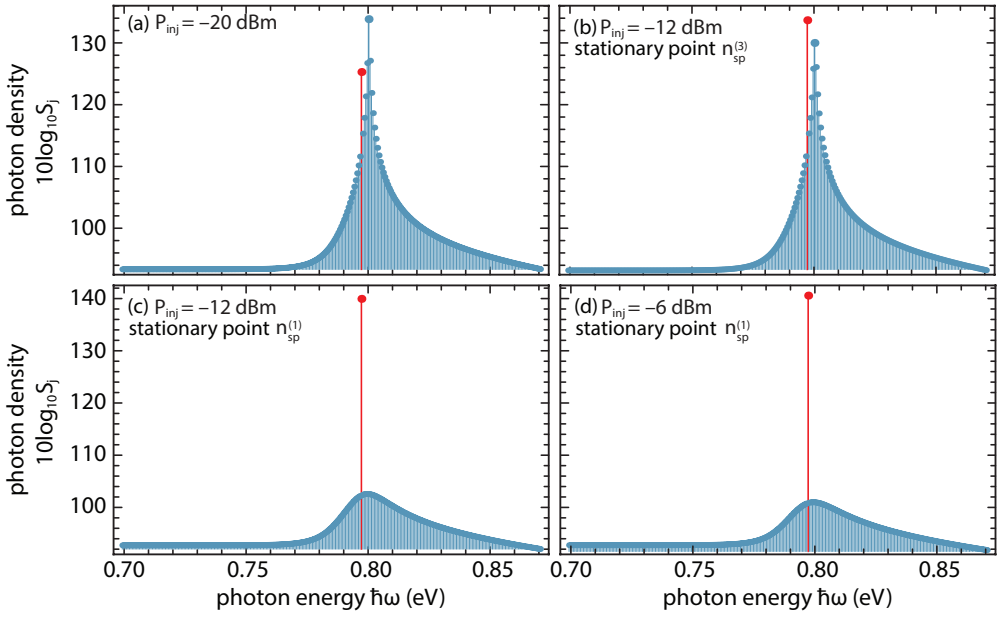

Figure 3.14: *Mode spectra for (a) low injection power ($P_{inj} = -20$ dBm) (b) moderate injection power ($P_{inj} = -12$ dBm), for $n_{sp}^{(3)}$ stationary point, (c) same as (b) but for $n_{sp}^{(1)}$ stationary point and (d) solitary $n_{sp}^{(1)}$ state in the case of high injection power ($P_{inj} = -6$ dBm).*

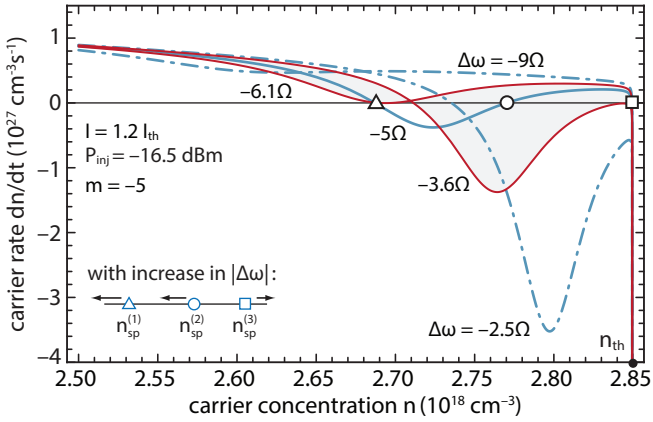

Figure 3.15: *Carrier concentration rate versus carrier concentration for different values of the frequency detuning $\Delta\omega$. Inset shows trends of stationary points' positions with respect to the horizontal axis with increase in $\Delta\omega$.*

points, $n_{sp}^{(1)}$ and $n_{sp}^{(2)}$, similar to the previous case of injection power variation. In the RMSP, as $\Delta\omega$ becomes less negative, both $n_{sp}^{(1)}$ and $n_{sp}^{(2)}$ shift towards higher carrier concentrations, i.e., in the direction of $n_{sp}^{(3)}$, since the maximum of the $S_m(n)$ profile moves towards higher carrier concentrations, as depicted in Fig. 3.10(b). Region of multiple stationary points exists in the certain range of $\Delta\omega$ ($-6.1\Omega < \Delta\omega < -3.6\Omega$), after which dn/dt–n phase plot remains with only one, $n_{sp}^{(1)}$ stationary point. Further variation of $\Delta\omega$ towards zero detuning and increase on the positive detuning side, will, unlike in the case of P_{inj} increase in the previous case, shift $n_{sp}^{(1)}$ further in the direction of n_{th}, thus pushing the slave laser dynamics closer to the free-running [cf. Fig. 3.15 for $\Delta\omega = -2.5\Omega$].

The mode spectra for injection with large magnitude negative $\Delta\omega = -9\Omega$, mode spectra at $n_{sp}^{(3)}$ and $n_{sp}^{(1)}$ in the region of RMSP, and finally in the case of injection with small magnitude negative detuning ($\Delta\omega = -2.5\Omega$), are depicted in the Figure 3.16(a) – (d), respectively. The evolution of the mode spectrum resembles the evolution in the case of P_{inj} variation (Fig. 3.14), expect the case of solitary $n_{sp}^{(1)}$ state [Figs. 3.14(d) and 3.16(d)], i.e., while increase in P_{inj} leads to further empowering of the injection-locked mode, increasing towards positive $\Delta\omega$ leads to the reduction of the injection-locked mode and reshaping the spectrum back towards the free-running form in which the central mode overpowers the injection-locked one. Figure 3.15 shows, that, regardless of the magnitude of injection power, the RMSP can exist only for negative values of the frequency detuning $\Delta\omega$, since for positive values $S_m(n)$ profile loses its parabolic shape, thus eliminating the possibility for formation of multiple stationary points in the dn/dt–n phase plots.

In order to analyze conditions for RMSP occurrence more thoroughly, we investigate the 2-D P_{inj}–$\Delta\omega$ space in which RMSP occurs (Fig. 3.17) [114]. The calculation is performed for several injection-locked side-modes, on both sides of the central mode

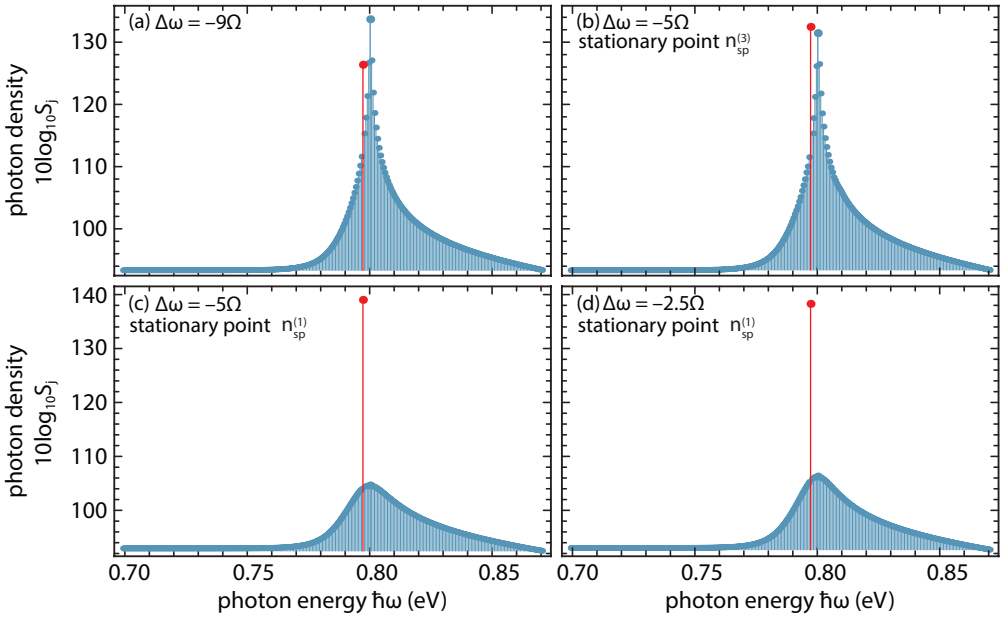

Figure 3.16: *Mode spectra for (a)* $\Delta\omega = -9\Omega$ *(b)* $n_{sp}^{(3)}$ *state for* $\Delta\omega = -5\Omega$ *(c)* $n_{sp}^{(1)}$ *state for* $\Delta\omega = -5\Omega$*, and (d)* $n_{sp}^{(1)}$ *state for* $\Delta\omega = -2.5\Omega$*.*

$j = 0$. The RMSP has a characteristic, saber-like profile that exhibits maximum width in terms of injection power at some negative frequency detuning. In addition to this, as the detuning becomes more negative, the RMSP shifts up to higher injection powers. This result can be inferred from the earlier discussion on the $S_m(n)$ and $\mathrm{d}n/\mathrm{d}t(n)$ profiles. For a fixed injection power, an increase in the magnitude of negative $\Delta\omega$ reduces and shifts the $S_m(n)$ maximum towards lower carrier concentrations [Fig. 3.10(b)]. Due to the smaller gain at lower carrier concentrations, higher injection power is required in order to pronounce the $S_m(n)$ profile enough so it creates a "dip" in the $\mathrm{d}n/\mathrm{d}t$–n phase plot, deep enough to make intersection with $\mathrm{d}n/\mathrm{d}t = 0$ axis, and thus add additional stationary points. The RMSP comprises somewhat larger area on the short-wavelength side, i.e., for positive side-modes ($m > 0$) than for long-wavelength side, i.e., negative ones ($m < 0$) due to the asymmetry of the gain profile, in particular due to the smaller gain defect on the short-wavelength spectrum side. However, on both spectrum sides, as the injection-locked mode order becomes higher, the detuning region, providing the RMSP, becomes narrowed and shifted towards more negative detuning values. The corresponding injection power range is also reduced and shifted toward smaller injection powers, so the RMSP saber-like areas become reduced in both P_{inj} and $\Delta\omega$ axis, and shifted down the P_{inj} axis. Again, this could be explained by introspection of the $S_m(n)$ profile dependence on the injection-locked mode order, depicted in Fig. 3.11. Since $S_m(n)$ profiles maxima are shifted toward higher carrier concentrations, higher order side-modes have reduced manoeuvre space for

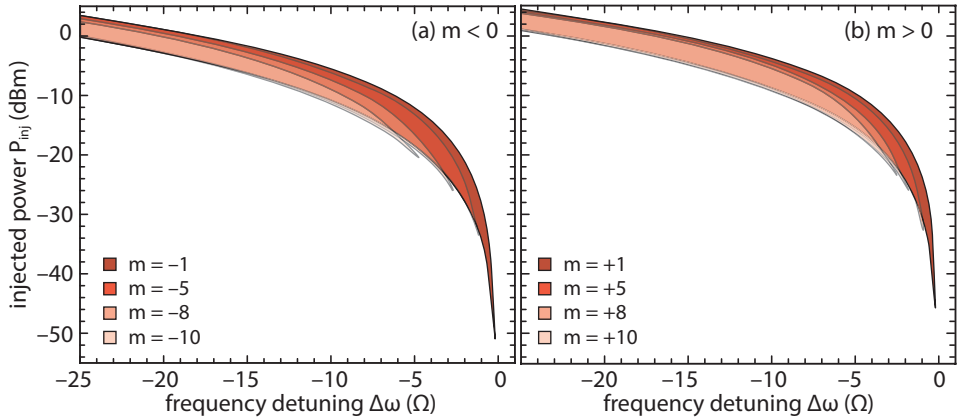

Figure 3.17: *Regions of multiple stationary points versus injected power P_{inj} and detuning frequency $\Delta\omega$, for several side-modes (a) below and (b) above the central longitudinal mode frequency.*

$\Delta\omega$, eliminating the possibility to achieve bistability for less negative $\Delta\omega$. Bistability can be obtained only for sufficiently negative $\Delta\omega$, which shifts the $S_m(n)$ maxima back to the lower values of the carrier concentration n, and thus enables the parabolic $S_m(n)$ profile to make a "dip" in the dn/dt–n phase plot. The RMSP region actually corresponds to the folded and overlapped region in the locking range Figure (Fig. 3.5). For injection powers above the saber-like profiles, the slave laser has only one stationary-point, while the region below the saber-like profiles corresponds to the FWM region.

3.5 Injection power and frequency detuning hysteresis

The existence of two stable stationary points $n_{\mathrm{sp}}^{(1)}$ and $n_{\mathrm{sp}}^{(3)}$ leads to the optical bistbility, which is manifested with the appearance of the hysteresis cycle in the slave laser output. The formation of the hysteresis loop can be understood by introspection of the dn/dt–n phase plot evolution. In Fig. 3.18 we present the output photon density in the injection-locked mode m [Fig. 3.18(a)], as well as accompanying phase difference θ_m [Fig. 3.18(b)], obtained for the same working conditions (bias current, injection-locked mode order, and frequency detuning) as dn/dt–n phase plot evolution depicted in the Fig. 3.13. At low injection powers ($P_{\mathrm{inj}} < -15$ dBm), as showed in Fig. 3.13, slave laser has only one steady-state close to the free-running regime, with similar dynamics [cf. Fig. 3.14(a)]. This state corresponds to the lower tail part of the hysteresis, for which injection-locked mode m has low photon density. The photon density is given in the logarithmic scale, as $10\log_{10}(S_m)$. The phase difference θ_m in this state is close to $\pi/2$ (≈ 1.5 rad), i.e., this state corresponds to the upper tail part of the θ_m hysteresis. Once the injection power enters a RMSP region (-15 dBm $< P_{\mathrm{inj}} < -9.5$ dBm) the dn/dt–n phase plot acquires an addi-

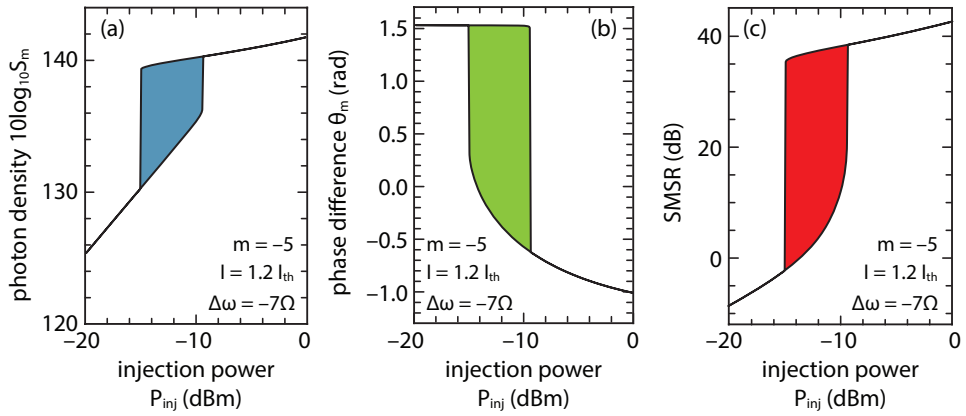

Figure 3.18: *Output (a) photon density S_m in logarithmic scale, (b) phase difference θ_m in rad, and (c) SMSR in dB, with respect to injection power P_{inj}.*

tional stable stationary point ($n_{sp}^{(1)}$). However, since previously settled in $n_{sp}^{(3)}$ point, slave laser will stay in this stationary point as long as it is provided, thus up to $P_{inj} = -9.5$ dBm, outlining the lower S_m hysteresis branch [Fig. 3.18(a)]. At this critical injection power $n_{sp}^{(3)}$ stationary point coincides with $n_{sp}^{(2)}$ and vanishes, and for $P_{inj} > -9.5$ dBm dn/dt–n phase plot remains with only one stationary point provided [c.f. Fig. 3.13], which is located at considerably lower carrier concentration in comparison to the $n_{sp}^{(3)}$ point. Due to this, at this critical injection power, carrier concentration in the active region of the slave laser exhibits a sudden drop to this lower steady-state, which results in a jump in the injection-locked mode m photon density, which represents the right S_m hysteresis edge in the Fig. 3.18(a). On the other hand, the phase difference θ_m exhibits the drop from $\pi/2$ down to the negative value around $\theta_m = -0.5$ rad [c.f. Fig. 3.18(b)]. Further increase of the injection power will only shift the carrier concentration to even lower values, thus increasing the photon density S_m, which corresponds to the upper tail part of the S_m hysteresis [Fig. 3.18(a)]. At high injection powers, the phase difference becomes more negative, corresponding to the lower tail part of the θ_m hysteresis [Fig. 3.18(b)]. Once injection power starts to decrease, due to its prehistory, the slave laser will stay settled in the $n_{sp}^{(1)}$ point as long as it is provided. This means that in the direction of the injection power decrease the slave laser will surpass the right hysteresis edge, outlining the upper S_m and correspondingly lower θ_m hysteresis branch, until the injection power reaches the second critical power ($P_{inj} = -15$ dBm) for which $n_{sp}^{(1)}$ coincides with $n_{sp}^{(2)}$ and vanishes, leaving only one available stationary point in the vicinity of free-running carrier threshold concentration n_{th} (Fig. 3.13). In the S_m hysteresis [Fig. 3.18(a)] this is manifested through the sudden drop of the photon density at the left hysteresis edge, while the θ_m suddenly jumps to the value close to $\pi/2$ [Fig. 3.18(b)]. Further injection power decrease shifts the slave laser to lower hysteresis tail in terms of S_m output, i.e., upper hysteresis tail in terms

of the phase difference θ_m. In this way, gradual increase followed by the gradual decrease of injection power encircles a counter-clockwise hysteresis cycle in the injection-locked mode power photon density (i.e., power) output and clockwise hysteresis cycle in the slave and master laser phase difference θ_m. The RMSP region, in which two stationary points can exhibit stable dynamics, corresponds to the region between two critical powers, i.e., two hysteresis edges, in which hysteresis comprises two simultaneous branches, the one which corresponds to $n_{\mathrm{sp}}^{(1)}$ (upper S_m and lower θ_m hysteresis branch), and the one which corresponds to $n_{\mathrm{sp}}^{(3)}$ state (lower S_m and upper θ_m hysteresis branch). Depending on its prehistory, the slave laser settles in one of the two branches. In order to include complete slave laser output dynamics, in Fig. 3.18(c) we present SMSR–P_{inj} hysteresis cycle, which follows the pattern shown in Fig. 3.14, with SMSR defined as $10\log_{10}(S_m/S_0)$. For injection power smaller than right hysteresis edge, slave laser is in the state close to the free-running regime, exhibiting negative or very small positive SMSR, meaning that the slave laser emits at the wavelength of the central mode, or there are two competing modes in the output. The mode spectrum of the slave laser, for this case is depicted in the Fig. 3.14(a) and (b). Fig. 3.14(a) is an example of the mode spectrum for the case in which injection power is even smaller than the left hysteresis edge, i.e., outside of the bistability region, in which the SMSR is slightly negative. Fig. 3.14(b) shows an example of the lower hysteresis branch, corresponding to the $n_{\mathrm{sp}}^{(3)}$ stationary point, in which SMSR ratio is slightly positive, leading to the competition of the injection-locked and central mode. After injection power surpasses the right hysteresis edge, the injection-locked mode m rises in power, while other longitudinal modes (including the central mode) become highly suppressed leading to the SMSR rising from around 20 dB up to over 30 dB in favour of the injection-locked mode m, making the slave laser emit at the wavelength of the injection-locked mode (in this case 1555.7 nm). An example of this slave laser power spectral distribution is given in Fig. 3.14(c) and (d), for the upper hysteresis branch, and upper tail part, respectively. The state of high SMSR remains active with injection power decrease all the way until the left hysteresis edge, when SMSR drops back to the negative values, switching back the slave laser to the wavelength of the central mode (in this case 1550 nm).

Similar hysteresis output can be, according to Fig. 3.15, observed by frequency detuning variation. In Fig. 3.19(a) and Fig. 3.19(b) we present S_m and θ_m frequency detuning dependent hysteresis cycles, respectively. With fixed injection power ($P_{\mathrm{inj}} = -16.5$ dBm), at sufficiently negative detuning ($\Delta\omega < -6.1\Omega$), the d$n$/d$t$–$n$ phase plot (Fig. 3.15) reveals that the slave laser has only one steady-state, close to the free-running regime, corresponding to the lower tail part in S_m, and upper tail part in θ_m hysteresis, respectively. Due to its prehistory, the slave laser remains in this state even in the region of the

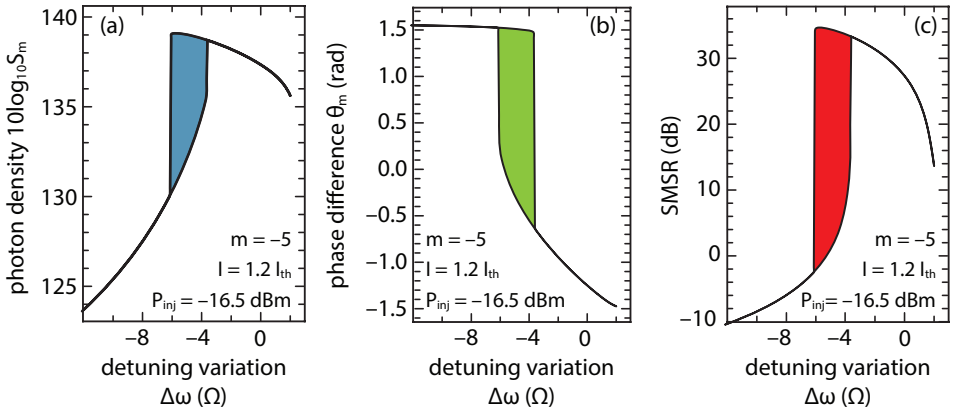

Figure 3.19: *Output (a) photon density S_m in logarithmic scale, (b) phase difference θ_m in rad, and (c) SMSR in dB, with respect to the frequency detuning $\Delta\omega$.*

bistability, between two hysteresis edges ($-6.1\Omega < \Delta\omega < -3.6\Omega$), until the frequency detuning reaches $\Delta\omega = -3.6\Omega$, when $n_{\mathrm{sp}}^{(3)}$ vanishes and slave laser switches into the only steady-state provided, located at lower carrier concentrations (Fig. 3.15). In terms of hysteresis, S_m jumps to the upper tail part, while θ_m drops down to the lower tail part [Fig. 3.19(a) and (b)]. On contrary to the case of injection power dependent hysteresis, further variation of the frequency detuning leads to a decrease in the S_m output, i.e., while the upper tail part of the hysteresis experienced an increase in the case of P_{inj} dependent hysteresis [Fig. 3.18(a)], here the upper tail part slowly decreases [Fig. 3.19(a)]. The reason for this was already explained in the discussion of the dn/dt–n phase plots in Fig. 3.15, which shows that as detuning becomes closer to zero and increases in the domain of positive values, the solitary stationary point, corresponding to the upper S_m hysteresis part, shifts towards free-running n_{th}, thus pushing the laser closer to the free-running regime, in this way decreasing the photon density in injection-locked mode m. Phase difference hysteresis resembles the one obtained for P_{inj} variation [Fig. 3.19(b)]. Now, making the $\Delta\omega$ variation in the opposite direction, i.e., varying the frequency detuning back to negative values will force the slave laser to stay in the $n_{\mathrm{sp}}^{(1)}$ state, as long as it is provided, thus outlining the upper S_m, and lower θ_m hysteresis branch. Finally, at critical $\Delta\omega = -6.1\Omega$, $n_{\mathrm{sp}}^{(1)}$ is not longer provided, and slave laser switches to the state close to the free-running n_{th}, i.e., S_m hysteresis drops down to the lower tail part, completing the counter-clockwise circle, while θ_m hysteresis jumps to the upper tail part, completing the clockwise circle. In Fig. 3.19(c) we present SMSR–$\Delta\omega$ hysteresis, which follows the pattern of mode spectrum evolution presented in the Fig. 3.16. From the S_m and SMSR–$\Delta\omega$ hysteresis, it can be seen that as detuning becomes less negative and increases in the positive direction, the output power of the injection-locked mode and consequently SMSR decrease, since $n_{\mathrm{sp}}^{(1)}$

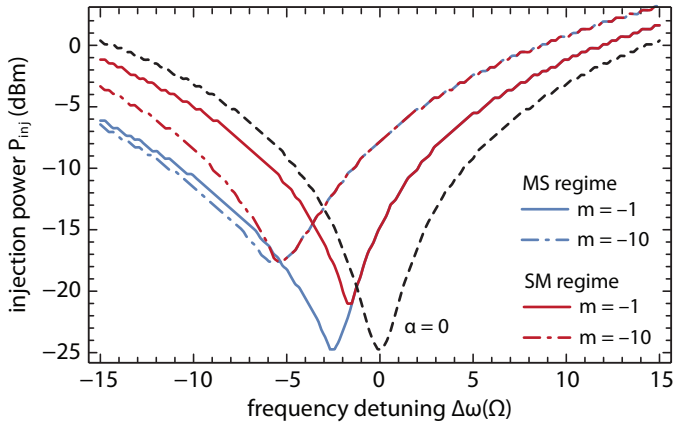

Figure 3.20: *Injection power required to achieve SMSR* $\geq$ 30 *dB versus frequency detuning* $\Delta\omega$.

point shifts towards n_{th}, as depicted in Fig. 3.15. As in the case of P_{inj} dependent hysteresis, in the region of the bistability, the separation of the two hysteresis branches is in the order of 30 dB.

The merit of 30 dB of side-mode-suppression-ratio is usually taken as a required condition for considering the laser to be single-mode [85–87]. The value of SMSR plays an important role in one of the trending applications of injection-locked Fabry-Pérot laser diodes for transmitter design in WDM-PON networks (Fig. 1.15), as discussed in Section 1.4. For that reason, we investigate the minimal required injection power in order to achieve SMSR $\geq$ 30 dB. The injection-locking induced bistability of the slave laser in the domain of the negative $\Delta\omega$, leads to the twofold dependence, as showed in the Fig. 3.20. In the domain of the positive frequency detuning, the minimal injection power is unambiguously defined, since there exists only one slave laser stationary state. We present the minimal required power for injection into the side-mode $m = -1$ (solid line) and $m = -10$ (dot-dashed line). The minimal injection power increases with an increase in the frequency detuning, since increased positive $\Delta\omega$ shifts the slave laser steady-state towards free-running regime, and thus promotes the central mode, instead of the injection-locked side-mode. The injection-locked mode $m = -10$ (dot-dashed line) requires somewhat higher injection power in comparison to the mode $m = -1$ (solid line), due to the larger gain defect. However, in the region of bistabilty, which can occur at negative values of the frequency detuning, only $n_{\text{sp}}^{(1)}$ stationary point can provide SMSR $\geq$ 30 dB. In one possible regime, laser prehistory can set the slave laser in the $n_{\text{sp}}^{(1)}$ point. We denote this regime as "MS" regime, in which master laser is kept in the "ON" state, while the slave laser in turned "ON"/"OFF". In this regime, in the domain of the bistability, the slave laser will be settled in $n_{\text{sp}}^{(1)}$ point, as long as it is provided, since it is the first steady-state encountered in the process of slave laser switching on. We depict this regime with blue lines in Fig.

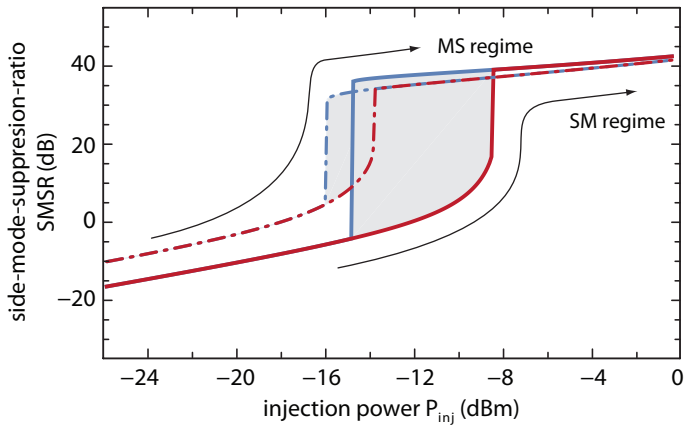

Figure 3.21: *Hysteresis cycles for injection into modes* $m = -1$ *and* $m = -10$.

3.20, both for injection into $m = -1$ (solid blue line) and $m = -10$ (dot-dashed blue line). In Fig. 3.21 we present hysteresis cycles for modes $m = -1$ (solid lines) and $m = -10$ (dot-dashed lines) for the case of $\Delta\omega = -7\Omega$.

In the "MS" regime, the laser is settled in the $n_{\mathrm{sp}}^{(1)}$ point, which corresponds to the upper hysteresis branch. The minimal injection power to provide SMSR $\geq$ 30 dB corresponds to the left hysteresis edge, since smaller injection powers shift the slave laser to the lower tail part of the hysteresis, which provides low SMSR. Figure 3.20 shows that the side-mode $m = -10$ has somewhat smaller minimal injection power in comparison to the side-mode $m = -1$, since higher order side-modes have RMSP shifted to smaller injection powers (c.f. Fig. 3.17), i.e., the hysteresis cycle for mode $m = -10$ is formed in the domain of lower injection powers than for $m = -1$ [cf. Fig. 3.21]. In addition to this, Fig. 3.20 shows that the minimal injection power increases with an increase in the magnitude of the negative $\Delta\omega$, since higher magnitude negative $\Delta\omega$ requires higher injection power in order to provide the $n_{\mathrm{sp}}^{(1)}$ point. However, in the other regime, the slave laser prehistory sets the slave laser in the $n_{\mathrm{sp}}^{(3)}$ point, i.e., in the lower hysteresis branch, which can not provide SMSR $\geq$ 30 dB. We denote this regime as "SM", in which the slave laser is kept in the "ON" state, while the master laser undergoes turning on and off. In this way, while the master laser is in the "OFF" state, the slave laser is in the free-running regime, and once the master laser is turned on, the slave laser will settle in the $n_{\mathrm{sp}}^{(3)}$ point, being the closest stationary point, as long as it is provided. This means that, in this case, the minimal injection power required to achieve SMSR $\geq$ 30 dB is the power which pushes the slave laser out of the bistability region, making the $n_{\mathrm{sp}}^{(3)}$ point disappear, leaving the slave laser with just one stationary point, which corresponds to the high injection-locked wavelength power, and thus high SMSR output. In other words, the slave laser has to be pushed out of the lower hysteresis branch, to the upper tail part which provides high

SMSR. Thus, in this case, the minimal injection power corresponds to the right hysteresis edge. In the Fig. 3.21 this produces additional branch depicted with red line. Again, injection side-mode of higher order (dot-dashed red line for $m = -10$) has lower minimal injection power in comparison to the injection side-mode closer to the central (solid red line for $m = -1$). Since right hysteresis edge is always at higher injection power that the left one, the minimal injection power in the "SM" regime (red line in Fig. 3.20, i.e., right hysteresis edge in Fig. 3.21) is always higher than the minimal injection power in the case of "MS" regime (blue line in Fig. 3.20, i.e., left hysteresis edge in Fig. 3.21). There is an experimental evidence of this dependence presented in Fig. 5 in [87]. If we assume a very small or negligible linewidth enhancement factor ($\alpha = 0$), the dependence of the minimal injection power symmetrically increases with detuning magnitude, resembling the dependence for finite linewidth, though the dependence loses its twofold character, since negligible linewidth can not provide for bistablity.

3.6 Theoretical analysis of hysteresis dimensions

The 2-D RMSP saber-like regions (Fig. 3.17) show that the width of the RMSP region varies with injection power P_{inj} and frequency detuning $\Delta\omega$, and that the region of the RMSP is also shifted and modified with respect to the injection mode order. For that reason we examine the formations and dimensions of the hysteresis loops for various values of injection parameters.

Injection power dependent hysteresis

In Fig. 3.22(a) – (d) we present hysteresis cycles for SMSR dependence on injection power, obtained for fixed values of frequency detuning ($\Delta\omega = -2\Omega, -6\Omega, -14\Omega, -20\Omega, -32\Omega, -44\Omega$), for injection into different side-modes ($m = -1, -5, -8, -10$). As detuning becomes more negative, hystereses boundaries are shifted towards higher values of injection power, and it can be noticed that with high magnitude negative $\Delta\omega$, their widths become smaller. However, with more negative $\Delta\omega$, as higher injection power is applied, both branches (lower and upper) are shifted to higher values of SMSR. As saber-like profiles (Fig. 3.17) suggest, modes closer to the central mode provide wider RMSP, which leads to wider hysteresis cycles in case of lower order injection-locked modes $m = -1$ or $m = -5$ [Fig. 3.22(a) and (b)] in comparison to higher order injection-locked modes $m = -8$ or $m = -10$ [Fig. 3.22(c) and (d)]. Moreover, as for higher order side-modes RMSP shifts to more negative values of $\Delta\omega$, modes $m = -8$ and $m = -10$ can not provide bistability for small magnitude negative $\Delta\omega$ such as -2Ω [Fig. 3.22(c) and (d)]. The upper

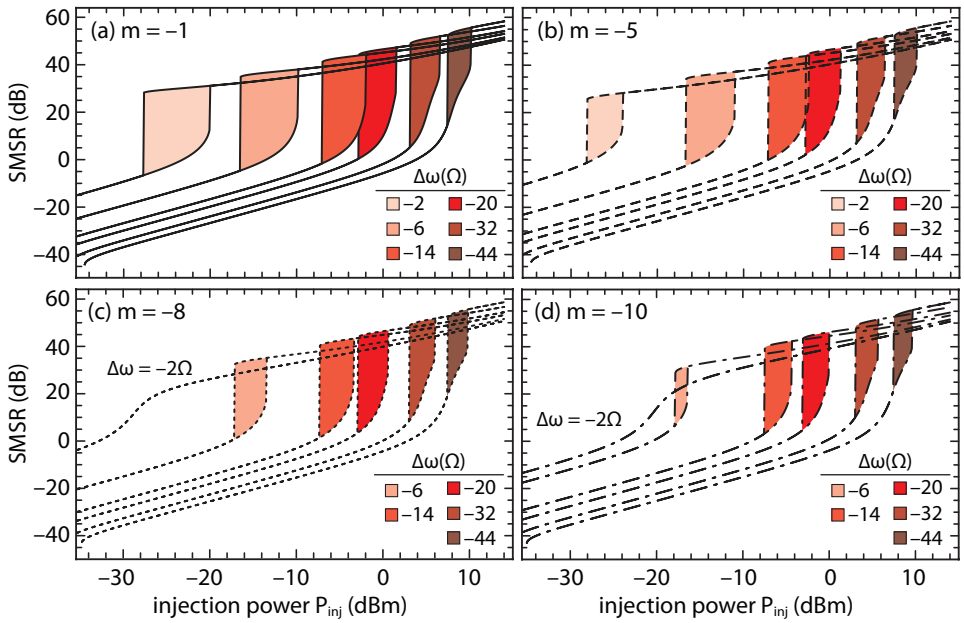

Figure 3.22: *SMSR with respect to injection power for different degrees of frequency detuning and injection-locked modes: (a) $m = -1$ (solid line), (b) $m = -5$ (dashed line), (c) $m = -8$ (dotted line), and (d) $m = -10$ (dot-dashed line).*

hysteresis branch is generally always above 30 dB, except for very small magnitude negative detuning (e.g. $\Delta\omega = -2\Omega$ for $m = -1$), while the lower branch is centered around 0 dB, for smaller magnitude negative detunings, while, as detuning becomes more negative, it becomes centered around higher values, even in order of 10 dB. However, in this case, the upper branch is shifted to around 50 dB, so that the separation of the branches, i.e., heights of the loops are almost always over 30 dB.

In Fig. 3.23 we present corresponding injection-locked mode phase θ_m versus injection power hysteresis cycles, which follow the same pattern as SMSR cycles from Fig. 3.22 in terms of widths. The upper branch, which corresponds to the $n_{\mathrm{sp}}^{(3)}$ stationary point gives the values of the phase around 1.5 rad, regardless of the $\Delta\omega$ magnitude, while the lower branch, which corresponds to the $n_{\mathrm{sp}}^{(1)}$ stationary point, gives negative values which tend to increase and become close to 0 rad, as detuning becomes more negative. As injection-locked mode order becomes higher, the hysteresis cycles at small magnitude $\Delta\omega$ become narrower and with reduced height, as the upper branch is shifted down, while eventually they disappear [c.f. Fig. 3.23(c) and (d)]. In terms of potential applications of the injection locking induced bistability in all-optical signal processing elements, such as all-optical flip-flops, all-optical switches, or other all-optical logic gates, the width, as well as the height of the loops represents an important parameter. The process of switching is dependent on the hysteresis width, since it determines the magnitude of the injection power change required to surpass the hysteresis boundary. In this way, the width of the

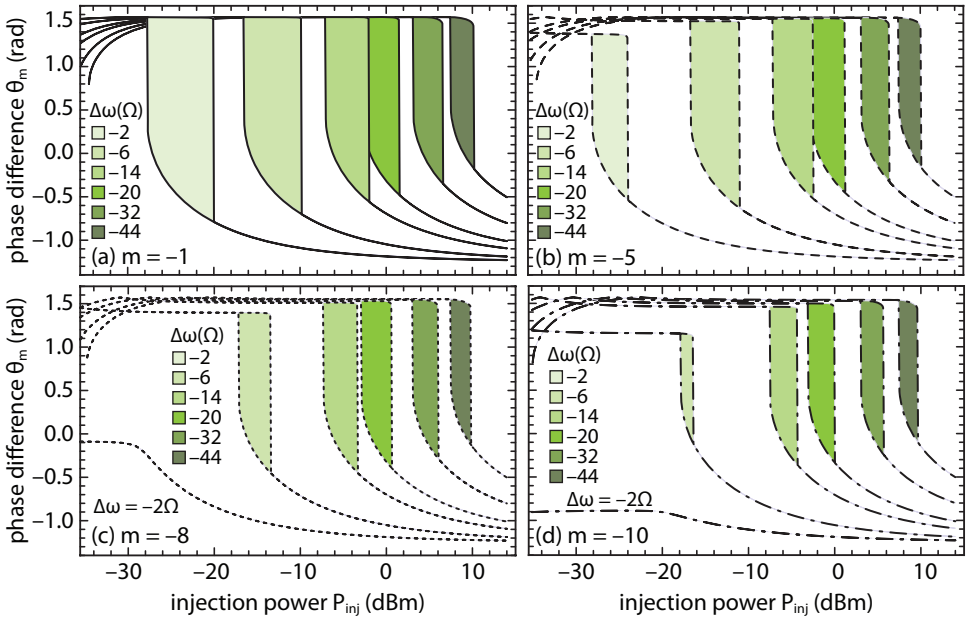

Figure 3.23: *Injection-locked mode m phase θ_m versus injection power for different degrees of detuning and injection-locked modes: (a) $m = -1$ (solid line), (b) $m = -5$ (dashed line), (c) $m = -8$ (dotted line), and (d) $m = -10$ (dot-dashed line).*

hysteresis cycle will prove to be of high importance for switching energies, which will be discussed in the last chapter of the thesis. On the other hand, the height, i.e., the branch separation determines extinction ratio in case of all-optical flip-flops. For that reason, in Fig. 3.24 we depict the width of the hysteresis cycles with respect to the frequency detuning $\Delta\omega$ and injection-locked mode m ($m = -1, -5, -8, -10$). It can be seen that the width of the hysteresis cycles steeply increases as detuning becomes more negative, and experience a maximum at some small magnitude negative $\Delta\omega$, after which the width decreases more steeply in case of low order side-modes ($m = -1, -5$) in comparison to higher-order side-modes ($m = -8, -10$). In addition to this, the maximum width is achieved at more negative values of frequency detuning as the order of the side-mode becomes higher, e.g., for $m = -1$ the maximum width is obtained around $\Delta\omega \approx -1\Omega$, while for $m = -10$ the maximum is shifted at around $\Delta\omega \approx -13\Omega$. However, as the order of the side-mode becomes higher, the value of this maximum becomes significantly smaller, from around 7.5 dB in the case of $m = -1$ to only around 2.5 dB in the case of $m = -10$. We limit the maximal applied frequency detuning to $\Delta\omega = -44\Omega$, since it represents the boundary of the intermodal space for particular injection-locked mode m.

In Fig. 3.25 we present heights, i.e., vertical openings of hystereses with respect to frequency detuning, in case of SMSR [Fig. 3.25(a)], injection-locked mode S_m [Fig. 3.25(b)], and injection-locked phase θ_m hysteresis [Fig. 3.25(c)]. The hystereses have larger openings, i.e., provide higher extinction ratios in the case of higher order side-

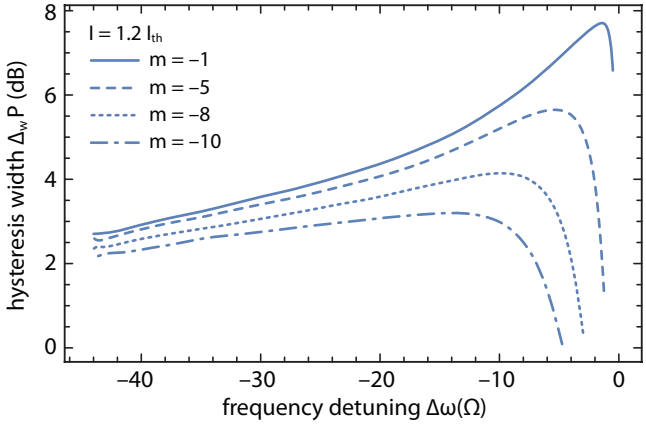

Figure 3.24: *Hystereses widths (Δ_w) in dB with respect to frequency detuning $\Delta\omega$ for $m = -1$ (solid line), $m = -5$ (dashed line), $m = -8$ (dotted line), and $m = -10$ (dot-dashed line).*

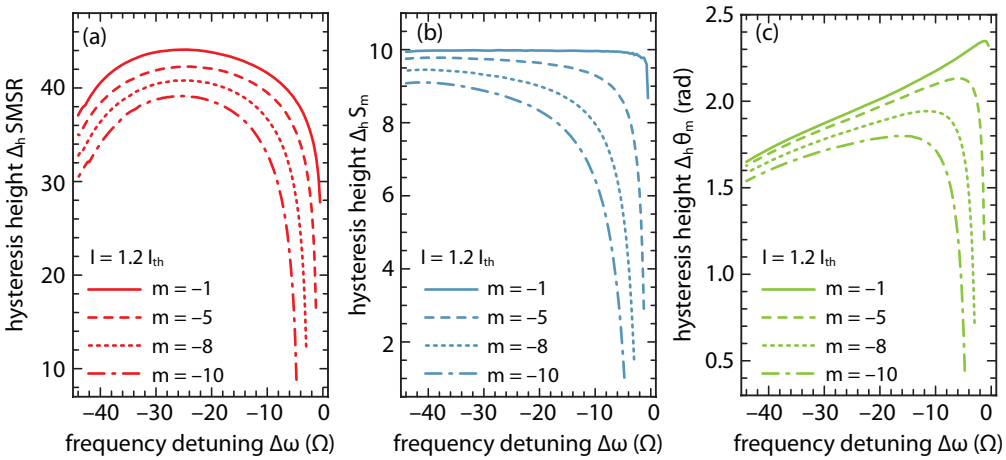

Figure 3.25: *Heights, i.e., vertical openings of hystereses with respect to frequency detuning $\Delta\omega$ for (a) SMSR hystereses (b) injection-locked mode S_m hystereses (c) injection-locked phase θ_m hystereses for $m = -1$ (solid line), $m = -5$ (dashed line), $m = -8$ (dotted line), and $m = -10$ (dot-dashed line).*

modes. In the case of θ_m hystereses [cf. Fig. 3.25(c)], openings exhibit maxima in a similar fashion as the widths in Fig. 3.24. The maximal opening is achieved for small magnitude negative frequency detuning, somewhat less negative than in the case of hystereses widths, e.g., the maximal opening for $m = -1$ is achieved at $\Delta\omega \approx -0.5\Omega$, while for $m = -10$ it is achieved at $\Delta\omega \approx -12.5\Omega$. The maximal obtained opening is around $3/4\pi$ rad, while for sufficiently large magnitude negative detuning, all injection-locked side-modes provide more or less the same opening, somewhat larger than $\pi/2$ rad. On the other hand, SMSR and S_m hystereses openings have different frequency detuning dependences. SMSR openings [cf. Fig. 3.25(a)] exhibit their maxima for sufficiently large magnitude negative detuning, and all presented injection-locked side-modes exhibit their maxima at mutually similar values of $\Delta\omega$, somewhere around $\Delta\omega \approx -24\Omega$. All maxima are well above 30 dB, in the case of $m = -1$, even above 40 dB. In this region of medium magnitude negative $\Delta\omega$, the presented profiles are flat, meaning that this high opening is maintained for wide range of $\Delta\omega$ values. At small magnitude negative $\Delta\omega$ hystereses exhibit openings below 30 dB, however the openings increase steeply and reach 30 dB level. Large magnitude negative detuning leads to the decrease of the openings, however, even for high order side-mode $m = -10$, the opening does not drop below 30 dB level. Finally, the S_m hystereses increase their openings as detuning becomes more negative and reach their maxima at highly negative detuning [cf. Fig. 3.25(b)]. The increase in the region of small magnitude negative detuning is very steep in the case of low order side-modes ($m = -1, -5$) after which the opening profiles saturate at high values in order of 10 dB in very wide range of frequency detuning. In the case of $m = -1$ this range is almost whole negative detuning half of the intermodal space, while in the case of $m = -5$ the range in which high hysteresis opening can be maintained is in order of 33Ω. Low order side-modes converge to high opening values more slowly, reducing the range of $\Delta\omega$ in which this high opening can be maintained.

Frequency detuning dependent hysteresis

In Fig. 3.26 we present SMSR dependence with respect to frequency detuning, i.e., SMSR hysteresis cycles obtained for fixed values of injection power P_{inj} and varying frequency detuning $\Delta\omega$. As in case of Fig. 3.22, in Fig. 3.26(a) – (d) we present cycles for different side-modes ($m = -1, -5, -8, -10$, respectively), for different levels of injection ($P_{\text{inj}} = 6$ dBm, 0 dBm, -6 dBm, -12 dBm, -18 dBm, -24 dBm, -40 dBm). As injection power decreases, the hysteresis cycles shift to smaller magnitude negative $\Delta\omega$, generally become narrower, and eventually disappear. Again, as in case of injection power dependent hysteresis, low order side-modes [Fig. 3.26(a) and (b)] have wider hysteresis loops in comparison to high order side-modes [Fig. 3.26(c) and (d)]. As injection power becomes

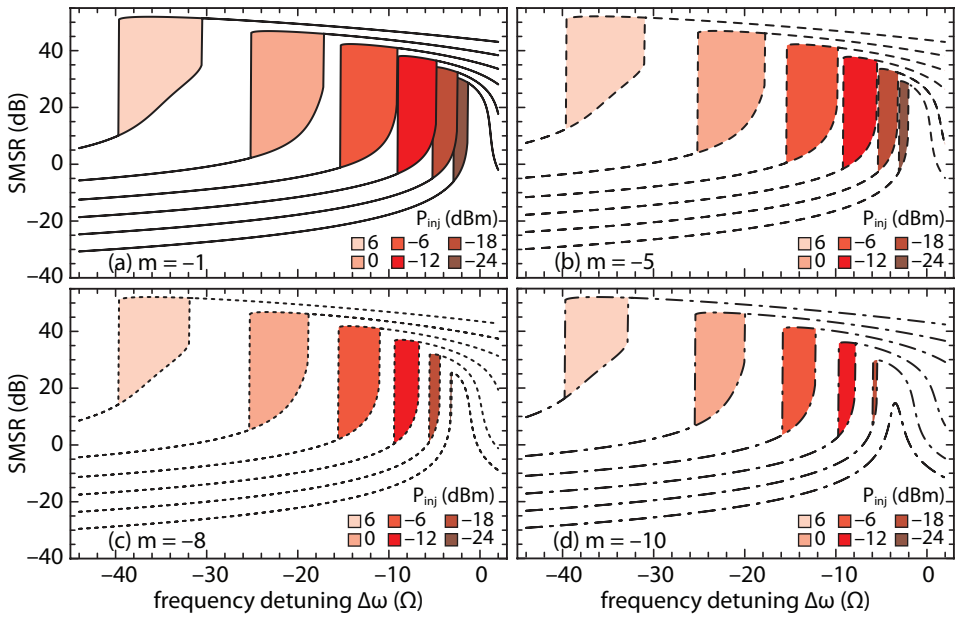

Figure 3.26: *SMSR with respect to frequency detuning for different levels of injection power and injection-locked modes: (a) $m = -1$ (solid line), (b) $m = -5$ (dashed line), (c) $m = -8$ (dotted line), and (d) $m = -10$ (dot-dashed line).*

smaller, both hysteresis branches shift down, at lower values of SMSR. The upper branch shifts down from around 50 dB (in case of high P_{inj} and consequently large magnitude negative $\Delta\omega$), to modest 20 dB (in case of low P_{inj} and consequently small magnitude negative $\Delta\omega$). On the other hand, the lower branch shifts down from around 20 dB to around 0 dB, which means that the separation of the branches is again in the order of 30 dB in wide range of P_{inj}, as it was in the case of injection power dependent hystereses.

In Fig. 3.27 we present corresponding injection-locked mode θ_m hysteresis cycles. The upper branch is practically fixed at around $\pi/2$, while the lower branch slightly varies with variation of the injection power. In terms of application in all-optical signal processing, we recognize this frequency detuning dependent hysteresis as very important aspect of injection locking induced bistability, since it enables that the variation of the master laser frequency, i.e., its phase, can lead to the switching between slave laser stable states. In other words, it can provide phase controlled slave laser, which is potentially very attractive for all-optical signal processing. For this reason we pay special attention to the widths and heights of frequency detuning dependent hysteresis cycles.

In Fig. 3.28 we present widths of the hysteresis cycles with respect to applied injection power. As opposed to the injection power dependent hystereses (Fig. 3.24), the widths of the frequency detuning dependent hystereses show monotonic increase with increase in the injection power. Low order side-mode have wider cycles in comparison to the higher order side-modes.

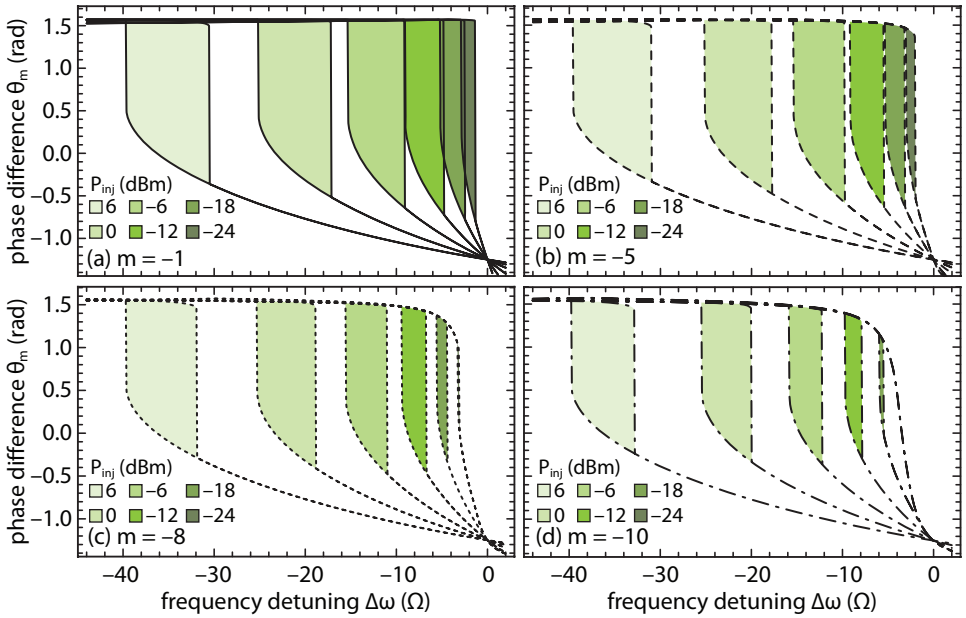

Figure 3.27: *Injection-locked mode m phase θ_m versus frequency detuning for different levels of injection power and injection-locked modes: (a) $m = -1$ (solid line), (b) $m = -5$ (dashed line), (c) $m = -8$ (dotted line), and (d) $m = -10$ (dot-dashed line).*

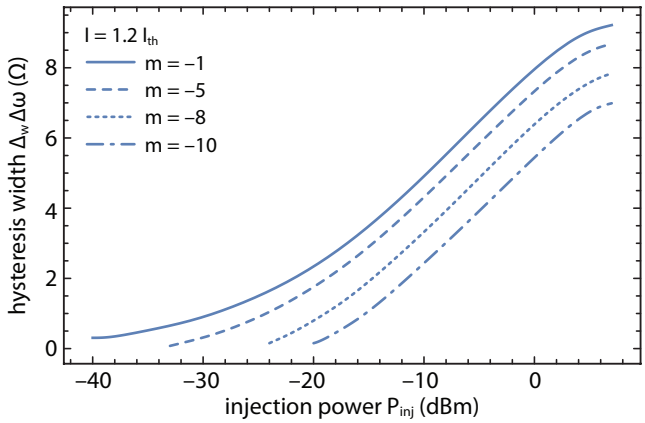

Figure 3.28: *Hystereses widths (Δ_w) in dB with respect to injection power for $m = -1$ (solid line), $m = -5$ (dashed line), $m = -8$ (dotted line), and $m = -10$ (dot-dashed line).*

Finally, we investigate vertical openings in the case of frequency detuning dependent cycles and present the vertical openings of SMSR, S_m, and θ_m hystereses in Fig. 3.29(a) – (c), respectively. SMSR openings exhibit maximum for high injection power, close to 0 dBm, for all injection-locked side-modes [cf. Fig. 3.29(a)]. The maximal opening is in the order of 45 dB in the case of side-mode $m = -1$, while it reduces to somewhat over 35 dB in the case of side-mode $m = -10$. Side-mode $m = -1$ has the widest range of injection powers in which the opening is over 30 dB, i.e., opening is over 30 dB in almost whole range of applied injection powers, which is in order of 50 dB. However, this injection power range, in which SMSR $>$ 30 dB, decreases with an increase in the mode order, making the range in order of 20 dB for side-mode $m = -10$. Openings of S_m hystereses saturate at high values of injection power [cf. Fig. 3.29(b)]. At these high values of injection power, the openings are maximal, ranging from around 10 dB in the case of $m = -1$ to around 8.5 dB for $m = -10$. The side-mode $m = -1$ has almost constant opening in the whole range of injection powers, i.e., it is in order of 10 dB in very wide range of P_{inj}, in order of 35 dB. Higher order side-modes exhibit distinctive increase in the opening with injection power increase and retain high values in much smaller range of injection powers [c.f. Fig. 3.29(b)]. Finally, openings of θ_m hystereses exhibit maximum at certain value of injection power, which is shifted towards higher injection powers as mode order becomes higher [cf. Fig. 3.29(c)]. Side-mode $m = -1$ has very flat θ_m vertical opening profile in the vicinity of the maximum, enabling that high opening (in order of $3/4\pi$) is maintained in the wide range of injection powers (in order of 20 dB), which is located in the domain of very low injection powers (from -40 dBm to around -20 dBm). As in the case of S_m openings, higher order side-modes have more distinctive maxima, i.e., maintain extremum values of openings in much smaller range of injection powers, which is also shifted in the domain of higher injection powers.

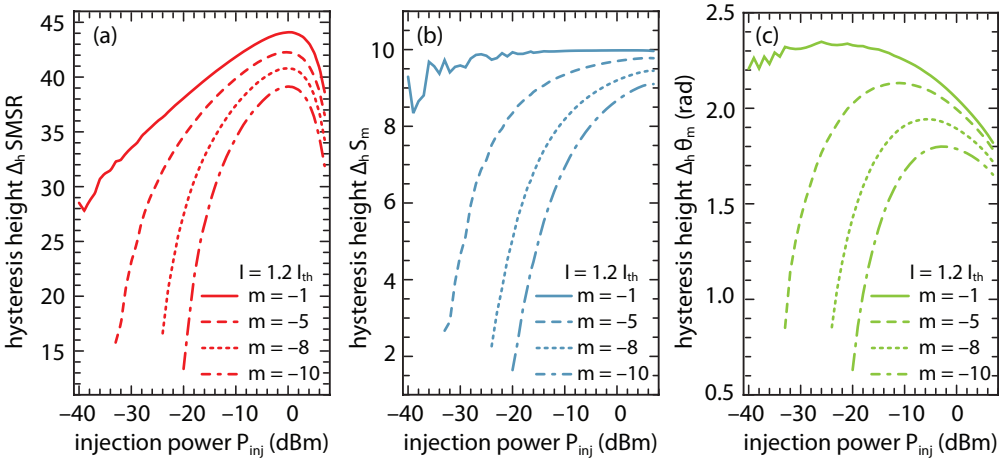

Figure 3.29: *Heights, i.e., vertical openings of hystereses with respect to injection power for (a) SMSR hystereses (b) injection-locked mode S_m hystereses (c) injection-locked phase θ_m hystereses for $m = -1$ (solid line), $m = -5$ (dashed line), $m = -8$ (dotted line), and $m = -10$ (dot-dashed line).*

Chapter 4

Dynamic characteristics of injection locking induced bistability

In this chapter we present dynamic characteristics of injection-locked bistable Fabry-Pérot laser diodes. We assume intermodal, i.e., side-mode injection and investigate Lyapunov stability of the slave laser with respect to injection power and frequency detuning. As a common procedure in the literature, we present slave laser stability map in the $\Delta\omega$–r space, where r is defined as the relative injection power. This stability map outlines and confirms theoretically derived locking range, and, in addition to this, disparts the regions in which the slave laser exhibits dynamical instabilities. From obtained stability map, we show that there exists a range of frequency detuning and injection power in which two stationary states are simultaneously dynamically stable, providing for the slave laser bistability. In addition to this, we find that the inclusion of the unlocked longitudinal modes significantly changes the distribution of slave laser instabilities, as well as the region of the bistability. For a full scale model of the rate equations, we present the distribution of the stationary points in the $\Delta\omega$–r space, i.e., we find the loci of the slave laser stationary points and correlate it to the obtained stability map. In the bistable region of the slave laser we perform an analysis of the switching mechanisms between the stable states, in particular, we investigate switching of the slave laser by master laser injection power (i.e., master laser amplitude) or frequency detuning (i.e., master laser phase) variation. In this way we achieve amplitude or phase controlled slave laser, respectively. In order to do so, we develop an analytical model for prediction of the minimal master laser injection power or frequency detuning pulse duration, which is required for the switching to be completed. On the basis of the analytical model we investigate master laser switching time and switching energy dependence on the slave laser linewidth enhancement factor α, as well as on slave laser structural parameters, such as active region volume. Further on, we develop a detailed numerical model through which we reveal and investigate ex-

act phase plot switching trajectories, and in addition to the injection parameter impulse duration, i.e., master laser switching time, we define the slave laser switching time, by investigating the transient dynamics of the photon density in the slave laser cavity. The analytical model proves to be very effective for a fair estimation of the master laser switching time, though it encounters certain limitations in the case of switching by frequency detuning variation. For this reason, in the case of this switching mechanism, we use the exact numerical model. On the basis of this model, we propose methods for optimization of the slave laser switching time, which include careful selection of the slave laser initial conditions, variation of the master laser switching time, and finally use of the external cavity resonator in the slave laser. In the case of switching by injection power variation, the results of the analytical model are in good agreement with the results obtained from numerical model, so in this thesis we focus on the numerical model only in terms of switching by frequency detuning variation. In addition to this, switching with frequency detuning variation can provide phase controlled slave laser, which we recognize as highly attractive applicative technique for novel advanced modulation formats.

4.1 Detailed stability map for IL FP-LDs

Calculation of the stability map is based on the equation system (3.8a) – (3.8c), described in the Section 3.2. From the stationary forms of injection-locked mode m photon density and phase equation, (3.8b) and (3.8c), respectively, we eliminate $\sin(\theta_m)$ and $\cos(\theta_m)$ and derive an equation with respect to the carrier concentration n [115]:

$$[\alpha A_m(n) - 2\Delta\omega]^2 + [A_m(n) + B(n)/S_m(n)]^2 - 4k_c^2 r = 0. \tag{4.1}$$

Using the stationary form of (3.8a), we express S_m as a function of n, as in [115]:

$$S_m(n) = \frac{\frac{I}{qV} - Q(n) + \sum\limits_{-l_1 \le j \le l_2}^{j \neq m} v_g g(n, \omega_j) \frac{B(n)}{A_j(n)}}{v_g g(n, \omega_m + \Delta\omega)}. \tag{4.2}$$

and return this dependence in the equation (4.1).

For a fixed value of the bias current and for a given set of injection parameters, frequency detuning $\Delta\omega$ and relative injection power $r = S_{\mathrm{inj}}/S_{\mathrm{m}}$, we insert equation (4.2) into (4.1) and obtain an transcendental equation with respect to the carrier concentration n. Similarly as in the case of the dn/dt–n phase plot analysis, by the means of the bisection method we find the carrier concentration n stationary values n_{s}. Using (4.2) we obtain stationary photon density in the injection-locked mode m, i.e., $S_m(n_{\mathrm{s}})$. Stationary values of the photon densities for all other, unlocked modes, are obtained as $S_j(n_{\mathrm{s}}) = B(n_{\mathrm{s}})/A_j(n_{\mathrm{s}})$,

while the stationary value of the phase difference $\theta_m(n_s)$ is obtained from (3.8c).

In Fig. 4.1(a), for $I = 1.2I_{th}$, we present solutions of the equation (4.1) in $\Delta\omega$–r space, where r is expressed in logarithmic scale as $\rho = \log_{10}(r)$ [115]. We find that for any $\Delta\omega$–r pair, there exists at least one, basic solution, which we denote as n_L. This solution corresponds to the green hatched part in Fig. 4.1(a). It can be seen that this basic solution spreads all over the locking range defined in 3.2, i.e., both for negative, as well as positive frequency detuning, although here we focus on the region of negative $\Delta\omega$, since in this region additional solutions may appear. More precisely, these additional solutions may appear for $\Delta\omega < -1.13\Omega$ where the FWM and r_- boundary cross (i.e., where the saber profile, representing the region of multiple stationary points ends as depicted in Fig. 3.5). In Fig. 4.1(a), the green hatched part, which corresponds to the region of the basic solution (n_L) is denoted as **L**. With **H** (blue shaded, double-hatched) we denote the region where each $\Delta\omega$–r point represents two solutions, the basic solution n_L and one more, which we denote as n_H, while **M** (dark, dense-hatched) is the narrow third-order root region, which in addition to n_L and n_H comprises solution n_M. In other words, the three denoted regions represent the three sets, the set $\mathbb{L}$, which comprises only $\mathbb{L} = \{n_L\}$, the set $\mathbb{H} = \{n_L, n_H\}$, and the set $\mathbb{M} = \{n_L, n_H, n_M\}$. The n_L solution is an element of all three sets, while n_H solution is common for $\mathbb{H}$ and $\mathbb{M}$ sets, i.e., the intersection of three sets is the n_L solution, while $\mathbb{H} \cap \mathbb{M} = \{n_H\}$. In further text, with n_s we denote any of the three roots n_L, n_H, or n_M. The locking boundary r_- separates the **H**- and **M**-regions as illustrated in the inset in Fig. 4.1(a) (dot-dashed line), and with the FWM boundary outlines the **H**-region. The **M**-region is very narrow and noticeable only for small negative detunings in the vicinity of the intersection of r_- and FWM boundary. For higher negative values of the frequency detuning ($\Delta\omega < -2\Omega$), it is compressed into a line which can be barely seen, as depicted in Fig. 4.1(a).

Each stationary point (n_s) of equation (4.1) corresponds to a certain $\rho = \log_{10}(r) = \log_{10}(S_{inj}^{(s)}/S_m^{(s)})$, i.e., each n_s determines one pair of injected photon density $S_{inj}^{(s)}$ and injection-locked mode photon density $S_m^{(s)}$. As discussed in Section 3.4, for a given $S_{inj} = S_{inj}^{(s)}$, the corresponding dn/dt–n phase plot may exhibit either one or three stationary points, which we denote in increasing order ($n_{sp}^{(1)} \leq n_{sp}^{(2)} \leq n_{sp}^{(3)} \leq n_{th}$) [114]. In the case in which corresponding phase plot comprises only one stationary point, n_s maps into that stationary point. However, the mapping becomes more complex in the cases when dn/dt–n phase plot provides more than one stationary point, when n_s has to map in only one of several provided stationary points.

The basic solution n_L, regardless of the belonging region, always maps into $n_{sp}^{(1)}$ point. This basic solution n_L in the first-order root region, i.e., $n_L \in \mathbb{L} \setminus \{\mathbb{H} \cup \mathbb{M}\}$ corresponds to a pair $S_{inj}^{(L)}$ and $S_m^{(L)}$, and our analysis shows that this $S_{inj}^{(L)}$ defines a dn/dt–n phase plot with

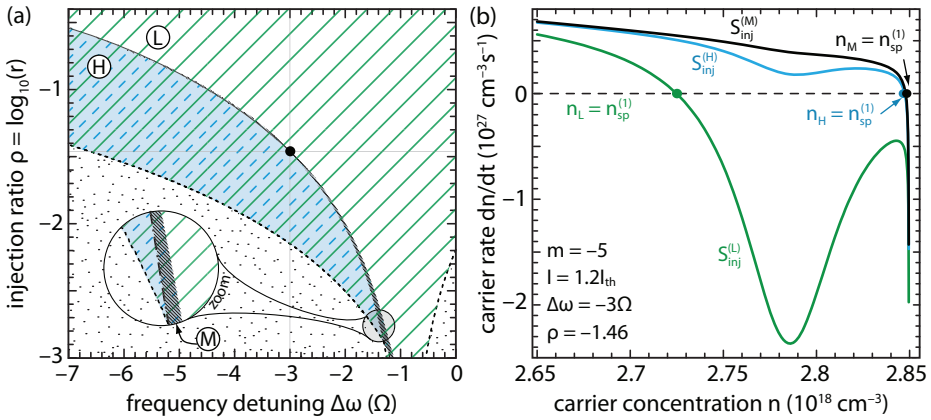

Figure 4.1: *(a) Distribution of the roots of equation (4.1): **L** (hatched), **H** (blue shaded, double-hatched), **M** (dark, dense-shaded) for all unlocked modes included. The dot corresponds to Δω–r pair, for which all three roots occur simultaneously. (Inset) r_ boundary (dot-dashed line) separates the **H**- and **M**-regions, and with the FWM boundary (dotted line) outlines the **H**-region. (b) dn/dt–n plots for all three roots at the point from the **M**-region and their corresponding mapping point $n_{sp}^{(1)}$ for $S_{inj}^{(L)} > S_{inj}^{(H)} > S_{inj}^{(M)}$. [115]*

only one stationary point, denoted as $n_{\mathrm{sp}}^{(1)}$ point. This point is not a consequence of the unlocked modes interplay, but rather a consequence of injection locking, i.e., it is created due to parabolic profile of the injection-locked mode photon density $S_m(n)$, and not due to the rapid increase of the photon density in the central mode in the vicinity of the threshold carrier concentration, as discussed in Section 3.4 and depicted in Fig. 3.9 [114].

The basic solution n_{L} from the $\mathbb{M}$ set (**M**-region) and its corresponding $S_{\mathrm{inj}}^{(\mathrm{L})}$ also define a dn/dt–n phase plot with only one stationary point, which is a consequence of the injection locking. More precisely, a point from the thin **M**-region represents third-order root solution, i.e., comprises three carrier concentration solutions $n_{\mathrm{s}} = n_{\mathrm{L}}, n_{\mathrm{H}}, n_{\mathrm{M}}$. Therefore, a point from this region corresponds to three pairs of $S_{\mathrm{inj}}^{(\mathrm{s})}$ and $S_m^{(\mathrm{s})}$ ($S_{\mathrm{inj}}^{(\mathrm{L})}, S_m^{(\mathrm{L})}$, $S_{\mathrm{inj}}^{(\mathrm{H})}, S_m^{(\mathrm{H})}$, and $S_{\mathrm{inj}}^{(\mathrm{M})}, S_m^{(\mathrm{M})}$), for each of three corresponding roots, respectively. In Fig. 4.1(a), with a black dot, we denote a point from this region, with coordinates $(\Delta\omega, \rho) = (-3\Omega, -1.46)$. We find that all three $S_{\mathrm{inj}}^{(\mathrm{s})}$ correspond to dn/dt–n phase plots with only one stationary solution, $n_{\mathrm{sp}}^{(1)}$, as depicted in the Fig. 4.1(b). As previously discussed, n_{L} from the set $\mathbb{M}$, similarly to the n_{L} from the $\mathbb{L}\setminus\{\mathbb{H}\cup\mathbb{M}\}$ set, always corresponds to the dn/dt–n phase plot stationary solution obtained as a consequence of injection locking [green line obtained for $S_{\mathrm{inj}}^{(\mathrm{L})}$ in Fig. 4.1(b)]. Remaining two solutions, n_{H} and n_{M} from the $\mathbb{M}$ set, also correspond to the dn/dt–n phase plots with only one stationary point, though now these points corresponds to the cases of low injection powers, i.e., these points are consequences of the unlocked modes interplay. Thus, points n_{H} and n_{M} map into the $n_{\mathrm{sp}}^{(1)}$ point close to the free-running regime as depicted in Fig. 4.1(b) (phase plots obtained for $S_{\mathrm{inj}}^{(\mathrm{H})}$ and $S_{\mathrm{inj}}^{(\mathrm{M})}$, respectively).

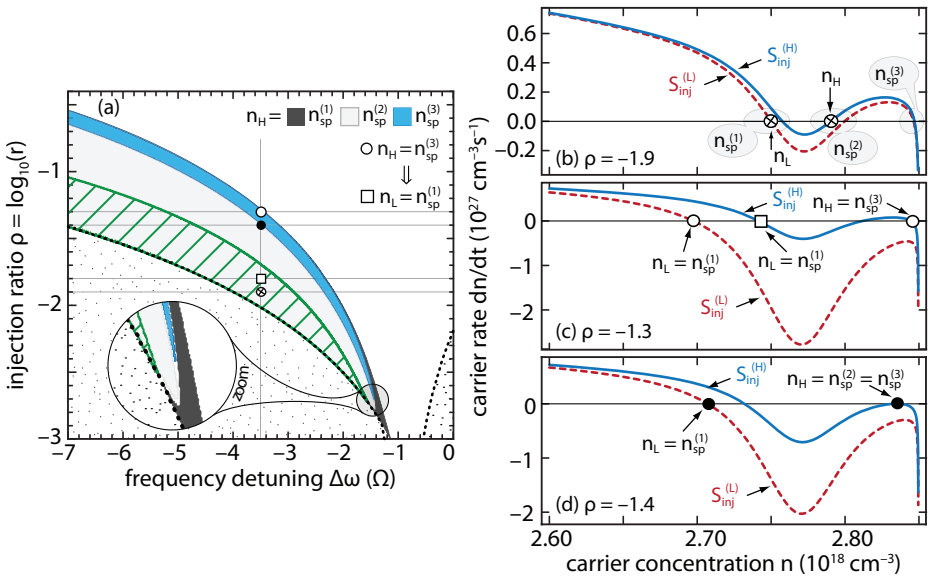

Figure 4.2: *(a) Partition of the **H**-region, with respect to the type of the stationary point n_H. The n_L point from the **H**-region always maps into $n_{sp}^{(1)}$ point, while n_H may map into $n_{sp}^{(1)}$ (thin black area), $n_{sp}^{(2)}$ (grey area), or $n_{sp}^{(3)}$ (blue area). The hatched region represents an area in which $n_L = n_{sp}^{(1)}$ coexist with $n_H = n_{sp}^{(3)}$, sharing the same injection power. (b) dn/dt–n plot and mapping of n_L and n_H into stationary points for $\Delta\omega = -3.5\Omega$ and $\rho = -1.9$. Same for (c) $\rho = -1.3$ and (d) $\rho = -1.4$. In (c) n_L for $\rho = -1.8$ (rectangular dot) coexists with n_H for $\rho = -1.3$ (circular dot), sharing the same injection power. [115]*

Point n_{H} always corresponds to higher injection power than the point n_{M}, i.e., $S_{\mathrm{inj}}^{(\mathrm{H})} > S_{\mathrm{inj}}^{(\mathrm{M})}$, and consequently $n_{\mathrm{H}} < n_{\mathrm{M}}$.

Finally, the n_{L} solution from the **H**-region ($n_{\mathrm{L}} \in \mathbb{H} \setminus \mathbb{M}$) also maps into the $n_{\mathrm{sp}}^{(1)}$ point, though in certain parts of the **H**-region this $n_{\mathrm{sp}}^{(1)}$ point corresponds to the dn/dt–n phase plot with three stationary points. Generally, points from the **H**-region exhibit a more complex mapping, which is why we pay a special attention to this region.

Each point from the **H**-region represents two roots, n_{L} and n_{H} ($n_{\mathrm{L}} < n_{\mathrm{H}}$), with two corresponding injection densities $S_{\mathrm{inj}}^{(\mathrm{L})}$ and $S_{\mathrm{inj}}^{(\mathrm{H})}$ ($S_{\mathrm{inj}}^{(\mathrm{L})} > S_{\mathrm{inj}}^{(\mathrm{H})}$), respectively. Our analysis shows that, similarly to the previous cases, the solution with lower values of carrier concentrations, n_{L}, always maps into $n_{\mathrm{sp}}^{(1)}$ point. This point can correspond to dn/dt–n phase plots in which $n_{\mathrm{sp}}^{(1)}$ is the only stationary solution provided by injection locking, or when $n_{\mathrm{sp}}^{(1)}$ point is the lowest one of three available stationary points. On the other hand, n_{H} exhibits complex mapping either into $n_{\mathrm{sp}}^{(2)}$ or $n_{\mathrm{sp}}^{(3)}$ or even into $n_{\mathrm{sp}}^{(1)}$ in the vicinity of the r_- boundary. Fig. 4.2(a) shows the complete partition of the **H**-region in terms of n_{H} mapping [115]. In the largest area of the **H**-region, n_{H} point maps into $n_{\mathrm{sp}}^{(2)}$ point [grey area in Fig. 4.2(a)]. For values of ρ which correspond to the upper boundary of the saber profile, i.e., for values of ρ somewhat below the r_- boundary, there exists a region in which n_{H}

maps into $n_{\mathrm{sp}}^{(3)}$ point [blue area in Fig. 4.2(a)]. Finally, for a thin region in the vicinity of the r_{-} boundary, n_{H} can even map into $n_{\mathrm{sp}}^{(1)}$ point [black area in Fig. 4.2(a)]. This region becomes somewhat larger for extremely low values of ρ, as depicted in the zoom in Fig. 4.2(a), which correspond to extremely low values of injection power. In this case corresponding dn/dt–n phase plots resemble those obtained for $S_{\mathrm{inj}}^{(\mathrm{M})}$, i.e., n_{H} maps into the $n_{\mathrm{sp}}^{(1)}$ point which is close to the free-running carrier threshold concentration, as in Fig. 4.1(b). Finally, the **H**-region comprises a hatched part, which will be addressed later. In order to provide a deeper analysis of the mapping we study the character of the dn/dt–n phase plots [Fig. 4.2(b) – (d)] corresponding to the **H**-region for a fixed detuning $\Delta\omega = -3.5\Omega$ and three different values of r, i.e., ρ, shown by circular dots in Fig. 4.2(a) [115].

In the first case we consider a point defined with $\rho = -1.9$ [crossed circular dot in Fig. 4.2(a)]. For this point equation (3.29) has two solutions, n_{L} and n_{H}. For the solution n_{L}, the injection ratio ρ corresponds to the a pair $S_{\mathrm{inj}}^{(\mathrm{L})}$ and $S_{m}^{(\mathrm{L})}$, and this $S_{\mathrm{inj}}^{(\mathrm{L})}$ defines a dn/dt–n phase plot which comprises three stationary states [red dashed line in Fig. 4.2(b)]. The n_{L} solution maps into the $n_{\mathrm{sp}}^{(1)}$ point. On contrary to the previously discussed mappings of the n_{L} solution, here, n_{L} maps into the $n_{\mathrm{sp}}^{(1)}$ point from the RMSP region. The other solution of the equation (3.29), the n_{H} solution, maps in the grey area, i.e., it maps into the $n_{\mathrm{sp}}^{(2)}$ point, on the dn/dt–n phase plot which corresponds to the $S_{\mathrm{inj}}^{(\mathrm{H})}$ [blue solid line in Fig. 4.2(b)].

The next considered point is the one defined with injection ratio $\rho = -1.3$, depicted with an open circular dot in the Fig. 4.2(a). The n_{L} solution maps into the $n_{\mathrm{sp}}^{(1)}$ point, though this time it corresponds to the dn/dt–n phase plot comprising only one stationary point [red dashed line in Fig. 4.2(c)]. The n_{H} solution, which now lies in the blue area of the **H**-region, maps into the $n_{\mathrm{sp}}^{(3)}$ point [blue solid line phase plot in Fig. 4.2(c)]. This means that corresponding $S_{\mathrm{inj}}^{(\mathrm{H})}$ defines a dn/dt–n phase plot which provides multistability, i.e., except $n_{\mathrm{sp}}^{(3)}$, provides $n_{\mathrm{sp}}^{(1)}$, and $n_{\mathrm{sp}}^{(2)}$ points. Both points also have their places on the mapping diagram Fig. 4.2(a), though they correspond to different values of ρ, due to different values of the injection-locked mode photon density $S_m(n)$. Since $n_{\mathrm{sp}}^{(1)} < n_{\mathrm{sp}}^{(2)} < n_{\mathrm{sp}}^{(3)}$, injection-locked mode photon density $S_m(n)$ which corresponds to $n_{\mathrm{sp}}^{(1)}$ has the greatest value ($S_{\mathrm{m}(n)^{(1)}} > S_{\mathrm{m}(n)^{(2)}} > S_{\mathrm{m}(n)^{(3)}}$. This further means that $n_{\mathrm{sp}}^{(3)}$ point has the greatest injection ratio ρ, i.e., that $n_{\mathrm{sp}}^{(2)}$ and $n_{\mathrm{sp}}^{(1)}$ points map somewhere on the vertical line below the $n_{\mathrm{sp}}^{(3)}$ point, denoted with the open circular dot in Fig. 4.2(a). The point $n_{\mathrm{sp}}^{(2)}$ has to be mapped into n_{H} point, so it maps somewhere in the grey area of the **H**-region. On the other hand $n_{\mathrm{sp}}^{(1)}$ has to be mapped into the n_{L} point, in particular in $n_{\mathrm{L}} \in \mathbb{H} \setminus \mathbb{M}$. In Fig. 4.2(c) we denote this $n_{\mathrm{sp}}^{(1)}$ point with open rectangular dot, sharing the same injection power with $n_{\mathrm{sp}}^{(3)}$ point (open circle), while in Fig. 4.2(a), we denote the location of this point in the $\Delta\omega$–r, i.e., $\Delta\omega$–ρ space (open rectangular dot).

Finally, for the point from the boundary of the grey and blue area [$\rho = -1.4$, denoted

with black circular dot in Fig. 4.2(a)], n_{L} still maps into the $n_{\mathrm{sp}}^{(1)}$ point which now corresponds to the single stationary point dn/dt–n phase plot [red dashed line in Fig. 4.2(d)]. The other, n_{H} solution corresponds to the limit case in which $n_{\mathrm{sp}}^{(2)}$ merges with $n_{\mathrm{sp}}^{(3)}$ point, as depicted in the Fig. 4.2(d).

This analysis shows that a point from the **H**-region maps into two points (n_{L} and n_{H}) each representing one stationary point in dn/dt–n phase plot [e.g., Fig. 4.2(b)]. Each of these points corresponds to one injected photon density $S_{\mathrm{inj}}^{(\mathrm{s})}$ and simultaneously exists with other stationary points, corresponding to the same injected photon densities, $S_{\mathrm{inj}}^{(\mathrm{L})}$ or $S_{\mathrm{inj}}^{(\mathrm{H})}$, but different r i.e., ρ. In these and similar cases [blue solid lines in Fig. 4.2(c) and (d)], coexistence of the stationary points may provide multistability.

Thus, we further study the range of r (ρ), for which multistability may occur. We again analyze dn/dt–n plots for $\Delta\Omega = -3.5\Omega$ and find that for $S_{\mathrm{inj}}^{(\mathrm{L})}$ and $\rho > -1.7$, there is only one stationary point i.e., n_{L} maps into $n_{\mathrm{sp}}^{(1)}$ point which is a part of the dn/dt–n phase plot comprising only one stationary point [red dashed lines in Fig. 4.2(c) and (d)]. In other cases, multistability becomes feasible, since for a fixed $S_{\mathrm{inj}}^{(\mathrm{s})}$ and consequently different r-values, there are three coexisting stationary points, $n_{\mathrm{L}} = n_{\mathrm{sp}}^{(1)}$, $n_{\mathrm{H}} = n_{\mathrm{sp}}^{(2)}$, and $n_{\mathrm{H}} = n_{\mathrm{sp}}^{(3)}$. Fig. 4.2(a) shows that mapping of n_{H} from the **H**-region into $n_{\mathrm{sp}}^{(2)}$ or $n_{\mathrm{sp}}^{(3)}$, leads to the partition of the **H**-region into two disjunctive subsets. However, for a fixed $S_{\mathrm{inj}}^{(\mathrm{s})}$ and detuning $\Delta\omega$, each point from one subset has a corresponding point in the other. In other words, for fixed $S_{\mathrm{inj}}^{(\mathrm{s})}$ and $\Delta\omega$, $n_{\mathrm{sp}}^{(2)}$ and $n_{\mathrm{sp}}^{(3)}$ always accompany each other. Therefore, both subsets of the **H**-region represent ranges of multistability for stationary points $n_{\mathrm{sp}}^{(2)}$ and $n_{\mathrm{sp}}^{(3)}$. It thus remains for us to find the multistability range corresponding to $n_{\mathrm{L}} = n_{\mathrm{sp}}^{(1)}$, i.e., find the range of n_{L} which corresponds to the $n_{\mathrm{sp}}^{(1)}$ points from the same dn/dt–n phase plots that comprise $n_{\mathrm{H}} = n_{\mathrm{sp}}^{(2)}$ and $n_{\mathrm{H}} = n_{\mathrm{sp}}^{(3)}$ [solid lines in Fig. 4.2(b) – (d)].

In order to do that, we search for the ρ, i.e., r-range for which $n_{\mathrm{L}} = n_{\mathrm{sp}}^{(1)}$ [e.g., open rectangular dot in Fig. 4.2(c)] coexists with points $n_{\mathrm{sp}}^{(3)}$ [open circular dot in Fig. 4.2(c)] and $n_{\mathrm{sp}}^{(2)}$ for a fixed $S_{\mathrm{inj}}^{(\mathrm{s})}$. For any given $\Delta\omega$, we find this range by calculating the photon density of the injection-locked mode $S_m^{(\mathrm{L})}$ for injected density $S_{\mathrm{inj}}^{(\mathrm{L})} = S_{\mathrm{inj}}^{(\mathrm{H})}$, where $S_{\mathrm{inj}}^{(\mathrm{H})}$ corresponds to $n_{\mathrm{H}} = n_{\mathrm{sp}}^{(3)}$ and accompanying $n_{\mathrm{sp}}^{(2)}$. This finally yields $r = S_{\mathrm{inj}}^{(\mathrm{H})}/S_m^{(\mathrm{L})}$. Fig. 4.2(a) depicts the hatched part of the **H**-region, in which $n_{\mathrm{L}} = n_{\mathrm{sp}}^{(1)}$ coexists with $n_{\mathrm{H}} = n_{\mathrm{sp}}^{(3)}$ and $n_{\mathrm{sp}}^{(2)}$ for the same $S_{\mathrm{inj}}^{(\mathrm{s})}$. The third narrow region, i.e., the third disjunctive subset of the **H**-region, in the vicinity of the r_- boundary, in which n_{H} maps into $n_{\mathrm{sp}}^{(1)}$, is irrelevant for multistability.

After identifying the areas in the $\Delta\omega$–r space where $n_{\mathrm{sp}}^{(1)}$, $n_{\mathrm{sp}}^{(2)}$, and $n_{\mathrm{sp}}^{(3)}$ coexist, we investigate their stability [115, 118]. This is done by calculating the eigenvalues of the linearized rate equations system, under the assumption of a small perturbation, as described in the Section 2.3. We simultaneously analyze how the number of modes included in the

analysis affects the stability. For that, we investigate three cases, for which we take into account (*i*) the injection-locked side-mode $m = -5$ only, (*ii*) the injection-locked side-mode $m = -5$ and the central mode $j = 0$, and finally (*iii*) the injection-locked side-mode $m = -5$ and all unlocked modes supported by the cavity of the slave laser. The stationary point is considered stable if all eigenvalues of the system, i.e., all eigenvalues of the $\widetilde{\mathcal{X}}$ matrix defined with equations (2.43) and (2.44), lie in the left-half of the complex plane [115, 123]. This means that all complex modulation phases ξ, defined in equations (2.35a) – (2.35c), comprise negative damping factors λ, leading to the oscillations suppression. The number of eigenvalues depends on the system dimension, i.e., on the number of modes taken into account. As discussed in Section 2.3, the dimension of the $\widetilde{\mathcal{X}}$ matrix is $(N + 2) \times (N + 2)$, where N is the number of modes taken into account. In the cases (*i*) – (*iii*), the number of modes taken into account is $N = 1$, $N = 2$ and $N = 291$, respectively, the number of the eigenvalues correspond to 3, 4, and $N + 2 = l_1 + l_2 + 1 + 2 = 293$ eigenvalues, respectively.

As shown in the Section 3.4, in the case (*i*), when only injection-locked mode is taken into account, the dn/dt–n phase plot can only comprise $n_{\mathrm{sp}}^{(1)}$ and $n_{\mathrm{sp}}^{(2)}$ points. In addition to this, only injection locking induced $n_{\mathrm{sp}}^{(1)}$ point is feasible, i.e., the model cannot recognize $n_{\mathrm{sp}}^{(1)}$ point formed in the vicinity of the free-running threshold carrier concentration due to unlocked modes interplay, since there are no other longitudinal modes in the model. This means that equation (3.29) has only two possible solutions: n_{L}, which always maps into injection locking induced $n_{\mathrm{sp}}^{(1)}$ point, and n_{H}, which now maps only into $n_{\mathrm{sp}}^{(2)}$ point.

For the case (*i*), in Fig. 4.3(a) we present the obtained stability map. Stability analysis confirms previously presented and discussed locking range, i.e., confirms the asymmetrical locking range, which is outlined by the FWM boundary on the negative frequency detuning side, and locking $\cos(\theta_{\mathrm{m}}) = 0$ boundary, which shrinks the locking range on the positive frequency detuning side. In the locking range, the basic n_{L} solution is stable in the most part of it [yellow shaded area in Fig. 4.3(a)], expect in the cross-hatched region in the domain of small negative and positive $\Delta\omega$ [cf. Fig. 4.3(a)]. The union of the unlocked (blank area) and this unstable region (cross-hatched area) for $n_{\mathrm{L}} = n_{\mathrm{sp}}^{(1)}$ in Fig. 4.3(a) is usually classified as the region of nonlinear dynamics [48], while the stability map of the $n_{\mathrm{L}} = n_{\mathrm{sp}}^{(1)}$, reproduces the common stability plot as predicted by earlier works [48–50]. However, Fig. 4.3(a) also shows the root loci $n_{\mathrm{H}} = n_{\mathrm{sp}}^{(2)}$, outlining the **H**-region [single hatched region in Fig. 4.3(a)], which appears even in the single side-mode analysis. As has been explained previously, the stationary points $n_{\mathrm{H}} = n_{\mathrm{sp}}^{(2)}$ represent an additional layer on the top of $n_{\mathrm{L}} = n_{\mathrm{sp}}^{(1)}$ root loci in the **H**-region. As discussed in the Section 3.4, a closer inspection of the dn/dt–n phase plot shape in the vicinity of the $n_{\mathrm{H}} = n_{\mathrm{sp}}^{(2)}$ point shows that this root behaves as the repelling fixed point, not attracting one, as should be in case

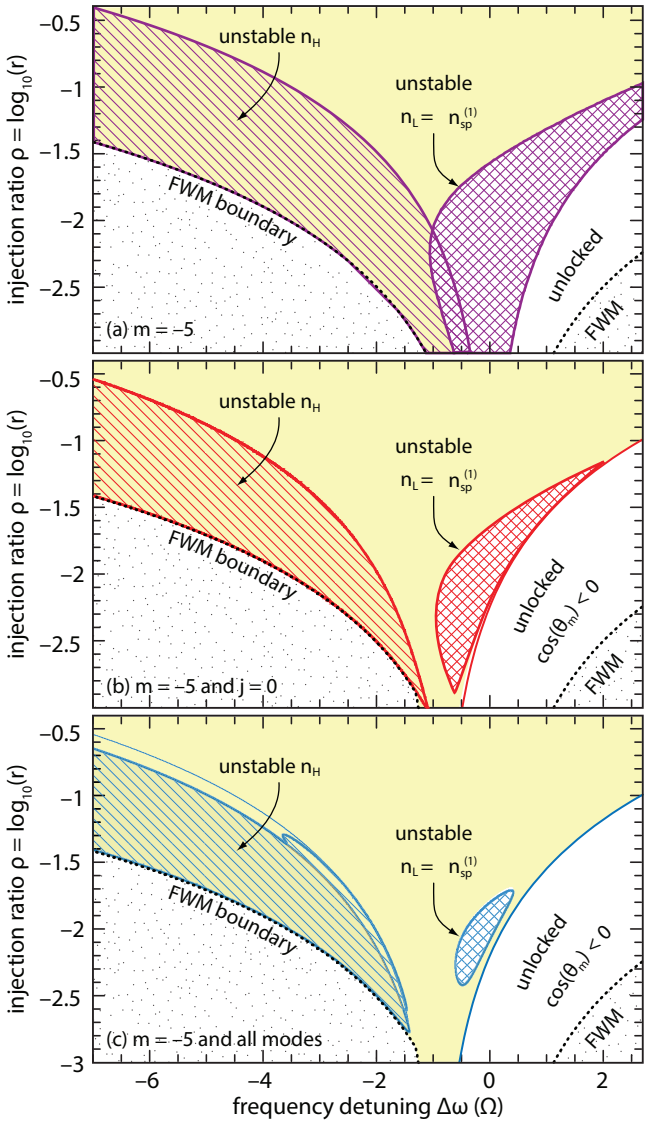

Figure 4.3: *(a) Stability plot for injection-locked mode $m = -5$ alone. Stable (shaded) and unstable (hatched) part of the locking range. The single-hatched region corresponds to the unstable $n_H = n_{sp}^{(2)}$, i.e., whole **H**-region is unstable. The cross-hatched region corresponds to the unstable $n_L = n_{sp}^{(1)}$. (b) Same, for two modes included, i.e., injection-locked mode $m = -5$ and $j = 0$. Although n_H comprises both $n_{sp}^{(2)}$ and $n_{sp}^{(3)}$, the whole **H**-region is still unstable. The unstable region of $n_L = n_{sp}^{(1)}$ (cross-hatched) is compressed in comparison to (a). (c) Same, for all modes included. The whole subset $n_H = n_{sp}^{(2)}$ is unstable, while $n_H = n_{sp}^{(3)}$ is unstable only for small negative detuning. The unstable region of $n_L = n_{sp}^{(1)}$ (cross-hatched) is significantly compressed in comparison to (a) and (b). For all three cases, n_L is stable in the whole **H**-region (yellow shaded under hatched). [115, 118]*

of a stable stationary point. The same is confirmed by the small signal analysis. Since the region for $n_H = n_{sp}^{(2)}$ is fully unstable and represents the layer which overlaps $n_L = n_{sp}^{(1)}$ layer in the **H**-region, one can conclude that the n_H region actually does not manifest its presence nor intersect the $n_L = n_{sp}^{(1)}$ layer. Therefore, this single hatched layer can be ignored in case (*i*), while the stability map remains as the one predicted in [48–50].

The model considered in case (*ii*) can, besides $n_{sp}^{(1)}$, and $n_{sp}^{(2)}$, recognize the third stationary state $n_{sp}^{(3)}$, as a result of the central mode $j = 0$ inclusion. As a result, the **H**-region besides $n_H = n_{sp}^{(2)}$, comprises $n_H = n_{sp}^{(3)}$, though we find that n_H is fully unstable for the whole **H**-region [cf. Fig. 4.3(b)], similarly as in the case (*i*). On the other hand, the cross-hatched area, representing the dynamically unstable region of $n_L = n_{sp}^{(1)}$, is compressed in comparison to the case (*i*) [cf. Fig. 4.3(a) and (b)].

Finally in Fig. 4.3(c), we present the stability map for model which takes into account injection-locked mode $m = -5$ and all supported unlocked longitudinal modes (case (*iii*)). In this case, our stability analysis shows in the **H**-region, $n_H = n_{sp}^{(2)}$ is always unstable, which was previously deducted, as $n_{sp}^{(2)}$ is a repelling stationary point. However, $n_H = n_{sp}^{(3)}$ is unstable only for a small negative detuning [cf. Fig. 4.3(c)]. The unstable region for $n_L = n_{sp}^{(1)}$ becomes even more compressed, i.e., it can be seen that this region significantly diminishes as the number of modes increases [cf. Fig. 4.3(a) – (c)]. For all three cases ((*i*) – (*iii*)), n_L corresponding to the **H**-region stays stable (yellow shaded beneath the hatched region).

In addition to the repelling fixed point instability related to the stationary point $n_H = n_{sp}^{(2)}$, which was also confirmed by the asymptotic Lyapunov stability check based on the small signal analysis, we find that a different type of instability is related to the other stationary points [115, 118]. In fact, instabilities which occur for positive detuning for $n_L = n_{sp}^{(1)}$ and negative detuning for $n_H = n_{sp}^{(3)}$ are related to the supercritical Hopf bifurcation [3, 50, 115, 118], for which the laser operates on only one mode with the oscillatory output, while the suppressed modes follow the same oscillatory behavior. In the stable regions and for the fixed conditions, the slave laser remains in one of the stable points and in the injected mode over the entire range. However, the multivalued character of the locking range allows coexistence of the two stable, attractive fixed points ($n_L = n_{sp}^{(1)}$ and $n_H = n_{sp}^{(3)}$) for a sufficiently large negative detuning. As we show next, these stable points may provide shifting between modes as a result of injection power (or detuning) variation, i.e., these stable points correspond to already presented and discussed hysteresis loops.

In Fig. 4.2 we outlined the region in which n_H maps into $n_{sp}^{(3)}$ point [blue area in Fig. 4.2(a)], and the corresponding region in which n_L from the **H**-region maps into the $n_{sp}^{(1)}$ point, coexisting with the $n_{sp}^{(3)}$, sharing the same S_{inj}, i.e., injection power [hatched area in Fig. 4.2(a)]. Furthermore, in Fig. 4.3(c), we concluded that the n_L solution from the

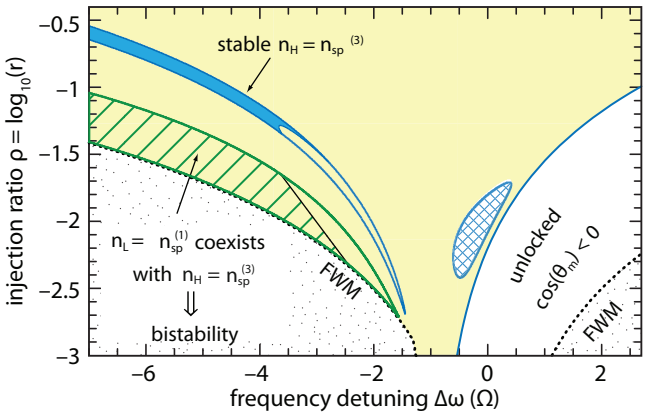

Figure 4.4: *Stable region for $n_H = n_{sp}^{(3)}$ (dark shaded) and the part of $n_L = n_{sp}^{(1)}$ (hatched) coexisting with it, for a fixed injection photon density S_{inj}, providing bistability. All modes are included. [115, 118]*

H-region always exhibits stable dynamic behavior, while $n_H = n_{sp}^{(3)}$ can be stable for sufficiently large negative frequency detuning. In Fig. 4.4 we present complete multivalued stability plot in $\Delta\omega$–r space, obtained for the full scale model, in which we, apart from denoting the regions where slave laser exhibits unstable operation, depict the region of the bistability. More precisely, we redraw the hatched n_L region from the Fig. 4.2(a), though here we accent the part of this region which corresponds to the stable part of $n_H = n_{sp}^{(3)}$ point, and thus provide bistable slave laser output, since two stable states share the same injection power (hatched area in Fig. 4.4). Therefore, we conclude that the bistability becomes feasible as a result of the multivalued character of the locking and stability plot. This result confirms that inclusion of unlocked modes in the analysis of the stability map is crucial for multi-mode in-plane lasers. It is not clear, whether this effect is relevant for single-mode in-plane lasers. However, it can be expected that in the case of the sufficient suppression of side-modes, single-mode lasers can be treated as before, i.e., regardless the influence of the unlocked modes. The presented stability analysis may be very useful for deeper analysis of modulation characteristics in multi-mode injection-locked lasers as in [75, 135], and in addition to this it can provide certain deeper understanding of the bistability effect found in quantum dash injection-locked lasers [136, 137].

Experiment

In order to validate our findings regarding bistability, we conduct an experiment in which for a slave Fabry-Pérot laser we measure the side-mode-suppression-ratio of the injection-locked mode $m = -5$ (with respect to the dominant mode) versus the injection power P_{inj}. The experiment setup is illustrated in Fig. 4.5(a), while the obtained SMSR versus P_{inj}

dependence is presented in Fig. 4.5(b) [115, 118]. We set $\Delta\omega = -5\Omega$ and $I = 1.4I_{\text{th}}$.

A widely tunable semiconductor laser source was connected to an erbium-doped fiber amplifier (EDFA), whose output was led to a variable attenuator, and a tunable optical filter. The signal was then coupled into an optical circulator, which was also connected to a Fabry-Pérot laser diode chip, through a lensed fiber, and to an optical spectrum analyzer (OSA) [cf. Fig. 4.5(a)]. Due to the circulator properties, only the signals generated by the FP-LD were detected and displayed on the OSA. The FP-LD was fabricated at University of California, Santa Barbara (UCSB), in a surface ridge platform [104]. The laser ridge is 500 μm long and 3 μm wide, and the active region consists of an offset quantum well stack, as detailed in, per example, [142]. The insertion loss through the system was characterized by measuring the power through the circulator, and the coupling losses for the laser chip were measured by reverse biasing the laser diode and by measuring the photocurrent generated by the input optical signal of known power.

The decrease followed by the increase of P_{inj}, or in other words, counterclockwise variation of the injection power clearly shows a hysteresis cycle, which proves the existence of the bistability [Fig. 4.5(b)]. For each value of the injection power, an optical spectrum trace was taken, from which the SMSR was then calculated [118]. With open dots we present measured SMSR in the case of injection power increase, while crosses represent measured SMSR in the direction of P_{inj} decrease. Through obtained set of measured points we interpolate a hysteresis loop. Next, we analyze and map certain parts of the loop to appropriate regions of the previously calculated stability map (Fig. 4.4). By using the measured power corresponding to S_m for $m = -5$ and P_{inj}, we generate the r versus SMSR plot [cf. Fig. 4.5(c)]. Since the laser used in this experiment has a larger active region volume than the one used in our calculations, we qualitatively compare Fig. 4.5(c) with Fig. 4.4 for a fixed negative detuning. The upper branch of the hysteresis loop falls into r-range defined with $0 < \rho < 0.5$ [green dotted line in Figs. 4.5(b) and (c)]. This corresponds to the hatched region in Fig. 4.4 for which $n_{\text{L}} = n_{\text{sp}}^{(1)}$ coexists with $n_{\text{H}} = n_{\text{sp}}^{(3)}$, sharing the same P_{inj}. For $\rho > 0.5$, corresponding to the upper branch outside of the hysteresis loop, we find only one stable stationary point [yellow line in Figs. 4.5(b) and (c)]. This result is supported by Fig. 4.4, which shows a stable region between the hatched and shaded areas, corresponding to the part of the upper branch outside of the bistability range, which is illustrated as yellow accented area in the inset in Fig. 4.5(c). Although it seems that this yellow accented area intersects with blue shaded area representing $n_{\text{H}} = n_{\text{sp}}^{(3)}$ it is not the case, i.e., it should be kept in mind that the locking range is folded along the FWM boundary, so that the part of the **H**-region where n_{H} maps into $n_{\text{sp}}^{(2)}$ and $n_{\text{sp}}^{(3)}$ is actually in the parallel plane above the plane in which n_{H} maps into $n_{\text{sp}}^{(1)}$. For a sufficiently large r ($\rho > 1.1$), there is an additional stable stationary point correspond-

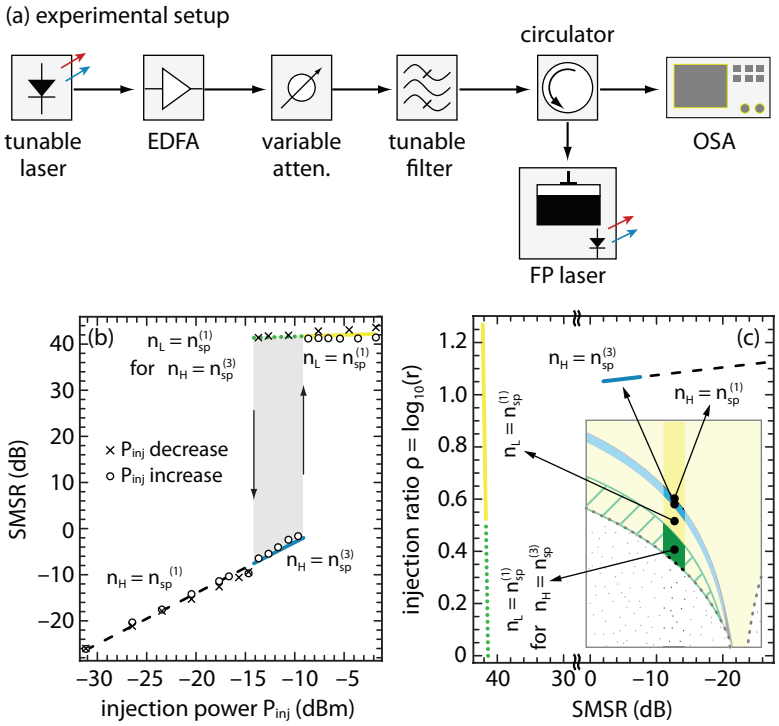

Figure 4.5: *(a) Experimental setup. (b) Measured SMSR for the mode $m = -5$ versus injection power P_{inj}. Counterclockwise variation of the injection power outlines a hysteresis loop, as predicted by the theory. (c) Branches of the hysteresis from (b), mapped into SMSR–ρ space: (left) upper branch within the bistability range (green dotted line) and outside the bistability range (yellow solid line); (right) lower branch within the bistability range (blue solid line) and outside the bistability range (black dashed line). (Inset) Schematic distribution of the hysteresis branches in the locking and the stability plot. [115]*

ing to lower branch of the hysteresis loop and $n_{\mathrm{H}} = n_{\mathrm{sp}}^{(3)}$ region in Fig. 4.4 [blue line in Figs. 4.5(b) and (c)]. The fact that for this range of r, we have two different values of SMSR, i.e., two different injected powers P_{inj} for one r, confirms the conclusion that the shaded region in Fig. 4.4 represents the multivalued function. The lower branch outside of the loop [black dashed line in Figs. 4.5(b) and (c)], corresponds to $n_{\mathrm{H}} = n_{\mathrm{sp}}^{(1)}$ [cf. Fig. 4.2(a)], which as we already mentioned, is not related to the bistability region. However, the experimental results suggest that the region corresponding to $n_{\mathrm{H}} = n_{\mathrm{sp}}^{(1)}$ comprises a somewhat wider r-range than the one predicted by our theory, which proposes almost horizontal line for $n_{\mathrm{H}} = n_{\mathrm{sp}}^{(1)}$ part in Fig. 4.5(c). It is likely that small injected powers in this case may cause a measurement uncertainty and consequently the small noticed discrepancy between the theory and the experiment. It is also possible that the experimental results include not only the **H**-, but also the **M**-region, which supports multiplicity of $n_{\mathrm{sp}}^{(1)}$ point. Therefore, the mapping shown in Fig. 4.5(c) completely resembles distribution of r-values in Fig. 4.4 and thin region $n_{\mathrm{H}} = n_{\mathrm{sp}}^{(1)}$ in Fig. 4.2(a).

Finally, according to the presented results, the excursion around the hysteresis loop in the $\Delta\omega$–ρ space (Fig. 4.4), begins in the narrow region in the vicinity of the r_{-} boundary, more precisely, in the **M**-region where $n_{\mathrm{L}} = n_{\mathrm{sp}}^{(1)}$, and **H**-region where $n_{\mathrm{L}} = n_{\mathrm{sp}}^{(1)}$, since these $n_{\mathrm{sp}}^{(1)}$ points correspond to the low injection powers, when the stationary point is formed as a consequence of unlocked modes interplay, near the free-running threshold concentration n_{th}. Since the slave laser operates close to the free-running regime, the SMSR, measured as the ratio between the power in the injection-locked mode relative to the power in the central mode, is low, due to the pronounced central mode.

Further increase of injection power leads to the case in which $\mathrm{d}n/\mathrm{d}t$–n phase plot acquires two additional stationary states, however the slave laser enters the $n_{\mathrm{sp}}^{(3)}$ point, being the closest one, in which the slave laser still has low SMSR. In the $\Delta\omega$–r space (Fig. 4.4) the operating point of the slave laser slides down to the blue shaded area $n_{\mathrm{H}} = n_{\mathrm{sp}}^{(3)}$, which correspond to the lower hysteresis branch. Once the injection power reaches the right hysteresis boundary, $n_{\mathrm{sp}}^{(3)}$ disappears and the slave laser jumps to the only steady state provided, which is now $n_{\mathrm{L}} = n_{\mathrm{sp}}^{(1)}$ state. This state now corresponds to high injection powers and consequently high values of SMSR. In the $\Delta\omega$–r space (Fig. 4.4), operating point of the slave laser switches from the bottom edge of the blue area, to the yellow shaded layer underneath, as it is the region of n_{L} solution. However, this n_{L} maps into the $n_{\mathrm{sp}}^{(1)}$ point which corresponds to the case in which $n_{\mathrm{sp}}^{(1)}$ is the only stationary point provided by the $\mathrm{d}n/\mathrm{d}t$–n phase plot. As denoted in Fig. 4.4, the hatched part of the yellow shaded area corresponds to the $n_{\mathrm{sp}}^{(1)}$ point accompanied by $n_{\mathrm{sp}}^{(3)}$, so upon exiting the blue shaded area of $n_{\mathrm{sp}}^{(3)}$ point (i.e., lower branch), the laser switches to the upper boundary outlining the hatched and plain yellow area. Further increase of injection power shifts

the operating point of the slave laser through yellow shaded $n_L = n_{sp}^{(1)}$ layer, now in the direction towards higher values of ρ. In the reverse direction, i.e., as injection power starts to decrease, the slave laser stays in the $n_L = n_{sp}^{(1)}$, as long as it is provided, hence the operating point of the slave laser slides down the yellow shaded area and passes through the hatched part representing the upper ($n_{sp}^{(1)}$) branch. Once $n_{sp}^{(1)}$ is not provided anymore the slave laser switches to the upper layer comprising the narrow region in the vicinity of the r_- boundary from which the excursion initially started.

4.2 Analytical study of the injection-power switching of IL FP-LDs

As presented in the Section 3.5 and in the previous section, in certain range of injection parameters, P_{inj} and $\Delta\omega$, the slave laser exhibits two dynamically stable states, providing for slave laser bistability. The presence of this bistability, reflected in formation of the hysteresis loop in the slave laser power output, can promote injection-locked lasers as candidates for realization of all-optical flip-flops, which are recognized as one of the crucial building elements of modern optical networks architectures, such as all-optical packet-switching networks. Indeed, such architectures are one of the trending research areas, aiming to surpass the limits of the electronic data processing schemes, which fail to satisfy increasing demands in traffic load for new and upcoming internet-based services, and impose a severe bottleneck in modern hybrid optical networks [20]. One of the key parameters for successful implementation of the bistable injection-locked semiconductor laser into all-optical elements is switching time between different stable states, which generally depends on the switching mechanism. Therefore, extensive effort has been made to investigate switching time for various switching mechanisms, both experimentally [45, 46] and by theoretical calculation [116, 138–140]. In this Section, we base our analysis of switching between bistable states on a simple analytical model [138–140]. Although this model is based on several approximations of the full scale rate equation model, comparison with numerical simulations of the full scale rate equation model, which are presented in the next Section, prove that the analytical approach is sufficiently precise to estimate the switching characteristics properly. Therefore, this analytical model provides an efficient tool for effortless both phenomenological, qualitative and quantitative description of the switching processes in injection-locked semiconductor laser diodes.

In derivation of the analytical switching model, we assume that the stationary photon density can be reached much faster than the carrier density. The second assumption is that the carrier concentration n does not change considerably as the slave laser switches between two stable points $n_{sp}^{(1)}$ and $n_{sp}^{(3)}$, compared to the case of complete turn on and off.

This assumption means that, depending on the switching direction, we may fix the total recombination rate $Q(n)$ in (2.21a) to a value corresponding to some switching carrier concentration n_x between $n_{sp}^{(1)}$ and $n_{sp}^{(3)}$ i.e. $Q(n_x) = A_{SRH}n_x + R_{sp}(n_x) + C_A n_x^3$, which we chose according to the switching direction. Since the slave laser is stabilized in the initial state before the switching, the laser will remain in its vicinity most of the switching time. As the switching is over once the final state is just reached, one can conclude that an average carrier concentration during the switching is closer to the initial carrier concentration than to the final one. Therefore, for the case of switching from $n_{sp}^{(3)}$ to $n_{sp}^{(1)}$ it is justified to assume that n_x corresponds to the initial carrier concentration, i.e. $n_x = n_{sp}^{(3)}$, while in the reverse direction, following the same logic, n_x is set to the $n_{sp}^{(1)}$. Finally, in order to enable the analytical approach, we make use of the fact that the profile of the dn/dt–n phase plot mainly depends on the injection-locked mode m for a wide range of n except in the vicinity of n_{th} [cf. Fig. 3.12 in Section 3.4]. This encourages us to, for the sake of analytical approach, remove the necessity for unlocked modes photon rate equations in further consideration and neglect their contribution in the carrier rate equation (2.21a). In one approach, we fully implement the reduced rate equation system, meaning that we calculate $n_{sp}^{(1)}$ point using the provided system, and since such system does not recognize $n_{sp}^{(3)}$ point, we make use of the fact that it is close to the n_{th} carrier concentration, we assume $n_{sp}^{(3)} = n_{th}$ [138]. However, in somewhat more precise approach [139], we keep the original values for $n_{sp}^{(1)}$ and $n_{sp}^{(3)}$ points, corresponding to derived hysteresis loops obtained from the full scale rate equation model with fixed recombination rate, and implement derived analytical model of switching time calculation on the exactly calculated hysteresis loops. Although all mentioned approximations reduce the accuracy of our switching model, they provide a possibility to analytically and more directly investigate not only the switching characteristics itself, but also the influences of some other laser parameters, such as linewidth enhancement factor α, or active region volume, i.e., number of quantum wells N_w it comprises, on the switching in injection-locked semiconductor laser diodes.

With all unlocked modes excluded from the model, it reduces to three coupled equations: the one which defines injection-locked mode photon density S_m, the one regarding injection-locked mode phase θ_m, and finally the one describing the slave laser carrier concentration n dynamics. We start from Eq. (3.24), with assumption that spontaneous emission term B in the photon density equation for the injection-locked mode can be neglected, thus with $B = 0$, we derive stationary S_m and consequently θ_m [138–140]:

$$S_m = \frac{4k_c^2 S_{inj}}{[A_m^2(1+\alpha^2) - 4A_m\alpha\Delta\omega + 4\Delta\omega^2]}, \tag{4.3}$$

$$\theta_m = \arcsin\left[\frac{\alpha A_m - 2\Delta\omega}{\sqrt{A_m^2(1+\alpha^2) - 4\alpha\Delta\omega A_m + 4\Delta\omega^2}}\right]. \tag{4.4}$$

We further modify the carrier rate equation (2.21a) in which we exclude the contribution of the unlocked modes, fix the contribution of radiative and nonradiative spontaneous recombination to $Q(n_x)$, and introduce the effective rate of the carrier injection into the slave laser as $Q_{net} = I/(qV) - Q(n_x)$. The described procedure leads to:

$$\frac{dn}{dt} = Q_{net} - v_g g(n, \omega_m + \Delta\omega) S_m(n). \tag{4.5}$$

4.2.1 Analytical expression for switching time calculation

In order to derive our switching model, we rewrite the last equation in terms of $A = A_m$. From $A = \Gamma v_g g(n, \omega_m + \Delta\omega) + \tau_p^{-1}$, we get $v_g g(n, \omega_m + \Delta\omega) = \Gamma^{-1}(A + \tau_p^{-1})$ and:

$$\frac{dA}{dt} = \Gamma v_g \frac{dg}{dt} = \Gamma v_g \frac{dg}{dn}\frac{dn}{dt} = \frac{1}{\xi}\frac{dn}{dt}, \tag{4.6}$$

where $\xi = [\Gamma v_g (dg/dn)]^{-1}$.

According to this, the differential equation regarding the carrier dynamics (4.5) can be written in terms of effective stimulated emission rate, as [138, 139]:

$$\xi \frac{dA}{dt} = Q_{net} - \frac{(A + \tau_p^{-1}) S_m}{\Gamma}. \tag{4.7}$$

Assuming that the stationary photon density is reached much faster than the carrier concentration, we substitute the stationary form of injection-locked mode photon density S_m, given by (4.3), and rewrite Eq. (4.7) in the following form [138, 139]:

$$\xi \left[\frac{1}{Q_{net}} + \frac{K_4 A + K_5}{K_1 A^2 + K_2 A + K_3} \right] dA = dt, \tag{4.8}$$

where $K_1 - K_5$ are coefficients given as [138, 139]:

$$K_1 = Q_{net}^2 \Gamma \tau_p (1 + \alpha^2), \tag{4.9a}$$

$$K_2 = -4 Q_{net} \tau_p (Q_{net} \alpha \Gamma \Delta\omega + k_c^2 S_{inj}), \tag{4.9b}$$

$$K_3 = 4 Q_{net} (Q_{net} \Gamma \Delta\omega^2 \tau_p - k_c^2 S_{inj}), \tag{4.9c}$$

$$K_4 = 4 k_c^2 S_{inj} \tau_p, \tag{4.9d}$$

$$K_5 = 4 k_c^2 S_{inj}. \tag{4.9e}$$

In order to obtain the switching time, we conduct definite integration of the Eq. (4.8):

$$\frac{\xi}{Q_{net}} \int_{A_i}^{A_f} dA + \xi \int_{A_i}^{A_f} \frac{K_4 A + K_5}{K_1 A^2 + K_2 A + K_3} dA = \int_{t_i}^{t_f} dt. \tag{4.10}$$

The rational function in the second integral can be decomposed as:

$$\int_{A_\mathrm{i}}^{A_\mathrm{f}} \frac{K_4 A + K_5}{K_1 A^2 + K_2 A + K_3} \mathrm{d}A = \int_{A_\mathrm{i}}^{A_\mathrm{f}} \frac{K_4 A}{K_1 A^2 + K_2 A + K_3} \mathrm{d}A + \int_{A_\mathrm{i}}^{A_\mathrm{f}} \frac{K_5}{K_1 A^2 + K_2 A + K_3} \mathrm{d}A. \tag{4.11}$$

The first integral gives a logarithmic function, while the denominator in the second integral can be further decomposed as:

$$\int_{A_\mathrm{i}}^{A_\mathrm{f}} \frac{K_5}{K_1 A^2 + K_2 A + K_3} \mathrm{d}A = \int_{A_\mathrm{i}}^{A_\mathrm{f}} \frac{K_5}{\left(\sqrt{K_1} A + \frac{K_2}{2\sqrt{K_1}}\right)^2 + K_3 - \frac{K_2^2}{4K_1}} \mathrm{d}A. \tag{4.12}$$

For $K_3 - K_2^2/4K_1 > 0$ the latter integral gives an inverse tangent function, while in the other case it results in an inverse hyperbolic tangent. However, the inverse hyperbolic tangent can be given in terms of inverse tangent, i.e., regardless of the sign of the factor $K_3 - K_2^2/4K_1$, the switching time can be obtained as [139]:

$$\begin{aligned} t_\mathrm{if} = {} & \frac{\xi(A_\mathrm{f} - A_\mathrm{i})}{Q_\mathrm{net}} + \frac{\xi K_4}{2K_1} \ln\left(\frac{K_1 A_\mathrm{f}^2 + K_2 A_\mathrm{f} + K_3}{K_1 A_\mathrm{i}^2 + K_2 A_\mathrm{i} + K_3}\right) \\ & + \frac{\xi(2K_1 K_5 - K_2 K_4)}{K_1 \sqrt{4K_1 K_3 - K_2^2}} \arctan\left[\frac{(A_\mathrm{f} - A_\mathrm{i})\sqrt{4K_1 K_3 - K_2^2}}{2K_1 A_\mathrm{f} A_\mathrm{i} + K_2(A_\mathrm{f} + A_\mathrm{i}) + 2K_3}\right]. \end{aligned} \tag{4.13}$$

The definite integral given by t_if represents the switching time between the initial $A_m = A_\mathrm{i}$ and the final $A_m = A_\mathrm{f}$ state, where subscript "i" stands for 1 or 3, i.e., corresponds to $n_\mathrm{sp}^{(1)}$ or $n_\mathrm{sp}^{(3)}$, while subscript "f" stands for 3 or 1, i.e., $n_\mathrm{sp}^{(3)}$ or $n_\mathrm{sp}^{(1)}$. In the expressions for coefficients $K_1 - K_5$ [Eqs. (4.9a) – (4.9e)], S_inj and $\Delta\omega$ correspond to injected photon density, i.e., applied injection power, and frequency detuning, respectively, during the process of the switching, which will depend on the desired switching mechanism.

4.2.2 Switching by injection power variation

In order to phenomenologically explain the process of switching, in Fig. 4.6, we show $\mathrm{d}n/\mathrm{d}t$–n phase plots obtained from (4.5) for $I = 1.2I_\mathrm{th}$, $\Delta\omega = -14\Omega$, and injection into side-mode $m = -5$ [139]. The solid plots in Fig. 4.6 are obtained for P_inj corresponding to the limiting values of the bistability range (red lines), $P_\mathrm{inj}^{(1)} = -6.6$ dBm ($n_\mathrm{sp}^{(2)}$ merges with $n_\mathrm{sp}^{(1)}$) and $P_\mathrm{inj}^{(2)} = -2.2$ dBm ($n_\mathrm{sp}^{(2)}$ merges with $n_\mathrm{sp}^{(3)}$) and for the injection power $P_0 = -4.4$ dBm (black line). The power P_0 corresponds to P_inj for which $n_\mathrm{sp}^{(1)}$ point lies in the middle of the carrier concentration range corresponding to the $n_\mathrm{sp}^{(1)}$ bistability range, although it may look like it coincides with the average power of the bistability range as depicted in

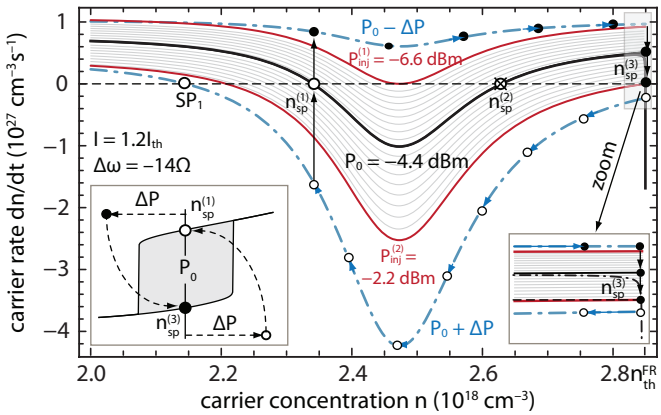

Figure 4.6: *dn/dt–n phase plots accounting only for the injection-locked side-mode m = −5 for $I = 1.2I_{th}$, $\Delta\omega = -14\Omega$. Red solid lines correspond to the phase plots outlining the bistability region (hatched area), i.e., correspond to the hysteresis edges, $P^{(1)}_{inj}$ and $P^{(2)}_{inj}$. Dot-dashed line from the figure inset represents the phase plot obtained for all modes included. Blue arrowed lines represent phase plots corresponding to switching powers $P_0 \pm \Delta P$. (Left inset) Schematic S_m hysteresis loop and trajectories of switching. (Right inset) Enlarged vicinity of the $n^{(3)}_{sp}$ state. [139]*

the left inset in Fig. 4.6. Injection powers $P^{(1)}_{\text{inj}}$ and $P^{(2)}_{\text{inj}}$ represent hysteresis edges, the left, and the right hysteresis edge, respectively. Fig. 4.6 also provides dn/dt–n phase plot at injection power P_0, for all modes included (injection-locked as well as all unlocked modes), based on Eq. (2.21a), and for a fixed spontaneous recombination term $Q(n_{\text{x}})$ (black dot-dashed line in Fig. 4.6 right inset). It can be seen that that this plot almost completely overlaps the one derived from Eq. (4.5) comprising only the injection-locked mode. The difference occurs only in the vicinity of n_{th} (cf. right inset in Fig. 4.6). It can be seen in the right inset of Fig. 4.6 that dn/dt–n phase plots corresponding to Eq. (4.5) do not intersect dn/dt = 0, which would have happened, if the unlocked modes had been included in Eq. (4.5) as they were in Eq. (2.21a). Nevertheless, the n-coordinate of the right ending point of the phase plot obtained from Eq. (4.5) almost completely coincides with $n^{(3)}_{\text{sp}}$, which means that the negligence of the unlocked modes is justified with respect to the dn/dt–n phase plot profile as long as the accurate position of $n^{(3)}_{\text{sp}}$ is known. In other words, if we use simplified model represented by Eq. (4.5) in describing dn/dt–n phase plots, the right ending point is equivalent and corresponds to $n^{(3)}_{\text{sp}}$. However, $n^{(3)}_{\text{sp}}$ has to be derived from the full scale rate equation model, or more precisely from Eq. (3.29), since Eq. (4.5) cannot provide it.

Here, we analyze the switching between stable points $n^{(1)}_{\text{sp}}$ and $n^{(3)}_{\text{sp}}$ and vice versa by variation of P_{inj}. In this analysis we focus on the points depicted in Fig. 4.6, which we obtain after simplifications imposed by the approximations of the model. This means that we start from P_{inj} set to P_0 for which the slave laser is either in the $n^{(1)}_{\text{sp}}$ (upper hysteresis

branch) or in the $n_{sp}^{(3)}$ state (lower hysteresis branch, c.f. left inset in the Fig. 4.6), depending on the slave laser prehistory. Nevertheless, in order to switch from $n_{sp}^{(3)}$ to $n_{sp}^{(1)}$, P_{inj} needs a variation (ΔP), i.e., it has to be rapidly increased to some $P_{inj} = P_0 + \Delta P > P_{inj}^{(2)}$ which corresponds to the case when only one steady state appears, which we denote as SP_1 (open dot in Fig. 4.6). The transition dn/dt–n phase plot, i.e., the dn/dt–n phase plot which corresponds to the applied injection power $P_{inj} = P_0 + \Delta P$ is depicted as lower blue arrowed line in Fig. 4.6. This power overcomes the right hysteresis edge ($P_{inj}^{(2)}$) and corresponds to the upper right tail of the hysteresis. If this power ($P_{inj} = P_0 + \Delta P$) is kept fixed for sufficiently long time interval, the slave laser will begin to gradually slide toward the only steady state provided (in the direction of the arrows), i.e., the carrier concentration in the active region of the slave laser will start to decrease towards the one provided by SP_1. When P_{inj} is returned back to P_0, instead of stabilizing in the SP_1 state, the slave laser is pushed back on the initial phase plot corresponding to the injection power P_0. As carrier concentration level is lowered from the level of the starting $n_{sp}^{(3)}$ point, the slave laser switches to $n_{sp}^{(1)}$ and completes the switching. However, if the variation of the master laser injection power impulse is not sufficiently long, once the injection power is returned to P_0, the carrier concentration level in the active region of the slave laser will be still closer to the initial $n_{sp}^{(3)}$ state, and switching will be unsuccessful. Since this switching direction corresponds to jumping from lower to upper hysteresis branch, we denote this direction as "switching up". In the reverse, "switching down" process, in order to switch from $n_{sp}^{(1)}$ to $n_{sp}^{(3)}$, i.e., from upper to lower hysteresis branch, P_{inj} has to be decreased to some $P_{inj} = P_0 - \Delta P < P_{inj}^{(1)}$, corresponding to the case when only stationary point near the free-running threshold carrier concentration appears. The transition dn/dt–n phase plot corresponding to $P_{inj} = P_0 - \Delta P$ is depicted as the upper blue arrowed line in Fig. 4.6. Here $P_{inj}^{(1)}$ represents the lower, i.e., left hysteresis edge. This power has to be kept fixed for some sufficiently long time interval in order for the slave laser to slide towards the steady-state in the vicinity of the n_{th}, and when the power is returned back to P_0, laser jumps back to the initial dn/dt–n phase plot, and stabilizes in the $n_{sp}^{(3)}$ state, which is in the vicinity of n_{th}.

4.2.3 Switching by frequency detuning variation

Similar switching can be achieved by variation of $\Delta\omega$ as shown in Fig. 4.7. It should be noted that bistability occurs for $\Delta\omega < 0$ [114, 115], and thus its decrease means that the magnitude of $\Delta\omega$ becomes larger, while an increase means that the magnitude becomes smaller up to the zero detuning, when it starts to increase again. In other words, an increase in $\Delta\omega$ corresponds to the frequency detuning variation towards positive values, while decrease corresponds to the variation towards more negative values. In Fig. 4.7, we

depict $\mathrm{d}n/\mathrm{d}t$–n phase plots corresponding to the hysteresis edges (red solid lines obtained for $\Delta\omega^{(1)}$ and $\Delta\omega^{(2)}$), and $\mathrm{d}n/\mathrm{d}t$–n phase plot corresponding to the initial, starting value $\Delta\omega = \Delta\omega_0$ (black solid line). First we consider the switching "down" direction [Fig. 4.7(a)]. If the slave laser is settled in the $n_{\mathrm{sp}}^{(1)}$ stationary point (open dot in Fig. 4.7), in order to switch "down", i.e., to switch to $n_{\mathrm{sp}}^{(3)}$ point (black dot in Fig. 4.7), one needs to make a sudden decrease towards more negative values of frequency detuning ($\Delta\omega = \Delta\omega - \delta\omega$), for which the slave laser has only one stationary state close to the free-running carrier threshold concentration n_{th}. This transitional $\mathrm{d}n/\mathrm{d}t$–n phase plot is depicted as blue arrowed line in Fig. 4.7(a). If this detuning variation is performed in sufficiently long time interval, upon restoring the original $\Delta\omega_0$, the slave laser will settle in the $n_{\mathrm{sp}}^{(3)}$ point corresponding to the original $\mathrm{d}n/\mathrm{d}t$–n phase plot. In other words, the magnitude of the frequency detuning variation ($\delta\omega$) has to be large enough to overcome the left hysteresis edge ($\Delta\omega_0 - \delta\omega < \Delta\omega^{(1)}$) and push the slave laser operating point from the upper branch towards the lower tail part of the loop. Provided that this variation lasted long enough to enable the slave laser to approach (or even reach) the lower tail part, upon restoring the initial value of the frequency detuning $\Delta\omega = \Delta\omega_0$, the laser will slide into the lower hysteresis branch, thus completing the switching process. The switching in the opposite direction needs an increase in the frequency detuning ($\Delta\omega = \Delta\omega_0 + \delta\omega$), which would push the laser from the lower hysteresis branch towards higher tail part of the loop, and eventually restore it in the upper branch, when $\Delta\omega$ is brought back to $\Delta\omega_0$. In terms of the $\mathrm{d}n/\mathrm{d}t$–n phase plots, the opposite switching direction is depicted in Fig. 4.7(b). The slave laser is settled in the $n_{\mathrm{sp}}^{(3)}$ point and increase of the frequency detuning (variation towards positive values of $\Delta\omega$), translates the laser onto a transitional phase plot depicted with blue arrows. However, the transitional steady-state n_{ts} in this case is larger than $n_{\mathrm{sp}}^{(1)}$ ($n_{\mathrm{ts}} > n_{\mathrm{sp}}^{(1)}$) [cf. Fig. 4.7(b)]. This transitional state corresponds to $n_{\mathrm{sp}}^{(1)}$ state of the $\mathrm{d}n/\mathrm{d}t$–n phase plot obtained for $\Delta\omega = \Delta\omega_0 + \delta\omega$. As the magnitude of $\delta\omega$ becomes larger, this state shifts more towards $n_{\mathrm{sp}}^{(3)}$, as discussed in the Section 3.4 [cf. Fig. 3.15]. As a consequence of this, at certain point, for sufficiently large $\delta\omega$, switching becomes impossible, i.e., slave laser stays in the initial $n_{\mathrm{sp}}^{(3)}$ state, since n_{ts} is closer to $n_{\mathrm{sp}}^{(3)}$ than $n_{\mathrm{sp}}^{(1)}$. In addition to this, this translation stationary point n_{ts} stands in front of the $n_{\mathrm{sp}}^{(1)}$ point i.e., it stands on the integration path, and prevents us from exploiting our method, since for this point $\mathrm{d}n/\mathrm{d}t = 0$. This implies that for our analytical model the desired final state is blocked by the transitional point, i.e., our model recongizes n_{ts} as the final switching state, making $n_{\mathrm{sp}}^{(1)}$ unreachable [138]. For this reason our analytical method is limited only to the case of switching "down", by frequency detuning decrease. However, there is a possibility to study the switching time in both directions by numerical means, which will be addressed later.

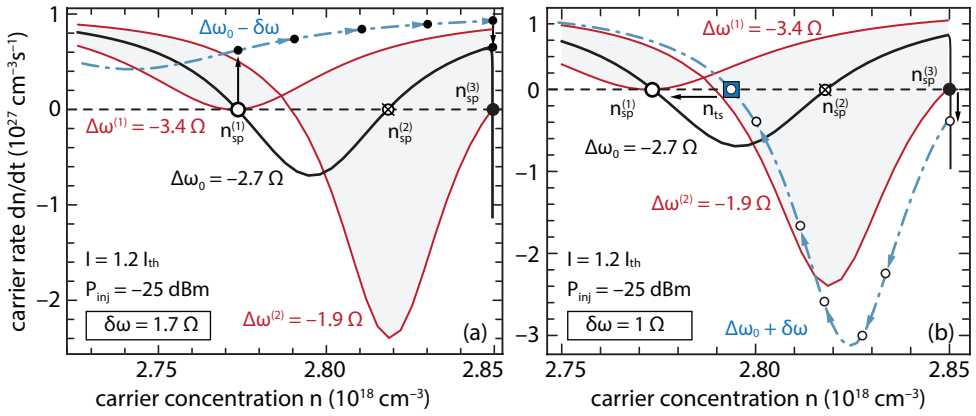

Figure 4.7: *dn/dt–n phase plots accounting only for the injection-locked mode $m = -5$ for $I = 1.2I_{th}$, $P_{inj} = -25$ dBm. Red solid lines correspond to the phase plots outlining the bistability region (gray area), i.e., correspond to the hysteresis edges $\Delta\omega^{(1)}$ and $\Delta\omega^{(2)}$. The phase plot corresponding to $\Delta\omega_0$ is obtained from the full scale MRE system. Blue arrowed lines represent the phase plots corresponding to switching detunings $\Delta\omega_0 \pm \delta\omega$. (a) Switching by frequency detuning decrease, i.e., switching from $n_{sp}^{(1)}$ to $n_{sp}^{(3)}$. (b) Switching by frequency detuning increase, i.e., switching from $n_{sp}^{(3)}$ to $n_{sp}^{(1)}$. The transitional point n_{ts} stands in front of the desired final state $n_{sp}^{(1)}$.*

Finally, in [140] we present and additional third switching mechanism conducted by the slave laser bias current variation, which relies on the fact that the hysteresis cycle in the slave laser output can be obtained by with respect to the bias current. Nevertheless, the preliminary analysis [140] shows the slave laser dynamic response to the bias current variation is much worse in comparison to the two presented mechanisms. However, this switching mechanism requires more deeper analysis, which will be in the scope of our further work.

4.2.4 Switching time and energy of injection-power switched IL FP-LDs

The calculation of the switching time follows the simple procedure. For some fixed value of bias current (in our simulations $I = 1.2I_{\text{th}}$), and fixed values of $\Delta\omega$ or P_{inj}, we calculate both the range of P_{inj}, and $\Delta\omega$, respectively, for which the bistability occurs, i.e., we calculate the injection power dependent hysteresis edges ($P_{\text{inj}}^{(1)}$ and $P_{\text{inj}}^{(2)}$), and frequency detuning dependent hysteresis edges ($\Delta\omega^{(1)}$ and $\Delta\omega^{(2)}$). These calculations are performed using the full scale model. Once hysteresis loops are obtained, depending on the hysteresis type, i.e., desired switching mechanism, we choose starting injection power on the injection power dependent hysteresis (P_0, switching with P_{inj} variation) or starting frequency detuning on the frequency detuning dependent hysteresis ($\Delta\omega_0$, switching by $\Delta\omega$ variation).

Since the switching with P_{inj} variation corresponds to the master laser amplitude variation, we also denote this switching mechanism as amplitude controlled switching. Similarly, as $\Delta\omega$ variation corresponds to the variation of the master laser phase, we also denote this mechanism as frequency or phase controlled switching. For the selected initial state, by the means of the full scale rate equation model, we find carrier concentrations for the switching states, $n_{\text{sp}}^{(1)}$ and $n_{\text{sp}}^{(3)}$ within the hysteresis loops. Stimulated photon generation rates, corresponding to these states, are given by $A_m(n_{\text{sp}}^{(1)}) = \Gamma v_{\text{g}} g(n_{\text{sp}}^{(1)}, \omega_m + \Delta\omega) - \tau_{\text{p}}^{-1}$, and $A_m(n_{\text{sp}}^{(3)}) = \Gamma v_{\text{g}} g(n_{\text{sp}}^{(3)}, \omega_m + \Delta\omega) - \tau_{\text{p}}^{-1}$. Depending on a desired direction of the switching, one of these states represents the initial state, and the other one is the final state.

Finally, by using (4.13), by setting S_{inj} to correspond to $P_{\text{inj}} = P_0 \pm \Delta P$ (in the case of amplitude controlled switching), or $\Delta\omega$ to correspond to $\Delta\omega = \Delta\omega_0 - \delta\omega$ (in the case of phase controlled switching), we calculate the switching time t_{if} with respect to the variation of injection power ΔP or frequency detuning $\delta\omega$. In this way we obtain the minimal required master laser variation time in order for the slave laser to switch between the stable states.

Finally, the hysteresis loops derived from the full scale rate equation model (2.21a) – (2.21d), slightly differ from the the loops that are derived directly from our simplified analytical model, i.e., the hysteresis edges which correspond to the full scale model, are somewhat different compared to the edges corresponding to (4.3) – (4.5). For that matter, in our calculations we adopt ΔP and $\delta\omega$ to be large enough in order to compensate for this small difference and to enable that analytical model remains on the safe side.

Apart from the calculation of the switching time, in the case of switching by injection power variation, we calculate the switching energy as:

$$E_{\text{if}} = \Delta P \cdot t_{\text{if}}. \tag{4.14}$$

In Fig. 4.8 we show switching times calculated from Eq. (4.13), for variation of the injection power (ΔP), in the case of injection in side-mode $m = -1$. We present switching times versus ΔP for different switching directions (switching "up", blue curves with upward arrows, and switching "down", red curves with downward arrows), and for different initial values of injection power P_0 and frequency detuning $\Delta\omega_0$. Fig. 4.8 shows that switching time in the case of switching up, can be order, or two orders of magnitude shorter in comparison to the switching down direction, i.e., there is a huge discrepancy between the switching directions. Switching time in both directions decreases with an increase in the injection power variation ΔP, and in the case of switching down it can be as low as few hundreds of ps (380 ps), while for switching up direction it can be even in order of 10 ps. Fig. 4.8 also shows that smaller negative values of the frequency detuning lead to shorter switching times in both directions, and that switching times increase with an

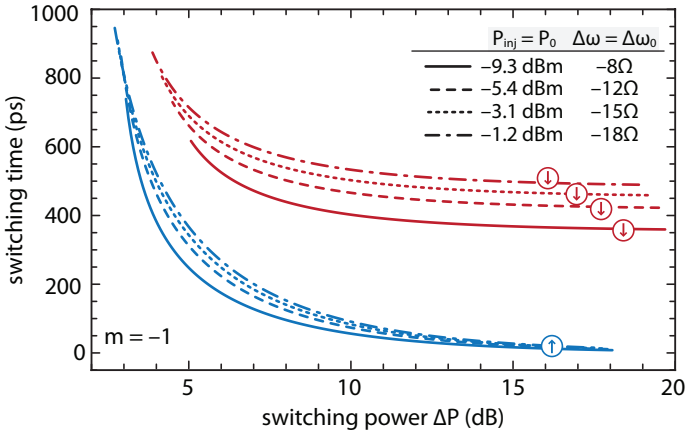

Figure 4.8: *Switching time with respect to injection power variation, ΔP for switching up (blue curves with upward arrows), and $-\Delta P$ for switching down direction (red curves with downward arrows) for injection into the side-mode $m = -1$. Legend in the figure gives the initial values of $P_{inj} = P_0$ and $\Delta\omega = \Delta\omega_0$.*

increase in the magnitude of negative frequency detuning. Actually, for less negative $\Delta\omega$, $n_{\mathrm{sp}}^{(1)}$ and $n_{\mathrm{sp}}^{(3)}$ are closer to each other [cf. Fig. 3.15], leading to a smaller $A_{\mathrm{f}} - A_{\mathrm{i}}$, and, due to a linear term in Eq. (4.13), switching time becomes shorter. For a transition $n_{\mathrm{sp}}^{(3)} \rightarrowtail n_{\mathrm{sp}}^{(1)}$, the linear term in Eq. (4.13) decreases the switching time, since $A_1 - A_3 < 0$. Because of the other two terms with positive contribution, switching time remains positive. For a transition in the opposite direction, the linear term in Eq. (4.13) has positive, while other two terms have negative contribution, which is reduced due to smaller K_4 and K_5, as a consequence of decreased P_{inj}. Thus, switching $n_{\mathrm{sp}}^{(1)} \rightarrowtail n_{\mathrm{sp}}^{(3)}$ lasts longer.

Fig. 4.9 depicts the corresponding switching energies. The switching down direction, although comprising higher switching times, here exhibits lower switching energies, since the injection power variation ΔP (dB) is much smaller in the direction of injection power decrease, compared to the direction of the injection power increase. As in the case of switching times, switching energies are lower for smaller negative frequency detuning, and for $\Delta\omega = -8\Omega$, the switching energies for both directions are in order of 10 fJ.

Figs. 4.10 and 4.11 show switching times and corresponding energies, respectively, for injection into side-mode $m = -10$. The higher order side-mode exhibits somewhat shorter minimal switching times, and switching energies in comparison to side-mode $m = -1$, however still retains discrepancy in terms of switching times for different switching directions. Smaller negative detunings again lead to shorter switching times, and consequently energies.

Finally, we present switching times for injection into modes $m = -1$ (green lines) and $m = -10$ (red lines) in the case of switching by frequency detuning variation, for only direction provided, i.e., switching down, Fig. 4.12. In this case, switching is faster for

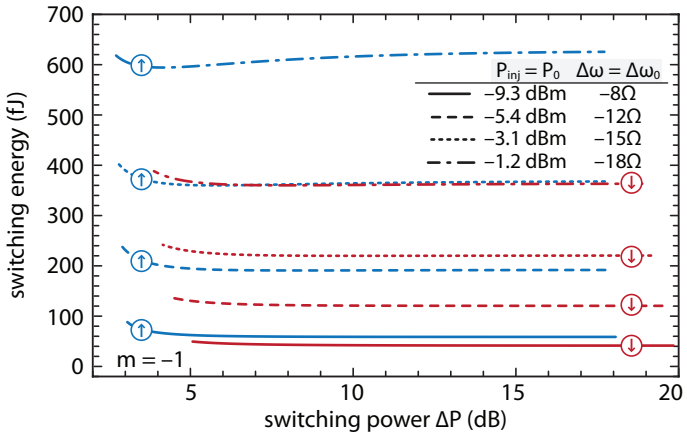

Figure 4.9: *Switching energy with respect to injection power variation, ΔP for switching up (blue curves with upward arrows), and $-\Delta P$ for switching down direction (red curves with downward arrows) for injection into the side-mode $m = -1$. Initial values of P_{inj} and $\Delta\omega$, correspond to the initial values P_0 and $\Delta\omega_0$ from Fig. 4.8.*

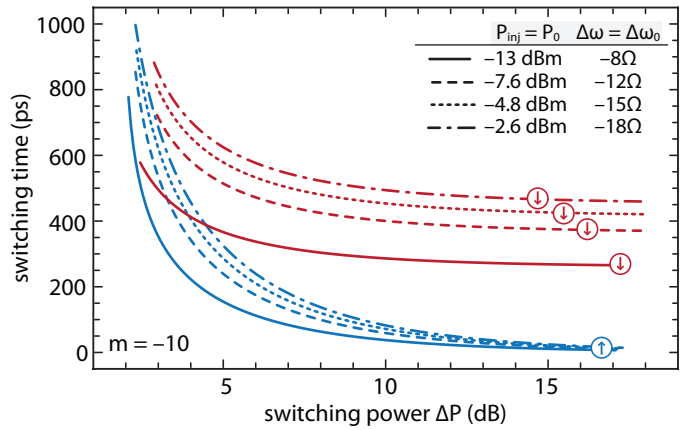

Figure 4.10: *Switching time with respect to injection power variation, ΔP for switching up (blue curves with upward arrows), and $-\Delta P$ for switching down direction (red curves with downward arrows) for injection into the side-mode $m = -10$. Legend in the figure gives the initial values of $P_{inj} = P_0$ and $\Delta\omega = \Delta\omega_0$.*

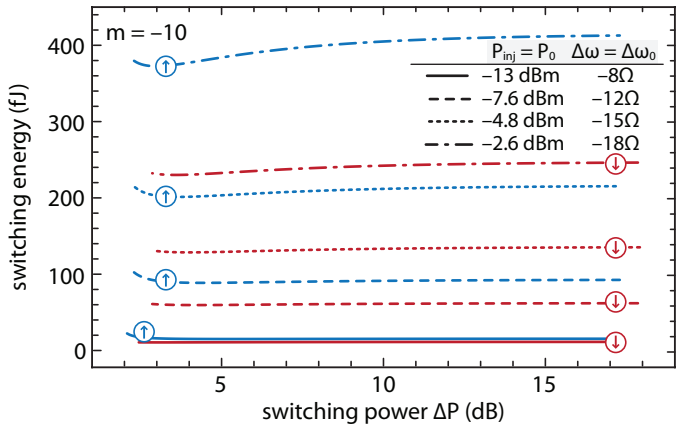

Figure 4.11: *Switching energy with respect to injection power variation, ΔP for switching up (blue curves with upward arrows), and $-\Delta P$ for switching down direction (red curves with downward arrows) for injection into the side-mode $m = -10$. Initial values of P_{inj} and $\Delta\omega$, correspond to the initial values P_0 and $\Delta\omega_0$ from Fig. 4.10.*

lower P_{inj} (solid lines in Fig. 4.12, for both $m = -1$ and $m = -10$), since the initial and the final states are closer. The minimal switching times for both modes are below 400 ps, though higher-order side-mode $m = -10$ has somewhat shorter minimal switching time around 350 ps.

It can be seen from equation (4.13) that an increase in Q_{net} can additionally reduce the switching time. In addition to this, our model shows that, for all other parameters fixed, an increase in α increases the hysteresis width and consequently changes the required magnitude of the injection parameter (ΔP or $\delta\omega$) needed for switching. Therefore, the further analysis presented in this section is focused on the influence of the linewidth enhancement factor α, and the number of the quantum wells N_{w} in the slave laser active region on the switching time between bistable states and the corresponding switching energy [139], since N_{w} defines the volume of the active region V, which contributes to Q_{net}. The linewidth enhancement factor α is of great importance for injection locking properties and, as shown in [115], affects the locking range and stability of the injection-locked lasers. Here we show that α also affects the width and the general profile of the hysteresis loops and thus, indirectly the time and energy of switching between the stable states. Although we can account for carrier-dependent refractive index variation spectrum [146], as well as dispersive linewidth enhancement factor, in this study we assume that the linewidth enhancement factor is non-dispersive and independent on the carrier density and gain spectrum. This assumption is motivated by the fact that the value of the linewidth enhancement factor affects only the injection-locked mode. For this particular mode, the frequency detuning is in the order of intermodal spacing, which is generally insufficient to cause significant variation of the linewidth enhancement factor as well as

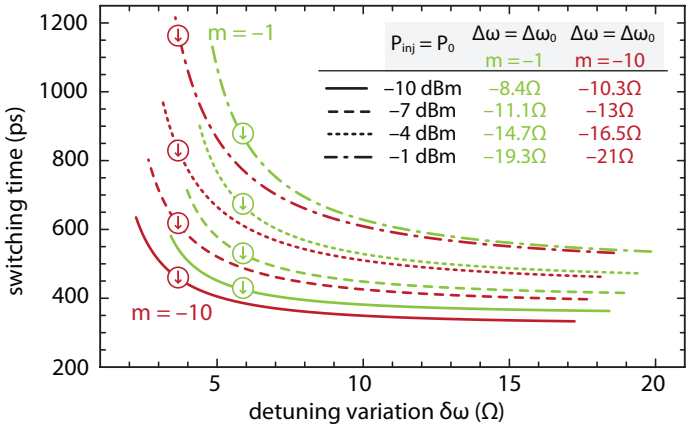

Figure 4.12: *Switching time with respect to frequency detuning variation, $-\delta\omega$ for switching for switching down direction for injection into the side-mode $m = -1$ (green curves) and $m = -10$ (red curves). Legend in the figure gives the initial values of $P_{inj} = P_0$ and $\Delta\omega = \Delta\omega_0$.*

the refractive index. Moreover, the switching between stable states corresponds to low variation of carrier density, which supports negligence of α factor variation with carrier density. Although different non-dispersive α factors generally correspond to different gain spectra, we investigate the influence of linewidth enhancement factor by using two fixed values of α for the same gain spectrum. This approach provides us better insight into shear influence of α factor on the hysteresis profiles and switching times between bistable states. Moreover, it can be seen that K_1 and K_2 (4.9a) – (4.9b), depend on α and directly affect the switching. On the other hand, the number of quantum wells N_w is directly proportional to the slave laser confinement factor Γ. Since ξ is inversely proportional to Γ, an increase in N_w leads to the decrease in ξ. The decrease in ξ does not directly affect the first term in Eq. (4.13) since its decrease is compensated by the increase in $A_m(n_{sp}^{(1)})$ and $A_m(n_{sp}^{(3)})$, which linearly increase with Γ. However, other two terms in Eq. (4.13) are proportional to ξ and decrease with it. The other parameters as K_1, K_2 and K_3 also depend on Γ, but affect Eq. (4.13) in a nontrivial way. In addition to this, the increase in N_w leads to the increase in the slave laser active volume, which causes the decrease in Q_{net}. On the other hand, the increase in Γ reduces the free-running threshold carrier concentration n_{th} and consequently the threshold current I_{th}. In the case of the fixed ratio of the applied and threshold current ($I/I_{th} = 1.2$), the applied current decreases as the threshold current, which together with the increase in V lead to an inevitable decrease in Q_{net}. Similarly as Γ, Q_{net} also affects K_1, K_2 and K_3 leading to complex dependence of t_{if} on the active region volume V.

According to the previous analysis, it is clear that α and N_w represent very important parameters in terms of injection-locked laser switching dynamics. In order to study their

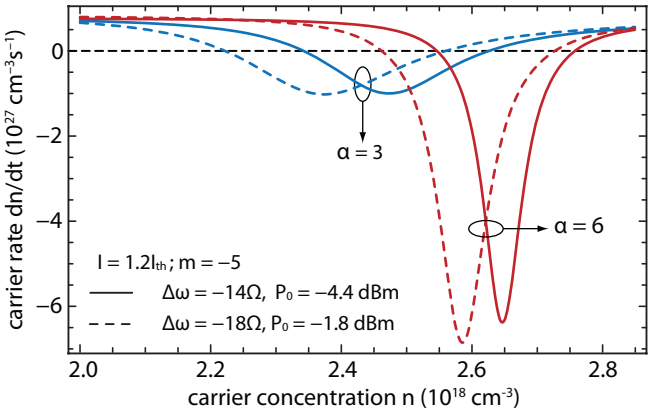

Figure 4.13: *dn/dt versus n phase plots in the case of $N_w = 3$, for two values of α (alpha = 3, blue lines, $\alpha = 6$, red lines) and $\Delta\omega$ ($\Delta\omega = -14\Omega$, solid lines, $\Delta\omega = -18\Omega$, dashed lines), with P_{inj} set to P_0 for a given value of α and $\Delta\omega$.*

influence, we investigate t_{if} and the corresponding E_{if} for two values for each of these parameters, providing four possible combinations for ordered pair $\{\alpha, N_{\text{w}}\}$. In the analysis we assume $\alpha = 3$ [107] or 6 [51] and $N_{\text{w}} = 3$ ($n_{\text{th}} = 2.85 \times 10^{18}$ cm^{-3}, $I_{\text{th}} = 8.16$ mA) or $N_{\text{w}} = 6$ ($n_{\text{th}} = 1.88 \times 10^{18}$ cm^{-3}, $I_{\text{th}} = 6.25$ mA). Apart from that, as we perform switching with P_{inj} variation, we analyze the influence of the frequency detuning on t_{if} and the corresponding E_{if}.

In order to get more detailed insight in the linewidth influence on the hysteresis loops, and consequently on switching time and energy, we study the dn/dt–n phase plots dependence on α. In Fig. 4.13 we present family of dn/dt–n phase plots obtained for two different values of α: $\alpha = 3$, blue lines, and $\alpha = 6$, red lines, and two values of $\Delta\omega$: $\Delta\omega = -14\Omega$, solid lines, and -18Ω, dashed lines. The phase plots are calculated by simplified model, using Eqs. (4.3) and (4.5), for $N_{\text{w}} = 3$ and $m = -5$. It can be seen that in phase plots obtained for higher values of α, $n_{\text{sp}}^{(1)}$ is shifted toward n_{th}, meaning that $n_{\text{sp}}^{(1)}$ and $n_{\text{sp}}^{(3)}$ states (which is close to n_{th}) are closer to each other, compared to the case of phase plots obtained for the lower values of α. The reason for this is related to Eq. (4.3) which changes more rapidly with the carrier concentration n for higher values of α. The rapid change occurs due to the reduced opening of the parabola in the denominator of Eq. (4.3), which becomes narrower with the increase in α. The proximity of the initial and the final stationary point for higher α leads to the reduction of the linear and other two terms in Eq. (4.13) and the corresponding switching time. In addition to this, the maximum of the denominator in Eq. (4.3) occurs for $A_m = 2\alpha\Delta\omega/(1 + \alpha^2)$. This means that for the more negative detuning $\Delta\omega$, A_m becomes more negative, which corresponds to the lower carrier concentration. Thus one can see that the phase plots for the same values of α, shift toward the lower carrier density as $\Delta\omega$ becomes more negative. As it can be seen in Fig.

4.13, for a fixed $\Delta\omega$ and P_{inj}, higher α leads to larger bending of the dn/dt–n phase plot, which means that bistability can be provided by lower P_{inj} than in the case of the lower linewidth enhancement factor α.

In Fig. 4.14 we present slave laser output photon density S_m as a function of P_{inj}, for different values of α, N_{w}, and $\Delta\omega$. The hysteresis loops in Fig. 4.14 are obtained from the full scale rate equation model, however, their analysis can be based on simplified equation (4.3). It can be seen that higher α leads to the lower S_m for higher branches of the hysteresis loops [cf. Fig. 4.14(a) and (c)]. Due to an increase in α, the denominator in Eq. (4.3) also increases. As shown in Fig. 4.13, higher α leads to larger $n_{\text{sp}}^{(1)}$, which corresponds to lower negative A_m, i.e. low $|A_m|$ (or gain defect). Although low, $|A_m|$ is not low enough to significantly reduce the increase of the denominator in Eq. (4.3), which consequently leads to a low output photon density S_m. However, a lower S_m is not a problem for bistability in the case of high linewidth, since the bending of the phase plot is significant, as previously discussed and shown in Fig. 4.13, so the intersection of the phase plot with n-axis is feasible. The range of P_{inj} for which hysteresis loops occur, and corresponding switching time and energy, are also dependent on the frequency detuning $\Delta\omega$. As discussed in the Sections 3.4 and 3.5, the more negative $\Delta\omega$ increases the denominator in Eq. (4.3), leading to lower S_m corresponding to the upper branch of the hysteresis loop. Low S_m may lead to an insufficient bending of the dn/dt–n phase plot and interruption of the bistability regime. The way to compensate for S_m decrease and to keep the slave laser in the bistability regime is to increase the injection photon density S_{inj}, i.e., P_{inj}. This means that more negative $\Delta\omega$ shifts the loops towards higher P_{inj} [c.f. Fig. 4.14(a) – (d)], resulting in the higher switching energy. Moreover, higher density of injected photons in the case of more negative $\Delta\omega$ means that $n_{\text{sp}}^{(1)}$ is shifted towards lower values, thus $n_{\text{sp}}^{(1)}$ and $n_{\text{sp}}^{(3)}$ are more separated (c.f. Fig. 4.13) leading to larger difference $A_{\text{f}} - A_{\text{i}}$. This difference increases all three terms in Eq. (4.13), which leads to a longer switching time.

An increase in N_{w} and consequently in V and Γ, lowers the value of the gain threshold, since the gain threshold is given by the equation (2.16). This further leads to the decreased value of n_{th}, and consequently to the smaller number of supported modes, since the threshold gain curve is lowered (cf. Fig. 3.2(b)). Since the slave laser operates at lower carrier concentrations, the output photon densities of all modes are lower, while the injection locking needs lower P_{inj} to achieve locking of a particular side-mode. In terms of the laser bistability, this means that hysteresis loops, obtained for higher N_{w}, have lower S_m densities, and that the loops are shifted toward lower values of injection power [cf. Fig. 4.14(b) and (d)]. Since hysteresis loops appear at lower values of P_{inj}, it can be expected that less energy has to be employed in order to switch between the hys-

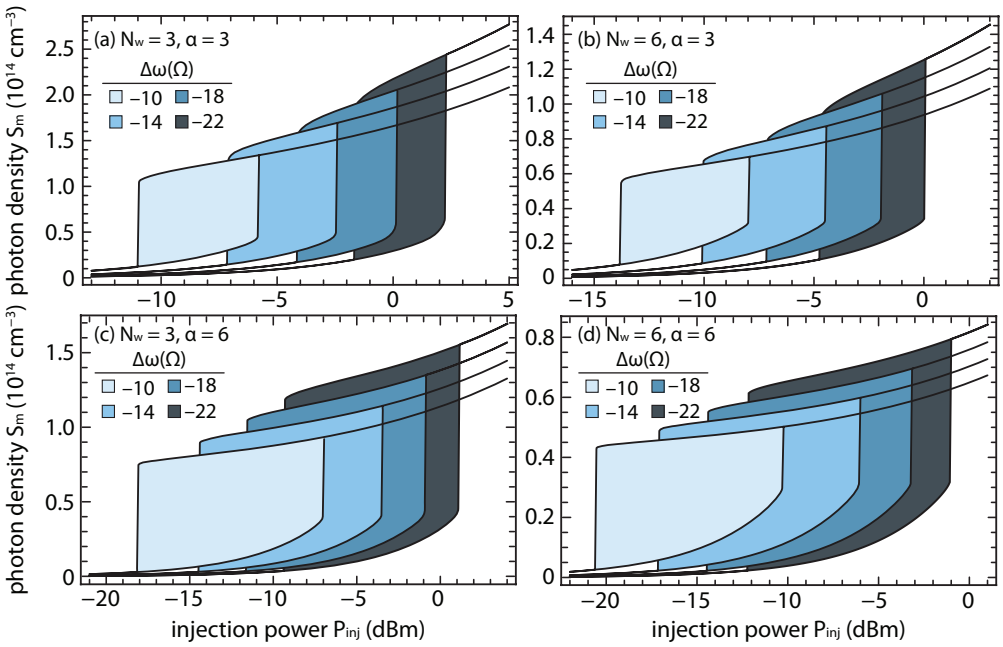

Figure 4.14: *Photon density S_m versus P_{inj} hysteresis loops for different values of $\Delta\omega$ (-22Ω, -18Ω,-14Ω, and -10Ω) for $\{N_w, \alpha\}$ taking values (a) $\{3, 3\}$, (b) $\{6, 3\}$, (c) $\{3, 6\}$ and (d) $\{6, 6\}$.*

teresis branches. In addition to this, due to the lower n_{th}, the threshold current is lower. For a fixed I/I_{th} ratio, the decrease in the threshold current and the increase in the active region volume lead to the lower well pumping, i.e. decrease in $I/(qV)$ term in Eq. (4.5). The lower bias current I, in combination with smaller carrier concentration for higher N_{w}, lowers the value of the effective rate for the carrier injection $Q_{\text{net}} = I/(qV) - Q(n_{\text{x}})$ in Eq. (4.7). This directly leads to longer switching time, since it dominantly increases the value of the integral given by Eq. (4.13).

In Fig. 4.15 we present calculated switching time [Fig. 4.15(a) and (b)] and energy [Fig. 4.15(c) and (d)] versus the variation of injection power (ΔP), measured from the starting injection power P_0, for relatively low adopted value of $\alpha = 3$ and two different numbers of quantum wells, $N_{\text{w}} = 3$ and $N_{\text{w}} = 6$. Fig. 4.15 shows the switching time and energy in the case of power increase (switching up, i.e., switching from $n_{\text{sp}}^{(3)}$ to $n_{\text{sp}}^{(1)}$, blue lines with upward facing arrow) and power decrease (switching down direction, i.e., switching from $n_{\text{sp}}^{(1)}$ to $n_{\text{sp}}^{(3)}$, red lines with downward facing arrow) for different values of $\Delta\omega$.

It should be mentioned that the same variation of the injection power, ΔP, expressed in dB, corresponds to different values of power variation expressed in SI units for switching in opposite directions. In other words, $+\Delta P$ represents larger power variation then $-\Delta P$, assuming the same P_0. Moreover, a decrease in P_0 leads to even smaller power variations

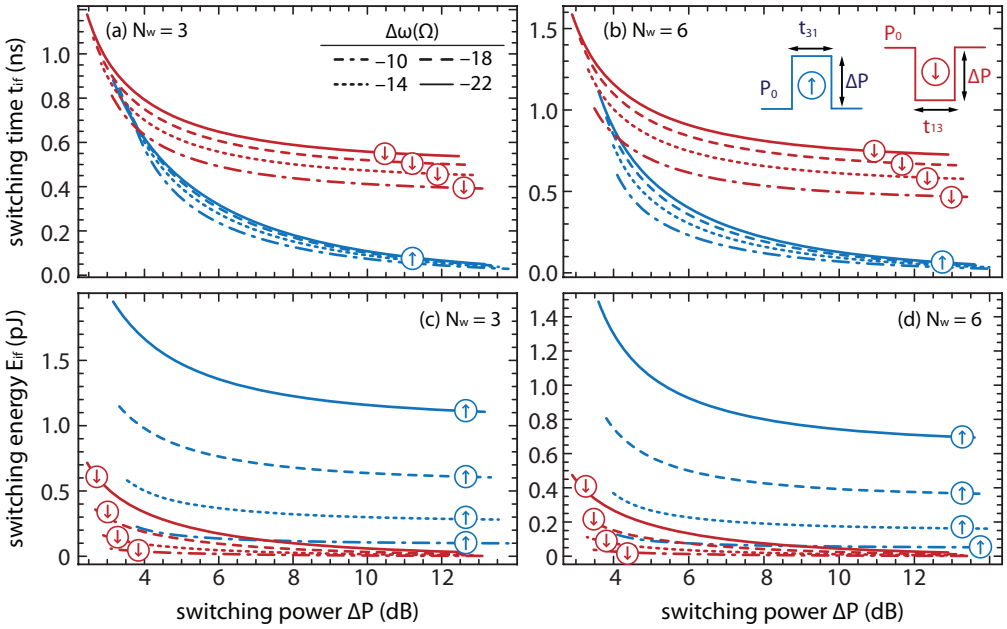

Figure 4.15: *Switching time for (a) $N_w = 3$, and (b) $N_w = 6$, and switching energy for (c) $N_w = 3$, and (d) $N_w = 6$, for $\alpha = 3$ and different values of $\Delta\omega$ in cases of power increase (switching from $n_{sp}^{(3)}$ to $n_{sp}^{(1)}$; curves with arrow up) and power decrease (switching from $n_{sp}^{(1)}$ to $n_{sp}^{(3)}$; curves with arrow down).*

for the fixed ΔP and usually means lower switching energy. In calculation of t_{if} we apply expression (4.13), and calculate E_{if} according to (4.14). It can be seen that switching from $n_{\mathrm{sp}}^{(1)}$ to $n_{\mathrm{sp}}^{(3)}$ lasts longer than the reverse process, but due to significantly lower P_{inj} the switching down direction needs lower switching energy. With an increase in N_{w}, switching time increases, as it can be seen by comparing Fig. 4.15(a) and (b). However, the switching energy becomes lower due to the decrease in the effective rate of the carrier injection Q_{net} [cf. Fig. 4.15(c) and (d)]. In addition to this, more negative $\Delta\omega$, as we already explained, leads to larger separation of the stationary points, and consequently to longer switching time and higher switching energy. In the case of switching by P_{inj} decrease (red lines with downward facing arrow), switching energies for higher values of N_{w} and less negative $\Delta\omega$ can be very low, in the order of 10 fJ [e.g., switching energy for $\Delta\omega = -10\Omega$ in Fig. 4.15(d)], though corresponding switching times are in the order of 0.5 ns [switching time for $\Delta\omega = -10\Omega$, dash-dotted line in Fig. 4.15(c)].

In Fig. 4.16 we present calculated switching time and corresponding energy for $\alpha = 6$ in cases of $N_{\mathrm{w}} = 3$ [Fig. 4.16(a) and (c)] and $N_{\mathrm{w}} = 6$ [Fig. 4.16(b) and (d)]. Fig. 4.16 clearly shows lower switching time in comparison with Fig. 4.15, as predicted in the previous discussion. However, this comparison does not take into account the width of the hysteresis loops, which are wider for larger values of the linewidth [cf. Fig. 4.14]. In other words, ΔP incorporates the power variation needed to exceed the hysteresis edge,

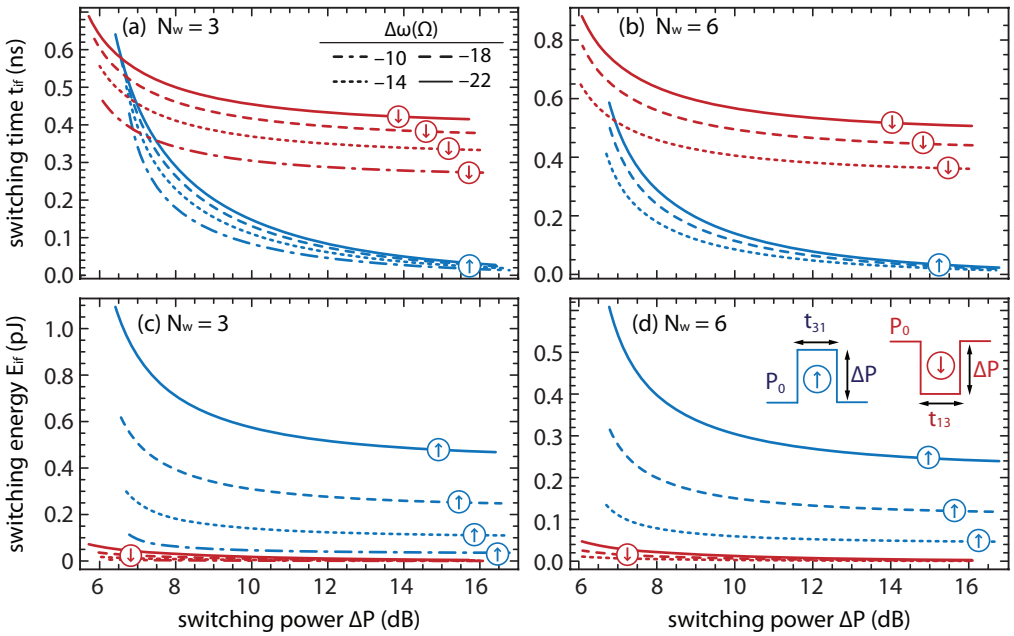

Figure 4.16: *Switching time for (a) $N_w = 3$, and (b) $N_w = 6$, and switching energy for (c) $N_w = 3$, and (d) $N_w = 6$, for $\alpha = 6$ and different values of $\Delta\omega$ in cases of power increase (switching from $n_{sp}^{(3)}$ to $n_{sp}^{(1)}$; curves with upward facing arrow) and power decrease (switching from $n_{sp}^{(1)}$ to $n_{sp}^{(3)}$; curves with downward facing arrow).*

which is higher for larger values of α. In order to provide a fair comparison for $\alpha = 3$ and $\alpha = 6$, we can define ΔP as the power variation counted from the hysteresis edge, rather than from its middle, and compare switching times for the same level of power variation ΔP to learn that switching times for $\alpha = 6$ are indeed shorter than the ones for $\alpha = 3$. In addition to this, an increase in α leads to a more energy efficient switching [Fig. 4.16(c) and (d) compared to Fig. 4.15(c) and (d)]. The reason for this lies in the shorter switching time, and the fact that hysteresis loops are shifted toward lower P_{inj}. In the case of $\alpha = 6$, $N_{\text{w}} = 6$, and $\Delta\omega = -10\Omega$ [Fig. 4.14(d)], small signal stability analysis [115] shows that $n_{\text{sp}}^{(3)}$ branch of the hysteresis loop is not stable, thus the switching between $n_{\text{sp}}^{(1)}$ and $n_{\text{sp}}^{(3)}$ does not occur, which is why there is no dot-dashed line in Fig. 4.16(b) and (d). Our model shows that for sufficiently large ΔP, with high values of α, switching time in the switching up direction can be very short, even shorter than 10 ps [blue dot-dashed line in Fig. 4.16(a)]. However, in such cases, due to large ΔP, switching energy is high, in the order of 100 fJ [blue dot-dashed line in Fig. 4.16(c)]. In the process of switching with power decrease, due to low values of P_{inj}, switching energy can be even lower than 1 fJ [cf. Fig. 4.16(c) and (d)], but on the account of longer switching time which is in the order of 0.4 ns [cf. Fig. 4.16(a) and (b)].

Presented analysis, based on the simple analytical model, shows that higher values of linewidth enhancement factor α reduce switching time and switching energy, since

higher values of α bring switching states closer with respect to their carrier concentrations. Moreover, hysteresis loops are shifted toward lower values of P_{inj} making switching more energy efficient. On the other hand, an increase in the active region volume can also lead to lower switching energy, since the laser gain threshold is lower. However, this causes the switching time to become longer, as a result of the lower value of the effective rate of carrier injection, which dominantly increases the switching time. Switching times and energies are also frequency detuning dependent, and shorter switching times, as well as lower switching energies are obtained for smaller magnitude negative $\Delta\omega$. Finally, switching times and energies are strongly dependent on the switching directions, i.e., regardless of the values of α and N_{w}, there is a huge discrepancy between the switching directions in terms of time and energy. The switching up direction is performed significantly (order of magnitude) faster, though needs higher (order of magnitude) energy in comparison to the switching down direction.

4.3 Switching in IL FP-LDs - a numerical approach

Analytical model, derived in the previous section, offers a simple and lightweight method to describe and analyze switching processes in injection-locked lasers. However, it lacks the possibility to fully describe the phase controlled switching, and fails to provide full insight in the switching trajectories of the slave laser. Moreover, the whole model relies on several approximations of the exact model of injection-locked lasers. In order to fully and exactly describe the dynamics, i.e., switching characteristic of a injection-locked Fabry-Pérot semiconductor laser, we study transitions between the stable stationary states of injection-locked laser, using the system of coupled nonlinear differential equations in its full scale, (2.21a) – (2.21d) [116]. This system of nonlinear differential equations is solved by means of the adaptive step size Runge-Kutta method [143] in a time span long enough to ensure that slave laser reaches the steady-state. Here, we exploit this exact numerical method to study the switching by frequency detuning variation. For that matter, during the simulations, i.e., in (2.21a) – (2.21d), we keep I and P_{inj} fixed, while the time-dependent input parameter is the frequency detuning $\Delta\omega$. For desired initial state, we set the initial conditions which fix the values of the carrier concentration n, photon densities S_j, and injection-locked phase θ_m to the values which correspond to the starting points, either $n_{\text{sp}}^{(i)} = n_{\text{sp}}^{(1)}$, or $n_{\text{sp}}^{(i)} = n_{\text{sp}}^{(3)}$, i.e., $n(t = 0) = n_{\text{sp}}^{(i)}$, $S_j(t = 0) = S_j(n_{\text{sp}}^{(i)})$, $S_m(t = 0) = S_m(n_{\text{sp}}^{(i)})$, and $\theta_m(t = 0) = \theta_m(n_{\text{sp}}^{(i)})$. For different values of the frequency detuning variation magnitude $\delta\omega$, and different durations of this variation, we investigate the slave laser system values $n(t)$, $S_j(t)$, $S_m(t)$, and $\theta_m(t)$, and analyze if those values correspond to the other stationary, i.e., the final state. In particular, as the most relevant parameters of the

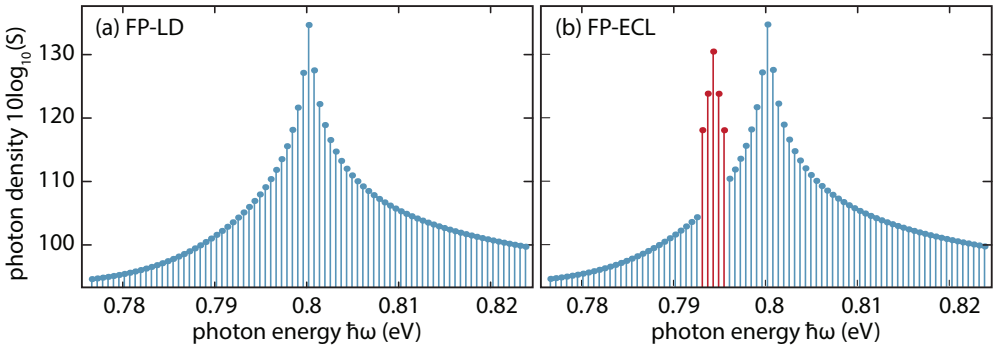

Figure 4.17: *The free-running spectrum of the modes in the (a) FP-LD and (b) FP-ECL.*

slave laser output, we analyze whether output photon density of the injection-locked mode (S_m), and corresponding phase (θ_m) reached the desired final state.

The analysis of the bistability controlled by the $\Delta\omega$ variation, as a first step requires the calculation of the frequency detuning dependent hysteresis loops for injection-locked Fabry-Pérot laser diode, which we calculate as in Section 3.5. However, apart from the standard Fabry-Pérot laser diode, we also consider the switching dynamics of a Fabry-Pérot with external cavity, as it may improve the switching characteristics [47]. In Fig. 4.17 we present free-running mode spectra for the standard Fabry-Pérot laser diode (FP-LD) [Fig. 4.17(a)], with a single dominant mode corresponding to the gain maximum, and for Fabry-Pérot external cavity laser diode (FP-ECL) [Fig. 4.17(b)] which we phenomenologically model by setting the higher τ_p for the cluster of side-modes around the side-mode $m = -10$. The mode spectra depict the intensity of the longitudinal modes in the logarithmic scale ($10\log_{10}(S_j)$). In the case of FP-ECL, since the cluster of the modes around side-mode $m = -10$ have higher τ_p, i.e., lower resonator losses, the intensities of those modes are increased, so that the side-mode $m = -10$ almost levels with the dominant mode $j = 0$. The photon concentration of the dominant mode in the free-running regime for standard Fabry-Pérot laser diode is close to 3×10^{13} cm^{-3}, while the mode $m = -10$ it is roughly 30 dB lower, yielding approximately 4×10^{10} cm^{-3}. In case of the FP-ECL and the free-running regime, the photon density of the dominant mode is the same as for the Fabry-Pérot laser diode, while the mode $m = -10$ reaches significantly higher photon densities in comparison to the standard FP-LD, just slightly below the dominant mode values.

In Fig. 4.18 we present the hysteresis loops in the case of FP-LD corresponding to the photon density S_m [solid lines in Fig. 4.18(a)], and the slave and the master laser phase difference, θ_m [solid lines in Fig. 4.18(b)], both for the injection into the side mode $m = -10$. Apart from this, we present the hysteresis loops obtained for FP-ECL [dashed lines in Figs. 4.18(a) and (b)], which are shifted to more positive values of the frequency

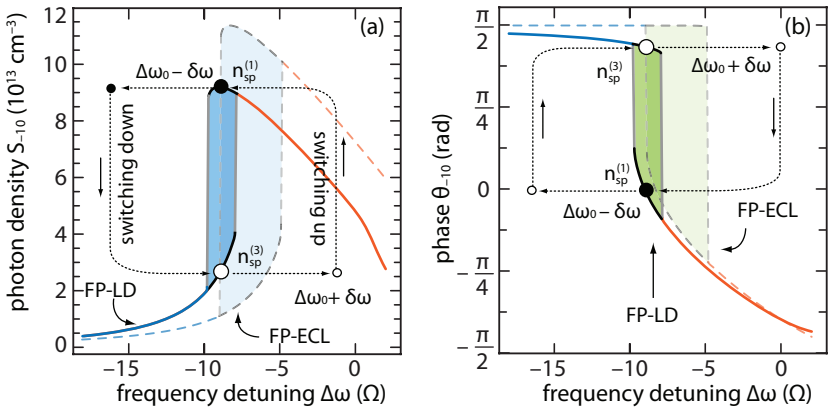

Figure 4.18: *Hysteresis plot for (a) S_m and (b) θ_m for injection-locked mode $m = -10$ in case of the standard FP-LD (solid lines) and FP-ECL (dashed lines). Dot-arrowed lines show the actual $\Delta\omega$ variation and the direction of circulation around the hysteresis.*

detuning $\Delta\omega$. In order to provide a clear physical insight into the hystereses origins, in Fig. 4.19 we present the corresponding dn/dt–n phase plots, with all the relevant switching trajectories [116].

The two phase plots, as indicated in Fig. 4.19, are obtained from the transient analysis and are related to the transient response. These two phase plots will be discussed later, at this moment we focus on the plots obtained from the stationary analysis. All other curves in Figs. 4.19(a) and (b) are calculated for $I = 1.2I_{\text{th}}$ and $P_{\text{inj}} = -12$ dBm, i.e., $S_{\text{inj}} = 6.55 \times 10^{12}$ cm^{-3}, under the assumption of stationary photon densities, as done in the Section 3.4, and their profiles depend only on $\Delta\omega$. In this case, each intersection of these phase plots with dn/dt = 0, represents one stationary point, and as explained earlier, the intersection with positive slope of dn/dt–n curve corresponds to the unstable, repelling stationary point $n_{\text{sp}}^{(2)}$, while those with the negative slope ($n_{\text{sp}}^{(1)}$ or $n_{\text{sp}}^{(3)}$) correspond to the attractive, dynamically stable stationary points. The thick solid line, corresponding to $\Delta\omega_0$, stands for the phase plot corresponding to the middle of the hysteresis loop, which is defined with two critical values of $\Delta\omega$, the left hysteresis boundary $\Delta\omega_{\text{L}}$, and right hysteresis boundary $\Delta\omega_{\text{R}}$, both in the cases of FP-LD [Fig. 4.19(a)] or FP-ECL [Fig. 4.19(b)]. The thin grey lines in Figs. 4.19(a) and (b) correspond to these limiting values of $\Delta\omega$. Thus, the shaded grey areas in the Figs. 4.19(a) and (b) correspond to the ranges of $\Delta\omega$ in which bistability occurs, i.e., to the domains of the hysteresis loops, depicted in Figs. 4.18(a) and (b). For $\Delta\omega$ larger than $\Delta\omega_{\text{R}}$ (less negative), or smaller than $\Delta\omega_{\text{L}}$ (more negative), phase plots denoted with $\Delta\omega_{\text{ER}}$ and $\Delta\omega_{\text{EL}}$ [arrowed dash-dot lines in Figs. 4.19(a) and (b)], exhibit only one stable stationary point, thus bistability does not exist. In both Figs. 4.18(a) and (b), solid lines stand for hysteresis loops corresponding to FP-LD, i.e., to the dn/dt–n phase plots from Fig. 4.19(a), while dashed lines stand for the

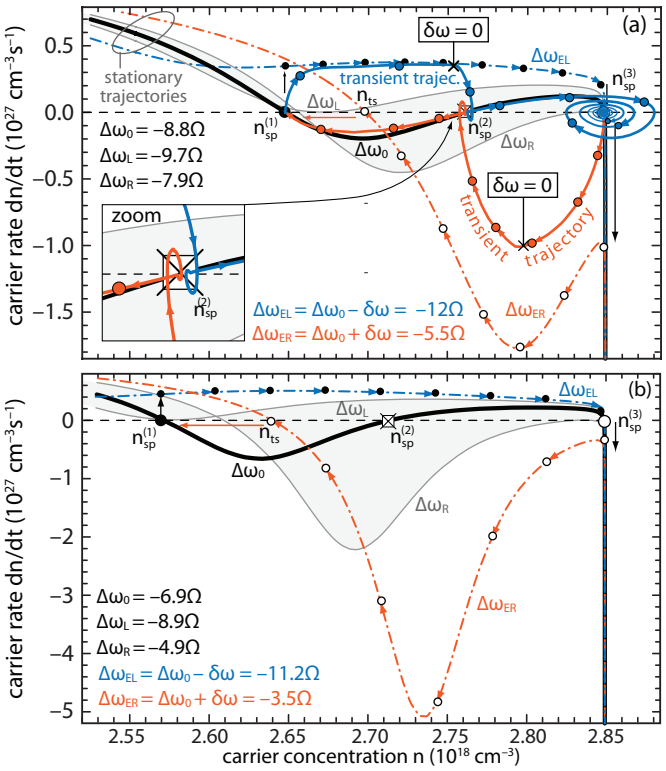

Figure 4.19: *(a) Phase plots for the standard FP-LD corresponding to the stationary photon density: thick solid line for $\Delta\omega = \Delta\omega_0$ corresponds to a phase plot comprising 3 stationary points ($n_{sp}^{(1)}$, $n_{sp}^{(2)}$, and $n_{sp}^{(3)}$); thin solid grey lines stand for the phase plots corresponding to $\Delta\omega = \Delta\omega_L$ and $\Delta\omega = \Delta\omega_R$, representing the left and right hysteresis edge, respectively; dash-dot lines (partially with arrows) correspond to the phase plots obtained for detuning during variation, i.e., $\Delta\omega_0 - \delta\omega = \Delta\omega_{EL}$ and $\Delta\omega_0 + \delta\omega = \Delta\omega_{ER}$. These phase plots provide a single stationary point ($n_{sp}^{(3)}$ and n_{ts}, respectively). Solid arrowed lines depict the transient phase plots, and the position in the phase plot for which the master laser turns off detuning variation $\delta\omega$. The grey area covers the loci of phase plots for stationary photon density, whose stable stationary points correspond to the branches of hysteresis for standard FP-LD in Fig. 4.18(a). Zoom depicts the transient phase trajectory in the vicinity of the unstable point $n_{sp}^{(2)}$.(b) Same as (a) but for the FP-ECL. In this case, the transient phase plots are not shown.*

hysteresis loops obtained for FP-ECL, Fig. 4.19(b). Figs. 4.18(a) and (b) show that the hysteresis loop for the FP-ECL is significantly wider than for the standard FP-LD. The higher photon lifetime corresponds to a smaller gain defect for the injection-locked mode, which provides the same laser emission for smaller carrier density, with respect to the FP-LD. Therefore, FP-ECL exhibits a lower carrier density value for $n_{sp}^{(1)}$ state and a larger range of $\Delta\omega$ for which the bistability can be achieved. The wider range of $\Delta\omega$ enables a more stable range of the bistability and gives more freedom in selecting the switching starting point on the hysteresis loop.

As previously discussed in the Section 3.5, in the case of output photon density hysteresis loop [Fig. 4.18(a)], the lower hysteresis branch with low injection-locked mode photon density corresponds to the $n_{sp}^{(3)}$ stationary point, while the upper, high power output, hysteresis branch corresponds to $n_{sp}^{(1)}$ stationary point. On the contrary, the phase, θ_{-10} hysteresis loop exhibits the opposite behavior, as shown in Fig. 4.18(b). The range of $\Delta\omega$ for which the bistability occurs ($\Delta\omega_L < \Delta\omega < \Delta\omega_R$) is shaded in Figs. 4.18(a) and (b), and corresponds to the shaded area between two critical phase plots, as depicted in Figs. 4.19(a) and (b). The hystereses vertical edges correspond to $\Delta\omega_L$ and $\Delta\omega_R$, while beyond this range, the loci of S_{-10} and θ_{-10} have only one branch, which is either extension of the upper or the lower hysteresis branch. Each locus on these extended branches corresponds to a line for which $\Delta\omega > \Delta\omega_R$ or $\Delta\omega < \Delta\omega_L$ [e.g. arrowed dash-dot lines in Figs. 4.19(a) and (b), for which $\Delta\omega_{ER} > \Delta\omega_R$ or $\Delta\omega_{EL} < \Delta\omega_L$].

The circulation around the hysteresis loop is in case of the photon density counterclockwise, while in case of the phase difference, it is clockwise. The circulation can be essentially divided in two steps: switching from the stationary state $n_{sp}^{(1)}$ to $n_{sp}^{(3)}$ (cf. Figs. 4.18(a) and (b), solid and open dot, respectively), and vice versa, from $n_{sp}^{(3)}$ to $n_{sp}^{(1)}$. Although the position of the stationary points corresponding to $n_{sp}^{(1)}$ and $n_{sp}^{(3)}$ is reversed on the photon density and the phase hystereses [cf. Figs. 4.18(a) and (b)], in choosing the switching direction we refer to the photon density hysteresis loop, and, as previously, denote the transition from $n_{sp}^{(1)}$ to $n_{sp}^{(3)}$ as "switching down", while the opposite transition, from $n_{sp}^{(3)}$ to $n_{sp}^{(1)}$, is denoted as "switching up". For switching down it is necessary to push detuning toward more negative values $\Delta\omega < \Delta\omega_L$, beyond the hysteresis edges: in the example shown in Figs. 4.19(a) and (b), detuning $\Delta\omega$ is pushed toward $\Delta\omega_{EL} < \Delta\omega_L$. This new detuning should correspond to the phase plot which has only one stationary point, in this case the one close to $n_{sp}^{(3)}$ [arrowed dash dot line for $\Delta\omega_{EL}$ in Figs. 4.19(a) and (b)], which will force the slave laser to migrate from the $n_{sp}^{(1)}$ to the $n_{sp}^{(3)}$ state. The necessary variation of detuning $\delta\omega > \Delta\omega_0 - \Delta\omega_L > 0$ is such that $\Delta\omega_{EL} = \Delta\omega_0 - \delta\omega$. If $\Delta\omega_{EL}$ is kept fixed for prolonged time, the slave laser may abandon the bistability region and start transition toward the only existing stationary point (close to $n_{sp}^{(3)}$). If $\delta\omega$ provided by the

master laser is switched off after a sufficiently long time, the slave laser will settle in $n_{sp}^{(3)}$. Otherwise, if the duration of the detuning shift is not sufficiently long, the slave laser will slide back to its initial state, $n_{sp}^{(1)}$.

However, as explained in the previous section, the switching in the reversed direction, from $n_{sp}^{(3)}$ to $n_{sp}^{(1)}$ is not straightforward as the previous one. As discussed, switching up requires $\delta\omega$ which can eliminate the starting point $n_{sp}^{(3)}$, leaving only one stationary point located beyond the right hysteresis edge in Figs. 4.18(a) and (b), i.e., point n_{ts}, denoted in Figs. 4.19(a) and (b). In Figs. 4.19(a) and (b), this stationary point belongs to the phase plot for $\Delta\omega > \Delta\omega_R$, in our example to $\Delta\omega_{ER} > \Delta\omega_R$ (arrowed dash-dot line). In this case $\Delta\omega_{ER} = \Delta\omega_0 + \delta\omega$, where $\delta\omega > \Delta\omega_R - \Delta\omega_0 > 0$. However, this single stationary point, n_{ts}, is far away from $n_{sp}^{(1)}$ corresponding to the bistability region. If $\delta\omega$ is kept fixed indefinitely, the trajectory of the transition will end up in this single intermediate state n_{ts}, somewhere between $n_{sp}^{(3)}$ and $n_{sp}^{(1)}$, and beyond the hysteresis loops. However, if $\delta\omega$ is switched on for finite, but sufficiently long time, the trajectory of the transition will approach n_{ts} and after $\delta\omega$ is switched off, the trajectory will turn toward the $n_{sp}^{(1)}$ state and complete the switching. As explained earlier, in order to do so, n_{ts} has to be closer to the $n_{sp}^{(1)}$ point than to $n_{sp}^{(3)}$ point, or else the laser will stay in the initial $n_{sp}^{(3)}$ point. For higher magnitudes of $\delta\omega$, the n_{ts} point shifts towards higher carrier concentration, i.e., it becomes closer to the $n_{sp}^{(3)}$ point, and switching fails. In our analytical attempt to study the switching up, from $n_{sp}^{(3)}$ to $n_{sp}^{(1)}$, the intermediate state has been the major obstacle for successful implementation of the analytical model in Section 4.2.3 [138]. Here, the numerical solving of the rate equations provides the possibility to successfully simulate the switching from $n_{sp}^{(3)}$ to $n_{sp}^{(1)}$.

The concept of the switching transition presented above is developed using the phase plots derived under the assumption of the stationary photon density, as in the previous section. It can be expected that such approach may help to roughly predict and grasp the transient trajectory of the switching. However, the exact numerical simulations of the transitions in both switching directions provide the transient phase plots [solid arrowed lines in Fig. 4.19(a)], which significantly differ from those presumed using the phase plots based on the stationary photon density. The transient phase plots clearly show that the switching between the stable states can be successfully completed with the assistance of the unstable repelling stationary point $n_{sp}^{(2)}$, which is a surprising result. In the switching down process ($n_{sp}^{(1)}$ to $n_{sp}^{(3)}$ switching), the switching trajectory follows the stationary trajectory (phase plot corresponding to $\Delta\omega_{EL} = \Delta\omega_0 - \delta\omega$ up to the vicinity of the $n_{sp}^{(2)}$ point [cf. Fig. 4.19(a)]. However, the $n_{sp}^{(2)}$ point first attracts, and then repels the trajectory, acting as a "slingshot" [cf. inset in Fig. 4.19(a)]. After this "phase loop" around $n_{sp}^{(2)}$ point, the trajectory ends with a characteristic spiral inward, which corresponds to dynamic regime of relaxation oscillations of the slave laser, which is pronounced at the

$n_{sp}^{(3)}$ point, due to its vicinity to n_{th}. This transient trajectory is obtained for the minimal duration of the $\Delta\omega$ variation which leads to the successful switching, which in this case yields 360 ps. The point in the trajectory, which corresponds to the time moment in which $\Delta\omega$ restores its initial value $\Delta\omega_0$ is denoted with $\delta\omega = 0$ in the Fig. 4.19(a), which is actually in the vicinity of $n_{sp}^{(2)}$ point. However, it can be expected that, if the detuning variation, i.e., the variation of the master laser phase were prolonged, the slave laser may surpass the $n_{sp}^{(2)}$ point in the switching process, and thus avoid the "phase loop". The exact switching trajectory in the opposite direction ($n_{sp}^{(3)}$ to $n_{sp}^{(1)}$) also provides surprising results. Again, the transient switching trajectory is obtained for minimal duration of the master laser variation, which now yields merely 100 ps. The master laser variation ends in the point denoted with $\delta\omega = 0$ in the Fig. 4.19(a). The transient switching trajectory significantly differs from the one predicted by the stationary analysis [cf. Fig. 4.19(a)], and instead of approaching transitional stationary state n_{ts}, the slave laser again exhibits a "phase loop" around the unstable $n_{sp}^{(2)}$ point. In this case, the slave laser enters the final, $n_{sp}^{(1)}$ state, without the spiral inward, since this point is the consequence of the injection locking, which suppresses the relaxation oscillations of the laser. For the particular case depicted in the Fig. 4.19(c), minimal switching times, i.e., minimal durations of master laser switching, are considerably different with respect to the switching direction, as predicted by our analytical method in the previous section.

4.3.1 Switching time of the master laser

In order to optimize switching characteristics of injection-locked Fabry-Pérot semiconductor laser, we investigate two separate optimization routes. The first one considers methods to obtain the shortest time of the master laser variation, sufficient to force the switching between the states of the slave laser, i.e., we apply and investigate various techniques to reduce the Δt_{ML} to the minimum ($\Delta t_{ML,min}$), still sufficient to provide the switching of the slave laser. Although higher values of the bias current may provide somewhat faster switching, at these values the range of the injection parameters (P_{inj} and $\Delta\omega$) in which the slave laser is dynamically stable, becomes narrower. In order to provide wider range of the slave laser bistability, we consider switching at lower bias currents $I = 1.2I_{th}$. In the range of moderate injection powers, i.e., in the range of photon density from 10^{12} cm^{-3} up to 10^{14} cm^{-3} for which we can neglect nonlinear gain suppression, Δt_{ML} is almost constant, even slightly shorter for smaller P_{inj}. For this reason we present the results obtained for lower values of P_{inj}. The second optimization route is tied to the switching speed of the bistable slave laser, and will be addressed later.

In Fig. 4.20, we present calculated switching times with respect to the master laser detuning variation magnitude $\delta\omega$, for switching up [Fig. 4.20(a)], and switching down di-

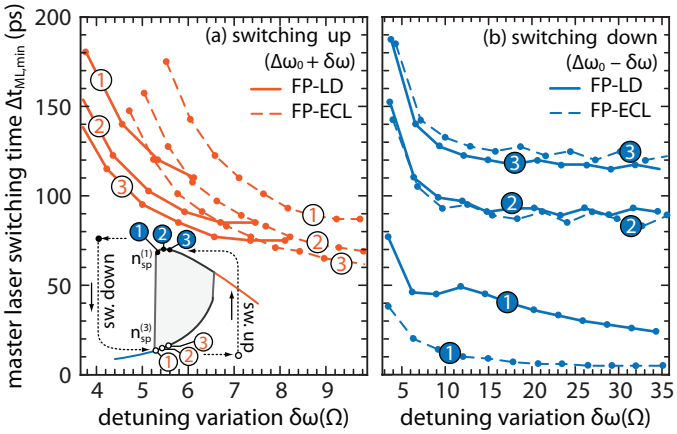

Figure 4.20: *The minimum of the master switching time Δt_{ML} for switching (a) up and (b) down, versus $\delta\omega$ for standard FP-LD (solid lines) and FP-ECL (dash lines) and for 3 different pairs of switching points on the hysteresis loop as shown in the inset.*

rection [Fig. 4.20(b)], both for FP-LD (solid lines) and FP-ECL (dashed lines), at constant injection power $P_{\text{inj}} = -12$ dBm. We present switching times for different initial points on the hysteresis loop, denoted with numbers $1-3$, though it will be addressed later. At this moment we discuss the switching time dependence on the master laser detuning variation magnitude $\delta\omega$ in general. The increase in $\delta\omega$, speeds up the transition for both directions, i.e., the switching time decreases with an increase in $\delta\omega$ (cf. Fig. 4.20). However, the detuning variation increase is more efficient for switching up, since the slave laser is more sensitive to the magnitude of $\delta\omega$ [switching time decreases more steeply in switching up direction, Fig. 4.20(a) in comparison to the switching down direction, Fig. 4.20(b)]. If $\delta\omega$ is large enough in the case of switching up, n_{ts} and $n_{\text{sp}}^{(2)}$ may exchange their positions since n_{ts} becomes closer to $n_{\text{sp}}^{(3)}$, leaving $n_{\text{sp}}^{(2)}$ between $n_{\text{sp}}^{(1)}$ and n_{ts}. This enables trajectory to circumvent n_{ts} in a short period of detuning variation. After that, the trajectory will autonomously reach $n_{\text{sp}}^{(2)}$, and from there it will follow the phase plot for $\Delta\omega_0$ slowly converging toward $n_{\text{sp}}^{(1)}$. However, the increase of $\delta\omega$ beyond the upper limit causes that n_{ts} point becomes very close, and eventually almost coincides with the starting $n_{\text{sp}}^{(3)}$ point, thus disabling the slave laser to reach $n_{\text{sp}}^{(2)}$, and finally desired $n_{\text{sp}}^{(1)}$ point. On the other hand, highly negative detuning during the switching down reduces the locking regime up to the limit in which the slave laser enters the free-running regime since $n_{\text{sp}}^{(3)}$ becomes almost equal to n_{th}, determining the upper limit for $\delta\omega$ in case of switching down. Finally, for both directions of switching, the lower limit for $\delta\omega$ is determined by the hysteresis edges, i.e., $\delta\omega$ has to be large enough to surpass the appropriate hysteresis edge.

The second approach for reduction of Δt_{ML} is to choose a suitable starting point on the hysteresis loop, providing as fast as possible switching in one or the other direction. As we have already shown, switching down is more demanding, since higher negative detuning

fails to provide fast switching. Thus, we choose the starting point $\Delta\omega_0 = -9.63\Omega$, which is on the hysteresis loop, but close to the left hysteresis edge $\Delta\omega_L$ [c.f. inset in Fig. 4.20(a)]. This case is denoted by (1). It can be seen that in this case, switching up is slower than switching down. The major reason for that lies in the fact that phase plot for such chosen $\Delta\omega_0$ generates the unstable point $n_{sp}^{(2)}$ in the vicinity of $n_{sp}^{(1)}$. Such chosen $\Delta\omega_0$ produces the dn/dt–n phase plot similar to the one obtained for $\Delta\omega_L$, for which $n_{sp}^{(1)}$ and $n_{sp}^{(2)}$ coincide [cf. Figs. 4.19(a) and (d)]. In such case, the transitional n_{ts} point stands between $n_{sp}^{(2)}$ and $n_{sp}^{(3)}$, which causes long transition from $n_{sp}^{(3)}$ around the n_{ts} toward $n_{sp}^{(2)}$. Such transition consequently requires long Δt_{ML}, which can sustain long trajectory to $n_{sp}^{(2)}$. If balanced switching times are more desirable, the starting point should be chosen at $\Delta\omega_0 = -9.43\Omega$, which is approximately 1/8 of the hysteresis width away from $\Delta\omega_L$. This case is denoted by (2), and provides that both switching times are about 100 ps, or even lower [cf. Figs. 4.20(a) and (b)]. The case (3) corresponds to the initial detuning of $\Delta\omega_0 = -9.29\Omega$, which is about 1/4 of hysteresis width away from the left hysteresis edge $\Delta\omega_L$. The results obtained for this point show, that as the starting point comes closer to the middle of the hysteresis loop, the switching up becomes faster than the switching down.

An additional method for improvement of Δt_{ML} is implementation of the FP-ECL, enabling the longer photon lifetime for the injection-locked mode, and few modes in its vicinity. Our simulations show that this approach can significantly improve switching dynamics only in certain cases. In the switching up direction, this approach can lead to somewhat shorter switching times, though on expense of larger $\delta\omega$, since FP-ECL leads to wider hysteresis loops [cf. Figs. 4.18(a) and (b)]. In the switching down direction, this approach can lead to significant improvement of the switching time in case (1), though it leads to even worse results in case (3) [cf. Fig. 4.20(b)].

4.3.2 Switching time of the slave laser

The ideal transient characteristic of the injection-locked bistable laser would be the one, which simultaneously provides minimum for both Δt_{ML} and Δt_{SL}. In order to get full insight in the slave laser switching time, we analyze the transient response of the slave laser for the shortest possible, i.e., $\Delta t_{ML,min}$. The transient response is simulated by solving the system of rate equations in its full scale, for the corresponding detuning variation $\delta\omega$, and other fixed parameters. Fig. 4.21(a) shows the transient response of the photon density for the injection-locked mode in the case of switching up for standard FP-LD (solid line) and FP-ECL (dashed line), and for the three starting points on the hysteresis loop, as introduced in previous subsection. The duration of the master laser detuning variation is set to the minimum value, which in most cases corresponds to the maximum of detuning variation shown in Fig. 4.20. It might look like that the steady state in Fig.

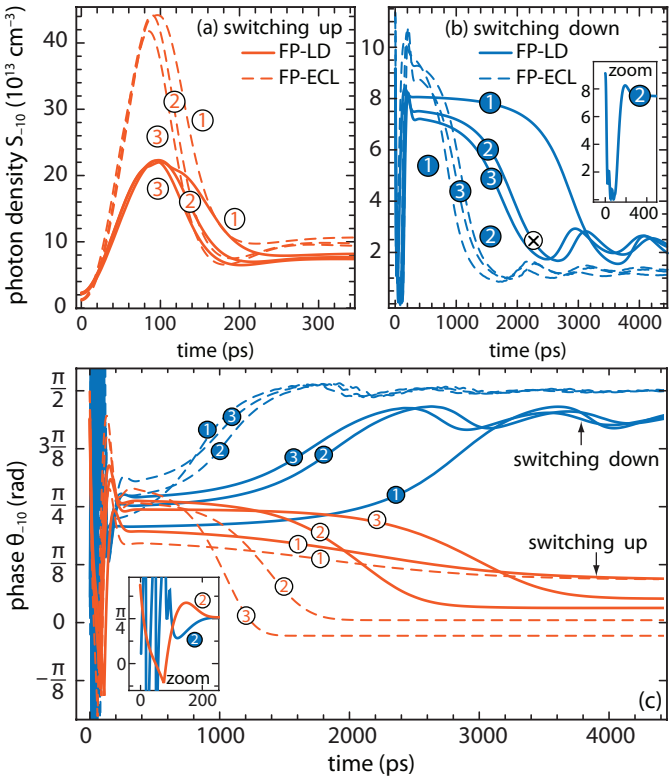

Figure 4.21: *The photon density (S_{-10}) transient response of injection-locked mode $m = -10$, for the $\Delta t_{ML,min}$ and for the switching (a) up and (b) down, for standard FP-LD (solid lines) and FP-ECL (dashed lines), and 3 different pairs of switching points on the HL. (c) The corresponding phase transient response for both switching directions. Insets in (b) and (c) show zoom of S_{-10} and θ_{-10}, respectively, for the first several hundreds of ps for switching states corresponding to case (2).*

4.21(a) is reached in less than 300 ps. However, the fact is that the slave laser is still in the vicinity of the $n_{sp}^{(2)}$ state after that time, while the transition from $n_{sp}^{(2)}$ to $n_{sp}^{(1)}$ needs one order of magnitude longer time. However, this transition corresponds to relatively small increase of the photon density, i.e., the laser will slowly, yet slightly increase its photon density, and reach the final steady-state in a time span in order of few ns. On contrary to the case of photon density, the transition from $n_{sp}^{(2)}$ to $n_{sp}^{(1)}$ corresponds to considerably large change of the phase [cf. Fig. 4.21(c)]. From the Fig. 4.21(c) it can be seen that the actual steady-state in the case of switching up is reached in few ns, depending on the starting point. On the other hand, in the case of switching down, the slave laser experiences strong relaxation oscillations [cf. Figs. 4.21(b) and (c)]. As in the case of switching up, depending on the starting point on the hysteresis loop, the slave laser needs a few ns to reach the final photon density, or phase, though here it continues to exhibit underdamped oscillations around this steady-state.

The criterion for estimation of Δt_{SL} in case of the transient response with overshoots

can be based on the common definition of rise/fall time for underdamped second order systems, which is the time required for the response to overcome the difference between the final and initial value from 0 to 100% [144]. However, the rise/fall time criterion is unrealistic, since all the responses shown in Fig. 4.21 are far away from the stationary state after rise/fall time. In addition to this, it favours the switching time for both switching directions, predicting the slave laser switching times in order of few tens of ps. Another approach is to use the "settling time" criterion, which defines the response time as the time required for the response curve to reach and stay within a range of certain percentage of the final value [145]. However, looking at the absolute values, the margins of the criterion will be different for each of the stationary states. A more serious problem comes from the fact that temporal response does not correspond to a linear second order system, but rather to a nonlinear system, which may exhibit transient response oscillations around slowly varying bounded mean value, or with non-monotonically time varying amplitudes, as we will show later. In these cases, the "settling time" criterion is too harsh, since it may unfairly prolong the switching time, even in the cases when it is obvious that slave laser has already reached the desired state. In order to achieve a more realistic estimation of Δt_{SL}, we set a new "locking time" criterion which defines Δt_{SL} as a time interval which starts simultaneously with the switching on of the master laser detuning variation, and finishes when the photon density of slave laser reaches the stationary value for the first time, followed by the quasi-relaxation oscillations regime around the stationary value of the destination state [e.g. cross marker for the case (2) in Fig. 4.21(b)]. Such definition of the switching time is not numerically rigid and accurate as the former two, however, it is more natural for the type of transitions corresponding to switching, and can provide more physically justified estimation of Δt_{SL}. It should be mentioned that the switching criterion could comprise both, the photon density and the phase, leading to different results for the slave laser switching time depending on key variable.

After applying the locking time definition, we find that $\Delta t_{\mathrm{SL}} < 200$ ps, for the switching-up transitions shown in Fig. 4.21(a). As can be expected, the starting point (3) has a slight advantage with respect to the switching time, since it is the closest one to the right hysteresis edge, which needs to be crossed during the switching. On the other hand, the switching down lasts one order of magnitude longer [c.f. Fig. 4.21(b)], introducing significant asymmetry of Δt_{SL}. The proposed improvements for Δt_{ML}, also become useful for optimization of Δt_{SL}. For the standard FP-LD, the fastest response can be achieved for the starting point (3), while in case of the FP-ECL, the results are best for the starting point (1) [cf. Fig. 4.21(b)]. The most important improvement for the switching down comes from the modification of the photon lifetime, which, in the best case, reduces Δt_{SL} twice in comparison with the result achieved for the regular photon lifetime.

Similar conclusions are valid for the phase difference temporal response [cf. Fig. 4.21(c)]. The fast variation of the phase in the first 200 ps is the consequence of the rapid photon density variation, which occurs for both switching directions. However, the phase variations are more damped for the switching up than for the switching down, due to an increase of the photon density, which suppresses the last term in the phase equation (2.21d). This term is, on the other hand, responsible for the oscillating behaviour of the phase, which intensifies with the photon density decrease. Therefore, these rapid oscillations of the phase are not related to the relaxation oscillations, which actually occur later, as shown in Fig. 4.21(b). For switching up, the fastest phase difference transition can be achieved using the FP-ECL, while the slowest using the standard FP-LD, both for starting point (3). Switching down is more dependent on photon lifetime than on the starting point. The corresponding phase transient response for the FP-ECL is almost two times faster than the one for the standard FP-LD, similarly as in the case of photon density response.

Proposed improvements are not sufficient to significantly balance the Δt_{SL} for switching up and down, and simultaneously reduce the switching down time. Since the slave laser response for switching down lasts one order of magnitude longer than all other transitions, it seems useful to investigate whether the decrease of Δt_{SL} can be achieved by an extension of Δt_{ML}, i.e., by prolonging the detuning variation. The increase of Δt_{ML} indeed leads to a decrease of Δt_{SL} for switching down, as shown in Fig. 4.22, and at the same time, does not significantly affect the transition time for switching up. In fact, for relatively short Δt_{ML}, the photon density overshoot in Fig. 4.21(a) slightly compresses with increase in Δt_{ML}, causing that Δt_{SL} somewhat decreases. The improvement shown in Fig. 4.22, achieved by the FP-ECL, is less important if the duration of the master laser detuning variation is sufficiently extended. The kinks in the dependence are the result of the proposed locking time definition and the peculiar temporal response, which is now significantly different than in the case of short Δt_{ML} [cf. Fig. 4.21(b)]. The inset in Fig. 4.22 depicts the temporal transition of the photon density for switching down, for Δt_{ML} corresponding to the minimum Δt_{SL} shown in Fig. 4.22.

The photon density temporal response reveals the nonlinear transient phenomena mentioned earlier. It can be seen that the mean value of relaxation oscillations slowly oscillates and approaches the steady-state. Additionally, the amplitude of the oscillations periodically increases and decreases. As Δt_{ML} increases, the initial peak of the relaxation oscillations becomes more suppressed. This means that for shorter Δt_{ML}, more time is needed for the transition to relax from the first relaxation peak to the stationary value for the first time. However, for a critical value of Δt_{ML}, the first relaxation oscillation peak becomes so much suppressed that the intersection with the stationary value occurs imme-

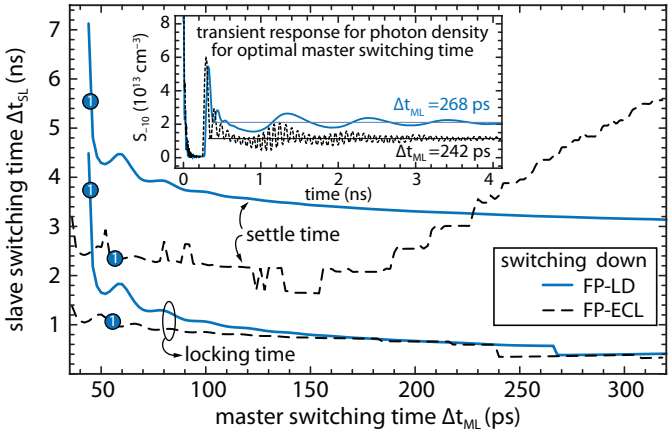

Figure 4.22: *The slave laser versus the master laser time for switching down for a pair of bistable points positioned at the left edge of the hysteresis loop for locking time and settle time criterion. (Insets) Photon density response of injection-locked mode $m = -10$ for the shortest Δt_{SL} according to locking time criterion.*

diately after it, which causes sudden drop of Δt_{SL} according to the locking time criterion. In other words, certain Δt_{ML} may lead to the special case where relaxation oscillations do not reach the stationary value after the first oscillation period, but rather require more of them, thus prolonging Δt_{SL}. This also means that the two transient responses may look very similar, but their corresponding switching times can be significantly different due to the adopted definition of locking time. However, the fact that the dependence shown in Fig. 4.22 is more or less continuous, with exception of the last part, indicates that the locking time criterion is able to detect the fine modifications of Δt_{SL} due to adjustment of Δt_{ML}. It should also be noted that the small absolute increase in Δt_{ML} (of the order of 100 ps), leads to a significant absolute decrease of Δt_{SL} (approximately 700 ps for the FP-ECL, and even 1000 ps for the standard FP-LD). After such improvement, Δt_{SL} for switching down becomes 350-400 ps. Although still larger, it is now comparable with the corresponding Δt_{ML}.

In addition, we estimate Δt_{SL} by using two standard definitions, as rise/fall time and the settling time with a range set to 10% of the steady state value. In comparison with the results obtained for the locking time definition, the standard definitions should in principle provide the extreme values of the switching time. All these definitions together might provide a deeper insight in the estimation of Δt_{SL}. First, we study rise/fall time criterion and find that in the case of both FP-LD and FP-ECL, Δt_{SL} varies from 30 to 40 ps for both switching directions. The application of the settling time criterion on the switching up transition leads to the peculiar results, according to which certain Δt_{ML} lead to the settling times shorter than the locking times, while for the others, the settling time can be one order of magnitude longer than the locking time. This essentially shows that the application of

the settling time criterion is not suitable in the case of the switching up transition due to its irregular character. However, the settling time becomes relevant figure of merit in the case of the switching down transition. Fig. 4.22 shows that the settling switching time for FP-LD structure is 3-4 times longer than the one deduced from the locking time criterion, except for the short Δt_{ML}, for which this ratio is smaller. For FP-ECL, which is switched by short Δt_{ML}, results are better than for FP-LD, since the ratio between the settling and the locking switching time is slightly larger than 2. However, for longer detuning variations the settling time for FP-ECL increases and exhibits ripples which occur due to highly nonlinear response of the slave laser. This means that implementation of FP-ECL is beneficial only if the Δt_{ML} is not too long, in this case not longer than approximately 220 ps.

The differences between the responses for the switching transitions shown in the inset of Fig. 4.22 and in Fig. 4.21(b) are related to the phase plots. As predicted in the discussion regarding the phase plots, the major difference is that responses shown in Fig. 4.22 correspond to the transient phase plot which does not involve a phase loop around the unstable point $n_{\mathrm{sp}}^{(2)}$, i.e., prolonged master laser switching time excludes the phase loop from the switching trajectory. In this case the phase trajectory almost entirely overlaps the phase plot for the stationary photon density for $\Delta\omega_{\mathrm{EL}}$, except in the vicinity of $n_{\mathrm{sp}}^{(3)}$ where, due to relaxation oscillations, characteristic spiral loop appears. However, on contrary to the theoretical prediction, the transitions for switching up, even in the case of long Δt_{ML}, comprise the phase loop around $n_{\mathrm{sp}}^{(2)}$, i.e., this phase loop cannot be avoided.

Chapter 5

Conclusion

Injection locking is a technique which relies on the general physical principle of coupled oscillators syhncronization. In this case, the technique is applied on two semiconductor lasers, representing two electrically driven electromagnetic oscillators. The coupling between the lasers is enabled via injecting the light from one (master) laser the resonator cavity of another (slave) laser. Under certain conditions, the slave laser becomes stably locked to the frequency and phase of the master laser.

Injection-locked lasers are receiving increased attention in the field of photonics since they have several potential fields of application. Since this technique enables remote locking, i.e., tuning, injection-locked lasers can substitute expensive and complex tunable lasers and offer cost-effective transmitter solution in modern architectures of optical networks such as wavelength division multiplexed passive optical networks. In addition to this, injection locking can be beneficial in terms of laser dynamics, since it has been proven that it reduces the relaxation oscillations, increases the modulation bandwidth, decreases the frequency chirp by decreasing the linewidth of the laser, reduces the mode partition noise, enhances the single-mode output, etc. Apart from this, injection-locked lasers can exhibit bistable operation, which can be put to use in photonics signal processing schemes, especially in systems comprising all-optical signal processing. For that matter, bistable injection-locked lasers can be used for realization of photonics bistable components such as all-optical flip-flops, switches, memories or different kinds of logical gates, representing the crucial building blocks for optical packet switching networks. From the perspective of all proposed applications, especially those in the field of all-optical processing, the static and dynamic characteristics of injection-locked lasers become highly important.

This thesis investigates static and dynamic characteristics of multi-mode InGaAsP/InGa AlAs multiple quantum well semiconductor laser with Fabry-Pérot cavity in the regime of side-mode, i.e., inter-modal injection locking. The investigation is based on the multi-

mode rate equation system, describing the dynamics of the carriers, photons, and their phases inside the cavity of the slave laser.

The main contributions of the thesis are following:

- A numerical algorithm for solving stationary multi-mode rate equations system is developed. The system comprises of large number of coupled nonlinear first order differential equations, which reduce to algebraic equations in the stationary analysis. This system is further reduced to a transcendental equation regarding carrier concentration, which is solved for stationary values, where each solution represents one slave laser stationary state.

- The algorithm provides possibility to determine slave laser's stationary states, and to investigate origins, as well as attractive/repelling natures of recognized stationary states. It is concluded that for positive values of frequency detuning, the slave laser exhibits only one stationary state which acts as an attractive stationary point. In the domain of negative frequency detuning, injection locking can provide up to two stationary points, among which only one is an attractor. It is shown that unlocked modes contribution leads to the formation of the third stationary point with attractive character. This point has not been a subject of discussion in the literature, since common models in the literature comprise only injection-locked longitudinal mode, while this point, and consequently slave laser's bistability, can be inferred only by a model which takes into account at least two modes (injection-locked one, and central longitudinal mode).

- Formation of the hysteresis loops in the slave laser output is theoretically investigated and hysteresis branches are correlated to the two attractors. It is shown that injection power or frequency detuning variation leads to counterclockwise hysteresis cycle in the output power and side-mode-suppression-ratio, and clockwise cycle in the output phase of the slave laser. The presence of the injection power variation induced hysteresis loop in the slave laser power output is confirmed experimentally.

- Widths and openings of the hysteresis loops are the theoretically investigated with respect to injection power, frequency detuning, and injection-locked mode order. It is shown that the output power hysteresis can exhibit an extinction ratio up to 10 dB, that separation between branches in terms of side-mode-suppression-ratio is over 30 dB, and that the phase hysteresis can exhibit opening up to $3\pi/4$ radians.

- As opposed to the common locking ranges found in the literature, the presented locking range map, for both intra- and inter-modal injection locking, predicts the downfolding of the locking range across the four-wave mixing boundary in the

domain of negative frequency detuning, which provides the multivalued character of the map, and consequently multistability of the slave laser.

- The stationary states distribution map, showing the loci of the stationary points in the relative injection power–frequency detuning space, is presented. The areas in which multiple states coexist simultaneously are recognized and discussed.

- The presented stability map provides the stability analysis of the slave laser on the basis of the Lyapunov asymptotic stability test. The system of multi-mode rate equations is linearized in the vicinity of the stationary points and stability is discussed with respect to the positions of the system eigenvalues. Stability map shows the regions in which the slave laser exhibits instabilities, one located in the domain of positive frequency detuning, and the other located for small negative detunings. In addition to this, in the domain of larger magnitude negative detunings, a region of bistable slave laser operation is presented. The stability map underlines the crucial importance of the detailed rate equation model, i.e., taking into account unlocked longitudinal modes. It is shown that the minimal requirement for bistability domain to be predicted and analyzed is a model which, apart from injection-locked mode, takes into account at least the central mode. Further expansion of the model is advised in order to increase the precision of the calculation, since it leads to significant shrinking of the regions of instabilities.

- Two switching mechanisms between the stable states are proposed: switching by injection power variation and switching by frequency detuning variation. Switching by injection power variation can provide amplitude controlled slave laser, while switching by frequency detuning variation can provide frequency or phase controlled slave laser.

- An approximate, simple analytical model for switching time calculation is developed and presented. Switching time is classified as master laser switching time, since it gives minimal required duration of the master laser's injection power or frequency variation, in order for the slave laser to switch between the stable states. In the case of injection power induced switching, a simple formula for switching energy is presented.

- Analytical model is employed in the estimation of the switching characteristics for both switching mechanisms. It is shown that master laser's switching time ranges from few ns to few tens of ps, and that with higher magnitude of injection power or frequency detuning variations, switching time decreases. However, in the case of switching by injection power variation, the model predicts noticeable discrepancy

between the switching directions: while one direction achieves very short minimal master laser's switching time (10 ps), the other direction requires few orders of magnitude longer times (few hundreds of ps). The master laser's switching energies are also unevenly distributed, for short switching times, energies are in order of few hundreds of fJ, while for longer switching times, energies can be as low as 1 fJ. In the case of frequency detuning variation, analytical model shows limited applicability, providing results for only one switching direction, which are qualitatively similar to the results obtained with the other switching mechanism.

- In the case of switching by injection power variation, it is shown that increase of the linewidth enhancement factor leads to decrease of both master lasers's switching time and energy, while increase in the active region volume can provide lower switching energies, on expense of somewhat prolonged switching time.

- Detailed numerical model and method for calculation of both master and slave laser's switching time, for both switching mechanisms is presented. Method relies on the employment of the Runge-Kutta fourth-order method on a large scale system of coupled nonlinear, non-autonomous differential equations. Numerical model is applied for calculation of the switching time in the case of frequency detuning variation, due to the limitations of the analytical model.

- Our numerical model confirmed the master laser's switching times in the range from few ns to few tens of ps. It is showed that the master laser's switching time can be improved by (*i*) increase of the magnitude of detuning variation, (*ii*) modification of the photon lifetime for injection-locked side-mode, and (*iii*) by careful selection of the initial detuning in the bistable region, corresponding to the starting point in the hysteresis loop.

- Exact numerical model is also employed in studying the slave laser's switching time, i.e., the time needed for the slave laser to lock to the desired state. It is shown that the slave laser's switching time is more critical in comparison to the time corresponding to the master laser's switching, and that there exists high discrepancy in terms of slave laser's switching time for different switching directions (around 300 ps for one, as opposed to 2–3 ns for the other switching direction). As a method of optimization, it is found that the modest increase of the master laser's switching time leads to the considerable reduction in the slave laser's switching time. Prolonging the variation of the master laser for 100 ps, brings the slave laser's switching time from 2–3 ns down to 350–400 ps, which can be obtained for both switching directions, thus balancing the discrepancy between them.

Presented investigation of static characteristics of injection-locked lasers can be useful for further development of all-optical flip-flops, based on the discussed bistability in the slave laser diode. Presented analysis regarding the formation and especially dimensions of the hysteresis loops, may be of great importance for the design parameters such as extinction ratio, or switching times and energies, which may depend on the hysteresis width. Furthermore, presented switching mechanisms can be employed for realizations of all-optical flip-flops, or even more complex all-optical processing systems such as logic gates. Both analytical and numerical model for switching time and energy estimation, providing deep insight in the slave laser dynamics, can be useful and reliable tool for development and optimization of such systems in terms of their dynamic characteristics. Finally, presented switching mechanism based on the frequency or phase control of the slave laser, combined with the results regarding the phase hysteresis opening, may be highly attractive for further implementation of advanced modulation formats comprising optical phase modulation as trigger or control signals.

Biography

Marko Krstić was born in Niš on December 29, 1984, where he attended elementary and high school. He received B.Sc. and M.Sc. degrees in electrical engineering at the School of Electrical Engineering, Department for Optoelectronics and laser techniques, University in Belgrade, in 2007 and 2009, with GPA of 8.82 and 9.83, respectively. He received his M.Sc. degree with thesis named "Analysis and modeling of injection-locked semiconductor lasers". In 2009 he started his PhD studies at the Department for Nanoelectronics and photonics, also with the School of Electrical Engineering in Belgrade.

From March 2009 he is an employee of the School of Electrical Engineering, at the Chair for Microelectronics and technical physics, where he works as a teaching assistant. In his teaching career, he has been involved in the courses regarding physics, optical communications, photonics, and electronics. In his scientific career, up to this point, he has published 13 scientific papers in the SCI journals, among which 8 are directly connected with the topic of the dissertation. During his career, he has participated in two national and two international projects. In 2014 he received the "profesor dr Ilija Stevanović" award for the best scientific paper published in the international SCI journal.

Bibliography

[1] A. Pikovsky, M. Rosenblum, and J. Kurths, *Synchronization: A Universal Concept in Nonlinear Sciences*, Cambridge University Press, 2001.

[2] D. S. Landes, *Revolution in Time: Clocks and the Making of the Modern World*, Belknap Press of Harvard University Press, 2000.

[3] S. H. Strogatz, *Nonlinear Dynamics and Chaos: With Applications to Physics, Biology, Chemistry, and Engineering*, Perseus Book Publishing, 1994.

[4] J. Buck, E. Buck, J. Case, and F. Hanson, "Control of flashing in fireflies," *Journal of Comparative Physiology A*, vol. 144, pp. 287–298, 1981.

[5] J. H. Vincent, "On some experiments in which two neighbouring maintained oscillatory circuits affect a resonating circuit," *Proceeding of the Royal Society of London B*, vol. 32, no. 1, pp. 84, 1919.

[6] E. V. Appleton, "The automatic synchronization of triode oscillators," *Proceedings of the Cambridge Philosophical Society*, vol. 21, pp. 231, 1922.

[7] E. V. Appleton, B. Van der Pol, "On the form of free triode vibrations," *The London, Edinburgh, and Dublin Philosophical Magazine and Journal of Science Series 6*, vol. 42, pp. 201–220, 1921.

[8] E. V. Appleton, B. Van der Pol, "On a type of oscillation-hysteresis in a simple triode generator," *The London, Edinburgh, and Dublin Philosophical Magazine and Journal of Science Series 6*, vol. 43, pp. 177–193, 1922.

[9] R. Adler, "A study of locking phenomena in oscillators," *Proceedings of IRE*, vol. 34, no. 6, pp. 351–357, June 1946.

[10] R. H. Pantell, "The laser oscillator with an external signal," *Proceedings of IEEE*, vol. 53, no. 5, pp. 474–477, May 1965.

[11] H. L. Stover, and W. H. Steier, "Locking of laser oscillators by light injection," *Applied Physics Letters*, vol. 8, no. 4, pp. 91–93, February 1966.

[12] C. J. Buczek, and R. J. Freiberg, "Hybrid injection locking of higher power CO_2 lasers," *IEEE Journal of Quantum Electronics*, vol. QE-8, no. 7, pp. 641–650, July 1972.

[13] R. Lang, "Injection locking properties of a semiconductor laser", *IEEE Journal of Quantum Electronics*, vol. QE-18, no. 6, pp. 976–983, June 1982.

[14] M. D. Petrović, J. Petrović, A. Daničić, M. Vukčević, B. Bojović, Lj. Hadžievski, T. Allsop, G. Lloyd and D. J. Webb, "Non-invasive respiratory monitoring using long-period fiber grating sensors," *Biomedical Optics Express* vol. 5, pp. 1136-1144, 2014.

[15] H. M. Gibbs, S. L. McCall, and T. N. C. Venkatesan, "Differential gain and bistability using a sodium-filled Fabry-Pérot interferometer," *Physical Review Letters*, vol. 36, no. 19, pp. 1135–1138, May 1976.

[16] C. Reis, G. Parca, M. Bougioukos, A. Maziotis, S. Pinna, G. Giannoulis, H. Brahmi, P. André, N. Calabretta, V. Vercesi, G. Berrettini, C. Kouloumentas, A. Bogoni, T. Chattopadhyay, D. Erasme, H. Avramopoulos, and A. Teixeira, "Experimental analysis of an all-pptical packet router," *Journal of Optical Communications and Networking*, vol. 6, no. 7, pp. 629–634, July 2014.

[17] B. E. A. Saleh, M. C. Teich, *Fundamentals of Photonics*, New York: Wiley-Interscience, 2007.

[18] B. Nakarmi, T. Q. Hoai, Y. H. Won, and X. Zhang, "Short-pulse controlled optical switch using external cavity based single mode Fabry-Pérot laser diode," *Optics Express*, vol. 22, no. 13, pp. 15424–15436, June 2014.

[19] L. Y. Chan, P. K. A. Wai, L. F. K. Lui, B. Moses, W. H. Chung, H. Y. Tam, M. S. Demokan, "Demonstration of an all-optical switch by use of a multiwavelength mutual injection-locked laser diode," *Optics Letters*, vol. 28, no. 10, pp. 837–839, May 2003.

[20] K. Huybrechts, G. Morthier, and R. Baets, "Fast all-optical flip-flop based on a single distributed feedback laser diode," *Optics Express*, vol. 16, no. 15, pp. 11405–11410, July 2008.

[21] Z. Wang, G. Verschaffelt, J. Danckaert, and Y. Siyuan, "Injection locking and switching operations of a novel retro-reflector-cavity-based semiconductor micro-ring laser," *IEEE Photonics Technology Letters*, vol. 20, no. 20, pp. 1673–1675, October 2008.

[22] D. J. McDoblumenthal, J. E. Bowers, L. Rau, H. Chow, S. Rangarajan, W. Wei, K. N. Poulsen, "Optical signal processing for optical packet switching networks," *IEEE Communications Magazine*, vol. 41, no. 2, pp. 23–29, 2003.

[23] D. Hayashi, K. Nakao, T. Katayama, and H. Kawaguchi, "All-optical 2-bit header recognition and packet switching using polarization bistable VCSELs," *Optics Express*, vol. 23, no. 7, pp. 8357–8364, March 2015.

[24] T. Katayama, T. Okamoto, and H. Kawaguchi, "All-optical header recognition and packet switching using polarization bistable VCSEL," *IEEE Photonics Technology Letters*, vol. 25, no. 9, pp. 802–805, 2013.

[25] S. Yao, Y. Mukherjee, S. J. B. Yoo, S. Dixit, "A unified study of contention-resolution schemes in optical packet- switched networks," *IEEE Journal of Lightwave Technology*, vol. 21, no. 3, pp. 672–683, March 2003.

[26] J. Wang, G. Meloni, G. Berrettini, L. Poti, and A. Bogoni, "All-optical binary counter based on semiconductor optical amplifiers," *Optics Letters*, vol. 34, no. 22, pp. 3517–3519, 2009.

[27] S. Zhang, Z. Li, Y. Liu, G. Khoe, and H. J. S. Dorren, "Optical flip-flop shift register based on an optical flip-flop memory with a single active element," *Optics Express*, vol. 13, no. 24, pp. 9708–9713, 2005.

[28] N. Pleros, D. Apostolopoulos, D. Petrantonakis, C. Stamatiadis, "Optical static RAM cell," *IEEE Photonics Technology Letters*, vol. 21, no. 2, pp. 73–75, January 2009.

[29] S. Osborne, K. Buckley, A. Amann, S. O'Brien, "All-optical memory based on the injection locking bistability of a two-color laser diode," *Optics Express*, vol. 17, no. 8, pp. 6293–6300, 2009.

[30] K. Huybrechts, T. Tanemura, K. Takeda, Y. Nakano, R. Baets, and G. Morthier, "All-optical 2R regeneration using the hysteresis in a distributed feedback laser diode," *IEEE Journal of Selected Topics in Quantum Electronics*, vol. 16, no. 5, pp. 1434–1440, 2010.

[31] H. Kawaguchi, "Bistable laser diodes and their applications: State of the art," *IEEE Journal of Selected Topics in Quantum Electronics*, vol. 3, no. 5, pp. 1254–1270, October 1997.

[32] E. Harvey, M. Pochet, J. Schmidt, and N. G. Usechak, "All-optical logic gates and wavelength conversion via the injection locking of a Fabry-Pérot semiconductor laser," *Proceedings of SPIE - THE INTERNATIONAL SOCIETY FOR OPTICAL ENGINEERING*, vol. 8628, March 2013.

[33] B. Nakarmi, H. Zhang, and Y. H. Won, "All-optical 4×10 Gbps NAND gate using single mode Fabry-Pérot laser diode," *Optics Express*, vol. 23, no. 21, pp. 26952–26961, October 2015

[34] J. Wu, B. Nakarmi, T. Q. Hoai, and Y. Hyub, "Optical bistability in side-mode injection locked dual-mode Fabry-Pérot laser diode," *AIP Advances*, vol. 3, pp. 082109, 2013.

[35] T. Q. Hoai, B. Nakarmi, and Y. H. Won, "All-optical address decoder using injection-locking property of external-cavity-based single-mode FP-LD," *IEEE Photonics Journal*, vol. 5, no. 2, pp. 7900811, April 2013.

[36] A. M. Kaplan, G. P. Agrawal, D. N. Maywar, "Optical square-wave clock generation based on an all-optical flip-flop," *IEEE Photonics Technology Letters*, vol. 22, no. 7, pp. 489–491, April 2010.

[37] C. Reis, L. Costa, A. Bogoni, A. Maziotis, A. Teixeira, C. Kouloumentas, D. Apostolopoulos, D. Erasme, G. Berrettini, G. Meloni, G. Parca, H. Brahmi, I. Tomkos, L. Poti, M. Bougioukos, P. S. Andreé, P. Zakynthinos, R. Dionisio, T. Chattopadhyay, and H. Avramoupoulos, "Evolution of all-optical flip-flops and their applications in optical communications networks," *IET Optoelectronics*, vol. 6, no. 6, pp. 263–276, December 2012.

[38] M. T. Hill, H. de Waardt, G. D. Khoe, and H. J. S. Dorren, "All-optical flip-flop based on coupled laser diodes," *IEEE Journal of Selected Topics in Quantum Electronics*, vol. 37, no. 3, pp. 405–413, March 2001.

[39] M. T. Hill, T. de Vries, H. J. S. Dorren, X. J. M. Leijtens, J. H. C. van Zantvoort, J. H. den Besten, E. Smalbrugge, Y. S. Oei, J. J. M. Binsma, G. D. Khoe, and M. K. Smit, "Integrated two-state AWG-based multiwavelength laser," *IEEE Photonics Technology Letters*, vol. 17, no. 5, pp. 956–958, 2005.

[40] M. T. Hill, H. de Waardt, G. D. Khoe, and H. J. S. Dorren, "Fast optical flip-flop by use of Mach-Zehnder interferometers," *Microwave and Optical Technology Letters*, vol. 31, no. 6, pp. 411–415, 2001.

[41] N. Calabretta, Y. Liu, F. M. Huijskens, M. T. Hill, H. de Waardt, G. D. Khoe, and H. J. S. Dorren, "Optical signal processing based on self-induced polarization rotation in a semiconductor optical amplifier," *Journal of Lightwave Technology*, vol. 22, no. 2, pp. 372–381, 2004.

[42] J. Wang, Y. Zhang, A. Malacarne, M. Yao, L. Poti, and A. Bogoni, "SOA fibre ring laser-based three-state optical memory," *IEEE Photonics Technology Letters*, vol. 20, no. 20, pp. 1697–1699, 2008.

[43] A. Trita, G. Mezosi, F. Bragheri, Y. Jin, S. Furst, W. Elsasser, I. Cristiani, M. Sorel, and G. Giuliani, "Dynamic operation of all-optical flip-flop based on a monolithic semiconductor ring laser," *ECO'08 Proceedings*, p. We2C3, Brussels 2008.

[44] M. T. Hill1, H. J. S. Dorren, T. de Vries, X. J. M. Leijtens, J. H. den Besten, B. Smalbrugge, Y. S. Oei, H. Binsma, G. D. Khoe, and M. K. Smit, "A fast low-power optical memory based on coupled micro-ring lasers," *Nature*, vol. 432, pp. 206–209, 2004.

[45] N. L. Hoang, J. S. Cho, Y. H. Won, and Y. D. Jeong, "All-optical flip-flop with high on-off contrast ratio using two injection-locked single-mode Fabry-Perot laser diodes," *Optics Express*, vol. 15, no. 8, pp. 5166–5171, April 2007.

[46] N. L. Hoang, J. S. Cho, Y. H. Won, H. J. Lee, and Y. D. Jeong, "All-optical flip-flop based on the bistability of injection locked Fabry-Perot laser diode," *Optics Express*, vol. 14, no. 9, pp. 4058–4063, May 2006.

[47] B. Nakarmi, T. Q. Hoai, Y. H. Won, and X. Zhang, "Short-pulse controlled optical switch using external cavity based single mode Fabry-Pérot laser diode," *Optics Express*, vol. 22. no. 13, pp. 15424–15436, Jun 2014.

[48] A. Murakami, "Phase locking and chaos synchronization in injection-locked semiconductor lasers," *IEEE Journal of Quantum Electronics*, vol. 39, no. 3, pp. 438–447, March 2003.

[49] A. Murakami, K. Kawashima, K. Atsuki, "Cavity resonance shift and bandwidth enhancement in semiconductor lasers with strong light injection," *IEEE Journal of Quantum Electronics*, vol. 39, no. 10, pp. 1196–1204, October 2003.

[50] J. Ohstubo, *Semiconductor Lasers: Stability, Instability, Chaos*, Springer-Verlag, Berlin, Germany, 2008.

[51] C. H. Henry, "Theory of the linewidth of semiconductor lasers," *IEEE Journal of Quantum Electronics*, vol. QE-18, no. 2, pp. 259–264, February 1982.

[52] C. L. Tang, A. Schremer, and T. Fujita, "Bistability in two-mode semiconductor lasers via gain saturation," *Applied Physics Letters*, vol. 51, no. 18, pp. 1392–1394, 1987.

[53] C. Lin, P. Ku, "Analysis of stability in two-mode laser systems," *IEEE Journal of Quantum Electronics*, vol. 32, no. 8, pp. 1377–1382, 1996.

[54] Y. C. Chen, and J. M. Liu, "Polarization bistability in semiconductor lasers," *Applied Physics Letters*, vol. 46, no. 1, pp. 16–18, January 1985.

[55] Y. C. Chen, and J. M. Liu, "Polarization bistability in semiconductor laser: Rate equation analysis," *Applied Physics Letters*, vol. 50, no. 20, pp. 1406–1408, May 1987.

[56] Y. Mori, J. Shibata, and T. Kajiwara, "Optical polarization bistability in TM wave injected semiconductor lasers," *IEEE Journal of Quantum Electronics*, vol. QE-25, no. 3, pp. 256–272, March 1989.

[57] Y. Mori, "Dynamic properties of transverse-magnetic wave injected semiconductor lasers," *IEEE Journal of Quantum Electronics*, vol. QE-27, no. 11, pp. 2415–2421, November 1991.

[58] Y. Mori, J. Shibata, and T. Kajiwara, "Analysis of optical polarization bistability in transverse-magnetic wave injected semiconductor lasers," *Journal of Applied Physics*, vol. 67, no. 5, pp. 2223–2228, March 1990.

[59] S. Kobayashi, T. Kimura, "Injection locking characteristics of an AlGaAs semiconductor laser," *IEEE Journal of Quantum Electronics*, vol. 16, no. 9, pp. 915–917, September 1980.

[60] K. Iwashita and K. Nakagawa, "Suppression of mode partition by laser diode light injection," *IEEE Journal of Quantum Electronics*, vol. 18, no. 10, pp. 1669–1674, October 1982.

[61] D. J. Maylon, A. P. McDonna, "102 km unrepeatered monomode fibre system experiment at 140 Mbit/s with an injection locked 1.52 μm laser transmitter," *Electronics Letters*, vol. 18, no. 11, pp. 445–447, 1982.

[62] C. H. Lee, *Microwave Photonics*, CRC Press, Taylor & Francis Group, 2007.

[63] C. Lin and F. Mengel, "Reduction of frequency chirping and dynamic linewidth in high-speed directly modulated semiconductor lasers by injection locking," *Electronics Letters*, vol. 20, pp. 1073–1075, 1984.

[64] S. Piazzolla, P. Spano, and M. Tamburrini, "Small signal analysis of frequency chirping in injection-locked semiconductor lasers," *IEEE Journal of Quantum Electronics*, vol. QE-22, pp. 2219–2223, 1986.

[65] P. Gallion, H. Nakajima, G. Debarge, C. Chabran, "Contribution of spontaneous emission to the linewidth of an injection-locked semiconductor laser," *Electronics Letters*, vol. 21, no. 14, pp.626–628, 1985.

[66] N. A. Olsson, H. Temkin, R. A. Logan et al., "Chirp-free transmission over 82.5 km of single mode fibers at 2 Gbit/s with injection locked DFB semiconductor lasers," *Journal of Lightwave Technology*, vol. 3, no. 1, pp. 63–67, February 1985.

[67] S. Mohrdiek, H. Burkhard, and H. Walter, "Chirp reduction of directly modulated semiconductor lasers at 10 Gb/s by strong CW light injection," *Journal of Lightwave Technology*, vol. 12, pp. 418–24, 1994.

[68] X. J. Meng, C. Tai, and M. C. Wu, "Improved intrinsic dynamic distortions in directly modulated semiconductor lasers by optical injection locking," *IEEE Transactions on Microwave Theory & Techniques*, vol. 47, pp. 1172–1176, 1999.

[69] T. B. Simpson, J. M. Liu, "Enhanced modulation bandwidth in injection-locked semiconductor lasers," *IEEE Photonics Technology Letters*, vol. 9, no. 10, pp. 1322–1324, 1997.

[70] J. Wang, M. K. Haldar, L. Lin, F. V. C. Mendis, "Enhancement of modulation bandwidth of laser diodes by injection locking," *IEEE Photonics Technology Letters*, vol. 8, pp. 34–36, January 1996.

[71] J. M. Liu, H. F. Chen, X. J. Meng, and T. B. Simpson, "Modulation bandwidth, noise, and stability of a semiconductor laser subject to strong injection locking," *IEEE Photonics Technology Letters*, vol. 9, pp. 1325–1327, 1997.

[72] L. Chrostowski, X. Zhao, C. J. Chang-Hasnain et al., "50-GHz optically injection-locked 1.55-μm VCSELs," *IEEE Photonics Technology Letters*, vol. 18, 367–369, 2006.

[73] E. K. Lau, H. Sung, M. C. Wu, "Frequency response enhancement of optical injection-locked lasers," *IEEE Journal of Quantum Electronics*, vol. 44, no. 1, pp. 90–99, January 2008.

[74] Y. Hong and K. A. Shore, "Locking characteristics of a side-mode injected semiconductor laser," *IEEE Journal of Quantum Electronics*, vol. 35, pp. 1713–1717, 1999.

[75] A. G. R. Zlitni, M. M. Krstić, and D. M. Gvozdić, "Modulation response and bandwidth of injection-locked Fabry-Pérot laser diodes," *Physica Scripta*, vol. T149, p. 014033, April 2012.

[76] X. Jin and S. L. Chuang, "Relative intensity noise characteristics of injection-locked semiconductor lasers," *Applied Physics Letters*, vol. 77, pp. 1250–1252, 2000.

[77] T. B. Simpson, J. M. Liu, and A. Gavrielides, "Bandwidth enhancement and broadband noise reduction in injection- locked semiconductor lasers," *IEEE Photonics Technology Letters*, vol. 7, pp. 709–711, 1995.

[78] C. W. Chow, C. S. Wong, H. K. Tsang, "All-optical modulation format conversion and multicasting using injection-locked laser diodes," *Journal of Lightwave Technology*, vol. 22, no. 11, pp. 2386–2392, 2004.

[79] Y. Wu, X. Xiong, Y. Zhu, J. Meng, and J. He, "All-optical wavelength conversion using optical injection induced wavelength switching in V-cavity laser," *Progress In Electromagnetics Research Symposium Proceedings*, Guangzhou, China, August 25–28, 2014.

[80] Y. Lu, F. Liu, M. Qiu, and Y. Su, "All-optical format conversions from NRZ to BPSK and QPSK based on nonlinear responses in silicon microring resonators," *Optics Express*, vol. 15, no. 21, pp. 14275–14282, 2007.

[81] T. Kawanishi, T. Sakamoto, and M. Izutsu, "All-optical modulation format conversion from frequency-shift-keying to phase-shift-keying," *Optics Express*, vol. 13, no. 20, pp. 8038–8044, 2005.

[82] R. Hui, "Optical PSK modulation using injection-locked DFB semiconductor lasers," *IEEE Photonics Technology Letters,* vol. 2, no. 10, pp. 743–746, October 1990.

[83] N. Kashima and K. Kikushima, "New optical star-bus network for subscriber," *Journal of Optical Communications*, vol. 11, no. 2, pp. 42–49, 1990.

[84] N. Kashima, "Upgrade of passive optical subscriber network," *Journal of Lightwave Technology*, vol. 9, no. 1, pp. 113–120, January 1991.

[85] N. Kashima, S. Yamaguchi, S. Ishii, "Optical transmitter using side-mode injection locking for high-speed photonic LANs," *Journal of Lightwave Technology*, vol. 22, no. 2, pp. 550–557, February 2004.

[86] N. Kashima, M. Watanabe, "Transient properties of side-mode injection locking in an FPLD," *Journal of Lightwave Technology*, vol. 24, no. 3, pp. 1523–1533, March 2006.

[87] N. Kashima, "Dynamic properties of FP-LD transmitters using side-mode injection locking for LANs and WDM-PONs," *Journal of Lightwave Technology*, vol. 24, no. 8, pp. 3045–3058, August 2006.

[88] C. W. Chow, C. S. Wong, and H. K. Tsang, "8×10 Gb/s multi-wavelength injection locking of a FP laser diode for WDM multicast," *presented at IEEE Lasers and Electro-Optics Society*, Tucson, Arizona, 2003.

[89] Z. Xu, Y. J. Wen, W. Zhong, C. Chae, X. Cheng, Y. Wang, C. Lu, and J. Shankar, "High-speed WDM-PON using CW injection-locked Fabry-Pérot laser diodes," *Optics Express*, vol. 15, no. 6, pp. 2953–2962, 2007.

[90] A. Kaszubowska, P. Anandarajah, and L. P. Barry, "Improved performance of a hybrid radio/fiber system using a directly modulated laser transmitter with external injection,"" *IEEE Photonics Technology Letters*, vol. 14, pp. 233–235, 2002.

[91] L. Hai-Han, H. Hsu-Hung, S. Heng-Sheng, and W. Ming-Chuan, "Fiber optical CATV system-performance improvement by using external light-injection technique," *IEEE Photonics Technology Letters*, vol. 15, pp. 1017–1019, 2003.

[92] C. Lin, H. Lu, C. Li, P. Wu, P. Peng, T. Jhang, and C. Lin, "Employing injection-locked FP LDs to set up a hybrid CATV/MW/MMW WDM light wave transmission system," *Optics Letters*, vol. 39, no. 13, 3931–3934, 2014.

[93] F. Mogensen, H. Olesen, and G. Jacobsen, "Locking conditions and stability properties for a semiconductor laser with external light injection," *IEEE Journal of Quantum Electronics*, vol. QE-21, pp. 784–793, 1985.

[94] I. Petitbon, P. Gallion, G. Debarge, and C. Chabran, "Locking bandwidth and relaxation oscillations of an injection-locked semiconductor laser," *IEEE Journal of Quantum Electronics*, vol. 24, pp. 148–154, 1988.

[95] J. Sacher, D. Baums, P. Panknin, W. Elsasser, and E. O. Gobel, "Intensity instabilities of semiconductor lasers under current modulation, external light injection and delayed feedback," *Physical Review A*, vol. 45, pp. 1893–1905, 1992.

[96] T. B. Simpson, J. M. Liu, A. Gavrielides, V. Kovanis, and P. M. Alsing, "Period doubling route to chaos in a semiconductor laser subject to optical injection," *Applied Physics Letters*, vol. 64, pp. 3539–3541, 1994.

[97] R. Hui, A. D'Ottavi, A. Mecozzi, and P. Spano, "Injection locking in distributed feedback semiconductor lasers," *IEEE Journal of Quantum Electronics*, vol. 27, no. 6, pp. 1688–1695

[98] R. Gordon, "Fabry-Pérot semiconductor laser injection locking," *IEEE Journal of Quantum Electronics,* vol. 42, no. 4, pp. 353–356, April 2006.

[99] P. Debernardi, "Locking characteristics of Fabry-Pérot semiconductor laser oscillators with side-mode injection," *Optics Letters*, vol. 21, no. 9, pp. 656–658, May 1996.

[100] S. K. Hwang, and J. M. Liu, "Dynamical characteristics of an optically injected semiconductor laser," *Optical Communications*, vol. 183, no. 1–4, pp. 195–205, September 2000.

[101] L. Lin, "Optical bistability in semiconductor lasers under intermodal light injection," vol. 32, no. 2, pp. 248–256, February 1996.

[102] V. Kovanis, T. Erneux, and A. Gavrielides, "Largely detuned injection-locked semiconductor lasers," *Optics Communications*, vol. 159, pp. 177–183, January 1999.

[103] Y. Hong, and K. A. Shore, "Observation of optical bistability in a GaAlAs semiconductor laser under intermodal injection locking," *Optics Letters*, vol. 23, no. 21, pp. 1689–1691, November 1998.

[104] L. A. Coldren, S. W. Corzine, and M. L. Mašanović, *Diode Lasers and Photonic Integrated Circuits*, New York: Wiley-Interscience, 2012.

[105] S. L. Chuang, *Physics of Optoelectronics Devices*, New York: Wiley-Interscience, 1995.

[106] E. K. Lau, L. J. Wong, X. Zhao, Y. Chen, C. J. Hasnain, M. C. Wu "Bandwidth enhancement by master modulation of optical injection-locked lasers," *Journal of Lightwave Technology*, vol. 26, no. 15, pp. 2584–2593, August 2008.

[107] E. K. Lau, L. J. Wong, M. C. Wu, "Enhanced modulation characteristic of optical injection-locked lasers: A tutorial," *IEEE Journal of Selected Topics in Quantum Electronics*, vol. 15, no. 3, pp. 618–633 May/June 2009.

[108] M. Pochet, N. A. Naderi, N. B. Terry, V. Kovanis, L. F. Lester, "Dynamics behaviour of an injection-locked quantum-dash Fabry-Pérot laser at zero-detuning," *Optics Express*, vol. 17, no. 23, pp. 20623–20630, October 2009.

[109] N. A. Naderi, M. Pochet, F. Grillot, N. B. Terry, V. Kovanis, L. F. Lester, "Modeling the injection-locked behaviour of a quantum dash semiconductor laser," *IEEE Journal of Selected Topics in Quantum Electronics*, vol. 15, no. 3. pp. 563–571 May/June 2009.

[110] C. Chang, L. Chrostowski, C. J. Hasnain, "Injection locking of VCSELs," *IEEE Journal of Selected Topics in Quantum Electronics*, vol. 9, no. 5, pp. 1386–1393 September 2003.

[111] K. Otsuka, S. Tarucha, "Theoretical studies on injection locking and injection-induced modulation of laser diodes," *IEEE Journal of Quantum Electronics*, vol. QE-17, no. 8, pp. 1515–1521 August 1981.

[112] J. Luo, M. Osinski, J. G. McInerney, "Side-mode injection locking of semiconductor lasers," *IEE Proceedings J*, vol. 136, no. 1, pp. 33–37, February 1989.

[113] T. B. Simpson, "Mapping the nonlinear dynamics of a distributed feedback semiconductor laser subject to external optical injection," *Optics Communications*, vol. 215, pp. 135–151, 2003.

[114] M. M. Krstić, J. V. Crnjanski, and D. M. Gvozdić , "Injection power and detuning-dependent bistability in Fabry-Pérot laser diodes," *IEEE Journal of Selected Topics in Quantum Electronics*, vol. 18, no. 2, pp. 826–833, March/April 2012.

[115] M. M. Krstić, J. V. Crnjanski, M. L. Mašanović, L. A. Johansson, L. A. Coldren, and D. M. Gvozdić , "Multivalued stability map of an injection-locked semiconductor laser," *IEEE Journal of Selected Topics in Quantum Electronics*, vol. 19, no. 4, pp. 1501408, May 2013.

[116] M. M. Krstić, J. V. Crnjanski, A. R. Totović and D. M. Gvozdić, "Switching of bistable injection-locked Fabry-Pérot laser by frequency detuning variation," *IEEE Journal of Selected Topics in Quantum Electronics*, vol. 21, no. 6, pp. 1801509, 2015.

[117] R. V. Pajković, M. M. Krstić, J. V. Crnjanski, A. R. Totović, and D. M. Gvozdić, "Phase space of tristability in dual injection-locked Fabry-Pérot laser diodes," *Telfor Journal*, vol. 7, no. 1, pp. 43–48, 2015.

[118] M.M. Krstić, M. L. Mašanović, J.V. Crnjanski, L. Johansson, L. Coldren, and D. M. Gvozdić, "Detailed stability map and bistability investigation for injection-locked Fabry-Pérot semiconductor lasers," *23rd IEEE International Semiconductor Laser Conference (ISLC)*, pp. 126–127, San Diego, CA 2012.

[119] M. M. Krstić, and D. M. Gvozdić, "Side-mode-suppression-ratio of injection-locked Fabry-Pérot lasers," *Acta Physica Polonica - Series A*, vol. 116, pp. 664–667, 2009.

[120] E. Kapon, *Semiconductor Lasers I: Fundamentals*, Academic Press, San Diego, CA, 1999.

[121] M. Willatzen, A. Uskov, J. Mørk, H. Olesen, B. Tromborg, A. Jahuo, "Nonlinear gain suppression in semiconductor lasers due to carrier heating," *IEEE Photonics Technology Letters*, vol. 3. no. 7, pp. 606–609, July 1991.

[122] C. H. Henry, N. A. Olsson, and N. K. Dutta, "Locking range and stability of injection locked 1.54 μm InGaAsP semiconductor lasers," *IEEE Journal of Quantum Electronics*, vol. QE-21, no. 8, pp. 1152–1156, August 1985.

[123] S. Kamaleddin, Y. Nikravesh, *Nonlinear Systems Stability Analysis: Lyapunov-Based Approach*, CRC Press, Taylor & Francis Gropup, 2013.

[124] M. N. Akram, C. Silfvenius, O. Kjebon, and R. Schatz, "Design optimization of InGaAsP-InGaAlAs 1.55 μm strain-compensated MQW lasers for direct modulation applications," *Semiconductor Science Technology*, vol. 19, pp. 615–625, 2004.

[125] C. G. Van de Walle, "Band lineups and deformation potentials in the model-solid theory," *Physical Review B*, vol. 39, pp. 1871–1883, January 1989.

[126] I. Vurgaftman, J. R. Meyer, and L. R. Ram-Mohan, "Band parameters for III-V compound semiconductors and their alloys," *Journal of Applied Physics*, vol. 89, pp. 5815–5875, 2001.

[127] A. T. Meney, B. Gonul, and E. P. O'Reilly, "Evaluation of various approximations used in the envelope-function method," *Physical Review B*, vol. 50, pp. 10893–10904, October 1994.

[128] D. M. Gvozdić and U. Ekenberg, "Superefficient electric-field-induced spin-orbit splitting in strained p-type quantum wells," *Europhysics Letters*, vol. 73, pp. 927–933, March 2006.

[129] K. A. Kaduki and W. Batty, "Envelope function approximation (EFA) bandstructure calculations for III-V nonsquare stepped alloy quantum wells incorporating ultra-narrow (~ 5 Å) epitaxial layers," *Physica Scripta*, vol. 61, pp. 213–221, 2000.

[130] J. Minch, S. H. Park, T. Keating, and S. L. Chuang, "Theory and experiment of $In_{1-x}Ga_xAs_yP_{1-y}$ and $In_{1-x-y}Ga_xAl_y$ as long-wavelength strained quantum well lasers," *IEEE Journal of Quantum Electronics*, vol. 35, no. 5, pp. 771–782, May 1999.

[131] V. Topić, J. Crnjanski, M. Krstić, A. Totović, and D. Gvozdić, "Analytical method for calculation of the photon lifetime and external coupling coefficient in index-coupled phase-shifted DFB lasers" *IEEE Journal of Selected Topics in Quantum Electronics*, vol. 21, no. 6, p. 1503209, 2015.

[132] N. Schunk, and K. Petermann, "Noise analysis of injection-locked semiconductor injection lasers," *IEEE Journal of Quantum Electronics*, vol. QE-22, no. 5, pp. 642–650, May 1986.

[133] C. Chang, "High speed vertical cavity surface emitting lasers with injection locking," Ph.D. dissertation, University of California at Berkley, 2002.

[134] R. Nietzke, P. Panknin, W. Elsässer, and E. O. Göbel, "Four-wave-mixing in GaAs/AlGaAs semiconductor lasers," *IEEE Journal of Quantum Electronics*, vol. 25, no. 6, pp. 1399–1406, June 1989.

[135] X. Jin and S. L. Chuang, "Bandwidth enhancement of Fabry-Pérot quantum-well lasers by injection locking," *Solid State Electronics*, vol. 50, pp. 1141, 2006.

[136] M. C. Pochet, N. A. Naderi, V. Kovanis, and L. F. Lester, "Modeling the dynamic response of an optically-injected nanostructure diode laser," *IEEE Journal of Quantum Electronics*, vol. 47, no. 6, pp. 827–833, Jun 2011.

[137] A. Hurtado, M. Nami, I. D. Henning, M. J. Adams, and L. F. Lester, "Bistability patterns and nonlinear switching with very high contrast ratio in a 1550 nm quantum dash semiconductor laser," *Applied Physics Letters*, vol. 101, pp. 161117–161121, 2012.

[138] D. M. Gvozdić, M. M. Krstić, and J. V. Crnjanski, "Switching time in optically bistable injection-locked semiconductor lasers," *Optics Letters*, vol. 36, no. 21, pp. 4200–4202, 2011.

[139] M. M. Krstić, J. V. Crnjanski and D. M. Gvozdić, "Switching time and energy in bistable injection-locked semiconductor multi-quantum-well Fabry-Pérot lasers," *Physical Review A*, vol. 88, pp. 063826, 2013.

[140] M. Krstić, J. Crnjanski, A. Totović, and D. Gvozdić, "Comparison of switching times in optically bistable injection-locked semiconductor lasers," *Physica Srcipta*, vol. T-162, p. 014036, 2014.

[141] C. W. Chow, C. S. Wong, H. K. Tsang, "All-optical data-format and wavelength conversion in two-wavelength injection-locked slave Fabry-Perot laser diodes," *Electronics Letters*, vol. 39, pp. 997–999, 2003.

[142] M. Mašanović, V. Lal, J. Summers, J. Barton, E. Skogen, L. Rau, L. Coldren, and D. Blumenthal, "Widely tunable monolithically integrated all-optical wavelength converters in InP," *IEEE Journal of Lightwave Technology*, vol. 23, pp. 1350–1362, 2005.

[143] Kendall E. Atkinson, *Numerical Analysis*, John Wiley & Sons, 1989.

[144] W. S. Levine, *The Control Handbook*, Boca Raton, FL: CRC Press, 1996.

[145] T. T. Tay, I. M. Mareels, and J. B. Moore, *High Performance Control*, Birkhauser, 1997.

[146] A. R. Totović, J. V. Crnjanski, M. M. Krstić, M. L. Mašanović, and D. M. Gvozdić, "A self consistent numerical method for calculation of steady-state characteristics of traveling-wave and reflective SOAs," *IEEE Journal of Selected Topics in Quantum Electronics*, vol. 19, pp. 3000411, 2013.

Прилог 1.

Изјава о ауторству

Потписани-а Марко Крстић

број индекса 2009/5024

Изјављујем

да је докторска дисертација под насловом

Statical and dynamical characteristics of injection-locked Fabry-Pérot laser diodes

- резултат сопственог истраживачког рада,
- да предложена дисертација у целини ни у деловима није била предложена за добијање било које дипломе према студијским програмима других високошколских установа,
- да су резултати коректно наведени и
- да нисам кршио/ла ауторска права и користио интелектуалну својину других лица.

Потпис докторанда

У Београду, 29.12.2015.

Марко Крстић

Прилог 2.

Изјава о истоветности штампане и електронске верзије докторског рада

Име и презиме аутора Марко Крстић

Број индекса 2009/5024

Студијски програм Наноелектроника и фотоника

Наслов рада Statical and dynamical characteristics of injection-locked Fabry-Pérot laser diodes

Ментор проф. др Дејан Поповић

Потписани/а Марко Крстић

Изјављујем да је штампана верзија мог докторског рада истоветна електронској верзији коју сам предао/ла за објављивање на порталу **Дигиталног репозиторијума Универзитета у Београду.**

Дозвољавам да се објаве моји лични подаци везани за добијање академског звања доктора наука, као што су име и презиме, година и место рођења и датум одбране рада.

Ови лични подаци могу се објавити на мрежним страницама дигиталне библиотеке, у електронском каталогу и у публикацијама Универзитета у Београду.

Потпис докторанда

У Београду, 29.12.2015.

Марко Крстић

Прилог 3.

Изјава о коришћењу

Овлашћујем Универзитетску библиотеку „Светозар Марковић“ да у Дигитални репозиторијум Универзитета у Београду унесе моју докторску дисертацију под насловом:

Statical and dynamical characteristics of injection-locked Fabry-Pérot laser diodes

која је моје ауторско дело.

Дисертацију са свим прилозима предао/ла сам у електронском формату погодном за трајно архивирање.

Моју докторску дисертацију похрањену у Дигитални репозиторијум Универзитета у Београду могу да користе сви који поштују одредбе садржане у одабраном типу лиценце Креативне заједнице (Creative Commons) за коју сам се одлучио/ла.

1. Ауторство

(2.) Ауторство - некомерцијално

3. Ауторство – некомерцијално – без прераде

4. Ауторство – некомерцијално – делити под истим условима

5. Ауторство – без прераде

6. Ауторство – делити под истим условима

(Молимо да заокружите само једну од шест понуђених лиценци, кратак опис лиценци дат је на полеђини листа).

Потпис докторанда

У Београду, 29.12.2015.

Марко Ђ.

1. Ауторство - Дозвољавате умножавање, дистрибуцију и јавно саопштавање дела, и прераде, ако се наведе име аутора на начин одређен од стране аутора или даваоца лиценце, чак и у комерцијалне сврхе. Ово је најслободнија од свих лиценци.

2. Ауторство – некомерцијално. Дозвољавате умножавање, дистрибуцију и јавно саопштавање дела, и прераде, ако се наведе име аутора на начин одређен од стране аутора или даваоца лиценце. Ова лиценца не дозвољава комерцијалну употребу дела.

3. Ауторство - некомерцијално – без прераде. Дозвољавате умножавање, дистрибуцију и јавно саопштавање дела, без промена, преобликовања или употребе дела у свом делу, ако се наведе име аутора на начин одређен од стране аутора или даваоца лиценце. Ова лиценца не дозвољава комерцијалну употребу дела. У односу на све остале лиценце, овом лиценцом се ограничава највећи обим права коришћења дела.

4. Ауторство - некомерцијално – делити под истим условима. Дозвољавате умножавање, дистрибуцију и јавно саопштавање дела, и прераде, ако се наведе име аутора на начин одређен од стране аутора или даваоца лиценце и ако се прерада дистрибуира под истом или сличном лиценцом. Ова лиценца не дозвољава комерцијалну употребу дела и прерада.

5. Ауторство – без прераде. Дозвољавате умножавање, дистрибуцију и јавно саопштавање дела, без промена, преобликовања или употребе дела у свом делу, ако се наведе име аутора на начин одређен од стране аутора или даваоца лиценце. Ова лиценца дозвољава комерцијалну употребу дела.

6. Ауторство - делити под истим условима. Дозвољавате умножавање, дистрибуцију и јавно саопштавање дела, и прераде, ако се наведе име аутора на начин одређен од стране аутора или даваоца лиценце и ако се прерада дистрибуира под истом или сличном лиценцом. Ова лиценца дозвољава комерцијалну употребу дела и прерада. Слична је софтверским лиценцама, односно лиценцама отвореног кода.